ALMA MATER STUDIORUM
UNIVERSITÀ DI BOLOGNA

DOTTORATO DI RICERCA IN

TECNOLOGIE INNOVATIVE E USO SOSTENIBILE DELLE RISORSE DI PESCA E BIOLOGICHE DEL MEDITERRANEO (FISHMED-PHD)

Ciclo 36

Settore Concorsuale: 03/B1 - FONDAMENTI DELLE SCIENZE CHIMICHE E SISTEMI INORGANICI
Settore Scientifico Disciplinare: CHIM/03 – CHIMICA GENERALE E INORGANICA

VALORIZATION OF BIOMATERIALS FROM CALCIFYING MARINE ORGANISM WASTE

Presentata da: Carla Triunfo

Coordinatore Dottorato
Stefano Goffredo

Supervisore
Giuseppe Falini

Esame finale anno 2024

Abstract

Marine aquaculture and fishery industries produce millions of tonnes of waste every year. According to FAO, global fish production reached about 179 million tonnes in 2018 and the 70 wt% of the processed seafood was discharged as waste. This waste is often just dumped in the sea or disposed in landfill in developing countries while in developed countries their disposal can be costly. Shells, in particular, represent the main marine waste but they also harbour useful chemicals such as chitin, protein and calcium carbonate. So, turning cast off shells into new materials, applying the concept of a circular economy, would benefit both the environment and the economy.

Mussel shells, for example, are mainly built up of single crystals of calcite and aragonite in an external and an internal layer, respectively. The recovery of these biomineral building units offers the possibility to overcome the synthetic difficulties in replicating the ability of organisms to act as crystal shapers and morphology modifiers.

Mollusk shells are a massive source of biogenic calcium carbonate (bCC) that can potentially substitute ground and precipitated calcium carbonate. These materials can be used as filler in polymeric matrices after a surface coating with hydrophobic molecules.

bCC may also be transformed into a new added-value material such as apatite with cytocompatible and osteoinductive properties for biomedical applications or it may be converted into nano-crystalline and amorphous calcium carbonate for applications that span from medical to material science.

bCC can also be extracted from crab and shrimp shells individually or in combination with other molecules such as proteins and chitin for potential applications as dye adsorbents.

Therefore, this thesis aimed to valorise seafood wastes from different calcifying marine organisms by recovering the biomaterials they are composed of and using them for different applications exploiting their unique features as biominerals.

Index

Chapter 1. General introduction

Biomineralization and biominerals in marine environment

The word biomineralization was introduced for the first time by H. K. Erben as the title of the journal "Biomineralization Research Reports" published for a few years around 1970 [1]. The term biomineralization refers to the process by which living organisms produce hierarchical organic/inorganic composites referred as biominerals [2]. This hybrid composition confers these materials unique structural and mechanical properties not obtainable via synthetic routes. In a general overview, this process involves the selective uptake of different elements from the surrounding environment and their incorporation into functional structures to form hard bioinorganic materials [3]. During the last decades, the scientific community paid much more attention on the formation mechanism, the structure and the proprieties of these biomaterials. Biominerals, in fact, are the objects of study in many fields such as archaeology, paleontology, orthopaedics, dentistry, oceanology, evolution and material science (Fig. 1) [2]. If you look around, you can observe this kind of structures everywhere. Just looking in the mirror, for example, you can see your theet that are formed of the mineral hydroxyapatite.

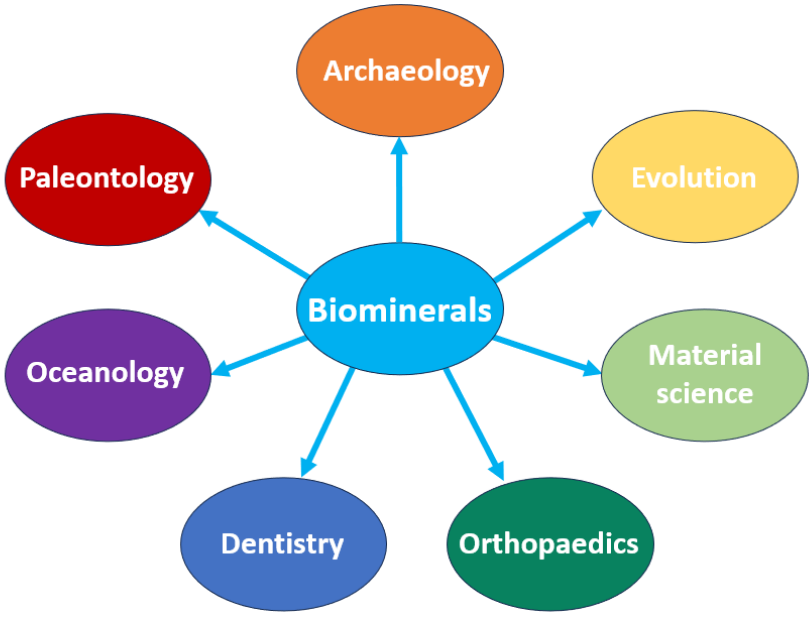

Figure 1. Different fields involving the study of biominerals.

The formation mechanism of biominerals presupposes a strict biological control by the organic matrix (proteins, carbohydrates and lipids) even if it is a minor constituent in term of weight percentage (1-5 wt%) [4]. By now it is known that for nucleation and growth to occur, biomineral formation requires a localized zone that achieves and maintains a sufficient supersaturation (Fig. 2). In most biological systems, the site of mineral deposition is isolated

from the environment by a physical delimiting geometry [5]. Ion supply occurs in this privileged space by two means: active pumping associated with organelles near the sites of mineralization or passive diffusion gradients. The cells involved in the space delimitation also synthetize an array of macromolecules which are then secreted into the extracellular space to form the organic matrix framework [2]. At is point it is important to make a distinction between biologically induced versus biologically controlled biomineralization. The former generally occurs when the side-products of metabolism that are dependent on environmental conditions create a chemical condition that favours the mineral formation but there is a minor control over the mineral features whereas the mineral formed by a biologically controlled mechanism are products of specialized, genetically controlled metabolic processes. The organic matrix, therefore, can act as an active surface to initiate the crystal nucleation and growth starting from an amorphous phase (in both the biologically induced and the biologically controlled mechanisms) that, as final step, crystallizes into a crystalline one [6]. In the biologically controlled biomineralization, moreover, the organic matrix also affects the shape, size, morphology, composition and the final location of the crystals [5].

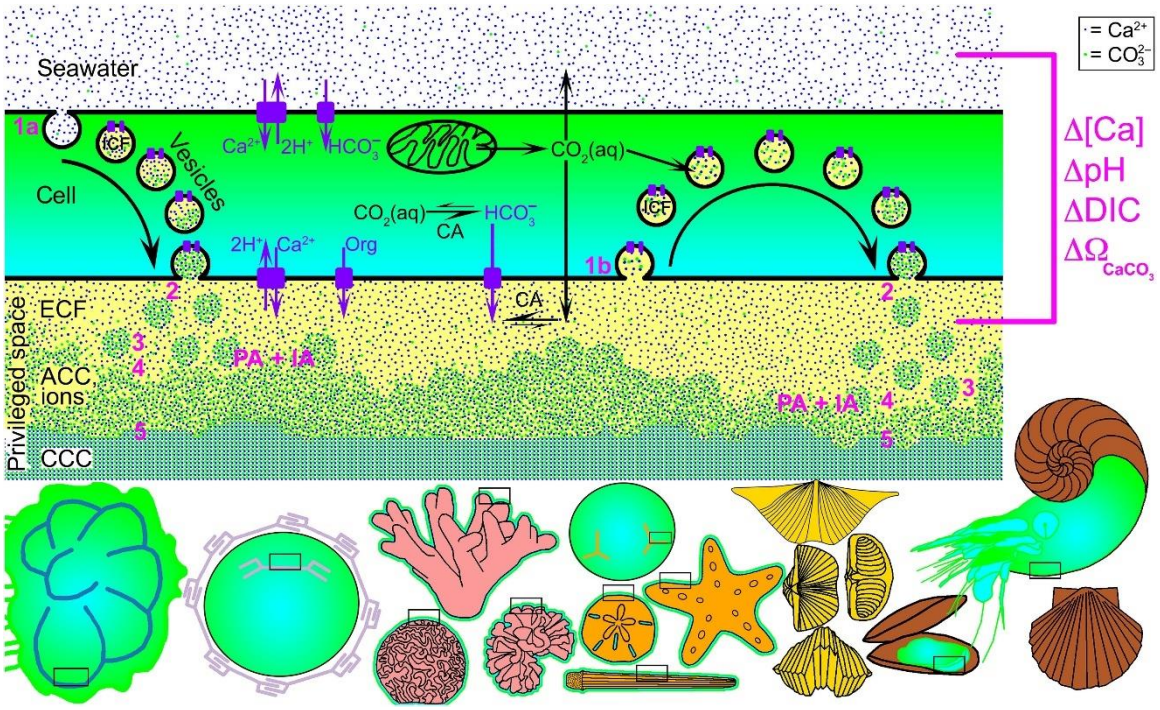

Figure 2. Integrated model for $CaCO_3$ biomineralization mechanisms in all marine organisms. Image source: [7]. Acronyms: ICF and ECF (Intra and Extracellular Calcifying Fluid), ACC and CCC (Amorphous and Crystalline Calcium Carbonate), PA and IA (Particle and Ion Attachment).

In the marine environment, biomineralization is performed by a wide range of living organisms going from mollusks, brachiopods, arthropods and sponges to corals, sea urchins, coccoliths, and foraminifera [4]. The biominerals they form can have several distinct functions such as tissues support, protection from mechanical damage as in the case of embryonic eggshells [8] or from UV radiations [9], photosynthesis like in coccoliths [10], earth magnetic field detection for magnetotactic bacteria [11], etc.

In nature there are more than 60 types of biogenic minerals and a huge variety of known biomineral structures depending on the diversity of the organic matrix [4]. Among the most diffuse biogenic minerals there are calcium carbonate, calcium phosphate, calcium oxalate and silica. Most of the marine organisms, anyway, secrets calcium carbonate to form their mineralized structure. Figure 3 shows some examples of marine calcifying organisms such as coccolithophores, sea urchins, mollusks, corals, and crustaceans.

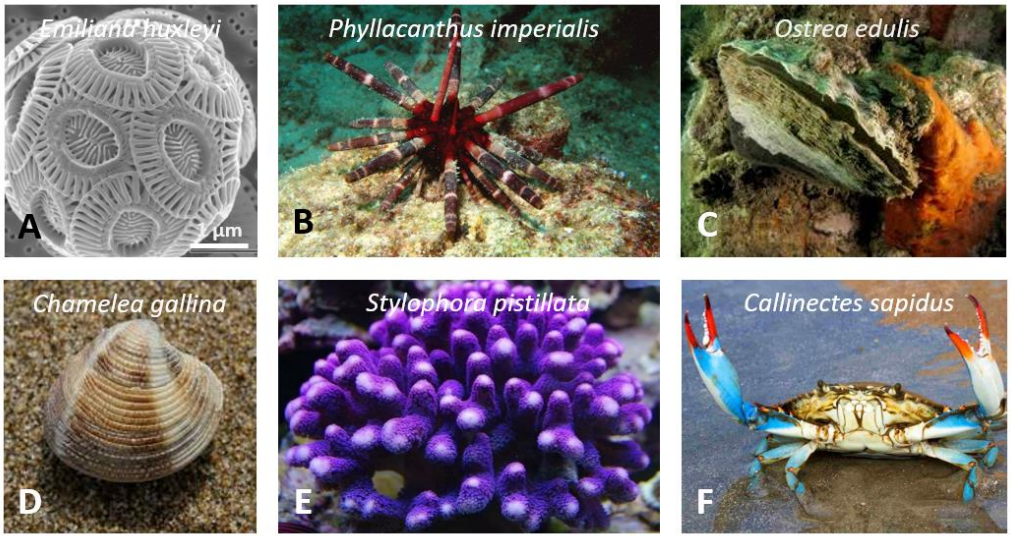

Figure 3. Some examples of marine calcifying organisms: Coccolithophores (A), sea urchins (B), mollusks (C, D), corals (E) and crustaceans (F).

Economic interest in calcium carbonate

Calcium carbonate ($CaCO_3$) is the most widely used mineral in the world in many industries such as paper, rubber, paints and construction both as a filler and as coating pigment due to its white colour (Fig. 4). The papermaking process, for example, uses the higher amount of this mineral as filler since it allows for the paper to be bright and smooth and it is inexpensive so it reduces the use of the expensive cellulose fibers [12]. When used as filler in polymeric matrices, instead, $CaCO_3$ improves the mechanical properties of the plastic material [13]. It is also used

as an additive for rubber leading to a double positive effect i. e. increasing the volume of the product, saving expensive natural rubber and reducing the production costs, and improving mechanical properties such as the tensile strength, the tear strength and the wear resistance [14]. $CaCO_3$ micro and nano particles are used for biomedical applications such as drug delivery due to its compatibility and non-toxicity [15]. Due to all these wide applications, it is not surprising that $CaCO_3$ market size was estimated at over 150 million tonnes in 2023 and it is expected to reach US$ 29.3 Bn by the end of 2031 [16].

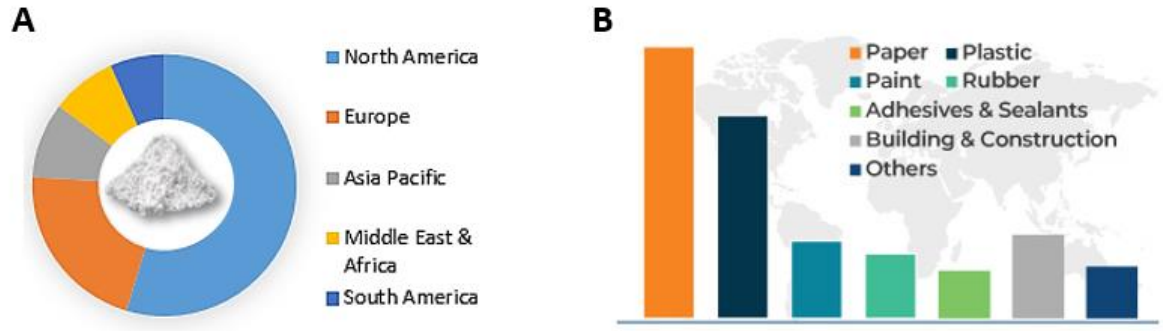

Figure 4. $CaCO_3$ regional market (A) and end-use industry in 2022 (B). Images source: [16].

The main current commercial forms of this mineral are ground calcium carbonate (GCC) from quarries, and precipitated calcium carbonate (PCC) from chemical synthesis.

GCC is commonly obtained by grinding natural minerals, mainly limestones, extracted from quarries. Limestones were the first rocks to be quarried in human history due to their wide-spread occurrence, and their softness and layered structure that made them easy to work [17]. So, GCC is quite inexpensive since the production method only involves mechanical crashing and grinding. GCC, in fact, accounted for the 70.5 % of the global $CaCO_3$ demand in 2021 [16]. The main issues related to GCC are firstly the absence of control over the purity of $CaCO_3$ crystals, since it only depends from the presence of contaminants in the rocks, that affects the whiteness of the powders. Moreover, quarries have an environmental impact since quarrying operations can alter pre-existing ecosystems and produce powder emissions and waste rocks [18]. The engineering activities during aggregate extraction and processing, in fact, can cause a change in the geomorphology which also involves a visual impact (Fig. 5A).

PCC is commonly derived from carbonate rocks such as limestone and dolomite by the so called solid–liquid–gas route, also known as carbonation process, or by the solid–liquid route [19]. In the first process, the carbonate-rich rocks are calcined using temperatures between 900 and 1200 °C to produce calcium oxide (lime) and carbon dioxide (CO_2). The obtained lime is then

treated with distilled water to produce calcium hydroxide called milk of lime. The resulting milk of lime is then purified and carbonated with the CO_2 obtained from the calcination process in order to get $CaCO_3$ crystals (Fig. 5B). The second process, instead, involves a direct reaction between Ca^{2+} and CO_3^{2-} ions in an aqueous solution.

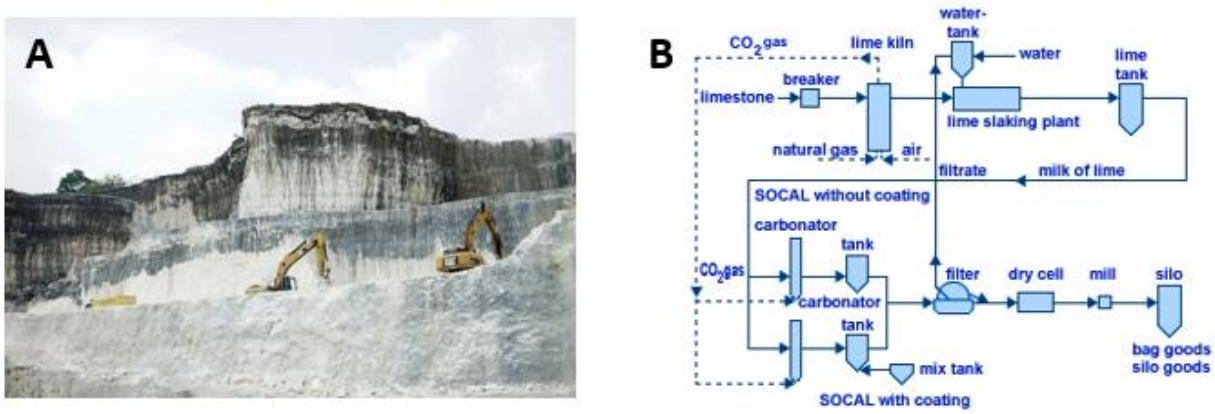

Figure 5. Visual impact caused by quarries (A) and schematic representation of PCC production by the solid–liquid–gas route (B).

So, it is clear that the main issue for PCC production is the high costs since it involves the use of expensive instrumentations in the first case, and reagents in the second case. Compared to GCC, on the other hand, PCC has better physical properties, including high brightness, opacity and purity [20]. The chemical synthesis, moreover, allows a better control over the polymorphism of the crystals, their size and shape broadening the already wide fields of applications for this mineral.

Circular economy to valorise seafood wastes

A circular economy (CE) can be defined as an economic model aimed at the efficient use of resources through waste minimisation, long-term value retention, reduction of primary resources, and closed loops of products, product parts, and materials within the boundaries of environmental protection and socio-economic benefits [21]. Ten strategies have been evaluated in order to develop the different CE targets i. e. recovering, recycling, repurposing, remanufacturing, refurbishing, repairing, re-using, reducing, rethinking, and refusing.

The concept of recycling applies quite well in the context of seafood waste. According to the Food and Agriculture Organization of the United Nations (FAO), in fact, global fish production is estimated to have reached about 179 million tonnes in 2018 (Fig. 6A). Aquaculture accounted for 46 % of the total production with its production growing at 7.5 percent per year since 1970.

In particular, the aquaculture production was dominated by finfish (54.3 million tonnes), molluscs, mainly bivalves (17.7 million tonnes), and crustaceans (9.4 million tonnes) (Fig. 6B) [22].

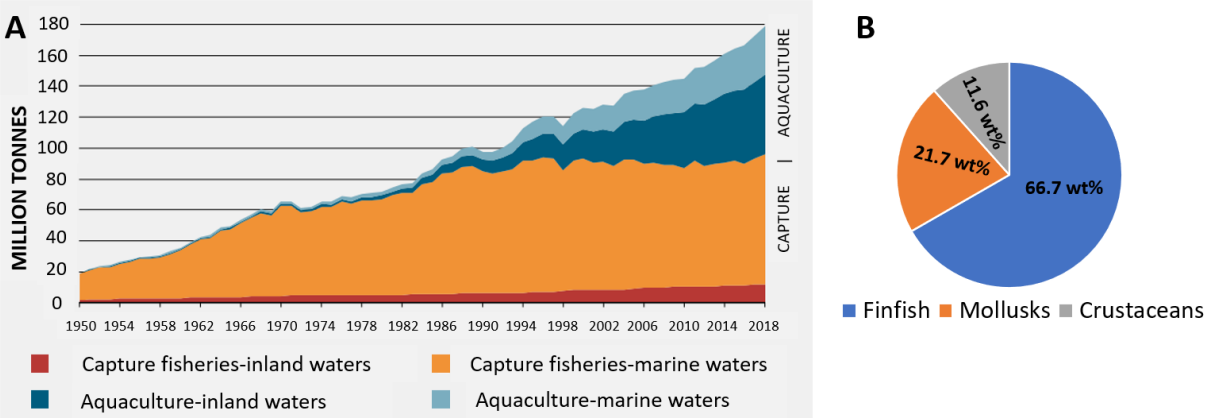

Figure 6. Global world capture fisheries and aquaculture production from 1950 to 2018 (A) and aquaculture production composition in 2018 reported as weight percentage (B). Image A source: [22].

The main issue linked to this huge production from fishery industry and marine aquaculture is the generation of a very big amount of waste by-products [23]. The 70 wt% of the processed seafood, in fact, is discharged as wastes [22]. Shells, in particular, represent the main marine waste since the most of mollusks and crustaceans body mass is not edible [24]. Every year, 6 to 8 million tonnes of waste shells are produced globally (Fig. 7) and these wastes are often just dumped in the sea causing damages to the marine ecosystem [25] or disposed in landfill affecting the quality of life for people living in proximity because of the unpleasant smell and causing health issues due to the microbial decomposition [26]. On the other hand, their disposal represents an environmental and economic issue since it involves the use of incineration or burial [27]. So, turning cast-off shells into new materials would benefit both the environment and economy [28].

Figure 7. Discarded shrimp (A) and oyster (B) shells. Image A source: [24].

Seafood wastes, in fact, harbour useful chemicals such as calcium carbonate, proteins (to use for fertilizers and animal feeds, for example) [29] and chitin (nitrogen-rich chemical for pharmaceuticals, cosmetics, textiles, soaps, water treatment, household cleansers) [30] so they offer a perfect example of circular economy.

Biogenic calcium carbonate and its applications

Calcium carbonate ($CaCO_3$) is the most abundant biogenic mineral forming marine organism hard tissues. Due to its abundance, in fact, the term *calcification* is often wrongly used as a synonym of biomineralization [31]. In nature we can find different forms of this mineral i. e. three anhydrous crystalline polymorphs (calcite, aragonite, and vaterite) as well as two hydrated crystalline phases, monohydrocalcite (MHC) ($CaCO_3 \cdot H_2O$) and ikaite ($CaCO_3 \cdot 6H_2O$) [32]. In addition to these crystalline phases, calcium carbonate also exists in various amorphous states, known as amorphous calcium carbonate (ACC), which, thanks to the presence of the organic matrix, play a crucial role in controlling the formation of crystalline calcium carbonate biominerals [33].

Among the crystalline phases, calcite is the most thermodynamically stable polymorph of $CaCO_3$ at room temperature and is the least soluble one in water as opposed to vaterite, which is the least stable polymorph and most soluble in water. These stability differences arise from the way the calcium and carbonate ions are assembled in the extended solid-state structures [34]. In particular, calcite has a rhombohedral crystal structure and usually exhibits a cubic morphology, aragonite has an orthorhombic crystal structure and a needle-like morphology and vaterite has a hexagonal crystal structure and spherical-like morphology (Fig. 8) [35].

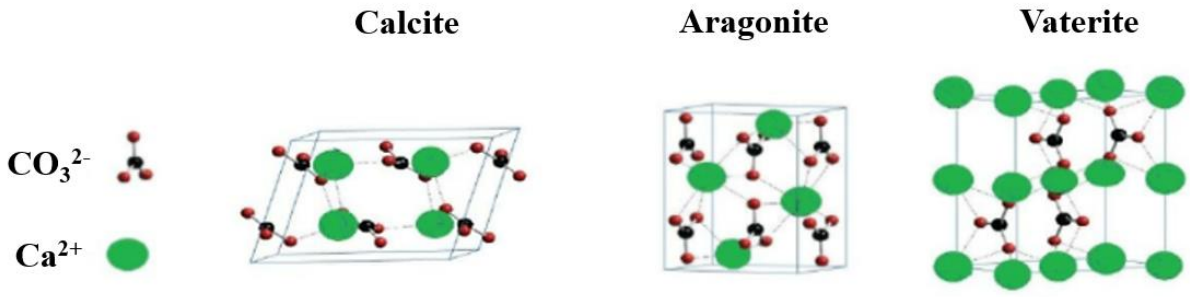

Figure 8. Schematic diagrams of the rhombohedral crystal structure of calcite, the orthorhombic one of aragonite and the hexagonal one of vaterite.

Marine organisms mainly form calcite and aragonite-based structures. Just think of corals that lead to a production of aragonite of about 10^{12} kg $year^{-1}$ through the biomineralization process allowing them to build the most important bioconstruction of the world, coral reefs [36] or mollusc shells containing both calcite and aragonite separated into distinct layer, the prismatic one and the nacreous one, respectively [37].

We have already seen in the previous paragraph that seafood industry processing leads to the production of tonnes of waste by-products every year, in particular waste shells. Seashells, on the other hand, may be also seen as a renewable and cheap alternative source for biogenic calcium carbonate [28]. There are several shell valorisation strategies that are currently exploited. Biogenic calcium carbonate, in fact, has widely been used for low added value applications such as livestock feed supplement [38], agricultural liming agent [39] and as aggregate substitute in concrete preparation [40]. On the other hand, biogenic calcium carbonate micro and nano particles are used for high value applications such as drug delivery [41], filler materials [42] and catalysis [43] (Fig. 9).

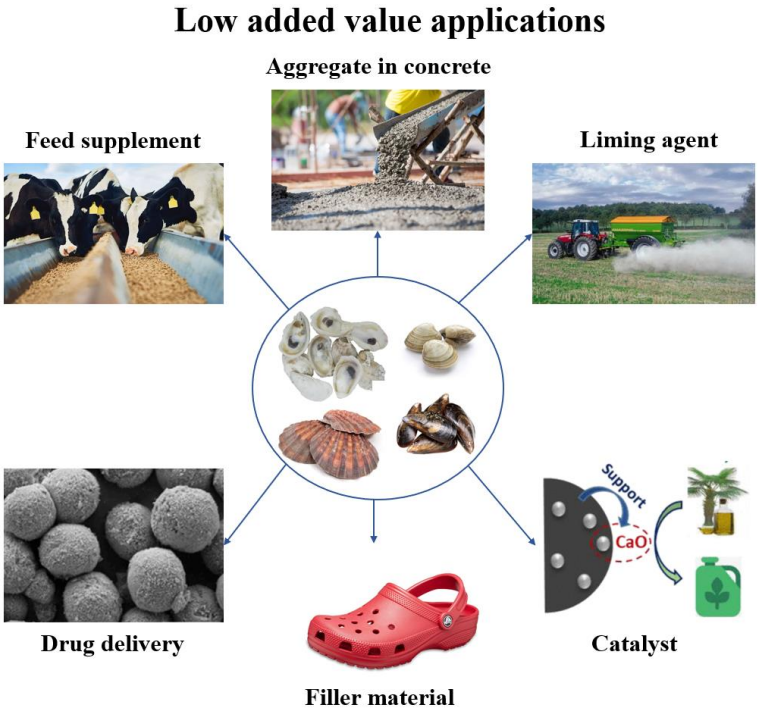

Figure 9. Overview of biogenic derived calcium carbonate applications from waste shells.

Shell valorization: challenges and unknowns

Shell waste reutilization is now a very widespread concept. We have seen in the previous paragraph that many applications have already been exploited with calcium carbonate being used as soil conditioner, catalyst, filler and construction material. However, the most of these waste shell employment strategies involves sustainability or economic challenges.

First of all, shells need to be cleaned from their soft tissues and flesh prior their utilization. When pure $CaCO_3$ is needed, for example for drug delivery purpose, shells are usually heated up to 500 ° C to remove organic material [44]. Otherwise, a more sustainable method could be the enzymatic cleaning [45] but it is too expensive when considering industrial applications.

The use of the shells derived $CaCO_3$ as catalysts for biodiesel production [46]or as inert material in concrete also requests heating at high temperature for quality material [47] but the environmental and economic impacts associated with the processing might be greater than those associated with conventional end-of-life disposal methods of the waste. So more environmentally friendly approaches to process seashells need to be explored.

Several studies have investigated the use of seashells as filler, especially in construction materials [48]. Since this waste is a functional biomaterial, biogenic $CaCO_3$ could also be used

as filler for polymers [49]. In this case a surface treatment of the filler with hydrophobic molecules, for example sodium stearate, would facilitate the dispersion in the hydrophobic polymeric matrices preventing loss of mechanical performances. However, the capability of $CaCO_3$ powders from shells to be coated with these molecules has not been studied so far.

The calcium carbonate component of seashells can be converted to calcium-based compounds suitable for biomedical applications such as hydroxyapatite which is the primary mineral component and constituent of human bones. The main issues, in this case, are the high energy demand required for the calcination process to transform $CaCO_3$ into CaO [50] and the expensive autoclaves necessary to reach high temperatures and pressures [51]. So new sustainable methods should be investigated to carry out this transformation.

We saw that $CaCO_3$ nano particles have several applications as well as amorphous $CaCO_3$ [52]. So, if we want to recycle waste seashells rather than synthetizing $CaCO_3$, it is necessary to find a method to convert the biogenic $CaCO_3$ into nano-crystalline and amorphous $CaCO_3$ on a potentially industrial scale.

$CaCO_3$ is also widely used for wastewater treatment being able to adsorb molecules such as dyes, heavy metals and phosphorous [53]. Calcium carbonate derived from crustacean shells, in particular, resulted to be very efficient as adsorbent as well as chitin derived from them but the adsorption capability of the combined materials ($CaCO_3$ and chitin) is still unexplored.

So, many studies have been published about waste shell valorization strategies and much more attention has been paid on this subject during the last years but there are still a lot of challenges to face and things to be discovered in order to take full advantage of this huge resource.

Aim of the thesis

The aim of this thesis was to valorise seafood wastes from different species by recovering the potential biomaterials they are composed of and using them for different applications.

The first project regarded the recovery of biomineral building units from the waste shells of the species *Mytilus galloprovincialis*, namely the fibrous calcite from the outer prismatic layer and the aragonite tablets from the inner nacre layer, by a simple and environmentally friendly procedure. This offered the possibility to overcome the synthetic difficulties in replicating the ability of organisms to act as crystal shapers and morphology modifiers and opened the possibility to use those crystals to purpose different from those for which they were biosynthesized. Here, in particular, fibrous calcite and the aragonite tablets were tested as dye adsorbents in an envisioned water remediation application.

The second project aimed to investigate for the first time the capability of aqueous stearate dispersions to coat biogenic calcium carbonate powders from the shell of market-relevant mollusk aquaculture species, namely the oyster *Crassostrea gigas*, the scallop *Pecten jacobaeus*, and the clam *Chamelea gallina* employing geogenic calcium carbonate as reference. The chemical-physical features of the materials were firstly extensively characterized by different analytical techniques, then the prepared materials from oyster shells were tested as fillers in an ethylene vinyl acetate compound used for the preparation of shoe soles on an industrial scale.

The third project, instead, focused on the transformation of biogenic calcium carbonate particles (bCCP) from oyster shell waste of the species *Crassostrea gigas* into hydroxyapatite (HA) micro/nanoparticles with suitable cytocompatible and osteoinductive properties for osteogenic applications using a one-step hydrothermal process. Compared to most of the methods reported in the literature so far, the method we suggested is straightforward, one-pot, and involves the full transformation of bCCP into HA nanoparticles in one step. Moreover, it is low-cost since it can avoid the use of expensive hydrothermal autoclaves, additives, and high-purity calcium reagents, and importantly, can be performed at relatively low hydrothermal temperatures without any pH adjustment.

The fourth project aimed to compare the capability of different sources of calcium carbonate, from quarries or biogenic, to be converted into nano-crystalline and amorphous calcium carbonate (ACC). The mollusk shells of clams (aragonite), oysters (low Mg-calcite) and scallops (medium Mg-calcite) were used. The working hypothesis was that the different polymorph, content of Mg and species-specific organic matrix could produce ACCs diverse in stability and transformation pathway in crystalline phases.

In the last study, chemical processes that allowed to extract singularly or combined the main different components from the Brown shrimp (BS) *Crangon crangon* and Chinese mitten crab (CMC) *Eriocheir sinensis* shells were applied. The characterization of the obtained materials was conducted in their chemical and physical features, and as proof of concept the combined or single components were used as adsorbents of dyes commonly used in textile industries. Finally, the treated materials coming from the shrimp and crab shells were compared in terms of their characteristics and performance.

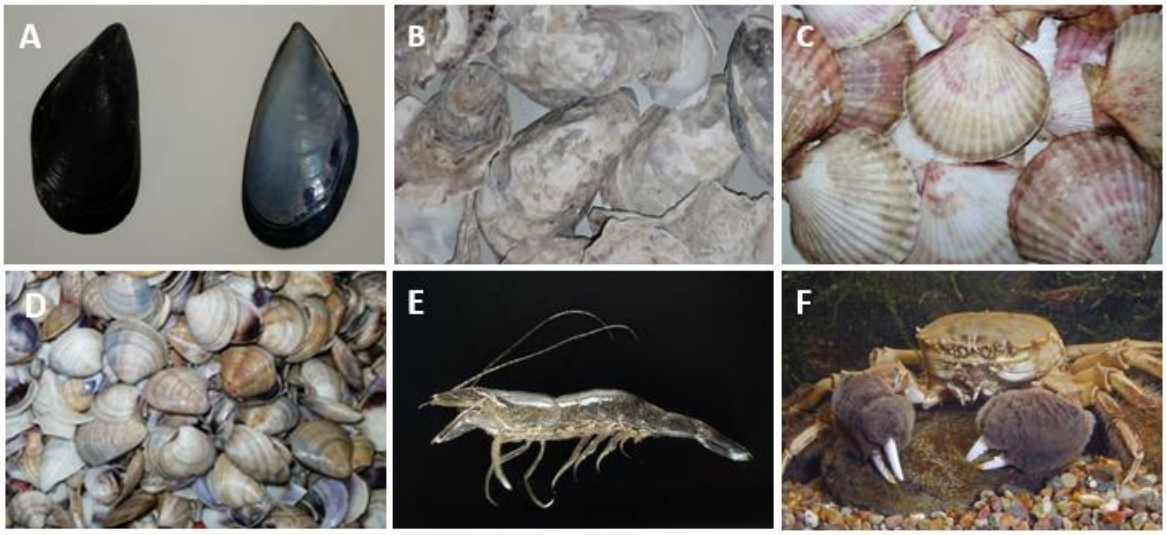

Figure 10. Species involved in the studies: *Mytilus galloprovincialis* (A), *Crassostrea gigas* (B), *Pecten jacobaeus* (C), *Chamelea gallina* (D), *Crangon crangon* (E) and *Eriocheir sinensis* (F).

References

[1] Y. Dauphin, "A brief history of biomineralization studies," *ACS Biomater Sci Eng*, 2022.

[2] H. A. Lowenstam and S. Weiner, *On biomineralization*. Oxford University Press on Demand, 1989.

[3] S. Mann, "Biomineralization: principles and concepts in bioinorganic materials chemistry," 2001.

[4] M. Cusack and A. Freer, "Biomineralization: elemental and organic influence in carbonate systems," *Chem Rev*, vol. 108, no. 11, pp. 4433–4454, 2008.

[5] S. Weiner and P. M. Dove, "An overview of biomineralization processes and the problem of the vital effect," *Rev Mineral Geochem*, vol. 54, no. 1, pp. 1–29, 2003.

[6] A. P. Wheeler and C. S. Sikes, "Regulation of carbonate calcification by organic matrix," *Am Zool*, vol. 24, no. 4, pp. 933–944, 1984.

[7] P. U. P. A. Gilbert *et al.*, "Biomineralization: Integrating mechanism and evolutionary history," *Sci Adv*, vol. 8, no. 10, p. eabl9653, 2022.

[8] P. Hunton, “Research on eggshell structure and quality: an historical overview,” *Brazilian Journal of Poultry Science*, vol. 7, pp. 67–71, 2005.

[9] A. C. Price, C. J. Weadick, J. Shim, and F. H. Rodd, “Pigments, patterns, and fish behavior,” *Zebrafish*, vol. 5, no. 4, pp. 297–307, 2008.

[10] H. R. Gordon and T. Du, “Light scattering by nonspherical particles: application to coccoliths detached from Emiliania huxleyi,” *Limnol Oceanogr*, vol. 46, no. 6, pp. 1438–1454, 2001.

[11] A. Scheffel, M. Gruska, D. Faivre, A. Linaroudis, J. M. Plitzko, and D. Schüler, “An acidic protein aligns magnetosomes along a filamentous structure in magnetotactic bacteria,” *Nature*, vol. 440, no. 7080, pp. 110–114, 2006.

[12] A. F. Lourenço, J. A. F. Gamelas, J. Sequeira, P. J. Ferreira, and J. L. Velho, “Improving paper mechanical properties using silica-modified ground calcium carbonate as filler,” *Bioresources*, vol. 10, no. 4, pp. 8312–8324, 2015.

[13] C. S. Baek, K. H. Cho, and J.-W. Ahn, “Effect of Grain Size and Replacement Ratio on the Plastic Properties of Precipitated Calcium Carbonate Using Limestone as Raw Material,” *Journal of the Korean Ceramic Society*, vol. 51, no. 2, pp. 127–131, 2014.

[14] M. S. Sobhy, D. E. El-Nashar, and N. A. Maziad, “Cure characteristics and physicomechanical properties of calcium carbonate reinforcement rubber composites,” *Egypt. J. Sol*, vol. 26, no. 2, pp. 241–257, 2003.

[15] Y. Boyjoo, V. K. Pareek, and J. Liu, “Synthesis of micro and nano-sized calcium carbonate particles and their applications,” *J Mater Chem A Mater*, vol. 2, no. 35, pp. 14270–14288, 2014.

[16] “Calcium Carbonate Market,” 2022.

[17] G. Marras, N. Careddu, and G. Siotto, “Filler calcium carbonate industrial applications: the way for enhancing and reusing marble slurry,” *Italian journal of engineering geology and environment*, vol. 2017, no. Special Issue 2, pp. 63–77, 2017.

[18] W. H. Langer, “Potential environmental impacts of quarrying stone in karst: a literature review,” 2001.

[19] O. A. Jimoh, K. S. Ariffin, H. Bin Hussin, and A. E. Temitope, “Synthesis of precipitated calcium carbonate: a review,” *Carbonates Evaporites*, vol. 33, pp. 331–346, 2018.

[20] M. A. Hubbe and R. A. Gill, “Fillers for papermaking: a review of their properties, usage practices, and their mechanistic role,” *Bioresources*, vol. 11, no. 1, pp. 2886–2963, 2016.

[21] P. Morseletto, “Targets for a circular economy,” *Resour Conserv Recycl*, vol. 153, p. 104553, 2020.

[22] FAO, “The State of World Fisheries and Aquaculture,” *Sustainability in action*, 2020, doi: 10.4060/ca9229en.

[23] J. P. Morris, T. Backeljau, and G. Chapelle, “Shells from aquaculture: a valuable biomaterial, not a nuisance waste product,” *Rev Aquac*, vol. 11, pp. 42–57, 2019, doi: 10.1111/raq.12225.

[24] N. Yan and X. Chen, “Sustainability: Don’t waste seafood waste,” *Nature*, vol. 524, no. 7564, pp. 155–157, 2015, doi: 10.1038/524155a.

[25] Y. Hou *et al.*, “Marine shells: Potential opportunities for extraction of functional and health-promoting materials,” *Crit Rev Environ Sci Technol*, vol. 46, no. 11–12, pp. 1047–1116, 2016.

[26] K. H. Mo, U. J. Alengaram, M. Z. Jumaat, S. C. Lee, W. I. Goh, and C. W. Yuen, “Recycling of seashell waste in concrete: A review,” *Construction and Building Materials*. pp. 751–764, 162, 2018. doi: 10.1016/j.conbuildmat.2017.12.009.

[27] D. Suteu *et al.*, “The seashell wastes as biosorbent for reactive dye removal from textile effluents,” *Clean–Soil, Air, Water*, vol. 40, no. 2, pp. 198–205, 2012.

[28] A. Hart, “Mini-review of waste shell-derived materials’ applications,” *Waste Management & Research*, vol. 38, no. 5, pp. 514–527, 2020.

[29] X. Hu *et al.*, “Green, Simple, and Effective Process for the Comprehensive Utilization of Shrimp Shell Waste,” *ACS Omega*, vol. 5, no. 30, pp. 19227–19235, Aug. 2020, doi: 10.1021/acsomega.0c02705.

[30] S. Kaur and G. S. Dhillon, “Recent trends in biological extraction of chitin from marine shell wastes: a review,” *Crit Rev Biotechnol*, vol. 35, no. 1, pp. 44–61, Jan. 2015, doi: 10.3109/07388551.2013.798256.

[31] H. A. Lowenstam and S. Weiner, *On biomineralization*. Oxford University Press on Demand, 1989.

[32] Z. Zou *et al.*, "A hydrated crystalline calcium carbonate phase: Calcium carbonate hemihydrate," *Science (1979)*, vol. 363, no. 6425, pp. 396–400, 2019.

[33] L. Addadi, S. Raz, and S. Weiner, "Taking advantage of disorder: amorphous calcium carbonate and its roles in biomineralization," *Advanced Materials*, vol. 15, no. 12, pp. 959–970, 2003.

[34] J. Perić, M. Vučak, R. Krstulović, L. Brečević, and D. Kralj, "Phase transformation of calcium carbonate polymorphs," *Thermochim Acta*, vol. 277, pp. 175–186, 1996.

[35] M. H. Azarian and W. Sutapun, "Biogenic calcium carbonate derived from waste shells for advanced material applications: A review," *Front Mater*, vol. 9, p. 1024977, 2022.

[36] M. J. H. Van Oppen, J. K. Oliver, H. M. Putnam, and R. D. Gates, "Building coral reef resilience through assisted evolution," *Proceedings of the National Academy of Sciences*, vol. 112, no. 8, pp. 2307–2313, 2015.

[37] R. A. Boulos, F. Zhang, E. S. Tjandra, A. D. Martin, D. Spagnoli, and C. L. Raston, "Spinning up the polymorphs of calcium carbonate," *Sci Rep*, vol. 4, no. 1, pp. 1–6, 2014.

[38] C. McLaughlan, P. Rose, and D. C. Aldridge, "Making the best of a pest: the potential for using invasive zebra mussel (Dreissena polymorpha) biomass as a supplement to commercial chicken feed," *Environ Manage*, vol. 54, pp. 1102–1109, 2014.

[39] C. H. Lee, D. K. Lee, M. A. Ali, and P. J. Kim, "Effects of oyster shell on soil chemical and biological properties and cabbage productivity as a liming materials," *Waste Management*, vol. 28, no. 12, pp. 2702–2708, 2008.

[40] E.-I. Yang, S.-T. Yi, and Y.-M. Leem, "Effect of oyster shell substituted for fine aggregate on concrete characteristics: Part I. Fundamental properties," *Cem Concr Res*, vol. 35, no. 11, pp. 2175–2182, 2005.

[41] R. Ismail *et al.*, "Synthesis and characterization of calcium carbonate obtained from green mussel and crab shells as a biomaterials candidate," *Materials*, vol. 15, no. 16, p. 5712, 2022.

[42] S. Owuamanam and D. Cree, “Progress of bio-calcium carbonate waste eggshell and seashell fillers in polymer composites: a review,” *Journal of Composites Science*, vol. 4, no. 2, p. 70, 2020.

[43] L. Nahas *et al.*, “Highly efficient scallop seashell-derived catalyst for biodiesel production from sunflower and waste cooking oils: Reaction kinetics and effect of calcination temperature studies,” *Renew Energy*, vol. 202, pp. 1086–1095, 2023.

[44] J. Zhan, J. Lu, and D. Wang, “Review of shell waste reutilization to promote sustainable shellfish aquaculture,” *Rev Aquac*, vol. 14, no. 1, pp. 477–488, 2022.

[45] J. N. Murphy, K. Hawboldt, and F. M. Kerton, “Enzymatic processing of mussel shells to produce biorenewable calcium carbonate in seawater,” *Green chemistry*, vol. 20, no. 12, pp. 2913–2920, 2018.

[46] R. Rezaei, M. Mohadesi, and G. R. Moradi, “Optimization of biodiesel production using waste mussel shell catalyst,” *Fuel*, vol. 109, pp. 534–541, 2013.

[47] K. H. Mo, U. J. Alengaram, M. Z. Jumaat, S. C. Lee, W. I. Goh, and C. W. Yuen, “Recycling of seashell waste in concrete: A review,” *Construction and Building Materials*. pp. 751–764, 162, 2018. doi: 10.1016/j.conbuildmat.2017.12.009.

[48] U. T. Bezerra, F. L. P. Almeida, L. B. Silva, N. P. Barbosa, T. A. Passos, and D. G. L. Cavalcante, “Production of filler aggregate from waste of bivalves molluscs shells,” *Journal of Civil Engineering and Architecture*, vol. 5, no. 4, 2011.

[49] M. Kumar and H. Jena, “Sea shell: a marine waste to filler in polymer composite,” in *International Conference on Artificial Intelligence in Manufacturing & Renewable Energy (ICAIMRE)*, 2019.

[50] S. Santhosh and S. Balasivanandha Prabu, “Thermal stability of nano hydroxyapatite synthesized from sea shells through wet chemical synthesis,” *Mater Lett*, vol. 97, pp. 121–124, 2013, doi: https://doi.org/10.1016/j.matlet.2013.01.081.

[51] D. F. Fitriyana, R. Ismail, Y. I. Santosa, S. Nugroho, A. J. Hakim, and M. S. Al Mulqi, “Hydroxyapatite synthesis from clam shell using hydrothermal method: A review,” in *2019 International Biomedical Instrumentation and Technology Conference (IBITeC)*, IEEE, 2019, pp. 7–11.

[52] B. Cantaert, D. Kuo, S. Matsumura, T. Nishimura, T. Sakamoto, and T. Kato, “Use of amorphous calcium carbonate for the design of new materials,” *Chempluschem*, vol. 82, no. 1, pp. 107–120, 2017.

[53] N. Topić Popović, V. Lorencin, I. Strunjak-Perović, and R. Čož-Rakovac, “Shell waste management and utilization: Mitigating organic pollution and enhancing sustainability,” *Applied Sciences*, vol. 13, no. 1, p. 623, 2023.

Chapter 2. Recovering and exploiting aragonite and calcite single crystals with biologically controlled shapes from mussel shells

(Published in ACS Omega)

Recovering and exploiting aragonite and calcite single crystals with biologically controlled shapes from mussel shells

Carla Triunfo,[1, 2] Stefanie Gärtner,[3] Chiara Marchini,[1, 2] Simona Fermani,[1] Gabriele Maoloni,[4] Stefano Goffredo,[2, 5] Jaime Gomez Morales,[6] Helmut Cölfen,[3] Giuseppe Falini*[, 1]

[1] Department of Chemistry "Giacomo Ciamician", University of Bologna, via F. Selmi 2, 40126 Bologna, Italy.

[2] Fano Marine Center, The Inter-Institute Center for Research on Marine Biodiversity, Resources and Biotechnologies, viale Adriatico 1/N 61032 Fano, Italy.

[3] Department of Chemistry, Physical Chemistry, University of Konstanz, Universitätsstrasse 10, Box 714, D-78457 Konstanz, Germany.

[4] Finproject S.p.A., Plant Ascoli Piceno, Via Enrico Mattei, 1—Zona Ind.le Campolungo, 3100 Ascoli Piceno.

[5] Department of Biological, Geological and Environmental Sciences, University of Bologna, via Selmi 3, 40126 Bologna, Italy.

[6] Laboratorio de Estudios Cristalográficos, Instituto Andaluz de Ciencias de la Tierra (CSIC-UGR), Avda. Las Palmeras, no 4, 18100 Armilla (Granada), Spain.

Abstract

The control over the shape and morphology of single crystals is a theme of great interest in fundamental science and for technological application. Many synthetic strategies to achieve this goal are inspired by biomineralization processes. Indeed, organisms are able to produce crystals with high fidelity in shape and morphology utilizing macromolecules that act as modifiers. An alternative strategy can be the recovery of crystals from biomineralization products, in this case, seashells. In particular waste mussel shells from aquaculture are considered. They are mainly built up of single crystals of calcite fibers and aragonite tablets in an external and an internal layer, respectively. A simple mechano-chemical treatment has been developed to separate and recover these two typologies of single crystals. The characterization of these single crystals showed peculiar properties with respect to the calcium carbonate from quarry or synthesis. We

exploited these biomaterials in the water remediation field using them as substrate adsorbing dyes. We found that these substrates show a high capability of adsorption for anionic dye, Eosin Y in this case, but a low capability of adsorption for cationic dyes, Blue Methylene in our case. The adsorption was reversible at pH 5.6. This application represents just an example of the potential use of these biogenic single crystals. We envision also potential applications as reinforcing fillers and optical devices.

Keywords: Mussel shell, recycling, fibrous calcite, aragonite tablets, water remediation.

Introduction

Biominerals are biomineralization products that are commonly characterized by a shape, morphology, polymorphism, and composition that differentiate them from their geogenic and synthetic counterparts [1-3]. The shell of the genus *Mytilus* is an example of biominerals characterized by three crystalline calcium carbonate regions: (i) the prismatic fibrous calcite, (ii) the aragonitic myostracum and (iii) the aragonitic nacre. Each region has a species-specific crystal shape, morphology, and composition [4-7].

In *Mytilus galloprovincialis* the outer layer of the shell, referred to as calcitic prismatic layer, is made of long, slender fibers of calcite (some 1–2 μm wide and hundreds of μm long), which reach the internal surface of the shell [4]. This microstructure has been called anvil-type fibrous calcite [8]. The myostracum is usually a very thin layer located in the attachment of the adductor muscle to the umbo of each valve. It is located under the calcitic prismatic layer and is in contact with the inner layer formed by the nacre [7, 9]. It is made of aragonite [10]. The nacre is a well-defined type of micro-structure characterized by small flat tablets (200-500 nm thick) of aragonite tightly packed together by a mineral bridge and an organic cement [11-14]. These peculiarities confer to the *M. galloprovincialis* shell unique mechanical properties that have been optimized by millions of years of evolution upon the organism's survival requests [15]. These features have attracted the attention of researchers stimulating them to produce biomimetic and biologically inspired synthetic laboratory processes to obtain biomaterials similar to the biogenic ones in shape, morphology, and composition for different technological applications [2]. Although this approach has produced an impressive number of biomimetic minerals, materials that perform as the biogenic ones have been rarely obtained.

Thus, a more pragmatic approach has been the use of the mollusc shells themselves. In this contest, it has to be considered that mollusc shells are waste by-products from mollusc

aquaculture [16], that has a global production of molluscs of about 15 Mton per year (year 2015) in which *M. galloprovincialis* and *Mytilus edulis* counts for about 1.5 Mton worldwide (year 2015) [17]. Waste mussel shells have been used for different scopes. They can be converted to calcium oxide by calcination and successfully used as catalysts for biodiesel production [18]. Seashells could be an inert material in concrete and other related cement-based products but heating at high temperature and crushing are requested for quality material [19]. However, a life cycle assessment analysis revealed that the valuation of shell waste through a calcination process may not generate environmentally friendly after effects, as the impacts associated with the processing and treatment of shell waste might be greater than those associated with conventional end-of-life disposal methods [19].

Taking into account these considerations an innovative approach can be the waste mollusc shell valorisation exploiting some of the unique features of the biominerals, which are effectively biomaterials due to their physio-chemical features and organic inorganic composite structures [1, 20]. Magnabosco et al. took advantage of the unique presence of the intra-skeletal organic matrix to obtain a covalent bond functionalization [21]. The intraskeletal organic matrix was also exploited to favour the polymeric coating of oyster shell particles to improve their metal ion adsorption [22]. The calcite fibers from the prismatic layer of the *Mytilus edulis* shell were used to obtain spherical aggregates of calcite fibers, exploiting their peculiar aspect ratio [23].

Here we suggest the recovery and valorisation of biomineral building units, namely the fibrous calcite and the aragonite tablets by a simple and environmentally friendly procedure. This offers the possibility to overcome the synthetic difficulties in replicating the ability of organisms to act as crystal shapers and morphology modifiers and opens the possibility to use those crystals to purpose different from those for which they were bio-synthetized. As a case of study, we used the fibrous calcite and the aragonite tablets as dye adsorbents in an envisioned water remediation application.

Results

Mussel shells from a local market having an average length of 55 ± 35 mm were used after a preliminary washing with tap water and brushing to remove meat residues and mineral debris. Then they were treated overnight with a 5 vol% NaClO solution. This provoked the oxidation and removal of the periostracum as well as superficial organic contaminants from the shells. The shells changed the colour of the surface becoming more whitish (Fig. 1).

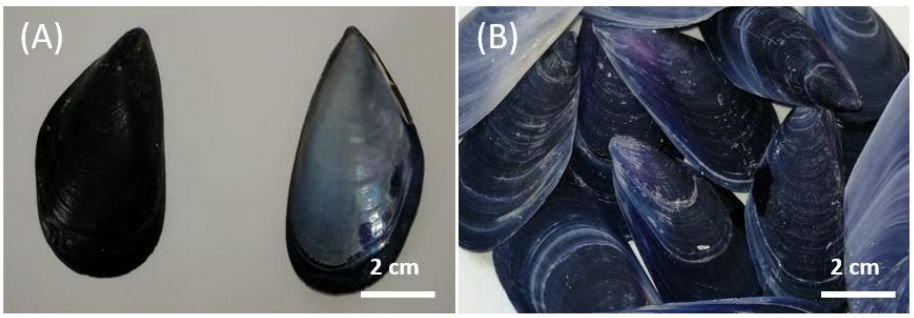

Figure 1. Camera images of mussel shell showing periostracum in the black regions and nacre in the white regions (A) and after bleaching with NaClO 5 % v/v solution (B).

The content of intraskeletal organic matrix in the bleached shells was 1.1 ± 0.3 wt% (Table 1). After this stage, the shells were treated at the temperature of 220 °C for 48 hours. This process provoked a mechanical separation of the external prismatic layer and the internal nacreous one (Fig. 2A and 2B), while the myostracum layer remained attached to the prismatic layer [24, 25], as can be observed in the SEM images (Fig. 2C and 2D).

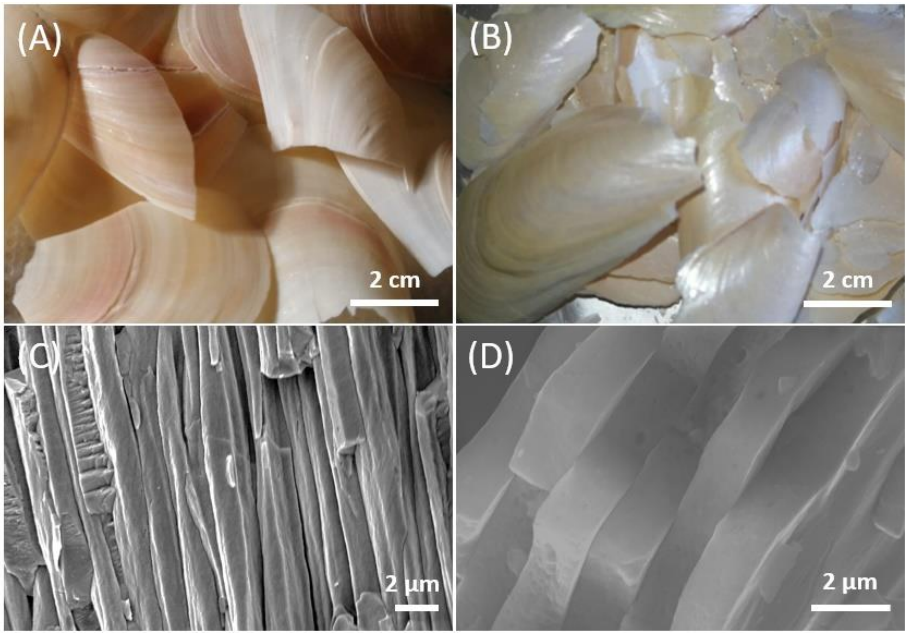

Figure 2. Camera and SEM images of the outer prismatic layer and myostracum (A, C) and the inner nacreous layer (B, D) after the thermal treatment.

The X-ray diffraction patterns showed only the presence of aragonite in the nacreous layer and the presence of calcite with trace (about 2.7 wt%) of aragonite in the prismatic layer, according to SEM observations (Fig. 3, Table 1).

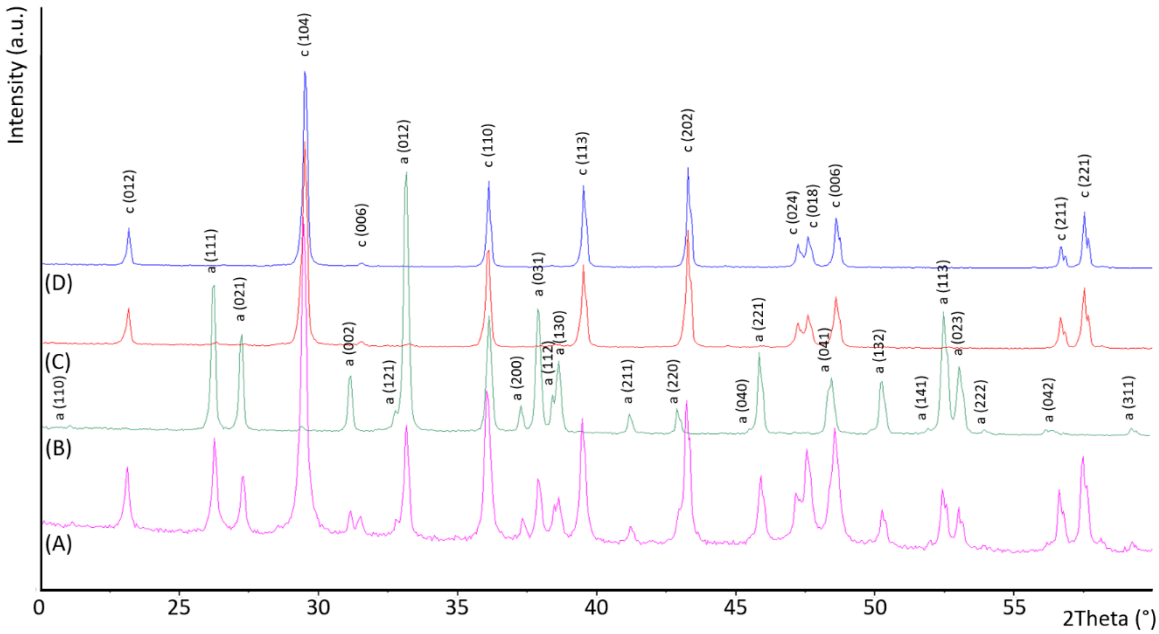

Figure 3. Powder X-ray diffraction patterns of mussel shell (A), nacre (B) and prismatic layer after the thermal (C) and acid treatment (D). The diffraction patterns were indexed accordingly to the PDF 00-005-0586 for calcite and PDF 00-005-0453 for aragonite.

Table 1. Percentage of mineral phase composition, intraskeletal material (structural water and organic matrix) content and particle size of bleached mussel shell (A), nacre (B), prismatic layer and myostracum (C) and isolated prismatic layer (D). The temperature range considered to estimate the content of intraskeletal organic material was between 150 °C and 450 °C.

Sample	**Calcite** (wt%)	**Aragonite** (wt%)	**Intraskeletal material** (wt%)	**D_{90}** (µm)
A	27.7 ± 0.3	72.3 ± 0.3	1.1 ± 0.3	-
B	-	100	1.42 ± 0.02	13.76 ± 0.05
C	97.3 ± 0.4	2.7 ± 0.4	1.0 ± 0.1	-
D	100	-	0.041 ± 0.001	9.40 ± 0.04

These results were also confirmed by the spectroscopic analysis (Fig. 4).

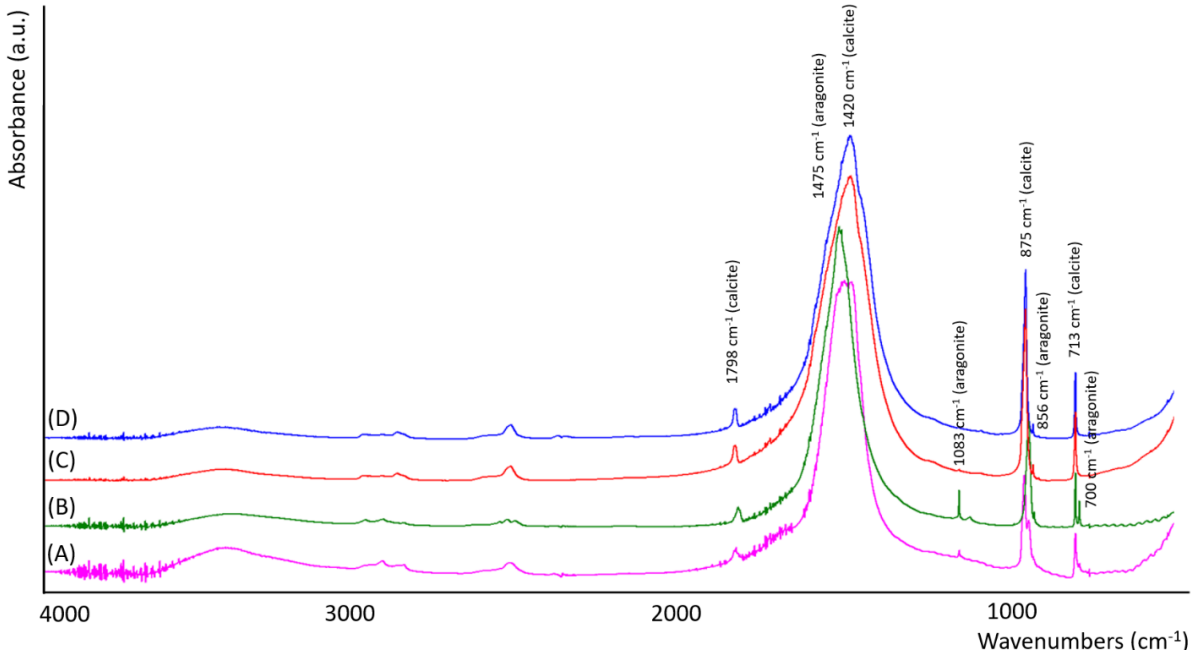

Figure 4. FTIR spectra of mussel shell (A), nacre (B), prismatic layer and myostracum (C) and isolated prismatic layer (D).

The thermal gravimetrical analyses of the two layers showed a content of intraskeletal organic material (structural water and organic matrix) of about 1.0 ± 0.1 wt% and 1.42 ± 0.02 wt% in the myostracum/prismatic layer and the nacre layer (Fig. 5, Table 1), respectively.

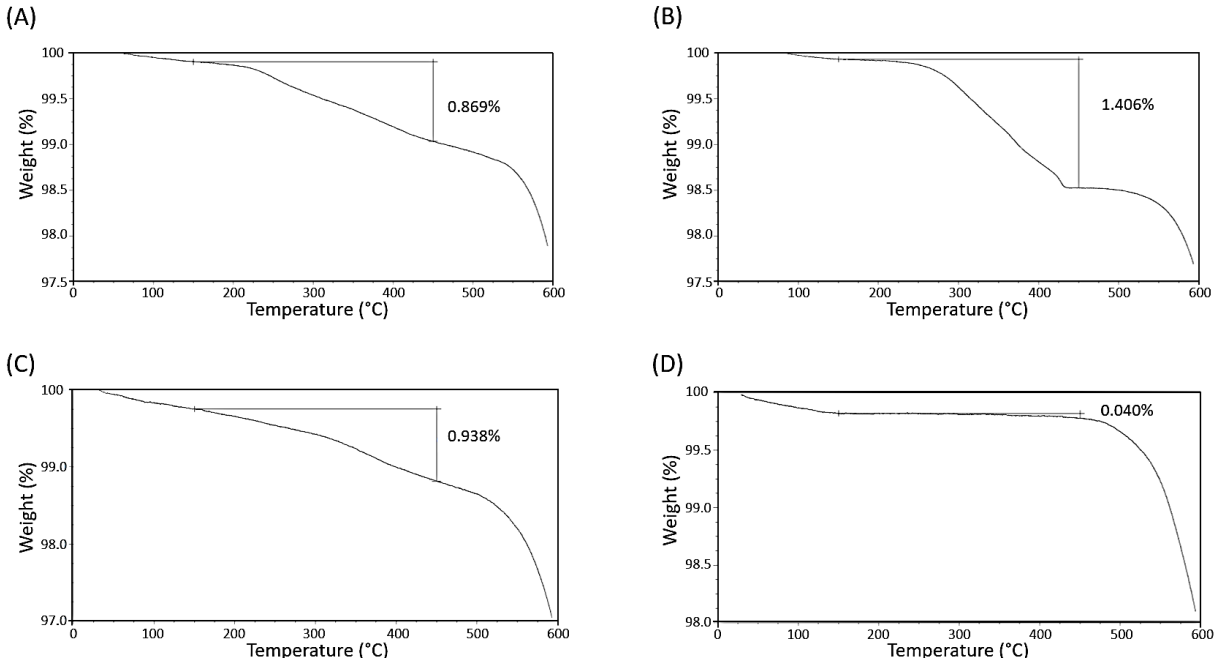

Figure 5. Thermogravimetrical analysis (TGA) profiles of bleached mussel shell (A), nacre (B), prismatic layer and myostracum (C) and isolated prismatic layer (D). The temperature range considered to estimate the content of intraskeletal organic matrix was between 150 °C and 450 °C.

Following this separation, the two main layers were subject to diverse treatments. The myostracum/prismatic layer was treated with a 5 % v/v acetic acid solution for 24 h with the consequent complete dissolution of the myostracum, as shown by the absence of the diffraction peaks of aragonite in the diffraction pattern of the remaining prismatic calcite (Fig. 3).

As the last preparative step, the treated prismatic calcite layer was lightly crushed, 600 µm sieved and bleached to remove the remaining superficial organic matrix. The obtained material was mainly constituted by single fibrous crystals of pure calcite (Fig. 6A and B) having a content of intraskeletal organic matrix of 0.041 ± 0.001 wt%, a surface area of 1.7 m^2/g, a particle size of 9.40 ± 0.04 µm and an aspect ratio no lower than 5 (Fig. 7A and B, Table 2).

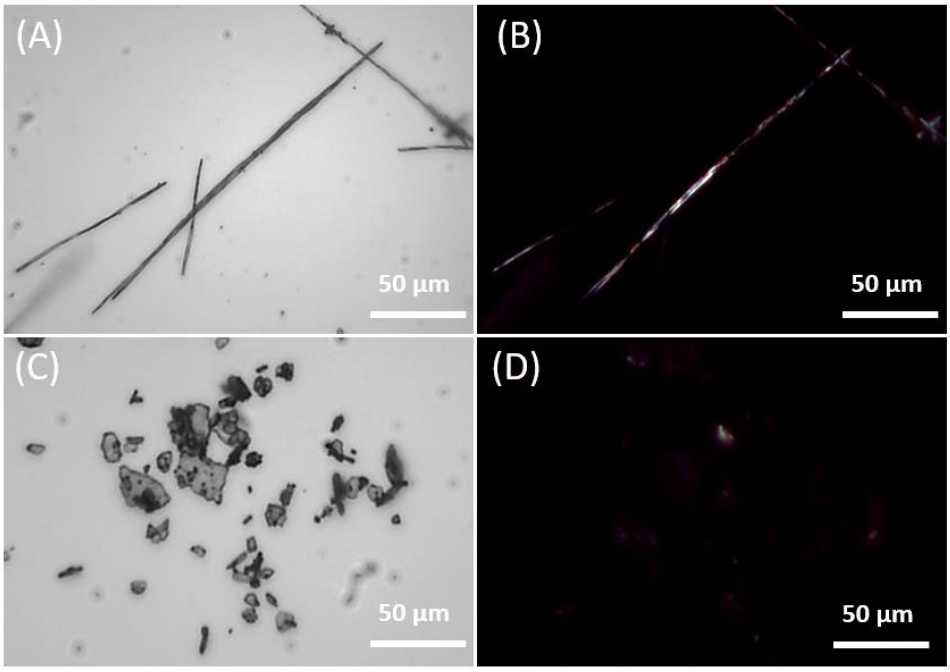

Figure 6. Optical microscopy images of isolated calcite fibers (A and B) and nacre tablets (C and D). B and D are images A and C, respectively, observed using polarized light.

Table 2. Size distribution of isolated prismatic layer (A) and nacre (B).

Sample	D_{10} (µm)	D_{50} (µm)	D_{90} (µm)
A	1.202 ± 0.004	3.156 ± 0.009	9.402 ± 0.037
B	3.182 ± 0.008	7.212 ± 0.008	13.76 ± 0.05

The thermally treated nacreous layers separated into almost single tablets after removal of the inter-tablet organic matrix through a bleaching and sonication process (Fig. 6C and D). After such process the organic matrix content remains unaltered (1.59 ± 0.02 wt%) indicating that the inter-crystalline organic matrix was already eliminated by the thermal process (Fig. 4) and the mineral phase remained pure aragonite (Table 1). The single crystal aragonite tablets were in majority single tablets, but also particles formed by casted two or three tablets were observed (Fig. 7C and D).

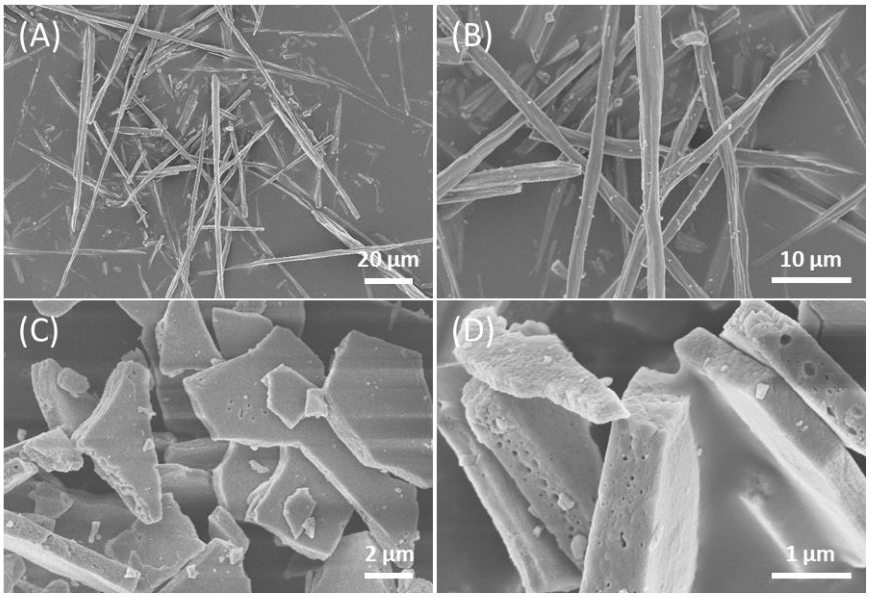

Figure 7. SEM images of isolated calcite fibers (A and B) and nacre tablets (C and D).

The two typologies of single crystals of calcite and aragonite, were also tested for their capability to adsorb model dye molecules, Eosin Y (EY) and Blue Methylene (BM), in the perspective of their use as substrates for water remediation. The results of the isothermal adsorption experiments (Fig. 8) showed that EY and BM have different adsorption profiles on the fibrous calcite and the tablets of aragonite.

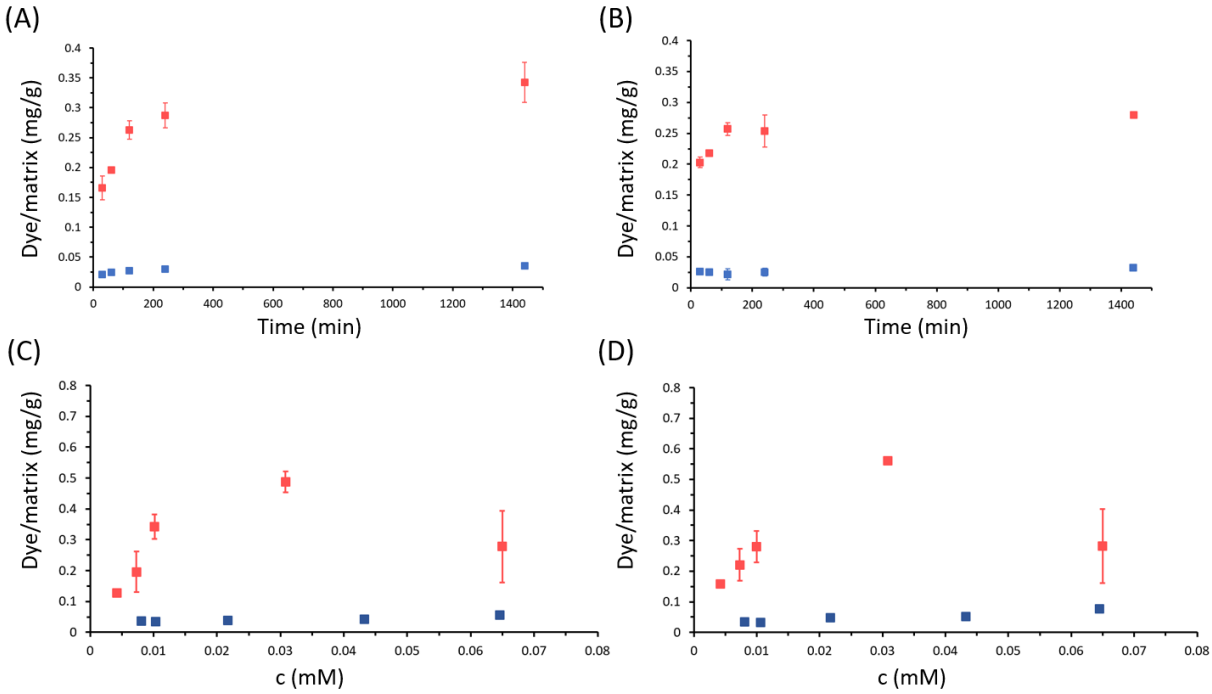

Figure 8. Adsorption kinetics and isotherms of Blue Methylene (blue dots) and Eosin Y (red dots) solutions at pH 7.2 on calcite fibers (A, C) and nacre tablets (B, D). The dye adsorbed is reported as the mass of dye (mg), normalized over the mass of calcite fibers/nacre tablets (g). The error bars associated to Blue Methylene measures are small and not visible in the graphs.

The adsorption of the EY and BM on biogenic single crystals reaches equilibrium within 24 h (Fig. 8). In order to evaluate the adsorption kinetics mechanisms, the experimental data were fitted by pseudo first-order and pseudo-second-order kinetic models [26]. The diffusion-based Weber–Morris model was tested as well [27]. It is noted that the pseudo-second-order kinetic model fits the adsorption data better than pseudo-first-order model as indicated by higher R^2 values (Table 3).

EY isotherm absorption data fitted the best with a Langmuir isotherm with a Langmuir constant K_L = 0.12 and 0.19 L/mg, and a q_{max} = 0.52 and 0.45 mg/g on fibrous calcite and aragonitic tablets, respectively. The BM isothermal data fitted better with a Freundlich isotherm with K_F = 5.84 and 2.70 mg/g and n = 0.03 and 0.02 for adsorption on fibrous calcite and aragonitic nacre, respectively (Table 4). When considered the fitting using the Langmuir adsorption isotherm the q_{max} of EY was higher than that of BM almost of a factor 10.

Table 3. Parameters for pseudo-first-order and pseudo-second-order as well as Weber–Morris models.[a]

Dye/ substrate		Pseudo-first-order model[b]			Pseudo-second-order model[c]			Weber–Morris model[d]		
	$q_{max, exp}$ (mg g^{-1})	$q_{max, cal}$ (mg g^{-1})	k_1 (min^{-1})	R^2	$q_{max, cal}$ (mg g^{-1})	k_2 (g mg^{-1} min^{-1})	R^2	C (mg g^{-1})	k_{ip} (mg g^{-1} $min^{-1/2}$)	R^2
EY/ calc. fib.	0.3424	0.2467	0.007	0.88	0.3265	0.089	0.95	0.1138	0.0074	0.66
EY/ arag. tab.	0.2801	0.3433	0.002	0.49	0.2726	0.3128	0.91	0.1363	0.0051	0.43
BM/ calc. fib.	0.0552	0.0269	0.083	0.72	0.05331	1.6211	0.96	0.026	0.001	0.44
BM/ arag. tab.	0.0764	0.0532	0.0086	0.92	0.07584	0.5815	0.93	0.024	0.001	0.26

[a] The reaction conditions were based on 0.01 mM EY, 0.07 mM BM and pH 7.2. [b] The pseudo-first-order model is given by $\ln (q_{max} - q_t) = \ln q_{max} - k_1 t$, where q_{max} and q_t are the amounts of adsorbed dye (EY or BM) at equilibrium and at time t (mg g^{-1}), respectively. k_1 is the equilibrium rate constant of pseudo-first-order kinetics (min^{-1}). [c] The pseudo-second-order model is determined by $1/q_t = 1/k_2 q_{max}^2 \; 1/t + 1/q_{max}$ where k_2 is the equilibrium rate constant of the pseudo-second-order kinetics (g mg^{-1} min^{-1}). [d] The Weber–Morris model is expressed by $q_t = k_{ip} t^{1/2} + C$, where k_{ip} is the intra-particle diffusion rate constant (mg g^{-1} $min^{-1/2}$) and C (mg g^{-1}) is a constant that reflects the thickness of the boundary layer.

Table 4. Calculated parameters from the fitting of the adsorption isotherms with different models. The R^2 values from the isotherm model(s) that indicated the best fitting are highlighted in bold.

Dye/substrate	Langmuir			Freundlich			Dubinin–Radushkevich		
	K_L (mg^{-1})	q_m (mg g^{-1})	R^2	K_F (mg g^{-1})	n	R^2	K_D (mol^2 kJ^{-2})	q_D (mg g^{-1})	R^2
EY/calc. fib.	0.12	0.52	**0.81**	0.13	3.20	0.45	2.1	0.37	0.77
EY/arag. tab.	0.19	0.45	**0.80**	0.14	3.52	0.46	0.99	0.17	0.65
BM/calc. fib.	0.85	0.05	0.71	5.84	0.03	**0.84**	0.99	0.16	0.55
BM/arag. tab.	0.310	0.07	0.84	2.70	0.02	**0.90**	1.02	0.06	0.68

The desorption experiment showed that at pH 7.2 or 6 the dyes are not removed from the substrates, while at pH 5.6 a partial dissolution of $CaCO_3$ was observed, the dyes were completely removed and the single crystal substrates were completely regenerated.

The zeta potential of the crystals was measured in water, in the dye loading buffers and after the dye adsorption. It was no possible to obtain a zeta potential value for the nacre tablets since

the measurements were not homogeneous. For the calcite fibers, instead, the zeta potential was -20.3 ± 0.6 mV in water (pH = 8.3), -11.6 ± 0.4 mV in the dye loading buffer (pH = 7.2) and -15.4 ± 0.1 mV and -19.8 ± 1.0 mV after the adsorption of EY and BM, respectively.

Discussion

The sustainable and green production of biomaterial is a research theme of growing interest. Shells are waste by-products from mollusc aquaculture, which represents a sustainable type of food production since the molluscs, as herbivores, are low in the trophic chain. Mollusc shells are a biogenic source of calcium carbonate, whose potentialities as biomaterials have been poorly exploited so far. Their use as materials with a high added value can represent a perfect example of circular economy. If the market demand increases, this will be a trigger to increase production. The current study shows that by a simple thermal and chemical treatment it is possible to obtain surface organic matrix free single crystals of calcite and aragonite having the peculiar shape of long slender fibers and tablets, respectively. Synthetic calcite fibers with diameters ranging from 100 to 800 nm were produced by a liquid-phase mineral precursor (PILP) on existing calcite substrate crystals by the addition of poly(aspartic acid) to a crystallizing solution [28]. Nano-fibers of calcite analogous to those produced via a PILP were produced using a positively charged additive poly(allylamine hydrochloride) [29]. Nano-wire of calcite particles precipitated in the pores, from 50 nm to 200 nm, of track etch membranes in the presence of acid macromolecules from a PILP precursor phase [30]. Into the same matrix, rod-like $CaCO_3$ crystals having a diameter of about 200 nm formed from amorphous calcium carbonate nanoparticles [31-34]. Via an amorphous precursor route thin tablets (∼600 nm thick) of aragonite were grown at the air−water interface using poly(acrylic acid−sodium salt) in combination with Mg^{2+} ion [35]. Mixed surfactant solutions of Ca and Mg dodecyl sulfate were used for the fabrication of pseudohexagonal and porous aragonite tablets with a triplet twinning and single-crystal-like nature [36]. Synthetic nacre, morphologically indistinguishable from the natural archetype was synthesized with amorphous calcium carbonate precursors by confinement in the scaffold of the original insoluble nacre matrix [37].

All these synthetic methods offered the advantage to have a rigorous control over shape, morphology and composition, opening the possibility to produce single crystals with shapes and morphologies not observed in nature. On the other side the production of massive amounts and the specificity on shape, morphology, composition and polymorphism can be potential issues. Mussel shells, and in general many biominerals, are produced under biological control

with high fidelity in crystal size morphology, composition and polymorphism. Moreover, the fine features of the crystalline units forming the shell can be modified by the environmental conditions in which the organism lives [38].

Our research showed that by a simple chemical, thermal and mechanical treatment the single crystal building units - the fibrous calcite and the aragonite tablets - that form the shell can be separated. These materials can have potential application in many fields, in optics [39], polymer science [40], medicine [41] and the paper industry [42, 43], among many others. $CaCO_3$ whiskers in paper were for example found to increase its strength.

Here we tested the use of single crystals of fibrous calcite and the aragonite tablets for water remediation. A powder from bivalve shells of *Anadara uropigimelana* was tested as a potential bio-sorbent for BM and showed a capability of adsorbing of 0.357 mg/g [44]. Fibrous calcite from the mussel shell of *Mytilus edulis* was used for the removal of crystal violet from water solutions with high efficiency [23].

The two substrates were able to, efficiently and in a reversible way, adsorb EY, bearing a negative charge, but were less efficient with BM (bearing a positive charge). The adsorption rate is an index for analysing the adsorption process. The pseudo-first-order and the pseudo-second-order kinetic model were employed to fit the adsorption kinetics of EY and BM on the biogenic crystals [45]. The R^2 of the pseudo-second-order model was higher than the pseudo-first-order model in all cases (Table 3). This indicated that chemical adsorption is dominant [46]. Nevertheless, in the case of BM adsorption on aragonite tablets a pseudo-first-order kinetic model is also suitable, because of the $R^2>0.98$. This indicates that there may be physical adsorption during the adsorption process [47]. Additionally, the calculated maximum adsorption capacity by the pseudo-second-order model was much closer to the experimental maximum adsorption capacity than the pseudo first-order, which further proved that adsorption process of EY and BM on biogenic crystals conformed to the pseudo-second-order model. The steps involved in this kinetic model are: (i) molecules diffuse from liquid phase to liquid–solid interface; (ii) molecules move from liquid–solid interface to solid surfaces; and (iii) molecules diffuse into the particle pores [48]. Herein, the first step is not rate-limited because the adsorption was performed under shaking conditions. The rate constant (k_2) of BM is higher than that of EY suggesting an initial faster occupation of the adsorption sites on the solid surface. The study of the isotherm models suggests that Langmuir isotherm is more suitable to describe the adsorption process of EY. This indicates a chemically controlled adsorption and dominated by monolayer formation, as also suggested by the kinetic analysis [49]. The driving force for

the adsorption should be, according with the value of K_L, the formation of a strong chemical bond between the surface and EY. Here, we reach 0.52 mg/g adsorption capacity for EY on the calcite fibers resp. 0.45 mg/g for the aragonite tablets, which is higher than literature results of 0.357 mg/g reported for BM [44].

The adsorption of BM is better described by a Freundlich isotherm, indicating a no site-specific interaction and formation of multilayers. The fibrous calcite surface has a negative charge that is pH dependant and we can suppose the same for the aragonite tablets. In the loading buffer (pH = 7.2) upon adsorption of dyes, EY or BM, there is an increase of the zeta potential, more marked for BM (from -11.6 mV to -15.4 mV for EY and -19.8 mV for BM). To understand these unexpected results, EY and BM having different charge, it can be supposed that other reactions can occur on the thermally treated and oxidized biogenic crystal surfaces, beside the expected electrostatic interaction. It has been reported that biogenic crystals have low crystalline order on their surface, even the presence of amorphous calcium carbonate [50, 51], and that after thermal treatment the carbonate groups are replaced by hydroxyl groups [52]. The combination of these two effects can change the distribution mechanisms of interaction of dyes. The isotherm data indicates that BM, positively charged, adsorbs on the biogenic calcite surface sites mainly by direct and fast no site-specific electrostatic interactions. Differently, the adsorption of EY, negatively charged on its carboxylate groups, should occur through the formation of a cationic coordination bond with the calcium ions present in solution; in this process the surface hydroxyl groups can participate to the coordination bond of calcium ions without affecting the net charge. The adsorption capability of BM was determined to be 5.84 mg/g for the fibers resp. 2.7 mg/g for the tablets, which is again higher than that observed for *A. uropigimelana* [44]. Although the loading capability of the proposed biogenic single crystal substrates is lower than that of other no mineral materials [53], the here described materials offer the advantage to be re-used since the dye desorption occurs under slightly acid conditions.

Conclusions

This research showed that single crystals of calcite and aragonite with a biologically controlled shape and morphology can be obtained from mussel shells by chemical and mechanical treatments. The separation process implies simple and sustainable processes. The obtained single crystals, due to their unique and no lab reproducible aspect ratio, can have many potential applications. Here they were used as a substrate for reversible dye removal, but other potential

applications are foreseen as filler to improve mechanical properties of matrices or as part of optical devices.

Materials and methods

Reagents and solvents were purchased from Merck. They were utilized without any further purification. For each experiment, daily fresh solutions were prepared. Mussels of *M. galloprovincialis* from Spain aquaculture were purchased. The shells were firstly washed with tap water to eliminate the meat residues and mineral debris and then mechanically stirred in a 5 % v/v sodium hypochlorite solution for 24 hours (1 g of shells in 10 ml solution). The shells were separated from the solution by decanting, washed with water and air dried. Next, they were heated in an oven at 220 °C for 48 hours and the thermal treatment allowed the mechanical separation of the inner nacreous layer from the outer prismatic layer of the shell.

Prismatic layer treatment for calcite fibers disassembly. The prismatic layer fragments were mechanically stirred in a 5 % v/v acetic acid solution for 24 hours in order to remove the remaining aragonitic layer of myostracum (2.2 g of fragments in 25 ml solution). The fragments were separated from the solution by decanting, washed with water and air dried. The isolated calcite layer fragments were then crushed by mortar and pestle, sieved at 600 μm and bleached.

Nacreous layer treatment for tablets disassembly. The nacreous layer fragments were crushed by mortar and pestle and sieved at 45 μm. The nacreous powder was mechanically stirred in a 5 % v/v sodium hypochlorite solution for 24 hours (1 g of powder in 10 ml solution) and then bath sonicated in the same solution for 15 minutes. The resulting suspension was centrifuged at 5000 rpm for 2 minutes and the supernatant was discarded. The nacreous powder was then washed 3 times with water by centrifuge (5000 rpm, 2 minutes) and the isolated powder was dried under vacuum in a desiccator overnight.

X-ray powder diffraction analysis. X-ray diffraction patterns were collected using a PanAnalytical X'Pert Pro diffractometer equipped with a multi-array X'Celerator detector using Cu Kα radiation generated at 40 kV and 40 mA ($\lambda = 1.54056$ Å). The diffraction patterns were collected in the 2θ range between 20 ° and 60 ° with a step size ($\Delta 2\theta$) of 0.05 ° and a counting time of 60 s.

Spectroscopic analysis. A Thermo Scientific™ Nicolet™ iS™10 FTIR Spectrometer was used to collect the FTIR spectra. Disk sample for FTIR analysis was obtained by mixing a small amount (2 mg) of product with 98 mg of KBr and applying a pressure of 45 tsi (620.5 MPa) to the mixture using a press. The spectra were obtained with 4 cm^{-1} resolution and 64 scans.

Thermal analysis. Thermogravimetric analysis (TGA) were performed using an SDT Q600 V 8.0 instrument (TA Instruments). The system was pre-equilibrated at 30 °C, then a ramp from 30 to 600 °C with a 10 °C min^{-1} heating rate was performed under nitrogen flow. The measurement was performed three times on 20 mg of each sample. The temperature range considered to estimate the content of intraskeletal organic matrix was between 150 °C and 450 °C.

BET. The specific surface area of the samples was measured by the multiple BET method using a Gemini VII 2390 Series Surface Area Analyzer (Micromeritics Instrument Corporation) with a nitrogen flow.

Dimensional distribution analysis. Particle size analyses were performed using a Mastersizer 3000 laser diffraction particle size analyser. The particles from each sample were dispersed in isopropanol for the measurement.

Scanning electron microscopy. All SEM images were acquired using a ZEISS Leo 1530 Gemini field emission scanning electron microscope (SEM) operating at 5 kV. All samples were dried under vacuum in a desiccator and gold-coated before their observation.

ζ-potential analysis. The zeta potential of the particles was evaluated using a Malvern Zetasizer Nano ZS equipped with a He-Ne laser source (633 nm, 5 mW).

Dye adsorption kinetics experiments. Adsorption kinetics experiments were carried out suspending 50 mg of each material in 10 mL of dye in a 50 mM pH 7.2 bis-tris buffer solution. The suspensions were kept in a 15 mL polypropylene conical centrifuge tubes at room temperature under mechanical stirring. Two dyes were tested that are Blue Methylene and Eosin Y both having an absorption maximum in the visible region (668 nm and 517 nm, respectively). The dye concentration in solution was measured by a UV-Vis spectrophotometer (Cary 300 Bio, Agilent Technologies) using a spectral range of 450-800 nm and the spectra were recorded after 30 minutes, 1 h, 2 h, 4 h and 24 h. For each measurement, the dye solution was centrifuged at

10000 rpm for 90 s and the supernatant was transferred into a plastic cuvette with 1 cm optical path.

Dye desorption experiments. Desorption kinetics experiments were carried out suspending 25 mg of each sample from the dye adsorption experiments in 5 mL of a 50 mM pH 5.6 citrate buffer solution. The suspensions were kept in a 15 mL polypropylene conical centrifuge tubes at room temperature under mechanical stirring and the concentration of the dye released in the solution was measured using the same procedure of the adsorption experiments.

Author Contributions

CT carried out the prismatic layer and the nacreous layer treatment for calcite fibers and aragonite tablets disassembly, respectively, dye adsorption kinetics experiments and dye desorption experiments. CT also performed the crystals characterization by X-ray powder diffraction analysis, spectroscopic analysis, thermal analysis, scanning electron microscopy and ζ-potential analysis. CT contributed to the writing of this manuscript.

References

[1] Lowenstam, H. A.; Weiner, S. *On Biomineralization*; Oxford University Press on Demand, 1989.

[2] Meldrum, F. C.; Cölfen, H. Controlling Mineral Morphologies and Structures in Biological and Synthetic Systems. *Chem. Rev.* **2008**, *108* (11), 4332–4432.

[3] Meldrum, F. C. Calcium Carbonate in Biomineralisation and Biomimetic Chemistry. *International Materials Reviews*. 2003, pp 187–224. https://doi.org/10.1179/095066003225005836.

[4] Grégoire, C. Structure of the Conchiolin Cases of the Prisms in Mytilus Edulis Linne. *J. Cell Biol.* **1961**, *9* (2), 395–400.

[5] Grenier, C.; Román, R.; Duarte, C.; Navarro, J. M.; Rodriguez-Navarro, A. B.; Ramajo, L. The Combined Effects of Salinity and PH on Shell Biomineralization of the Edible Mussel Mytilus Chilensis. *Environ. Pollut.* **2020**, *263*, 114555.

[6] Gao, P.; Liao, Z.; Wang, X.; Bao, L.; Fan, M.; Li, X.; Wu, C.; Xia, S. Layer-by-Layer Proteomic Analysis of Mytilus Galloprovincialis Shell. *PLoS One* **2015**, *10* (7),

e0133913.

[7] KENNEDY, W. J.; TAYLOR, J. D.; HALL, A. Environmental and Biological Controls on Bivalve Shell Mineralogy. *Biol. Rev.* **1969**, *44* (4), 499–530.

[8] Checa, A. G.; Pina, C. M.; Osuna-Mascaró, A. J.; Rodríguez-Navarro, A. B.; Harper, E. M. Crystalline Organization of the Fibrous Prismatic Calcitic Layer of the Mediterranean Mussel Mytilus Galloprovincialis. *Eur. J. Mineral.* **2014**, *26* (4), 495–505.

[9] Oberling, J.-J. Observations on Some Structural Features of the Pelecypod Shell. *Mitt. Natur. Ges. Bern* **1964**, *20*, 1–60.

[10] Castro-Claros, J. D.; Checa, A.; Lucena, C.; Pearson, J. R.; Salas, C. Shell-Adductor Muscle Attachment and Ca2+ Transport in the Bivalves Ostrea Stentina and Anomia Ephippium. *Acta Biomater.* **2021**, *120*, 249–262.

[11] Cartwright, J. H. E.; Checa, A. G. The Dynamics of Nacre Self-Assembly. *J. R. Soc. Interface* **2007**, *4* (14), 491–504.

[12] Addadi, L.; Weiner, S. A Pavement of Pearl. *Nature* **1997**, *389* (6654), 912–913.

[13] Göppert, A.; Cölfen, H. Infiltration of Biomineral Templates for Nanostructured Polypyrrole. *RSC Adv.* **2018**, *8* (59), 33748–33752. https://doi.org/10.1039/c8ra07805j.

[14] Cartwright, J. H. E.; Checa, A. G.; Escribano, B.; Sainz-Díaz, C. I. Spiral and Target Patterns in Bivalve Nacre Manifest a Natural Excitable Medium from Layer Growth of a Biological Liquid Crystal. *Proc. Natl. Acad. Sci.* **2009**, *106* (26), 10499–10504.

[15] Knoll, A. H. Biomineralization and Evolutionary History. *Rev. Mineral. Geochemistry* **2003**, *54* (1), 329–356. https://doi.org/10.2113/0540329.

[16] Morris, J. P.; Backeljau, T.; Chapelle, G. Shells from Aquaculture: A Valuable Biomaterial, Not a Nuisance Waste Product. *Rev. Aquac.* **2019**, *11*, 42–57. https://doi.org/10.1111/raq.12225.

[17] FAO. The State of World Fisheries and Aquaculture. *Sustain. action* **2020**. https://doi.org/10.4060/ca9229en.

[18] Rezaei, R.; Mohadesi, M.; Moradi, G. R. Optimization of Biodiesel Production Using Waste Mussel Shell Catalyst. *Fuel* **2013**, *109*, 534–541.

[19] Mo, K. H.; Alengaram, U. J.; Jumaat, M. Z.; Lee, S. C.; Goh, W. I.; Yuen, C. W. Recycling of Seashell Waste in Concrete: A Review. *Construction and Building Materials*. 2018, pp 751–764, 162. https://doi.org/10.1016/j.conbuildmat.2017.12.009.

[20] Addadi, L.; Weiner, S. Biomineralization: Mineral Formation by Organisms. *Phys. Scr.* **2014**, *89*, 098003. https://doi.org/10.1088/0031-8949/89/9/098003.

[21] Magnabosco, G.; Giuri, D.; Di Bisceglie, A. P.; Scarpino, F.; Fermani, S.; Tomasini, C.; Falini, G. New Material Perspective for Waste Seashells by Covalent Functionalization. *ACS Sustain. Chem. Eng.* **2021**, *9* (18), 6203–6208. https://doi.org/10.1021/acssuschemeng.1c01306.

[22] Zhou, X.; Liu, W.; Tian, C.; Mo, S.; Liu, X.; Deng, H.; Lin, Z. Mussel-Inspired Functionalization of Biological Calcium Carbonate for Improving Eu(III) Adsorption and the Related Mechanisms. *Chem. Eng. J.* **2018**, *351* (April), 816–824. https://doi.org/10.1016/j.cej.2018.06.142.

[23] Murphy, J. N.; Schneider, C. M.; Hawboldt, K.; Kerton, F. M. Hard to Soft: Biogenic Absorbent Sponge-like Material from Waste Mussel Shells. *Matter* **2020**, *3* (6), 2029–2041. https://doi.org/10.1016/j.matt.2020.09.022.

[24] Bourgoin, B. P. A Rapid and Inexpensive Technique to Separate the Calcite and Nacreous Layers in Mytilus Edulis Shells. *Mar. Environ. Res.* **1988**, *25* (2), 125–129.

[25] Murphy, J. N.; Schneider, C. M.; Mailänder, L. K.; Lepillet, Q.; Hawboldt, K.; Kerton, F. M. Wealth from Waste: Blue Mussels (Mylitus Edulis) Offer up a Sustainable Source of Natural and Synthetic Nacre. *Green Chem.* **2019**, *21* (14), 3920–3929.

[26] Tanis, E.; Hanna, K.; Emmanuel, E. Experimental and Modeling Studies of Sorption of Tetracycline onto Iron Oxides-Coated Quartz. *Colloids Surfaces A Physicochem. Eng. Asp.* **2008**, *327* (1–3), 57–63.

[27] Wang, X.; Shu, L.; Wang, Y.; Xu, B.; Bai, Y.; Tao, S.; Xing, B. Sorption of Peat Humic Acids to Multi-Walled Carbon Nanotubes. *Environ. Sci. Technol.* **2011**, *45* (21), 9276–9283.

[28] Olszta, M. J.; Gajjeraman, S.; Kaufman, M.; Gower, L. B. Nanofibrous Calcite Synthesized via a Solution− Precursor− Solid Mechanism. *Chem. Mater.* **2004**, *16* (12), 2355–2362.

[29] Cantaert, B.; Verch, A.; Kim, Y.-Y.; Ludwig, H.; Paunov, V. N.; Kröger, R.; Meldrum, F. C. Formation and Structure of Calcium Carbonate Thin Films and Nanofibers Precipitated in the Presence of Poly(Allylamine Hydrochloride) and Magnesium Ions. *Chem. Mater.* **2013**, *25* (24), 4994–5003. https://doi.org/10.1021/cm403497g.

[30] Kim, Y.; Hetherington, N. B. J.; Noel, E. H.; Kröger, R.; Charnock, J. M.; Christenson, H. K.; Meldrum, F. C. Capillarity Creates Single-crystal Calcite Nanowires from Amorphous Calcium Carbonate. *Angew. Chemie* **2011**, *123* (52), 12780–12785.

[31] Xu, Y.; Tijssen, K. C. H.; Bomans, P. H. H.; Akiva, A.; Friedrich, H.; Kentgens, A. P. M.; Sommerdijk, N. A. J. M. Microscopic Structure of the Polymer-Induced Liquid Precursor for Calcium Carbonate. *Nat. Commun.* **2018**, *9* (1), 2582. https://doi.org/10.1038/s41467-018-05006-w.

[32] Kajiyama, S.; Nishimura, T.; Sakamoto, T.; Kato, T. Aragonite Nanorods in Calcium Carbonate/Polymer Hybrids Formed through Self-Organization Processes from Amorphous Calcium Carbonate Solution. *Small* **2014**, *10* (8), 1634–1641.

[33] Nakayama, M.; Kajiyama, S.; Nishimura, T.; Kato, T. Liquid-Crystalline Calcium Carbonate: Biomimetic Synthesis and Alignment of Nanorod Calcite. *Chem. Sci.* **2015**, *6* (11), 6230–6234.

[34] Nakayama, M.; Kajiyama, S.; Kumamoto, A.; Ikuhara, Y.; Kato, T. Bioinspired Selective Synthesis of Liquid-Crystalline Nanocomposites: Formation of Calcium Carbonate-Based Composite Nanodisks and Nanorods. *Nanoscale Adv.* **2020**, *2* (6), 2326–2332.

[35] Amos, F. F.; Sharbaugh, D. M.; Talham, D. R.; Gower, L. B.; Fricke, M.; Volkmer, D. Formation of Single-Crystalline Aragonite Tablets/Films via an Amorphous Precursor. *Langmuir* **2007**, *23* (4), 1988–1994.

[36] Liu, F.; Gao, Y.; Zhao, S.; Shen, Q.; Su, Y.; Wang, D. Biomimetic Fabrication of Pseudohexagonal Aragonite Tablets through a Temperature-Varying Approach. *Chem. Commun.* **2010**, *46* (25), 4607–4609.

[37] Gehrke, N.; Nassif, N.; Pinna, N.; Antonietti, M.; Gupta, H. S.; Cölfen, H. Retrosynthesis of Nacre via Amorphous Precursor Particles. *Chem. Mater.* **2005**, *17* (26), 6514–6516. https://doi.org/10.1021/cm052150k.

[38] Gilbert, P. U. P. A.; Bergmann, K. D.; Myers, C. E.; Marcus, M. A.; DeVol, R. T.; Sun,

C.-Y.; Blonsky, A. Z.; Tamre, E.; Zhao, J.; Karan, E. A. Nacre Tablet Thickness Records Formation Temperature in Modern and Fossil Shells. *Earth Planet. Sci. Lett.* **2017**, *460*, 281–292.

[39] Sulimai, N. H.; Rani, R. A.; Khusaimi, Z.; Abdullah, S.; Salifairus, M. J.; Alrokayan, S.; Khan, H.; Sermon, P. A.; Rusop, M. Facile Synthesis of CaCO3 and Investigation on Structural and Optical Properties of High Purity Crystalline Calcite. *Mater. Sci. Eng. B* **2019**, *243*, 78–85. https://doi.org/https://doi.org/10.1016/j.mseb.2019.03.006.

[40] Zuiderduin, W. C. J.; Westzaan, C.; Huétink, J.; Gaymans, R. J. Toughening of Polypropylene with Calcium Carbonate Particles. *Polymer (Guildf).* **2003**, *44* (1), 261–275. https://doi.org/https://doi.org/10.1016/S0032-3861(02)00769-3.

[41] Magnabosco, G.; Giosia, M. Di; Polishchuk, I.; Weber, E.; Fermani, S.; Bottoni, A.; Zerbetto, F.; Pelicci, P. G.; Pokroy, B.; Rapino, S.; et al. Calcite Single Crystals as Hosts for Atomic-Scale Entrapment and Slow Release of Drugs. *Adv. Healthc. Mater.* **2015**, *4* (10), 1510–1516. https://doi.org/10.1002/adhm.201500170.

[42] Smith, C. A. Calcium Carbonate as a Pigment for Paper Coating: A Review of the Properties and Applications with Particular Reference to the Paper Industry. *Pigment Resin Technol.* **1982**, *11* (11), 15–16.

[43] Chen, X.; Qian, X.; An, X. Using Calcium Carbonate Whiskers as Papermaking Filler. *BioResources* **2011**, *6* (3), 2435–2447.

[44] Elwakeel, K. Z.; Elgarahy, A. M.; Mohammad, S. H. Use of Beach Bivalve Shells Located at Port Said Coast (Egypt) as a Green Approach for Methylene Blue Removal. *J. Environ. Chem. Eng.* **2017**, *5* (1), 578–587. https://doi.org/https://doi.org/10.1016/j.jece.2016.12.032.

[45] Liao, P.; Yuan, S.; Xie, W.; Zhang, W.; Tong, M.; Wang, K. Adsorption of Nitrogen-Heterocyclic Compounds on Bamboo Charcoal: Kinetics, Thermodynamics, and Microwave Regeneration. *J. Colloid Interface Sci.* **2013**, *390* (1), 189–195. https://doi.org/https://doi.org/10.1016/j.jcis.2012.09.037.

[46] Kubo, M.; Moriyama, R.; Shimada, M. Facile Fabrication of HKUST-1 Nanocomposites Incorporating Fe3O4 and TiO2 Nanoparticles by a Spray-Assisted Synthetic Process and Their Dye Adsorption Performances. *Microporous Mesoporous Mater.* **2019**, *280*, 227–

235.

[47] Li, Q.; Sun, J.; Ren, T.; Guo, L.; Yang, Z.; Yang, Q.; Chen, H. Adsorption Mechanism of 2, 4-Dichlorophenoxyacetic Acid onto Nitric-Acid-Modified Activated Carbon Fiber. *Environ. Technol.* **2018**, *39* (7), 895–906.

[48] Ho, Y. S.; McKay, G. Pseudo-Second Order Model for Sorption Processes. *Process Biochem.* **1999**, *34* (5), 451–465. https://doi.org/https://doi.org/10.1016/S0032-9592(98)00112-5.

[49] Wang, W.; Zhang, H.; Feng, S.; San Emeterio, J.; Mallapragada, S.; Vaknin, D. Iron Ion and Iron Hydroxide Adsorption to Charge-Neutral Phosphatidylcholine Templates. *Langmuir* **2016**, *32* (30), 7664–7670.

[50] Gong, Y. U. T.; Killian, C. E.; Olson, I. C.; Appathurai, N. P.; Amasino, A. L.; Martin, M. C.; Holt, L. J.; Wilt, F. H.; Gilbert, P. Phase Transitions in Biogenic Amorphous Calcium Carbonate. *Proc. Natl. Acad. Sci.* **2012**, *109* (16), 6088–6093.

[51] Baronnet, A.; Cuif, J.-P.; Dauphin, Y.; Farre, B.; Nouet, J. Crystallization of Biogenic Ca-Carbonate within Organo-Mineral Micro-Domains. Structure of the Calcite Prisms of the Pelecypod Pinctada Margaritifera (Mollusca) at the Submicron to Nanometre Ranges. *Mineral. Mag.* **2008**, *72* (2), 617–626.

[52] Ban, M.; Luxbacher, T.; Lützenkirchen, J.; Viani, A.; Bianchi, S.; Hradil, K.; Rohatsch, A.; Castelvetro, V. Evolution of Calcite Surfaces upon Thermal Decomposition, Characterized by Electrokinetics, in-Situ XRD, and SEM. *Colloids Surfaces A Physicochem. Eng. Asp.* **2021**, *624*, 126761.

[53] Montroni, D.; Piccinetti, C.; Fermani, S.; Calvaresi, M.; Harrington, M. J.; Falini, G. Exploitation of Mussel Byssus Mariculture Waste as a Water Remediation Material. *RSC Adv.* **2017**, *7*, 36605–36611. https://doi.org/10.1039/c7ra06664c.

Chapter 3. Stearate coated biogenic calcium carbonate from waste sea shells: A sustainable plastic filler

(Published in ACS Omega)

Stearate coated biogenic calcium carbonate from waste sea shells: A sustainable plastic filler

Maria Luisa Basile,[1, ‡] Carla Triunfo,[1, 2, ‡] Stefanie Gärtner,[3, ‡] Simona Fermani,[1, 4] Davide Laurenzi,[5] Gabriele Maoloni,[5] Martina Mazzon,[6] Claudio Marzadori,[6] Alessio Adamiano,[7] Michele Iafisco,[7] Devis Montroni,[1] Jaime Gómez Morales,[8] Helmut Cölfen,[3] and Giuseppe Falini[1, 9, *]

[1] Department of Chemistry "Giacomo Ciamician", University of Bologna, via F. Selmi 2, 40126 Bologna, Italy.

[2] Fano Marine Center, The Inter-Institute Center for Research on Marine Biodiversity, Resources and Biotechnologies, viale Adriatico 1/N 61032 Fano, Italy.

[3] Department of Chemistry, Physical Chemistry, University of Konstanz, Universitätsstrasse 10, Box 714, D-78457 Konstanz, Germany.

[4] Interdepartmental Centre for Industrial Research Health Sciences & Technologies, University of Bologna, 40064 Bologna, Italy.

[5] Finproject S.p.A., Plant Ascoli Piceno, Via Enrico Mattei, 1—Zona Ind.le Campolungo, 3100 Ascoli Piceno, Italy.

[6] DiSTA, Department of Science and Technology of Agriculture and Environment, Alma Mater Studiorum - Università di Bologna, via Fanin 40, 40127 Bologna, Italy.

[7] Institute of Science, Technology and Sustainability for Ceramics (ISSMC), National Research Council (CNR), Via Granarolo 64, 48018 Faenza, Italy.

[8] Laboratorio de Estudios Cristalográficos, Instituto Andaluz de Ciencias de la Tierra (CSIC-UGR), Avda Las Palmeras 4, 18100 Armilla (Granada), Spain.

[9] CNR, Institute for Nanostructured Materials, via Gobetti 101, 40129, Bologna, Italy.

Abstract

Waste sea shells from aquaculture are a massive source of calcium carbonate that so far has been unexplored in their unique and peculiar features such as polymorphic selection and fidelity, crystalline texture, and the presence of an intra-crystalline organic matrix. Biogenic calcium carbonate (bCC) can be a potential substitute for ground calcium carbonate and precipitated calcium carbonate. These last materials find several applications after a surface coating with hydrophobic molecules, being stearate among them one of the most used at the industrial scale. The capability of bCC powders to be coated with stearate has not been studied so far. Here, we investigate for the first time the capability of aqueous stearate dispersions to coat bCC powders from the shell of market-relevant mollusc aquaculture species, namely the oyster *Crassostrea gigas*, the scallop *Pecten jacobaeus*, and the clam *Chamelea gallina*. The chemical-physical features of the materials were extensively characterized by different analytical techniques. The results show that the adsorption capability of the bCC powders was different among the calcium carbonate from different species and the geogenic calcium carbonate, employed as reference. The oyster shell powder is the bCC with a higher content of organic matrix and showed the highest adsorption capability (about 23 wt% compared to 10 wt% of geogenic calcite). These results agree with the mechanism proposed in literature in which stearate adsorption mainly involves the formation of calcium stearate micelles in the dispersion before the physical adsorption. The prepared materials from oyster shells were tested as fillers in an ethylene vinyl acetate compound used for the preparation of shoe soles. The compound showed better mechanical performances than that one prepared using ground calcium carbonate from limestone. In conclusion, we can state that bCC can replace ground and precipitated calcium carbonate, has a higher stearate adsorbing capability, and represents an environmentally friendly and sustainable source of calcium carbonate.

Keywords: Biogenic calcium carbonate, waste sea shells, stearate, adsorption, polymer filler.

Introduction

Calcium carbonate ($CaCO_3$) is one of the most widely used materials, having a sale of about 150 Mton per year [1]. It is commonly obtained by grinding the geogenic raw mineral, limestone, forming ground calcium carbonate mineral (GCC), or by carbonation of a calcium

hydroxide slurry, generating the so-called precipitated calcium carbonate (PCC) [2]. GCC is classified according to the size of the grains that have the shape of irregular rhombohedra. This material is made of calcite, the most thermodynamically stable $CaCO_3$ polymorph, and no chemical change is involved in its preparation process [3]. On the other hand, the manufacture of PCC requires more stages such as calcination, hydration/slacking, carbonation, filtration, and drying. The size and shape of PCC grains can be controlled, and impurities are removed during the synthetic process. PCC is generally obtained as rhombohedral or scalenohedral calcite, but aragonite and vaterite, the kinetically favoured and the metastable $CaCO_3$ polymorph, respectively, can be also obtained [2]. In PCC a rigorous $CaCO_3$ polymorphic selection is a difficult task and often traces of other polymorphs co-exist with the preponderant one. However, PCC particles are mostly uniform in size and regular in shape when compared to GCC. Thus, PCC is used in more advanced applications than those of GCC [4,5].

$CaCO_3$ is also the main component of mollusc shells and other skeletal structures of many calcifying invertebrates, where it usually represents more than 95 wt% of the mass [6,7]. The $CaCO_3$ formed by organisms is obtained under accurate and faithful biological control. This implies, by example, that different species are able to form structures of aragonite, calcite, or with a precise spatial distribution of both polymorphs [8]. In the latter case, they are located in different layers and never mixed together [7]. In biogenic $CaCO_3$ (bCC) the crystalline texture and the presence of trace elements is species-specific [9,10]. This depends on the geochemical features of the living site of the calcifying organism and can be customized [11]. Thus, bCC offers controlled species- and site-specific features that are difficult to find and reproduce in GCC and PCC, respectively.

An important source of bCC is mollusc shells from aquaculture [12,13]. This is a farming sector of growing economic relevance and nowadays the production of mollusc shells by aquaculture is about 15 Mton per year [14]. The majority of these shells are not collected and become waste which represents a major economic and environmental issue [14–17]. Their valorisation by sustainable and green processes is desirable and can be a good example of circular economy [18,19].

Presently, mollusc shell powders are used as calcium integrator in poultry's feed, liming agents in agriculture, and inert filler in diverse composite materials [12,15]. When used as filler, the bCC powders act as an inert and do not provide any additional performance advantage to the material. Two exemplative cases are their application in polymers and concretes.

$CaCO_3$ is the most widely used inorganic filler in polymers [20]. The GCCs are low in price

and used primarily to reduce formula costs. By contrast, the PCCs are higher in price and used to modify various properties of polymer composites [2]. Oyster shell powder imparted to ethylene-vinyl acetate/low-density polyethylene resulted in a material with a remarkably enhanced thermal stability and antimicrobial activity against Gram-positive and Gram-negative bacteria [21]. Mussel shell $CaCO_3$ was used as filler for a compostable matrix made of polylactic acid and poly(butylene adipate-co-terephthalate). In this case, thermal, mechanical, morphological, and physical investigations of these bio-composites showed that their performances were comparable with those produced with GCC [22].

Eo et al. prepared concrete with different oyster shell powder contents (10 wt%, 20 wt%, and 30 wt%) and found that the mechanical properties of concrete replaced by 10 wt% oyster shell powder were basically the same as that of ordinary concrete [23]. However, the use of oyster shell powder as fine aggregates had a negative impact on the durability of concrete [24]. It was reported that, when compared with ordinary concrete, the one enriched with oyster shell powder showed a higher water absorption [25].

Hydrophobic modification of the surface of $CaCO_3$ is an effective method to improve its applications as filler in particular in the case of mollusc shell powder [26]. This surface treatment facilitates the dispersion in hydrophobic polymeric matrices, for example preventing loss of mechanical performances, such as impact resistance. In addition, moisture pick-up by $CaCO_3$ may pose additional problems during handling and processing [27]. In concretes, it prevents water from penetrating concrete increasing corrosion resistance [28].

Among a variety of $CaCO_3$ surface coaters such as silanes, phosphates, and titanates, the most widely used are fatty acids [29]. In particular, a blend of stearic acid and palmitic acid (stearin) and pure stearic acid are the most commonly used for industrial applications and laboratory research, respectively. The process of stearic acid/stearate adsorption on the calcite surface can occur in “dry” conditions or using “wet” methods [30]. Generally, the industrial coating is done in water because of the low cost and the simplicity of the process [31,32]. It has been suggested that in water suspension, in the presence of significant amounts of dissolved ions, the adsorption and subsequent rearrangement of fatty acid micelles is probably the controlling mechanism of coating rather than chemical surface adsorption [31–33].

Here, we suppose that the stearate adsorption mechanism on bCC powders should be similar to that of GCC and PCC. This is because the process is mainly controlled by the presence of micelles of calcium stearate in aqueous dispersions [31–33]. But, we also suppose that the polymorphism, the crystalline texture, and the presence of the intra-crystalline organic matrix,

which are a unique signature of bCC and affect the structure and release of Ca ions [34,35], may influence the adsorption capability of stearate. To test this hypothesis, we use bCC powders from waste sea shells from aquaculture, namely oyster shells, scallop shells and clam shells and compared the results with those obtained using GCC powder. Finally, the selected stearate coated bCC sample was tested as filler in an ethylene vinyl acetate compound used for the industrial preparation of shoe soles.

Materials and methods

Reagents and solvents were bought from Merck and utilized without any further purification. For each experiment, daily fresh solutions were prepared. Mollusc shells of *Crassostrea gigas* (oyster), *Pecten jacobaeus* (scallops) and *Chamelea gallina* (clams) were purchased from F.lli Terzi (Palosco, BG, Italy). Commercial GCC and stearate coated (about 1.5 wt%) GCC were kindly provided by Finproject S.p.a..

Preparation of bCC powders. Mollusk shells were firstly cleaned with tap water to eliminate mineral debris. Then, they were treated with a 5 vol% sodium hypochlorite solution for 24 hours to remove the organic residues from the surface, washed with deionized water, and air dried. The dry shells were finally crushed by a hammer mill and sieved at 45 μm by analytical sieving to remove the particles with higher size. The bleached materials were obtained by milling each powder (15 g) with 15 vol% sodium hypochlorite solution (100 ml) for 72 hours using a tube roller and ZrO_2 spheres (175 g). The suspension was then filtered under vacuum and the powder was washed with deionized water, dried in an oven at 40 °C and sieved at 45 μm.

Preparation of the sodium stearate solution. Sodium stearate was first dissolved by adding it to water at 60 °C with a concentration of 40 mM or 400 mM. The mixture was stirred for about 30 min until a homogeneous dispersion was obtained.

$CaCO_3$ coating with stearate. The coating was carried out by adding 2.0 g of the $CaCO_3$ particles, biogenic or geogenic, to the sodium stearate solution (50 ml) at 60 °C. The suspension was stirred for 2 hours. The coated $CaCO_3$ was then separated by vacuum filtration, aboundingly washed with water at 60 °C, and dried in an oven at 105 °C overnight [31].

Physical characterization of the $CaCO_3$ materials. X-ray diffraction patterns of the samples were collected using a PanAnalytical X'Pert Pro diffractometer equipped with a multi-array

X'Celerator detector using Cu Kα radiation generated at 40 kV and 40 mA (λ = 1.54056 Å). The diffraction patterns were collected in the 2θ range between 20 ° and 60 ° for the starting materials and 1.5 ° and 12 ° for the coated ones with a step size (Δ2θ) of 0.05 ° and a counting time of 60 s. The analysis of the diffraction pattern to obtain the polymorphic composition and crystallite dimensions was performed using the software Profex.[36] FTIR spectra were collected using a Thermo Scientific™ Nicolet™ iS™10 FTIR Spectrometer. Disk samples for FTIR analysis were prepared by mixing a small amount (2 mg) of sample with 98 mg of dry KBr and applying a pressure of 45 tsi (620.5 MPa) to the mixture using a press. The spectra were recorded with 4 cm^{-1} resolution and 64 scans. Scanning electron microscope (SEM) measurements of the samples were acquired on the Carl Zeiss Leo 1530 Gemini field emission scanning electron microscope. The microscope was used with an accelerating voltage of 5 kV. The samples were glued on a carbon tape, dried under vacuum in a desiccator, and 10 nm gold-coated before their observation. The size distribution measurements were performed with a Mastersizer 2000 (Malvern Panalytical Ltd) laser diffraction particle size analyzer by dispersing bCC or GCC particles in isopropanol and measuring the distribution in isopropanol. Average value was calculated for five measurements. The specific surface area of the samples was measured by the multiple BET method using a Gemini VII 2390 Series Surface Area Analyzer (Micromeritics Instrument Corporation) with a nitrogen flow. Thermogravimetric analysis (TGA) was carried out under nitrogen flow at a heating rate of 10 °C min^{-1} by TA SDT Q600 V 8.0 instrument. The system was pre-equilibrated at 30 °C, then a ramp from 30 to 900 °C was performed. For the measurement, 10 mg of each sample in an alumina crucible were used and the temperature ranges considered to estimate the organic material and stearate content were different depending on the nature of the samples and were chosen based on the derivative thermogravimetric profiles (DTG). Differential scanning calorimetry (DSC) measurements were carried out under nitrogen flow at a heating rate of 10 °C min^{-1} from 0 to 200 °C with a TA Q100 instrument. The analysis was performed using 5 mg of each sample in a hermetic aluminum crucible to clarify the presence of hydrated calcium stearate. The contact angle (CA) with sessile water drops (volume 10 μL) was measured using an optical system (Drop Shape Analyzer DSA30S, Krüss GmbH). Average values were calculated for five measurements on different points of each surface. The sample was compressed in a pellet before the measurement. Quantitative color measurements were acquired by an Eoptis CLM-194 colorimeter using a D65 light source and $BaSO_4$ as reference. The results were reported in the CIEL*a*b* system,

where L* represents brightness, while a* and b* color parameters (a* on the red-green scale and b* on the yellow-blue scale).

$CaCO_3$ elemental composition. The sample was set in a Teflon holder with 0.5 mL of H_2O_2 (30 vol%, Carlo Erba) and 6 mL of HNO_3 (65 vol%, Honeywell). The holder was set in a microwave oven (Milestone) operating as follows: 2 min at 250 Watt, 2 min at 400 Watt, 1 min at 0 Watt, and 3 min at 750 Watt. The digested sample was quantitatively collected, diluted to 10 mL with water, and filtered on paper. All the liquid samples obtained were measured three times, 12 s each, with 60 s of pre-running, using an ICP-OES, Spectro Arcos-Ametek, Inductively Coupled Plasma Optical Emission Spectroscopy. The calibration curve was made using certified standards in water.

Synthesis of the coated bCC / ethylene vinyl acetate compounds. The stearate-coated bCC / ethylene vinyl acetate compounds were prepared according to an industrial procedure. Briefly, polymers and raw materials, in the right mass ratio, were cold introduced into a closed mixer (Comerio Ercole S.p.A.). Through friction the mixture reached the temperature of 90 °C and then was discharged into the hopper of a granulation extruder (Filmex SAS). Successively, the granules were introduced into the hopper of an injection press (Main Group), plasticized at 95 °C, and injected into the mold at about 200 °C, where the expansion and cross-linking reactions take place for a curing time of about 7 min. The specimens were cooled in a temperature-controlled environment at 23 °C and stored at the same temperature.

Mechanical and aesthetic characterization of polymeric compounds. The mechanical and aesthetic characterization of the polymeric compounds were performed after a preliminary specimen preparation in which a splitting machine (Camoga C420) was used to remove the external skins and a pneumatic cutter (NOSELAB ATS 10019000) was used for the preparation of specimens having the shape requested by the ISO regulation (Fig. SI1). For the measurement of the tensile strength and elongation at break a Zwick/Roell Z010 dynamometer with 10 KN load cell and Long Stroke extensometer with 800 mm extension was used. The test was conducted according to the ASTM D412 technical standard with a clamp removal speed of 200 mm min^{-1}. The aesthetic features were evaluated by images obtained using an optical microscope in reflection conditions.

Results and discussion

In this work we have employed sea shells from species that have (*i*) a strong relevance in aquaculture [12], (*ii*) are made of a single $CaCO_3$ polymorph and (*iii*) have diverse crystalline textures [14,35]. The bCC used in this study are the low Mg-calcite from the oyster *C. gigas*, the medium Mg-calcite from the scallop *P. jacobaeus*, and the aragonite clam *C. gallina* (Fig. 1).

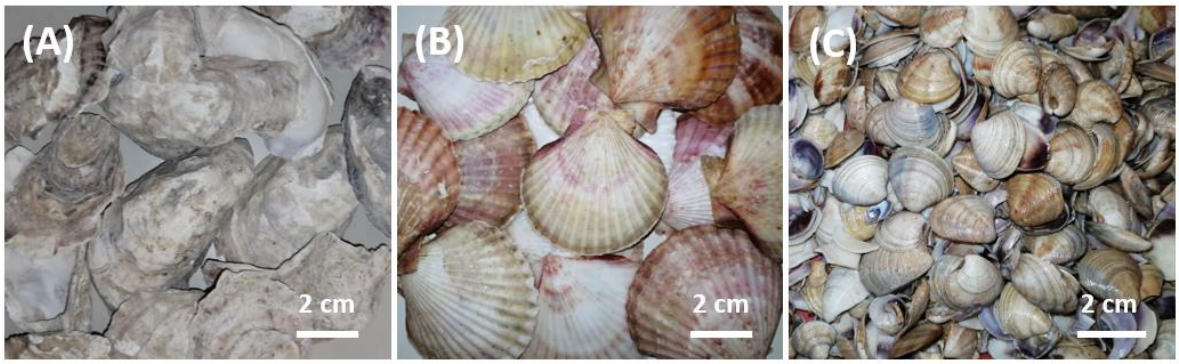

Figure 1. Camera images of pristine shells from the oyster *C. gigas* (A), the scallop *P. jacobaeus* (B) and the clam *C. gallina* (C).

In analysing their capability to be coated with stearate, the sea shell powders were homogenized in grain size, performing ball milling and sieving at 45 μm. The same process was done for GCC, as comparison. In addition, to evaluate the effects of the surface-exposed organic matrix an aliquot of the bCC powder was bleached. The characteristics of the obtained powders are reported in Tables 1 and 2. The X-ray powder diffraction patterns (Fig. 2 and 3) showed that that in the powder from clam shells, upon the dry grinding process, a phase transition of about 10 wt% from aragonite to calcite occurred. This is in agreement with some literature data that reported that this phase transition is associated to the temperature increase produced by frictional heating of grinding [37,38], due to the highest thermodynamic stability of calcite,[29] but disagrees with other researches reporting the opposite [39,40]. The bleaching treatment in wet conditions favoured this phase transition and the content of calcite increased to about 19 wt%. A similar behaviour was reported for abalone shells [41].

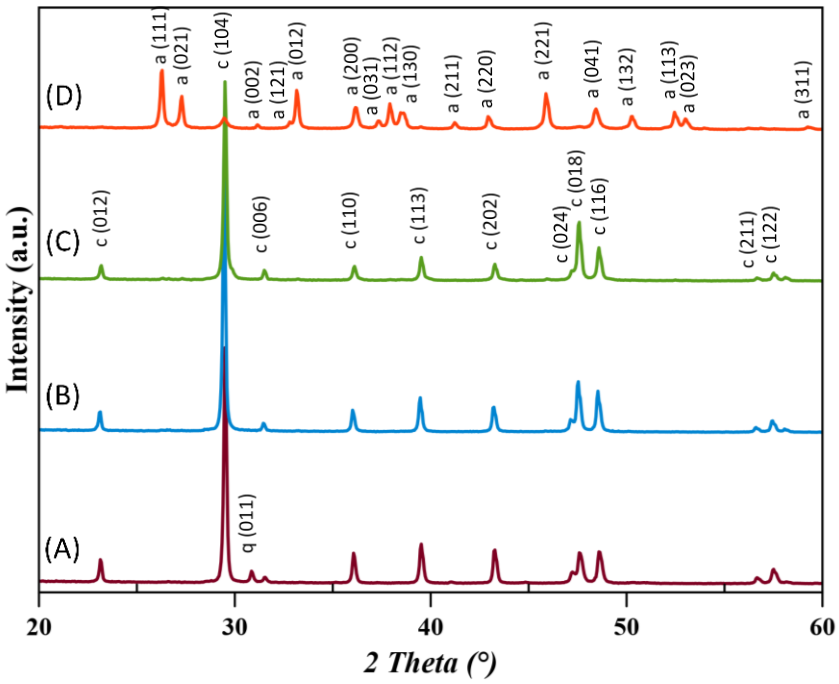

Figure 2. X-ray powder diffraction patterns of geogenic $CaCO_3$ (A), oyster shell (B), scallop shell (C) and clam shell powder (D). The diffraction patterns were indexed accordingly to the PDF 00-005-0586 for calcite (c), PDF 00-005-0453 for aragonite (a) and PDF 01-080-2148 for quartz (q).

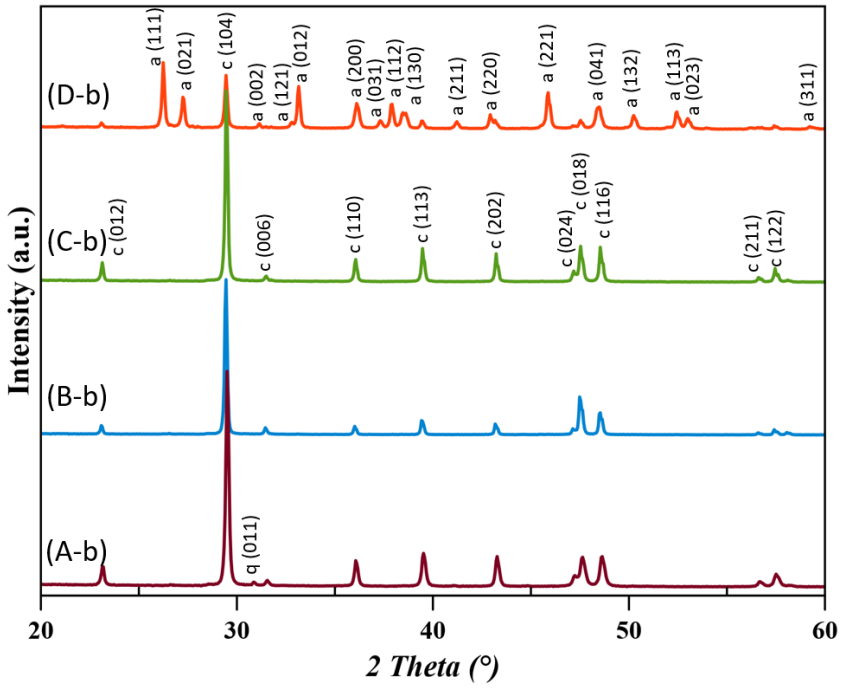

Figure 3. X-ray powder diffraction patterns of bleached geogenic $CaCO_3$ (A-b), oyster shell (B-b), scallop shell (C-b) and clam shell powder (D-b). The diffraction patterns were indexed accordingly to the PDF 00-005-0586 for calcite (c), PDF 00-005-0453 for aragonite (a) and PDF 01-080-2148 for quartz (q).

Interestingly, the content of intra-skeletal organic material did not change in a relevant way after the bleaching process (Fig. 4). This is due to the fact that the majority of the organic material is intra-crystalline, and only the organic macromolecules on the grain surface are oxidized and removed by the bleaching process [18].

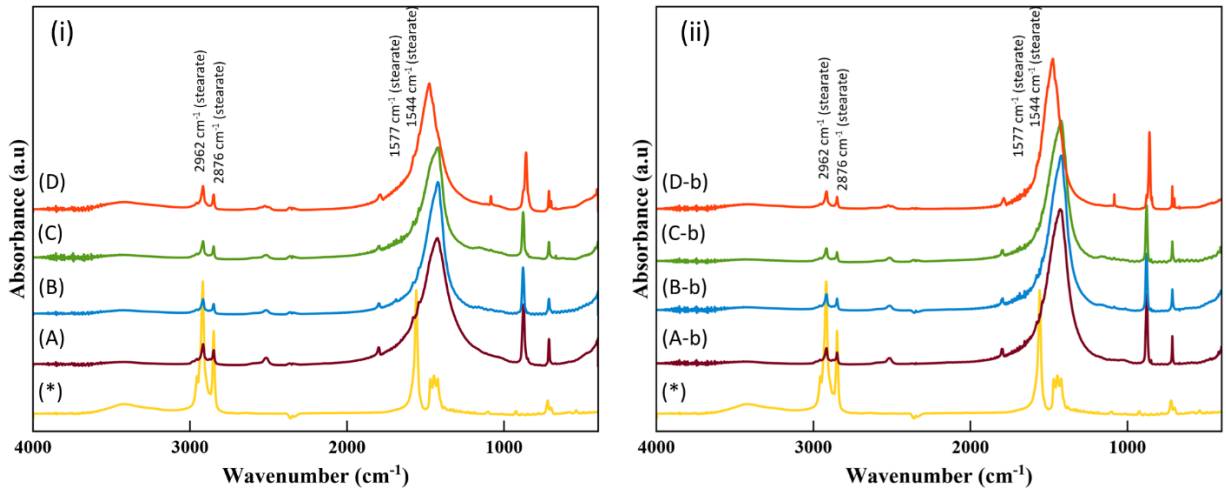

Figure 4. FTIR spectra of unbleached and bleached powders (A) geogenic $CaCO_3$, (B) oyster shells, (C) scallop shells and (D) clam shells coated using a 40 mM stearate solution. (i) unbleached $CaCO_3$ samples. (ii) bleached $CaCO_3$ samples. (*) Sodium stearate FTIR spectrum.

The surface area of the samples did not increase in a relevant way after the bleaching process, despite the decrease of the particle size, both in the biogenic and geogenic $CaCO_3$ samples. The latter observation suggests that the reduction in grain size is more related to the grinding associated with the bleaching process than the removal of organic macromolecules.

We excluded a process of dissolution and reprecipitation for GCC since the crystallite sizes ($d_{(104)}$), which were determined by the analyses of the X-ray powder diffraction profile, did not change relevantly. On the contrary, the crystalline domains of mollusc shell powder increased after the bleaching process. This could be due to a recrystallization process of the external layer of the crystallites that has been shown to be formed by amorphous calcium carbonate [42,43].

The results of the elemental analyses are reported in Table 2 and agree with the expected elemental composition [44]. The weight percentage of calcium is around 40 wt%, and the content of magnesium is higher in scallop shells than in oyster shells, while strontium is present only in the aragonite shell of the clam. The content of other elements is quite low. After the bleaching, only the concentration of the minor elements changed, probably due to the dissolution of some soluble salts present in traces in the pristine shells.

Table 1. Percentage $CaCO_3$ polymorph, organic matrix (OM) content, particle size distribution, specific surface area (SSA), and crystallite size of calcite of GCC (A), oyster shell (B), scallop shell (C) and clam shell powder (D) after 45 μm sieving. The suffix -b indicates that the samples were subject to a bleaching/grinding process.

Sample	Calcite (wt%)*	OM content (wt%)[#]	D_{90} (μm)	SSA (m^2 g^{-1})	$d_{(104)}$[$] (nm)
A	99.0	0.2	19.39	2.9	79.7
B	100	1.3	32.55	3.9	103.9
C	100	0.8	29.01	4.6	84.1
D	9.5	0.6	24.41	4.0	66.5[§]
A-b	99.0	0.2	4.34	4.0	69.4
B-b	100	1.3	6.88	5.9	209.0
C-b	100	0.7	4.60	5.2	134.6
D-b	19.8	0.5	7.72	3.5	93.4[§]

*The complement to 100 % is represented by quartz for sample A and aragonite for sample D. [#] The temperature range considered to estimate the organic material content was between 300 °C and 550 °C. [$]Crystallite size of calcite along the [104] direction. [§] Crystallite size of aragonite along the [211] direction.

Table 2. Elemental composition of the most relevant elements in geogenic $CaCO_3$ (A), oyster shell (B), scallop shell (C) and clam shell powder (D) powder after 45 μm sieving. The suffix -b indicates the samples that were subject to a bleaching/grinding process.

Sample	Ca (mg g^{-1})	Fe (mg g^{-1})	K (mg g^{-1})	Mg (mg g^{-1})	Na (mg g^{-1})	Sr (mg g^{-1})
A	385	0.56	5.6	7.28	23.52	ND[#]
B	392	ND	0.56	1.68	3.36	1.12
C	379	ND	ND	2.8	2.8	1.12
D	373	ND	ND	ND	3.36	1.68
A-b	357	0.56	0.56	6.16	1.68	ND
B-b	382	ND	1.12	1.68	3.92	0.56
C-b	395	ND	1.12	2.24	2.8	1.12
D-b	378	ND	ND	ND	2.8	1.68

[#] The concentration was below the instrumental detection limit.

The morphological appearance of the obtained powder particles is shown in Figures 5 and 6. The geogenic calcite did not change the grain morphology upon the bleaching process, even if the particle size was reduced, in agreement with the grain size distribution (Fig. 5A and B). Differently, the mollusc shell powders showed a change in the morphology of the particles because of the bleaching process (Fig. 5C-H). This effect appears specie-specific, being different in the texture, the polymorphism, and the composition among species. The oyster *C. gigas* shells are made of low Mg-calcite with an isomorphic substitution of magnesium to calcium of about 5 mol% [45]. Both valves of the adult oyster shell are predominantly composed of foliated calcite [46], which is bound on the outermost surface by prismatic calcite and is interrupted by lenses of chalky calcite [47]. The image clearly shows that the (001) surface of the laths making the foliated calcite is smooth before the bleaching and becomes rough and highly porous (Fig. 5C and D). This provokes a slight increase of the specific surface area, which mainly also contributes to the reduction of the grain size. The shell of the scallop *P. jacobaeus* is composed of calcite foliated layers [46], except for a thin aragonitic prismatic pallial myostracum [48]. The content of Mg in the calcite structure is of about 7 mol% [45]. As observed for the shell of *C. gigas* the bleaching induced an increase of the surface roughness and porosity of the laths (Fig. 5E and F), which is associated with an increase of the surface area. The aragonite shell of the clam *C. gallina* presents in the internal layer a granular texture in which the grains do not show any apparent micro-structure and a thinner external prismatic layer. These structural motifs do not change in a relevant way their morphology after the bleaching process (Fig. 5G and H), except a reduction of the grain size, which is not associated with a relevant change of the surface area.

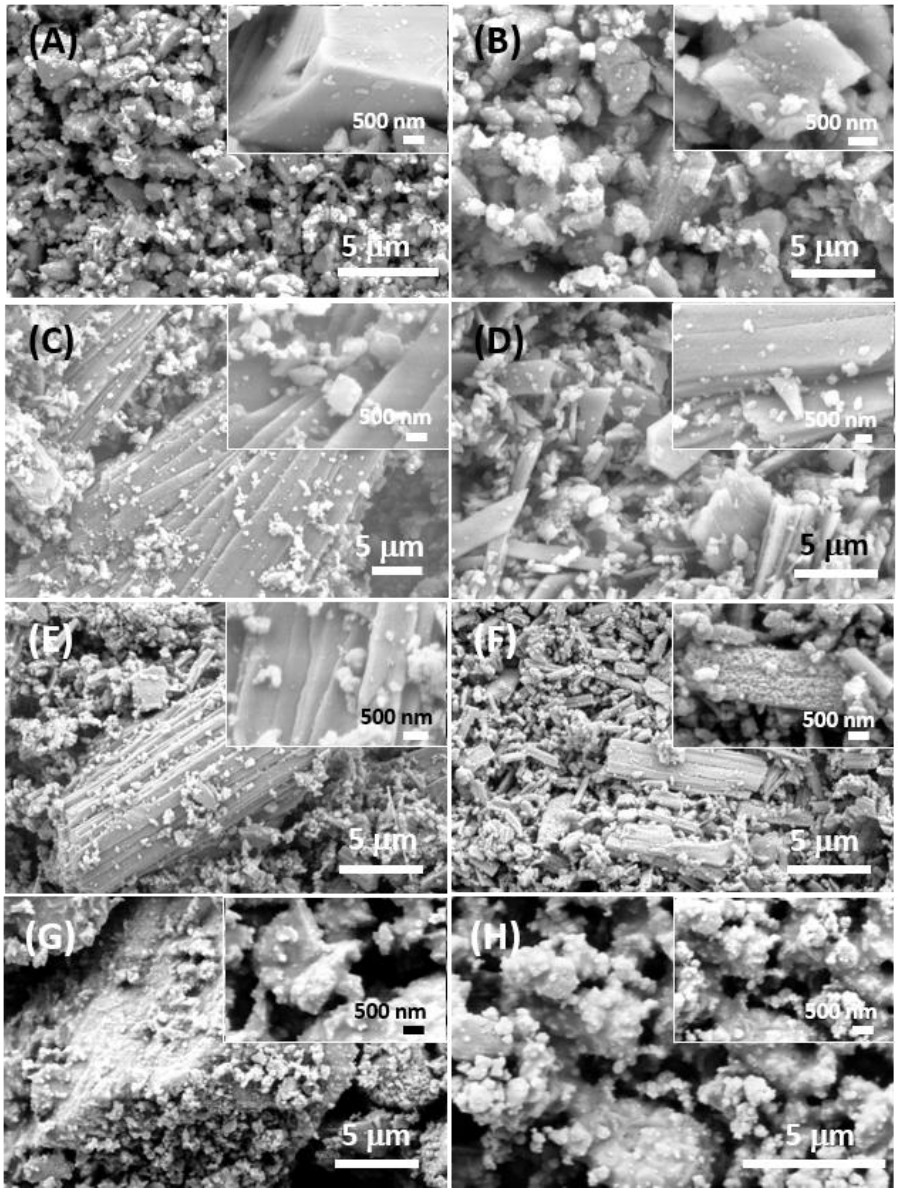

Figure 5. SEM images of unbleached (A, C, E and G) and bleached (B, D, F and H) powders from geogenic $CaCO_3$ (A, B), oyster shells (C, D), scallop shells (E, F) and clam shells (G, H). The insets report high-magnification images. These images are representative of the entire population of particles.

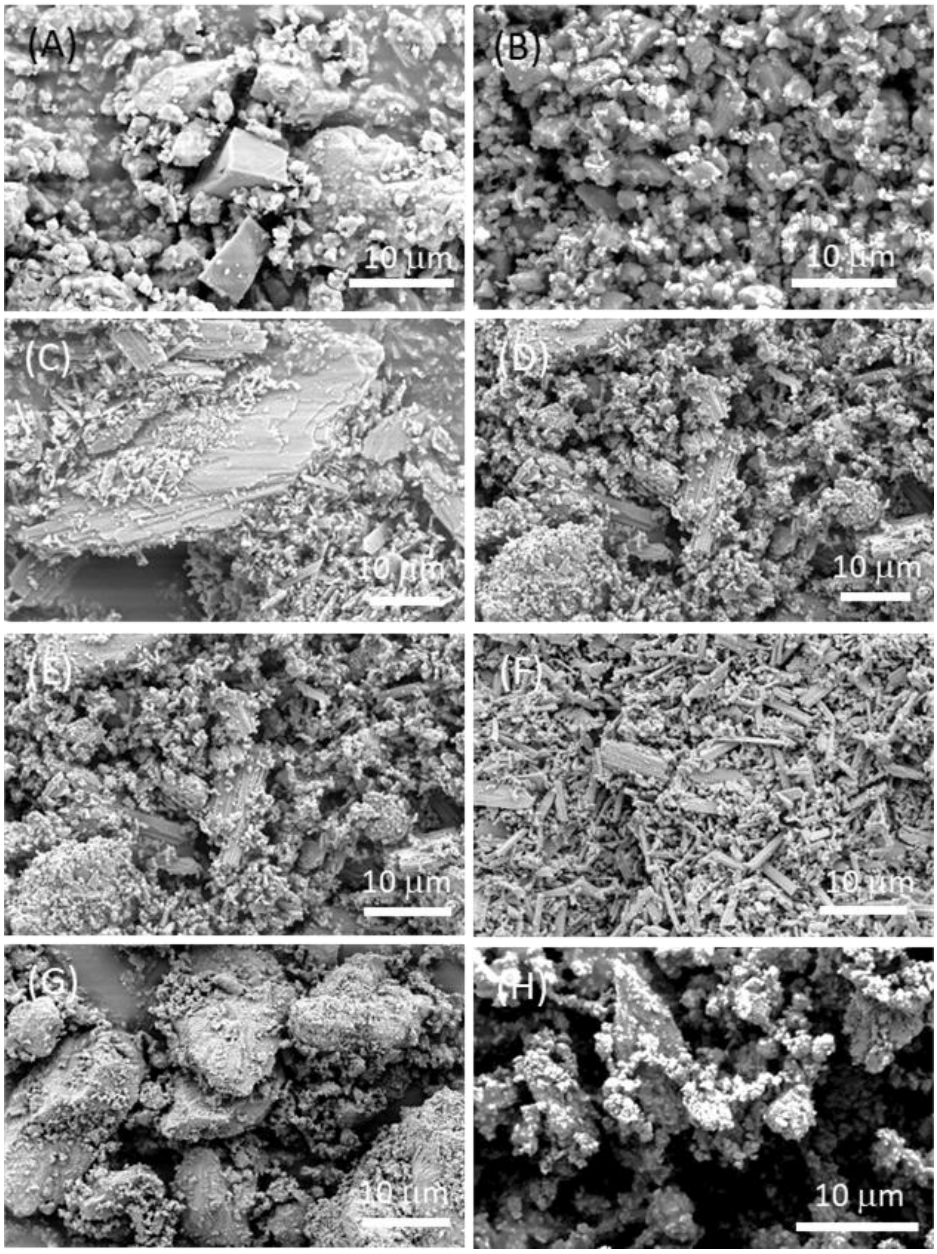

Figure 6. Low magnification SEM images of unbleached (A, C, E and G) and bleached (B, D, F and H) powders from geogenic calcite (A, B), oyster shells (C, D), scallop shells (E, F) and clam shells (G, H). These images are representative of the entire population of particles.

The samples were also evaluated in their colour, which is an important parameter for industrial applications. White fillers are in great demand by the industry because they allow a better control of the colouring of the material given by pigments and dyes [49]. The data (Table 3) show that the whiteness of bleached samples is higher than the untreated ones. This improvement was higher for clams than for oysters and scallops. A reason could be a lower

efficiency of the bleaching process or a higher content of coloured pigment present in clam shells.

Table 3. Colorimetric analysis of particles of: (A) geogenic $CaCO_3$; (B) oyster shells, (C) scallop shells; (D) and clam shell powders. The suffix -b indicates the samples that were subject to a bleaching/grinding process.

Sample	L*	a*	b*	dE^*_{ab}*
A	92.53	0.99	6.57	7.48
B	90.34	0.63	4348	6.71
C	89.43	2.04	5.46	8.37
D	87.86	0.64	6.61	9.90
A-b	92.61	0.98	6.81	7.42
B-b	92.52	0.22	3.55	4.57
C-b	91.12	1.89	5.33	7.36
D-b	92.09	0.67	3.81	5.12

The dE_{ab} values were calculated as follow: $dE^*_{ab}=\sqrt{(L^*_C - L^*)^2 + (a^*_C - a^*)^2 + (b^*_C - b^*)^2}$. L^*_C, a^*_C and b^*_C are the colorimetric values of the control $BaSO_4$.

The coating of the $CaCO_3$ particles was performed using 40 mM and 400 mM sodium stearate aqueous dispersions. These concentrations are both above the critical micellar concentration of stearate, which according to the literature, is from 0.45 mM (at 20 °C) to 0.7 mM (at 60 °C). [50] In a similar reference experiment, Shi et al. (2010) [31] used a 400 mM sodium stearate aqueous dispersion with precipitated $CaCO_3$ crystals having a surface area of about 65 g m^{-2}. This value is about 10 times higher than that of the $CaCO_3$ powders used (Table 1). Therefore, we used 40 mM, and also 400 mM for comparison, sodium stearate aqueous dispersions.

The adsorbed amount of stearate was determined by the weight loss in TGA experiment (Table 4, Fig. 7 and 8) in the range between about 250 °C and 500 °C. When a 40 mM sodium stearate aqueous dispersion was used, the particles were able to adsorb slightly different amounts of stearate according to their source (Table 4), on the other hand, these differences were more marked when a 400 mM stearate dispersion was used (Table 5). The biogenic calcite substrates, oyster and scallop ground shells, adsorbed more stearate than the biogenic aragonite from clam shells and geogenic calcite. Moreover, in all the samples, the bleached substrates adsorbed a higher amount of stearate than the untreated ones.

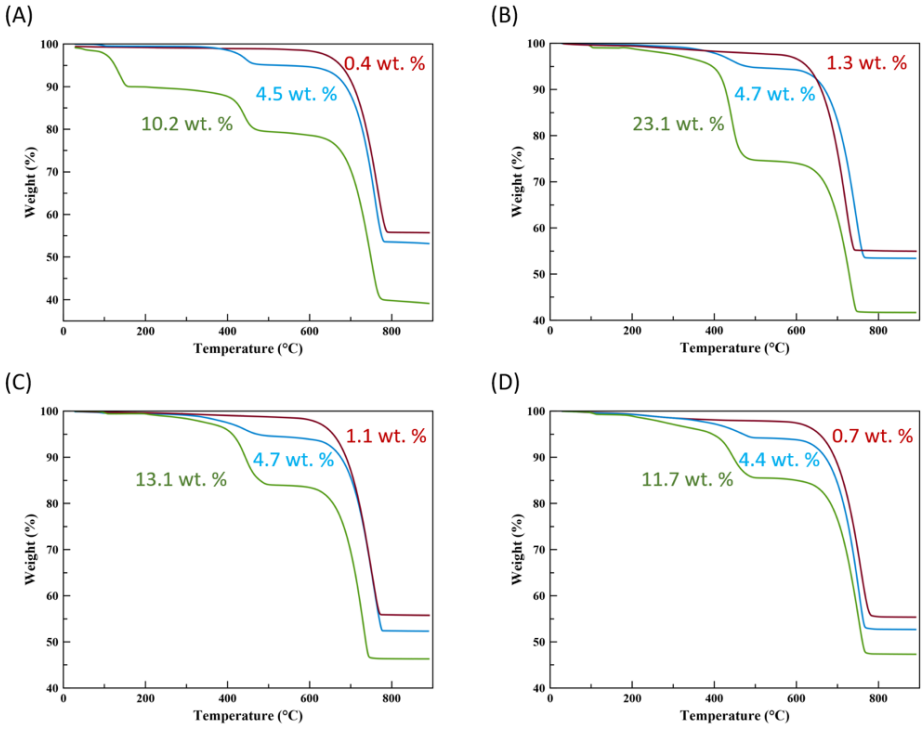

Figure 7. TGA profiles of powder of geogenic $CaCO_3$ (A), oyster shells (B), scallop shells (C) and clam shells (D) (red) and corresponding coated powder with 40 mM (blue) and 400 mM aqueous sodium stearate (green) solutions.

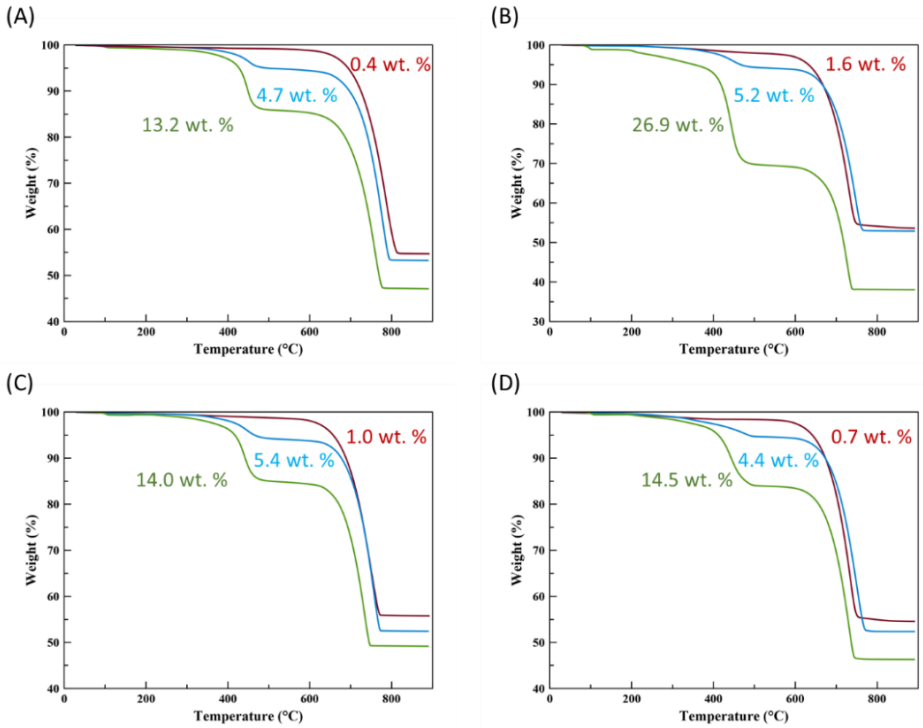

Figure 8. TGA profiles of bleached powder of geogenic $CaCO_3$ (A), oyster shells (B), scallop shells (C) and clam shells (D) (red) and corresponding coated powder with 40 mM (blue) and 400 mM aqueous sodium stearate (green) solutions.

This effect, which can be related to the increase of the specific surface area after bleaching, which was more marked for the biogenic calcite particles than for the biogenic aragonite. The stearate was adsorbed on the $CaCO_3$ particles in the form of Ca salt. These results can be explained by considering that less soluble calcium stearate forms by the exchange reaction between Na stearate and Ca ions in the water suspension [51]. As a consequence, Ca ions dissolve from uncoated areas of the surface of $CaCO_3$ particles to restore the equilibrium until only calcium stearate is present. The surface area covered by one molecule of the stearate at the equilibrium is one important parameter that depends on the crystal faces exposed by the $CaCO_3$ particles [33]. Kralj et al. reported the cross-sectional area of one stearate molecule of 0.21 nm^2 on rhombohedral {104} calcite planes and 0.31 nm^2 for scalenohedral {211} planes in nonstoichiometric calcites [52]. Also the arrangement of the stearate molecules influences the cross-sectional area [53]. Assuming a cross-sectional area of stearate 0.2 nm^2, which corresponds to the surface area for one stearate molecule in a perpendicular orientation [54], for the mean surface areas of $CaCO_3$ particles used (5 m^2 g^{-1}) the theoretical full monolayer coverage would be about 1.2 wt% for stearate coating. At both concentrations investigated in this study, the adsorbed amount of stearate is beyond the theoretical monolayer coverage, as shown in Tables 4 and 5. This indicates that the stearate on the $CaCO_3$ particle surface exists in a multilayer form, with the number of layers increasing as the adsorbed amount of stearate increases.

The adsorbed Ca stearate on the $CaCO_3$ particle surface can be expected to have complex calorimetric properties since the process conditions used during water coating can favour the formation of its hydrate form, calcium stearate monohydrate [55].

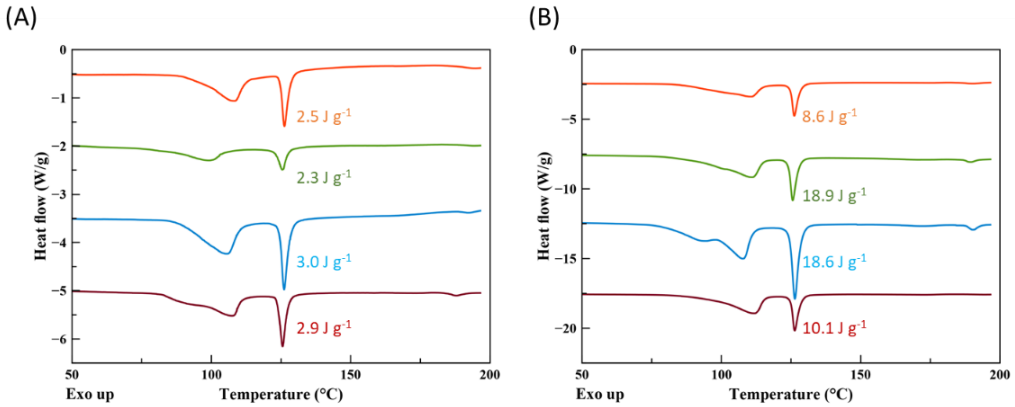

Figure 9. DSC profiles of powder of geogenic $CaCO_3$ (red), oyster shells (blue), scallop shell (green) and clam shell (orange) coated with 40 mM (A) and 400 mM (B) aqueous sodium stearate solutions.

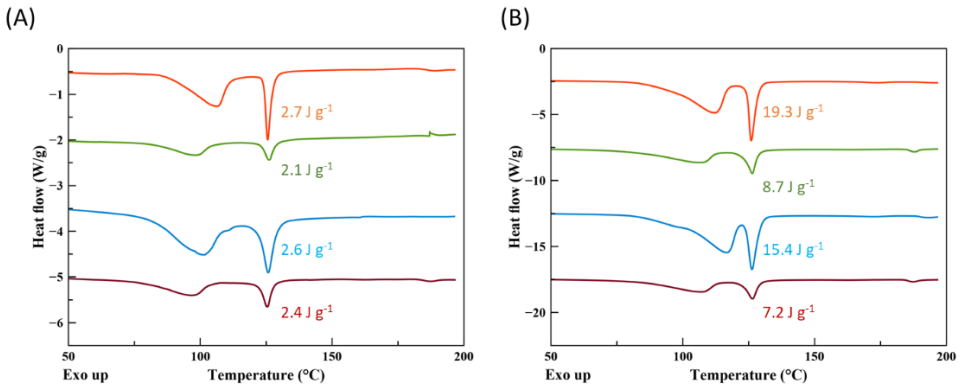

Figure 10. DSC profiles of powder of bleached geogenic $CaCO_3$ (red), oyster shells (blue), scallop shells (green) and clam shells (orange) coated with 40 mM (A) and 400 mM (B) aqueous sodium stearate solutions.

The DSC profiles (Figures 9 and 10) show, as the temperature increases, first a dehydration peak (115 °C) and then a peak corresponding to the transitions from the crystalline-to-smectic phase (130 °C), which agrees with what is reported in the literature for this material [56]. The relationship between the dehydration enthalpy and the crystalline-to-smectic transition enthalpy for the Ca stearate layer adsorbed on the $CaCO_3$ particles surface versus the adsorbed amount of stearate, determined by TGA measurement, is presented in Figure 11. Both enthalpies increase linearly as the adsorbed amount of stearate increases when the 400 mM stearate dispersion was used. Because the crystalline-to-smectic peak and dehydration peaks in the DSC measurements only belong to the physically adsorbed part of Ca stearate, it means that the physically adsorbed part increases in a proportional way to the total organic amount of surfactant and that the chemisorbed part remains at a constant value for each substrate.

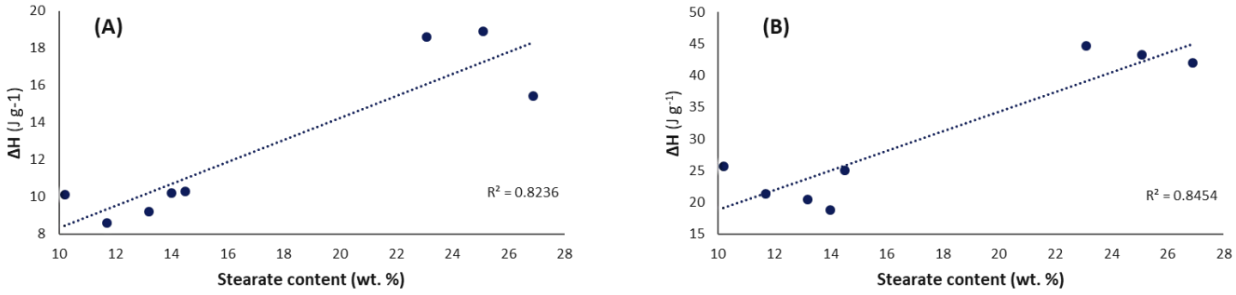

Figure 11. Relationship between the dehydration enthalpy and the crystalline-to-smectic transition enthalpy for the Ca stearate layer adsorbed on the $CaCO_3$ particles surface versus the adsorbed percentage of stearate.

Important information comes from the evaluation of the adsorption capacity (Tables 4 and 5), that here it is defined as the mass of stearate for surface unit of the $CaCO_3$ particles. The data clearly show that when a 40 mM stearate dispersion was used the GCC and the oyster shell powder adsorbed the highest amount of stearate for surface unit, but when the 400 mM stearate dispersion was used the oyster shell powder showed an absorption capacity higher than GCC. The rationalization of this observation needs to recall the specific features of the bCC. Among them, the presence of the intra-skeletal organic matrix, which is the highest in oyster shell powder among the samples analysed. Its presence destabilizes the calcium carbonate structure and thus increases its solubility [57, 58]. Thus, according to the proposed mechanism that implies the formation of calcium stearate, a higher amount of this salt is formed during the interaction between stearate micelles and the powder.

Table 4. Thermal and surface analyses of geogenic $CaCO_3$ (A), oyster shell (B), scallop shell (C) and clam shell powder (D) coated using a 40 mM sodium stearate aqueous dispersion. The temperature range considered to estimate the organic matrix (OM) and stearate (St) content was selected according to the derivate profile of the thermogravimetry curve. The suffix -b indicates the samples that were subject to a bleaching/grinding process.

Sample	**OM + St content** (wt%)	**Adsorption capacity** (g m^{-2})	**Contact angle** (°)	**Crystalline-to-smectic** (°C)	**ΔH** (J g^{-1})
A	4.5	15.5	139.4	125.5	2.9
B	4.7	9.0	137.7	126.1	3.0
C	4.8	9.1	133.4	125.4	2.3
D	4.4	9.9	147.5	126.2	2.5
A-b	4.9	12.3	150.1	125.4	2.5
B-b	5.2	6.9	135.0	125.2	2.6
C-b	5.4	9.5	146.3	126.1	2.1
D-b	4.4	11.6	159.0	125.5	2.7

Table 5. Thermal and surface analyses of geogenic $CaCO_3$ (A), oyster shell (B), scallop shell (C), and clam shell powder (D) coated using a 400 mM sodium stearate aqueous dispersion. The temperature range considered to estimate the organic matrix (OM) and stearate (St) content was selected according to the derivate profile of the thermogravimetry curve. The suffix -b indicates the samples that were subject to a bleaching/grinding process.

Sample	**OM + St content** (wt%)	**Adsorption capacity** (g m^{-2})	**Contact angle** (°)	**Crystalline-to-smectic** (°C)	**ΔH** (J g^{-1})
A	10.2	27.2	135.4	126.4	10.1
B	23.1	60.9	136.4	126.4	18.6
C	13.1	20.2	137.3	125.6	18.9
D	11.7	20.9	139.0	126.1	8.6
A-b	13.2	25.3	149.0	126.4	9.2
B-b	26.9	45.1	92.2	126.2	15.4
C-b	14.0	18.6	146.3	126.3	10.2
D-b	14.5	35.3	128.8	125.9	10.3

The structure of the adsorbed stearate was further investigated by SEM, FTIR, and X-ray powder diffraction. In Figure 12 are shown the FTIR spectra of $CaCO_3$ particles coated using a 400 mM dispersion of stearate. The two bands at about 2919 cm^{-1} and 2852 cm^{-1} are due to the antisymmetric and symmetric methyl stretching vibration modes (ν_{aCH3} and ν_{sCH3}), respectively. The absorption bands at 1577 cm^{-1} and 1544 cm^{-1} are due to the antisymmetric ν_{aCOO-} stretching vibration of carboxylate groups in uni-dendate and bi-dendate coordination with Ca ions, respectively [59]. No other bands associated with carboxylate groups were present, thus only calcium stearate formed [32]. Other absorption bands are due to vibration modes associated with calcite and aragonite or to the alkyl chains of the stearate. No band shift was observed among samples and only the relative intensities of the bands changed according to the composition of stearate-calcium carbonate materials. When a 40 mM stearate dispersion was used, the low relative amount of adsorbed stearate (Table 4) did not allow its detection, and the FTIR spectra showed only the typical adsorption bands of calcite and aragonite (Figure 10).

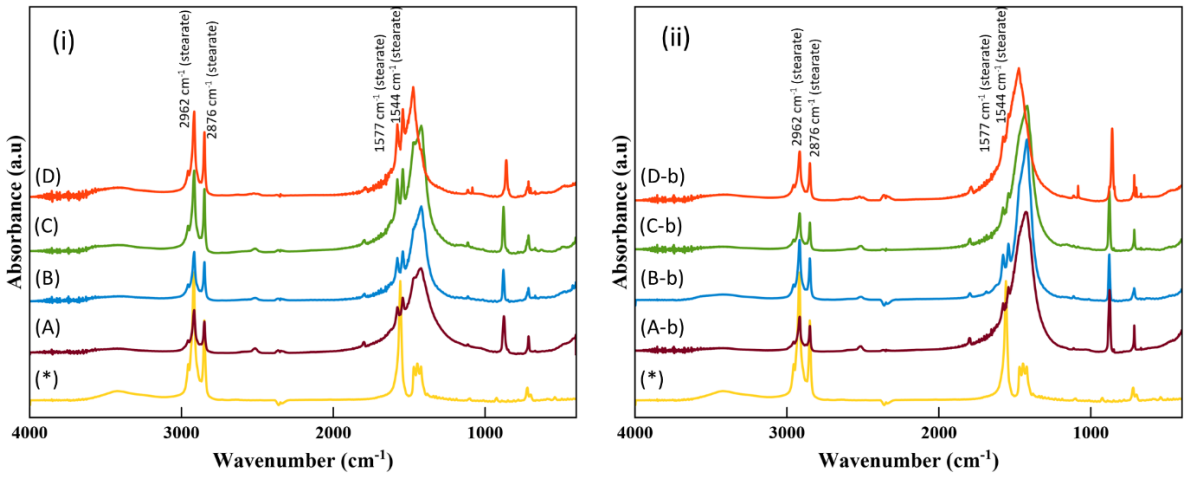

Figure 12. FTIR spectra of unbleached and bleached powders (A) geogenic $CaCO_3$, (B) oyster shells, (C) scallop shells and (D) clam shells coated using a 400 mM stearate dispersion. (i) unbleached $CaCO_3$ samples. (ii) bleached $CaCO_3$ samples. (*) Sodium stearate spectrum.

The examination of X-ray powder diffraction patterns of the materials provided information on the crystal form of calcium carbonate (Mg-calcite or aragonite) and also on the structure of its stearate coating.

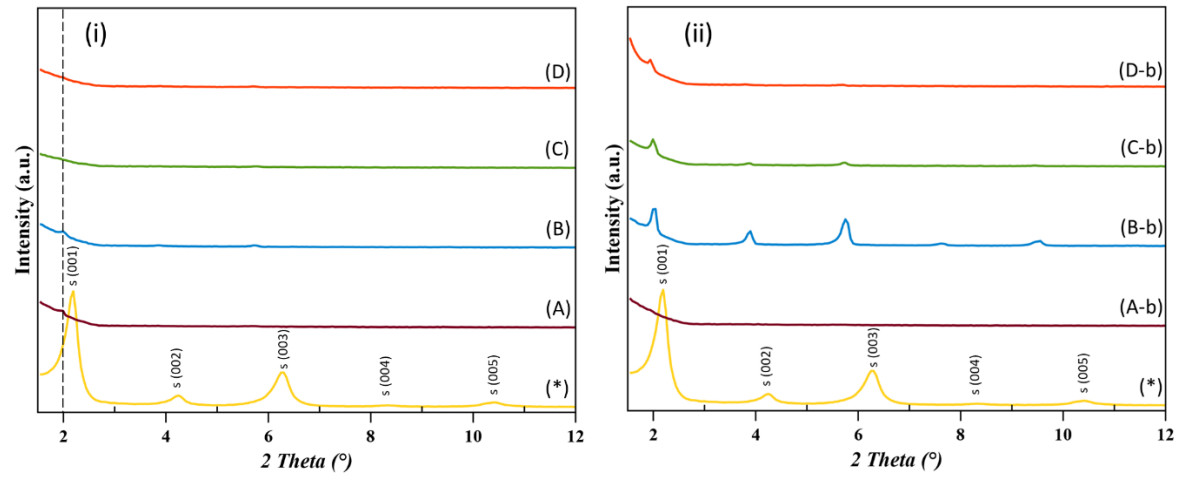

Figure 13. X-ray powder diffraction patterns of unbleached and bleached powders (A) geogenic $CaCO_3$, (B) oyster shells, (C) scallop shells and (D) clam shells coated using a 40 mM stearate solution. (i) unbleached $CaCO_3$ samples. (ii) bleached $CaCO_3$ samples. (*) Sodium stearate X-ray powder diffraction pattern.

The diffraction peaks at small Bragg angles ($2\theta < 12$ °) from the coated particles using the 40

mM stearate dispersion (Fig. 13) did not show diffraction peaks for the unbleached samples, which contained the lowest percentage of stearate (Table 4). The only exception was observed when the oyster powder was used. In this case, a weak diffraction peak was detected at 1.98 °. Using the same stearate dispersion, the associated diffraction peaks were detected on the bleached samples. These were at 2θ values of 1.98 °, 3.90 °, 5.72 °, 7.59 ° and 9.48 ° corresponding to the first five orders of the laminar structure of calcium stearate (46.5 Å) having extended chains oriented almost normal to the plane containing the ionic groups [60]. When the 400 mM stearate dispersion was used the low angle diffraction peaks were more intense, as expected having a higher concentration of stearate (Fig. 14). This effect was more evident for the bleached samples (Table 5). Also, in this set of experiments, it can be noted that the oyster shell powder was the substrate with the most intense calcium stearate diffraction peaks.

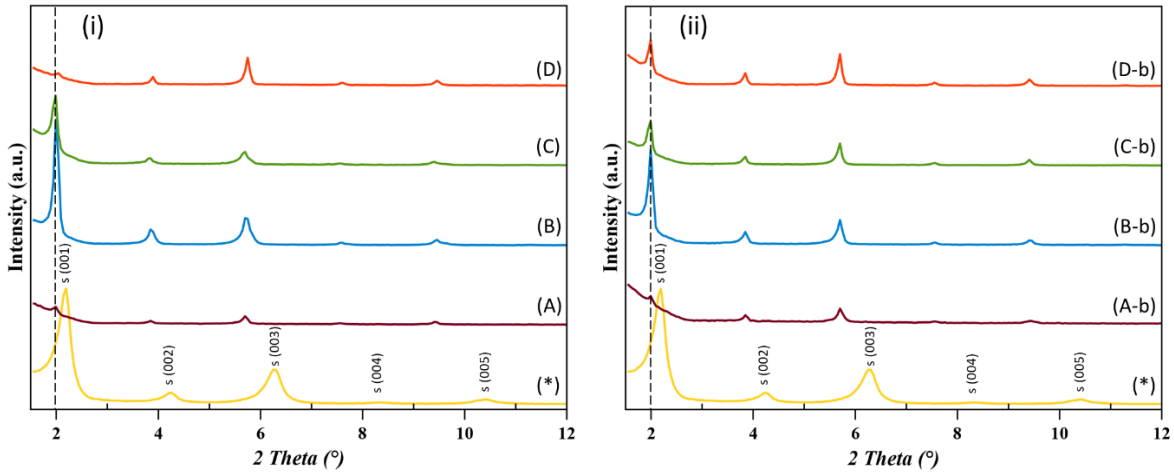

Figure 14. X-ray powder diffraction patterns of powders of: (A) geogenic $CaCO_3$, (B) oyster shells, (C) scallop shells and (D) clam shells coated using a 400 mM stearate dispersion. (i) unbleached $CaCO_3$ samples. (ii) bleached $CaCO_3$ samples. (*) Sodium stearate diffraction pattern.

The absence of diffraction peaks in the samples with the lower content of stearate could be due to the detection limit of the method but also because the chemisorbed stearate does not give diffraction peaks, as previously reported [31]. Thus, where diffraction peaks are detected, the majority of calcium stearate is physiosorbed on the surface of stearate chemisorbed $CaCO_3$ particles.

The SEM images of the samples treated with a 40 mM and 400 mM stearate dispersion are reported in figures 15 and 16, respectively. The samples treated with the 40 mM stearate dispersion (Fig. 15) generally preserve all the textural and morphological features of the

samples before the coating process. This is expected since a low amount of stearate is adsorbed, no more than a few layers, on the unbleached samples. These layers do not change the overall morphology and do not induce a relevant aggregation of the particles. The higher amount of stearate adsorbed on the bleached samples does not change in a relevant way the morphology of the particles, even if the X-ray data indicate the presence of crystalline layers able to generate a diffraction pattern. The $CaCO_3$ particles treated with the 400 mM stearate dispersion and containing a high percentage of stearate lose many of the surface characteristics of the uncoated samples (Fig. 16). Moreover, the presence of deposits of layered structures, which may embed $CaCO_3$ particles is observable.

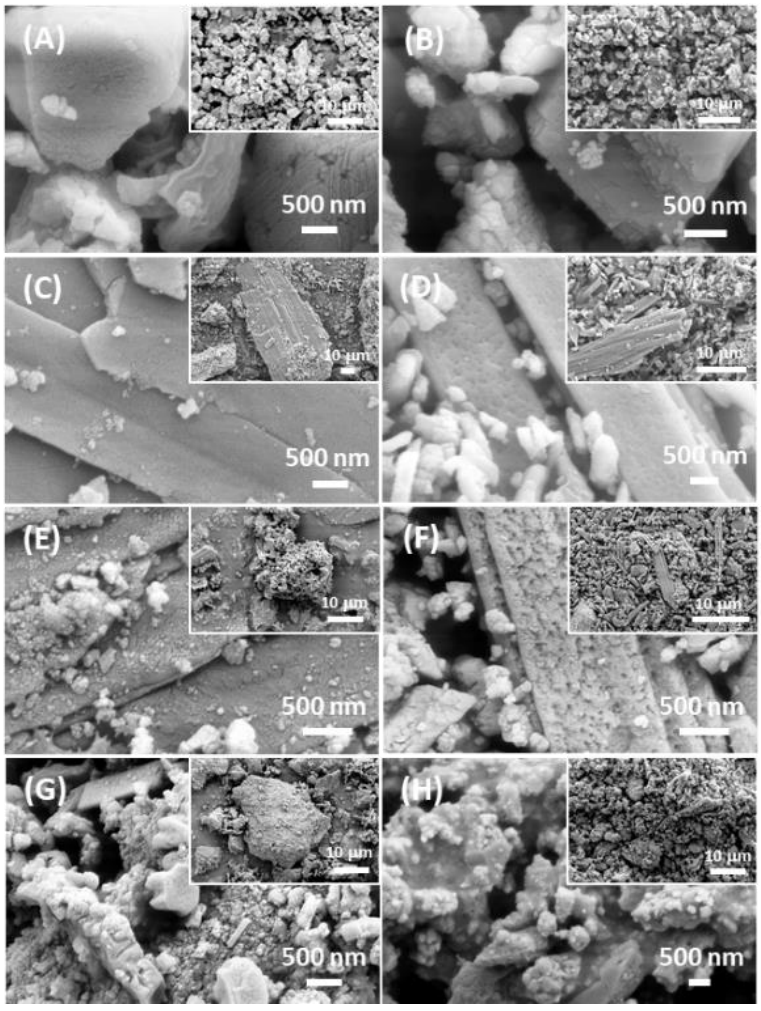

Figure 15. SEM images of $CaCO_3$ particles coated using a 40 mM stearate dispersion. (A) geogenic $CaCO_3$, (B) bleached geogenic $CaCO_3$, (C) oyster shell powder, (D) bleached oyster shell powder, (E) scallop shell powder, (F) bleached scallop shell powder, (G) clam shell powder and (H) bleached clam shell powder. The insets report a low-magnification image for each sample. The images are representative of the entire population of particles.

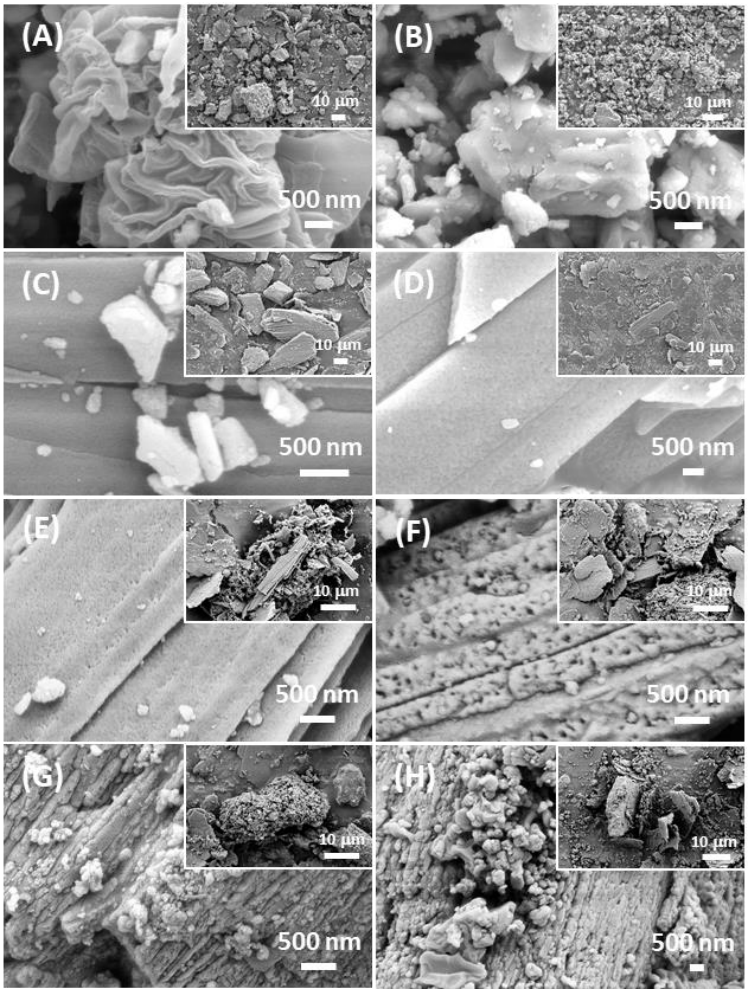

Figure 16. SEM images of $CaCO_3$ particles coated using a 400 mM stearate dispersion. (A) geogenic $CaCO_3$, (B) bleached geogenic $CaCO_3$, (C) oyster shell powder, (D) bleached oyster shell powder, (E) scallop shell powder, (F) bleached scallop shell powder, (G) clam shell powder and (H) bleached clam shell powder. The insets report a low-magnification image for each sample. The images are representative of the entire population of particles.

According to the reported data in the aqueous coating using a hot dispersion of sodium stearate, a chemisorbed-monolayer first forms, on which the precipitation of micelles generates additional physically adsorbed layers of calcium stearate. During the deposition/drying process the aliphatic groups reorganize and orient outwards of the surface, leading to a hydrophobic $CaCO_3$ surface and a low surface energy [31, 32]. Moreover, the diverse textures and polymorphisms of the bCC favour the chemical-physical processes associated to the adsorption process, generating stacked multilayers [61], being this effect particularly marked for the oyster shell powder.

Some of the prepared materials were finally tested as fillers in an ethylene vinyl acetate

compound for the preparation of shoe soles. The $CaCO_3$ particles were used in a 10 wt% concentration, as commonly done in the industrial process. We tested the oyster shell coated materials since they were the substrates with the highest capability of stearate adsorption. The process was performed according to the industrial procedure, thus giving room for a future potential scale-up. In a separate set the ethylene vinyl acetate matrices were loaded with the same mass percentage of 45 µm sieved commercial stearate coated GCC, as control. Polymeric compound specimens were prepared to test mechanical and aesthetic properties (Fig. 17).

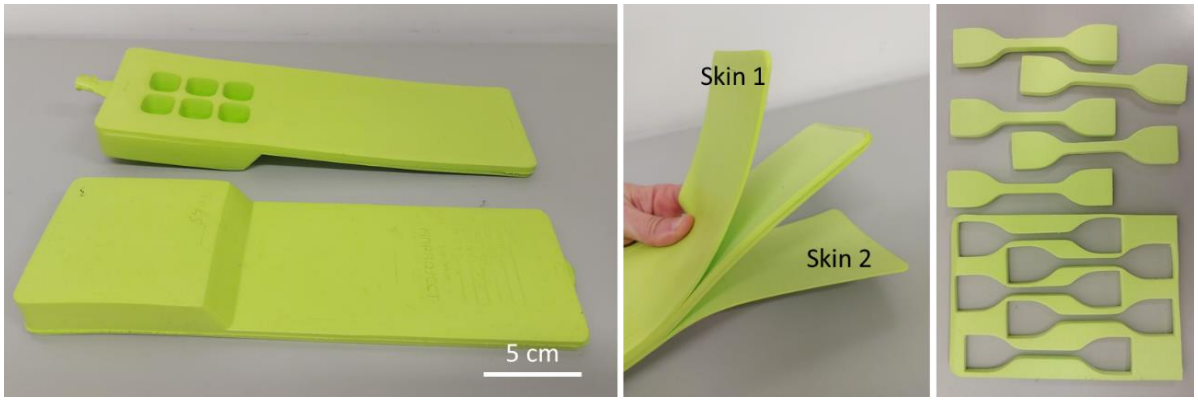

Figure 17. Polymeric compound specimen preparation for mechanical and aesthetic evaluations.

The optical images in Figure 18 show that the foamability, the qualitative distribution of pores, of the shoe soles did not change when the commercial stearate-coated GCC was replaced with the bCC coated with different amounts of stearate. This is an important parameter that affects the overall aesthetic feature of the compound [62], and thus its commercialization.

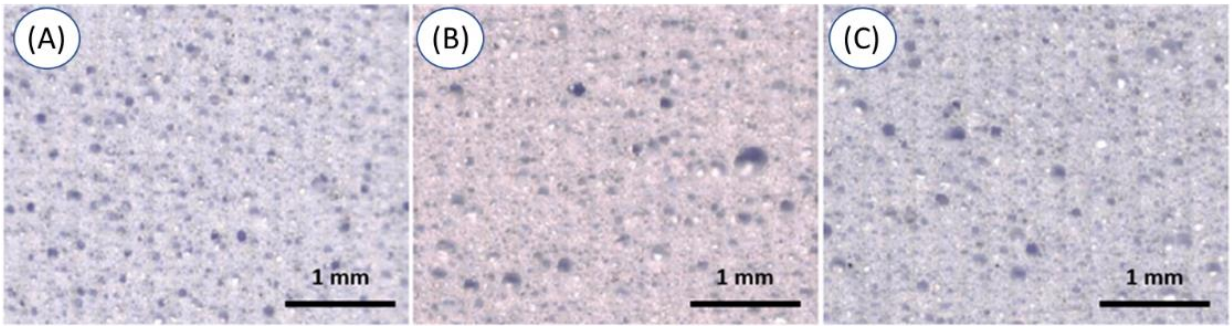

Figure 18. SEM images of the $CaCO_3$ /ethylene vinyl acetate compound. (A) compound obtained using commercial stearate coated geogenic $CaCO_3$ particles. (B) compound obtained using oyster shell particles coated the 40 mM stearate dispersion. (C) compound obtained using oyster shell particles coated the 400 mM stearate dispersion.

The data reported in Figure 19 show that the oyster powder coated with stearate improved the maximum elongation at break with respect to the control and this effect was more marked when the sample with the lower percentage of adsorbed stearate was used. The improvement was about 55 %. No relevant improvement on tensile strength, being about 10 %, was observed. Both sets of data indicate that a too high amount of physiosorbed calcium stearate has a negative effect on the mechanical performances of the ethylene vinyl acetate – $CaCO_3$ composite material. The deleterious effect of the high amount of adsorbed stearate was also reported for an ethylene vinyl acetate composite containing $Mg(OH)_2$ crystals stearate coated [63].

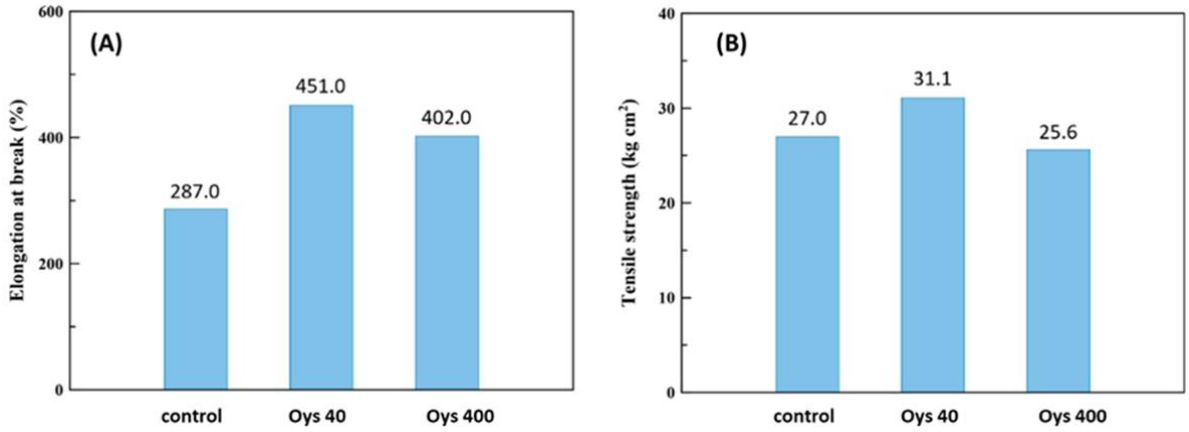

Figure 19. Mechanical characterization, (A) elongation to break and (B) tensile strength of $CaCO_3$ / ethylene vinyl acetate compounds. The control is the compound prepared using a commercial sample of stearate coated geogenic $CaCO_3$. Oys_{40} and Oys_{400} indicate oyster shell powder coated using a 40 mM and 400 mM stearate dispersion, respectively.

Conclusions

This study has shown that bCC from waste sea shells can be successfully coated with an aqueous dispersion of sodium stearate. All the experimental data indicate that the adsorption process is similar to that already reported for synthetic and geogenic calcite. Shortly, at a first layer of chemisorbed stearate is followed by the deposition of several layers of physiosorbed calcium stearate. The peculiar properties of bCC affect the adsorption capacity of the substrate, being particularly efficient in the case of oyster shell powders. The coated oyster powder has been utilized as filler in an ethylene vinyl acetate compound and improved the mechanical properties with respect to a control using commercial stearate coated calcium carbonate. Finally, this work demonstrates that it is possible to recover calcium carbonate from sea shells for application as fillers in replacement to geogenic calcium carbonate, thus improving the

circularity and the sustainability of the industries, as in the studied case of ethylene vinyl acetate compounds.

Author Contributions

CT carried out the preparation of bCC powders, the sodium stearate solution, the $CaCO_3$ coating process with stearate and the physical characterization of the starting and coated materials by X-ray powder diffraction analysis, spectroscopic analysis, scanning electron microscopy, thermogravimetric analysis and differential scanning calorimetry. CT also contributed to the writing of this manuscript.

References

[1] Calcium carbonate market - growth, trends, and forecasts, (2022). https://www.mordorintelligence.com/industry-reports/calcium-carbonate-market.

[2] O.A. Jimoh, K.S. Ariffin, H. Bin Hussin, A.E. Temitope, Synthesis of precipitated calcium carbonate: a review, Carbonates and Evaporites. 33 (2018) 331–346.

[3] Z. Chen, Z. Nan, Controlling the polymorph and morphology of $CaCO_3$ crystals using surfactant mixtures, J. Colloid Interface Sci. 358 (2011) 416–422.

[4] N. Erdogan, H.A. Eken, Precipitated calcium carbonate production, synthesis and properties, Physicochem. Probl. Miner. Process. 53 (2017).

[5] R. Agnihotri, S.K. Mahuli, S.S. Chauk, L.-S. Fan, Influence of surface modifiers on the structure of precipitated calcium carbonate, Ind. Eng. Chem. Res. 38 (1999) 2283–2291.

[6] N. Watabe, Crystal growth of calcium carbonate in the invertebrates, Prog. Cryst. Growth Charact. 4 (1981) 99–147.

[7] H.A. Lowenstam, S. Weiner, On biomineralization, Oxford University Press on Demand, 1989.

[8] A.H. Knoll, Biomineralization and Evolutionary History, Rev. Mineral. Geochemistry. 54 (2003) 329–356. doi:10.2113/0540329.

[9] A. Berman, J. Hanson, L. Leiserowitz, T.F. Koetzle, S. Weiner, L. Addadi, Biological control of crystal texture: a widespread strategy for adapting crystal properties to function, Science (80-.). 259 (1993) 776–779.

[10] P.U.P.A. Gilbert, K.D. Bergmann, N. Boekelheide, S. Tambutté, T. Mass, F. Marin, J.F. Adkins, J. Erez, B. Gilbert, V. Knutson, Biomineralization: Integrating mechanism and evolutionary history, Sci. Adv. 8 (2022) eabl9653.

[11] A. Honig, R. Etter, K. Pepperman, S. Morello, R. Hannigan, Site and age discrimination using trace element fingerprints in the blue mussel, Mytilus edulis, J. Exp. Mar. Bio. Ecol. 522 (2020) 151249.

[12] J.P. Morris, T. Backeljau, G. Chapelle, Shells from aquaculture: a valuable biomaterial, not a nuisance waste product, Rev. Aquac. 11 (2019) 42–57. doi:10.1111/raq.12225.

[13] F. Nekvapil, M. Aluas, L. Barbu-Tudoran, M. Suciu, R.-A. Bortnic, B. Glamuzina, S.C. Pinzaru, From blue bioeconomy toward circular economy through high-sensitivity analytical research on waste blue crab shells, ACS Sustain. Chem. Eng. 7 (2019) 16820–16827.

[14] FAO, The State of World Fisheries and Aquaculture, Sustain. Action. (2020). doi:10.4060/ca9229en.

[15] A. Hart, Mini-review of waste shell-derived materials' applications, Waste Manag. Res. 38 (2020) 514–527.

[16] N. Yan, X. Chen, Don't waste seafood waste: Turning cast-off shells into nitrogen-rich chemicals would benefit economies and the environment, Nature. 524 (2015) 155–157.

[17] N. Topić Popović, V. Lorencin, I. Strunjak-Perović, R. Čož-Rakovac, Shell waste management and utilization: Mitigating organic pollution and enhancing sustainability, Appl. Sci. 13 (2023) 623.

[18] G. Magnabosco, D. Giuri, A.P. Di Bisceglie, F. Scarpino, S. Fermani, C. Tomasini, G. Falini, New material perspective for waste seashells by covalent functionalization, ACS Sustain. Chem. Eng. 9 (2021) 6203–6208. doi:10.1021/acssuschemeng.1c01306.

[19] V. Vandeginste, Food waste eggshell valorization through development of new composites: A review, Sustain. Mater. Technol. 29 (2021) e00317.

[20] S. Owuamanam, D. Cree, Progress of bio-calcium carbonate waste eggshell and seashell fillers in polymer composites: a review, J. Compos. Sci. 4 (2020) 70.

[21] K. Park, K. Sadeghi, P.K. Panda, J. Seo, J. Seo, Ethylene vinyl acetate/low-density

polyethylene/oyster shell powder composite films: Preparation, characterization, and antimicrobial properties for biomedical applications, J. Taiwan Inst. Chem. Eng. 134 (2022) 104301.

[22] V. Gigante, P. Cinelli, M.C. Righetti, M. Sandroni, L. Tognotti, M. Seggiani, A. Lazzeri, Evaluation of mussel shells powder as reinforcement for pla-based biocomposites, Int. J. Mol. Sci. 21 (2020) 5364.

[23] S.-H. Eo, S.-T. Yi, Effect of oyster shell as an aggregate replacement on the characteristics of concrete, Mag. Concr. Res. 67 (2015) 833–842.

[24] K.H. Mo, U.J. Alengaram, M.Z. Jumaat, S.C. Lee, W.I. Goh, C.W. Yuen, Recycling of seashell waste in concrete: A review, Constr. Build. Mater. (2018) 751–764, 162.

[25] Q. Song, Q. Wang, S. Xu, J. Mao, X. Li, Y. Zhao, Properties of water-repellent concrete mortar containing superhydrophobic oyster shell powder, Constr. Build. Mater. 337 (2022) 127423.

[26] M.Z. Rong, M.Q. Zhang, W.H. Ruan, Surface modification of nanoscale fillers for improving properties of polymer nanocomposites: a review, Mater. Sci. Technol. 22 (2006) 787–796.

[27] T. Kato, A. Sugawara, N. Hosoda, Calcium carbonate–organic hybrid materials, Adv. Mater. 14 (2002) 869–877.

[28] J. Wei, Z. Wang, W. Sun, R. Yang, Durability Performance and Corrosion Mechanism of New Basalt Fiber Concrete under Organic Water Environment, Materials (Basel). 16 (2023) 452.

[29] Y.-Q. Niu, J.-H. Liu, C. Aymonier, S. Fermani, D. Kralj, G. Falini, C.-H. Zhou, Calcium carbonate: controlled synthesis, surface functionalization, and nanostructured materials, Chem. Soc. Rev. 51 (2022) 7883–7943.

[30] S.R. Mihajlović, D.R. Vučinić, Ž.T. Sekulić, S.Z. Milićević, B.M. Kolonja, Mechanism of stearic acid adsorption to calcite, Powder Technol. 245 (2013) 208–216.

[31] X. Shi, R. Rosa, A. Lazzeri, On the coating of precipitated calcium carbonate with stearic acid in aqueous medium, Langmuir. 26 (2010) 8474–8482. doi:10.1021/la904914h.

[32] X. Shi, I. Bertóti, B. Pukánszky, R. Rosa, A. Lazzeri, Structure and surface coverage of

water-based stearate coatings on calcium carbonate nanoparticles, J. Colloid Interface Sci. 362 (2011) 67–73.

[33] R. Rothon, C. Paynter, Calcium carbonate fillers, Fill. Polym. Appl. Rothon, R., Ed.; Springer Int. Publ. Cham, Switz. (2017) 149–160.

[34] L. Addadi, S. Weiner, Biomineralization: Mineral formation by organisms, Phys. Scr. 89 (2014) 098003. doi:10.1088/0031-8949/89/9/098003.

[35] F. Marin, G. Luquet, Unusually acidic proteins in biomineralization, Handb. Biominer. (2007) 273–290.

[36] N. Doebelin, R. Kleeberg, Profex: a graphical user interface for the Rietveld refinement program BGMN, J. Appl. Crystallogr. 48 (2015) 1573–1580.

[37] R.B. Gammage, D.R. Glasson, The effect of grinding on the polymorphs of calcium carbonate, J. Colloid Interface Sci. 55 (1976) 396–401.

[38] H. Momota, M. Senna, M. Takagi, Effects of wet vibro-milling on the polymorphic conversion of aragonite into calcite, J. Chem. Soc. Faraday Trans. 1 Phys. Chem. Condens. Phases. 76 (1980) 790–796.

[39] J.H. Burns, M.A. Bredig, Transformation of calcite to aragonite by grinding, J. Chem. Phys. 25 (1956) 1281.

[40] T. Li, F. Sui, F. Li, Y. Cai, Z. Jin, Effects of dry grinding on the structure and granularity of calcite and its polymorphic transformation into aragonite, Powder Technol. 254 (2014) 338–343.

[41] F. Garcia, N. Le Bolay, C. Frances, Changes of surface and volume properties of calcite during a batch wet grinding process, Chem. Eng. J. 85 (2002) 177–187.

[42] I. Segovia-Campos, A. Martignier, M. Filella, J. Jaquet, D. Ariztegui, Micropearls and other intracellular inclusions of amorphous calcium carbonate: an unsuspected biomineralization capacity shared by diverse microorganisms, Environ. Microbiol. 24 (2022) 537–550.

[43] Y. Politi, T. Arad, E. Klein, S. Weiner, L. Addadi, Sea urchin spine calcite forms via a transient amorphous calcium carbonate phase, Science (80-.). 306 (2004) 1161–1164.

[44] K.K. Turekian, R.L. Armstrong, Magnesium, strontium and barium concentrations and

calcite-aragonite ratios of some recent molluscan shells, J. Mar. Res. 18 (1960) 133–151.

[45] X. Long, Y. Ma, L. Qi, Biogenic and synthetic high magnesium calcite - A review, J. Struct. Biol. 185 (2014) 1–14. doi:10.1016/j.jsb.2013.11.004.

[46] O.B. Boggild, The shell structure of the mollusks, Det K. Danske Vidensk. Selsk. Skr. Naturvidenskabelig Og Math. Afd. Raekke 9. 2 (1930) 231–326.

[47] A.G. Checa, E.M. Harper, A. González-Segura, Structure and crystallography of foliated and chalk shell microstructures of the oyster Magallana: The same materials grown under different conditions, Sci. Rep. 8 (2018) 1–12. doi:10.1038/s41598-018-25923-6.

[48] E.S. Grefsrud, Y. Dauphin, J.-P. Cuif, A. Denis, Ø. Strand, Modifications in microstructure of cultured and wild scallop shells (Pecten maximus), J. Shellfish Res. 27 (2008) 633–641.

[49] R.S. Berns, Billmeyer and Saltzman's Principles of Color Technology, John Wiley & Sons, J Hoboken, NJ, USA, 2019.

[50] M.N.G. de Mul, H.T. Davis, D.F. Evans, A. V Bhave, J.R. Wagner, Solution phase behavior and solid phase structure of long-chain sodium soap mixtures, Langmuir. 16 (2000) 8276–8284.

[51] P. Fenter, N.C. Sturchio, Structure and growth of stearate monolayers on calcite: First results of an in situ X-ray reflectivity study, Geochim. Cosmochim. Acta. 63 (1999) 3145–3152.

[52] M. Ukrainczyk, J. Kontrec, D. Kralj, Precipitation of different calcite crystal morphologies in the presence of sodium stearate, J. Colloid Interface Sci. 329 (2009) 89–96.

[53] E.H.M. Wright, N.C. Pratt, Solid/solution interface equilibria for aromatic molecules adsorbed from non-aromatic media. Part 2.—Aromatic carboxylic acids, J. Chem. Soc. Faraday Trans. 1 Phys. Chem. Condens. Phases. 70 (1974) 1461–1471.

[54] E. Fekete, B. Pukánszky, A. Tóth, I. Bertóti, Surface modification and characterization of particulate mineral fillers, J. Colloid Interface Sci. 135 (1990) 200–208.

[55] P. Garnier, P. Gregoire, P. Montmitonnet, F. Delamare, Polymorphism of crystalline phases of calcium stearate, J. Mater. Sci. 23 (1988) 3225–3231.

[56] G.W.H. Höhne, W. Hemminger, H.-J. Flammersheim, Differential scanning calorimetry, Springer, 2003.

[57] J.W. Morse, R.S. Arvidson, A. Lüttge, Calcium carbonate formation and dissolution, Chem. Rev. 107 (2007) 342–381.

[58] E. Busenberg, L.N. Plummer, Thermodynamics of magnesian calcite solid-solutions at 25 C and 1 atm total pressure, Geochim. Cosmochim. Acta. 53 (1989) 1189–1208.

[59] M. Gonen, S. Ozturk, D. Balkose, S. Okur, S. Ulku, Preparation and characterization of calcium stearate powders and films prepared by precipitation and Langmuir− Blodgett techniques, Ind. Eng. Chem. Res. 49 (2010) 1732–1736.

[60] B. Pukánszky, E. Fekete, Adhesion and surface modification, Miner. Fill. Thermoplast. I Raw Mater. Process. (1999) 109–153.

[61] M. Ricci, J.J. Segura, B.W. Erickson, G. Fantner, F. Stellacci, K. Voïtchovsky, Growth and dissolution of calcite in the presence of adsorbed stearic acid, Langmuir. 31 (2015) 7563–7571.

[62] Z.X. Zhang, X.R. Dai, L. Zou, S.B. Wen, T.K. Sinha, H. Li, A developed, eco-friendly, and flexible thermoplastic elastomeric foam from SEBS for footwear application., Express Polym. Lett. 13 (2019) 948–958.

[63] H. Huang, M. Tian, J. Yang, H. Li, W. Liang, L. Zhang, X. Li, Stearic acid surface modifying Mg (OH) 2: Mechanism and its effect on properties of ethylene vinyl acetate/Mg (OH) 2 composites, J. Appl. Polym. Sci. 107 (2008) 3325–3331.

Chapter 4. Sustainable one-pot path to transform seashell waste calcium carbonate to osteoinductive hydroxyapatite micro-nanoparticles

(Published in Journal of Materials Chemistry B)

Sustainable one-pot path to transform seashell waste calcium carbonate to osteoinductive hydroxyapatite micro-nanoparticles

Raquel Fernández-Penas[a], Cristóbal Verdugo-Escamilla[a], Carla Triunfo[b, c], Stefanie Gärtner[d], Annarita D´Urso[e], Francesca Oltolina[e], Antonia Follenzi[e], Gabriele Maoloni[f], Helmut Cölfen[d], Giuseppe Falini[b], Jaime Gómez-Morales[a*]

[a] Laboratorio de Estudios Cristalográficos, IACT (CSIC-UGR), Avda. Las Palmeras, nº 4, 18100 Armilla, Spain.

[b] Department of Chemistry "Giacomo Ciamician", University of Bologna, via F. Selmi 2, 40126 Bologna, Italy.

[c] Fano Marine Center, The Inter-Institute Center for Research on Marine Biodiversity, Resources and Biotechnologies, viale Adriatico 1/N 61032 Fano, Italy.

[d] Physical Chemistry, Dpt. of Chemistry, University of Konstanz, Universitätsstrasse 10, Box 714, D-78457 Konstanz, Germany.

[e] Dipartimento di Scienze della Salute, Università del Piemonte Orientale, "A. Avogadro" Via Solaroli, 17, 28100 Novara, Italy.

[f] Finproject S.p.A., Plant Ascoli Piceno, Via Enrico Mattei, 1-Zona Ind.le Campolungo, 3100 Ascoli Piceno, Italy.

Abstract

We have developed a straightforward, one-pot, low-temperature hydrothermal method, to transform oyster shell waste particles (bCCP) from the species *Crassostrea gigas* (Mg-calcite, 5 wt% Mg) into hydroxyapatite (HA) micro/nanoparticles. The influence on the transformation process of the P reagents (H_3PO_4, KH_2PO_4, and K_2HPO_4), P/bCCP molar ratios (0.24, 0.6, and 0.96), digestion temperatures (25 – 200 °C), and times (1 week - 2 months) were thoroughly investigated. At 1 week, the minimum temperature to yield the full transformation significantly reduced from 160 ºC to 120 ºC when using K_2HPO_4 instead of KH_2PO_4 at P/bCCP 0.6, and even to 80 ºC for P/bCCP ratio 0.96. The transformation took place by a dissolution-

reprecipitation mechanism driven by the favourable balance between HA precipitation and bCCP dissolution, due to the lower solubility product of HA than that of calcite at any of the tested temperatures. Both the bCCP and the derived HA particles were cytocompatible for MG-63 human osteosarcoma cells and m17.ASC murine mesenchymal stem cells, and additionally, they promoted the osteogenic differentiation of m17.ASC, especially the HA particles. Because of their physicochemical features and biological compatibility, both particles could be useful osteoinductive platforms for translational applications in bone tissue engineering.

Keywords: Oyster shell, biogenic calcium carbonate, hydroxyapatite micro-nanoparticles, sustainability, one-pot, hydrothermal, cytocompatibility, osteogenic differentiation.

Introduction

Seashells represent a waste by-product from fishery industry and marine aquaculture [1]. In 2018, world production of shelled molluscs reached 17.3 million tonnes representing 56 % of the production of marine and coastal aquaculture [2]. Waste seashells are often just dumped in the sea causing damages to the marine ecosystem [3] or disposed in landfill affecting the quality of life for people living in proximity because of the unpleasant smell and causing health issues due to the microbial decomposition [4, 5]. On the other hand, their disposal represents an environmental and economic issue since it involves the use of incineration or burial [6]. A way to overcome these issues may be turning cast-off waste seashells into new materials by observing the main circular economy targets, i.e., efficiency, recycling, recovering and reducing [7].

Mollusc shells are hierarchical organic/mineral composites made of $CaCO_3$ embedded within an organic framework (1-5 wt%) [8]. So far, this waste by-product has been used as a source of calcium carbonate in different fields [9]. Many studies report the use of $CaCO_3$ from the shells as calcium supplements for livestock feeding [10, 11], agricultural liming agents for soil acidity treatment [12] and as aggregate substitutes in concrete preparation [13, 14]. In recent years, several papers have been published regarding the transformation of biogenic $CaCO_3$ particles (bCCP) to calcium phosphates of the hydroxyapatite phase (HA).

HA [$Ca_{10}(PO_4)_6(OH)_2$] is the model phase representing the bone and teeth mineral component. Synthetic HA is the most largely studied calcium phosphate for biomedical applications such as coatings for dental implants, drug delivery systems, bioimaging and bone filling, substitution, replacement and regeneration in orthopaedics [15-21]. The global HA market

including nano-, micron- and larger sizes, is expected to grow to around USD 3,086.05 million by 2027 [22]. The interest in HA is due to its excellent features i.e., biocompatibility, bioactivity, no-toxicity and osteointegration [23]. Recently, HA nanoparticles in particular, have widely drawn attention due to their large surface-to-volume ratio, which mimics the dimensions of calcified tissue constituents allowing a higher biocompatibility and cell affinity and proliferation [24, 25, 15].

Different biogenic $CaCO_3$ sources have been employed as a source of calcium to produce HA such as eggshells [26], mussel shells [27], clam shells [28], cockle shells [29], oyster shells [30], snail shells [31], corals [32] and cuttlefish bones [33]. Among them, oyster shells are constituted by $CaCO_3$ in the form of calcite with an isomorphic substitution of magnesium to calcium of about 5 mol% [34]. Both valves comprise different microstructures of calcite that are layers of sheet-like foliae alternated with discontinuous lense-like chalk layers and a thin external layer of prisms 5-25 μm wide and 20-50 μm high which are in turn constituted by an internal laminated structure [35, 36]. HA particles obtained from oyster shells having biocompatibility and bioactivity properties have been already produced. However, nothing about the osteoinductive properties of these HA particles was reported [37, 38].

Several methods have been developed to convert bCCP in HA so far. Most of them are two-step processes involving the calcination of $CaCO_3$ to CaO at 900-1200 °C followed by the reaction with a phosphate reagent (typically H_3PO_4) with $Ca(OH)_2$ produced by hydration of CaO [39-42]. Calcium precursors for the wet chemical precipitation of HA can also be obtained by dissolving $CaCO_3$ in an acidic solution such as HCl or lactic acid [43, 44]. The hydrothermal method was used in a three-step method consisting of calcination of bCCP, hydration and carbonation of resulting CaO to produce precipitated $CaCO_3$ particles, which were then submitted to hydrothermal reaction with $(NH_4)_2HPO_4$ at 160 °C in an autoclave to yield HA nanoparticles [45]. Rod and flower-like HA nanoparticles were synthetized by a microwave irradiation method with the aid of EDTA as calcium chelating agent [46-48]. Agalya et al. performed a one-pot ultrasound-assisted synthesis to produce Fe-doped HA nanoparticles using mussel shells as calcium source with the aid of trisodium citrate as complexing agent [49]. HA nanoparticles were also obtained via wet mechanosynthesis by the use of ball milling but for the full conversion of bCCP to be achieved a thermal treatment had to be performed after the milling process [50]. Balu et al. introduced an oil-bath-mediated precipitation method at 80 °C for the synthesis of HA nanorods from cuttlefish bones powder by using basic pH [51].

In this work, we investigate the transformation of bCCP from oyster shell waste of the species

Crassostrea gigas into HA micro/nanoparticles with suitable cytocompatible and osteoinductive properties for osteogenic applications using a one-step hydrothermal process. Compared to most of the methods reported in the literature so far, the method we suggest here is straightforward, one-pot, easy to scale-up, and involves the full transformation of bCCP into HA nanoparticles in one step. Moreover, it is low-cost since it can avoid the use of expensive hydrothermal autoclaves, additives, and high-purity calcium reagents, and importantly, can be performed at relatively low hydrothermal temperatures without any pH adjustment. The method will benefit the environment since it proposes an efficient and low-cost production of HA particles with applications in medicine and therapeutics using waste seashells as starting material, thus contributing to reducing the waste material derived from the fishery industry and marine aquaculture.

Materials and methods

Preparation of bCCP. Oyster shells of *Crassostrea gigas* were purchased from F.lli Terzi (Palosco, BG, Italy). The shells were carefully washed with tap water to eliminate the meat residues and mineral debris. Then they were treated with 5 % v/v sodium hypochlorite solution for 24 hours to remove the organic residues from the surface, washed with tap water and air dried. The dry shells were finally crushed by a hammer mill and sieved at 45 μm by analytical sieving in order to get biogenic calcium carbonate particles (bCCP).

Reagents. Potassium phosphate monobasic (KH_2PO_4, ACS Reagent, >99%), potassium phosphate dibasic (K_2HPO4, ACS Reagent, ≥ 98%), and phosphoric acid (H_3PO_4, ACS reagent, 85 wt% in H_2O) were provided by Sigma-Aldrich. All solutions were prepared with deionized water (0.22 μS, 25 °C, Milli-Q, Millipore).

Experimental method. The experiments were carried out in a furnace with circulated forced air, using 10 mL glass Pyrex test tubes with PBT screw caps and a rubber disc coated by PTFE for temperatures in the range 25 °C ≤ T ≤ 80 °C. For higher temperatures (100 °C ≤ T ≤ 200 °C), an aluminium rack was designed to contain the tubes. The rack fits into a rectangular aluminium box with an aluminium cap to close the ensemble. Alternatively, we used the hydrothermal reactor Berghoff BR100 model with a 100 mL PTFE liner. All tubes were filled at 70 % volume with the bCCP aqueous dispersions. The dispersions were prepared with the bCCP by varying the phosphate reagent (KH_2PO_4, K_2HPO_4, H_3PO_4) and the P/$CaCO_3$ mol ratio to 0.24 (deficiency of phosphate), 0.6 (stoichiometric with respect to hydroxyapatite), and 0.96 (excess

of phosphate). The initial concentrations of phosphate and bCCP were the following: For $P/CaCO_3$ = 0.24, 120 mM P/500 mM bCCP, while for $P/CaCO_3$ = 0.6 and 0.96, 300 mM P/500 mM bCCP and 480 mM P/500 mM bCCP, respectively. The digestion time (t) varied depending on $P/CaCO_3$ mol ratio and the setting temperature. Thus, for $P/CaCO_3$ =0.24 in the range 25 °C ≤ T ≤80 °C the experiments lasted 1 and 2 months, while for the range 100 °C ≤ T ≤ 200 °C they lasted 1 week. This set of preliminary experiments allowed us to fix the time in further experiments with $P/CaCO_3$ =0.6 and 0.96 in 1 week. The initial pH was not adjusted but measured at the beginning and at the end of the experiments. Upon completion, the precipitates were subjected to 3 consecutive cycles of washing by centrifugation with deionized water to remove unreacted species or salts such as NaCl. Afterward, they were freeze-dried overnight at -50 ºC under vacuum (3 mbar).

Particle characterization. Different techniques were used for the characterization of the precipitates including X-ray diffraction (XRD), thermogravimetry, FTIR and Raman spectroscopies, inductively coupled plasma spectroscopy (ICP-OES), scanning and transmission electron microscopies (SEM, TEM and HRTEM), energy dispersive X-ray spectroscopy (EDS) analysis, and thermogravimetry. Selected samples were additionally analyzed by dynamic light scattering (DLS) and ζ-potential against pH.

XRD data were collected by using a Bruker D8 Advance Vario diffractometer with a Bragg-Brentano parafocusing geometry and Cu $K_{\alpha 1}$ radiation (1.5406 Å). Data processing of most matured samples was carried out with software TOPAS 6.0 (Bruker AXS, Karlsruhe) [52]. The contribution of the isotropic peak broadening due to domain size was modeled using the TOPAS macro based on the Scherrer approximation and considering the instrumental contribution from a measurement of LaB_6 standard (NIST SRM 660c).

Thermogravimetric analyses of some selected samples were performed with Shimadzu TGA-50H calorimeter at a flow rate 100 mL/min air in an alumina crucible. The measurements were carried out from 25 to 950 ºC at a rate of 20 ºC/min.

FESEM observations and EDS were performed with both a field emission high resolution microscope GEMINI LEO 1500 (Zeiss, Jenna, Germany) equipped with an energy dispersive X-ray (EDX) spectroscopy by Oxford Instruments.

Transmission electron microscopy (TEM) was performed with a Carl Zeiss Libra 120 Plus instrument at 80 kV. High-resolution transmission electron microscopy (HR-TEM) analyses were performed with a TITAN G2 60-300 FEI Instrument (FEI, Hillsboro, OR, USA) operating at 300 kV. The instrument is equipped with EDX Super X detector to perform microanalysis,

and STEM type HAADF. For both techniques the powder samples were ultrasonically dispersed in H_2O (MilliQ), and then a few droplets of the slurry were deposited on copper microgrids coated with FORMVAR carbon film prior to observation.

Fourier transform infrared spectra were initially recorded with an Invenio R FTIR spectrometer (Bruker) equipped with an attenuated total reflectance (ATR) accessory of diamond crystal. FTIR spectra in transmittance mode were recorded within the wavenumber range from 4000 cm^{-1} to 400 cm^{-1} at a resolution of 4 cm^{-1}.

Elemental analysis of Calcium and Phosphorous was carried out by inductively coupled plasma optical emission spectroscopy (ICP-OES) with an OPTIMA 8300 spectrometer (Perkin Elmer).

The analysis of both the crystal size distribution by dynamic light scattering (DLS) and the electrophoretic mobility (ζ-potential) of the HA samples was performed with a Zetasizer Nano ZS analyzer with a 633 nm laser (Malvern, UK) using disposable polystyrene cuvettes containing the particles suspended in deionized water (0.5 mg/ mL) at 25 °C. For the measurements of the ζ-potential versus pH, the MPT-2 autotitrator (Malvern, UK) connected to the analyzer was employed. Diluted HCl and NaOH solutions (0.25 and 0.1 M, respectively) were used as titration agents. No additional electrolytes were added. For oyster shell bCCP, the analysis was performed by laser diffraction with a Mastersizer 2000 (Malvern, UK) coupled to a Hydro 2000SM.

Biological tests

Cell Cultures. MG–63, a human osteosarcoma cell line (ATCC®CRL–1427™), was grown in Dulbecco modified Eagle's medium (DMEM) (Sigma-Aldrich, Milan, Italy) supplemented with 10 % fetal bovine serum (FBS), antibiotic solution (streptomycin 100 µg/mL and penicillin 100 U/mL, Sigma-Aldrich, Italy) and 2 mM L-glutamine (complete medium). m17.ASC cells (a spontaneously immortalized mouse mesenchymal stem cell clone from subcutaneous adipose tissue) [53] were maintained in Claycomb medium (Sigma-Aldrich), supplemented as above. All cells were incubated at standard conditions (37 °C, 5 % CO_2), and splitted when at 80–90 % confluency (at ratios, MG-63 of 1:8 and m17.1ASC of 1:10).

Cytocompatibility Tests. For cytocompatibility assays MG-63 cells (5 x 10^3/well) and m17.ASC (2 x 10^3/well) were seeded in complete medium for 24 hours and then different concentrations (ranging from 0.1 to 100 µg/mL) of both bCCP and HA nanoparticles obtained from oyster shell (here referred as Oy-bCCP and apatite NPs, respectively) were added in 100 µL of fresh medium. Hydrogen peroxide (1 µM) was used as an internal control of toxicity. After 72 hours

of incubation, cell viability was evaluated by the 3-(4,5-Dimethylthiazol-2-yl)-2,5-diphenyltetrazolium bromide) (MTT, Sigma-Aldrich) colorimetric assay as described in Gómez-Morales et al. [54]. Briefly, 20 µL of MTT solution (5 mg/mL in PBS solution) was added to each well and the plate was incubated at 37 °C for 2 hours. Afterward, supernatants were carefully aspirated, and then, 125 µL of 0.2 N HCl in isopropanol was added to dissolve formazan crystals. 100 µL were then removed carefully, and the optical density was measured in a multiwell reader (2030 Multilabel Reader Victor TM X4, Perkin Elmer) at 570 nm. The absorbance value of untreated cells was taken as 100 % viability, and values obtained from cells undergoing the different treatments were referred to this value. Experiments were performed at least for 3 times using 3 replicates for each sample.

Osteogenic Differentiation of mesenchymal stem cells. m17.ASC cells were seeded onto 12-well plates at a density of 1×10^4 cells per well and after 24 hours they were treated with an osteogenic medium (DMEM containing FBS 10 %, 50 µg/mL ascorbic acid, 10 mM β-glycerophosphate, and 10 nM dexamethasone) for 14 days. The culture medium was replaced every 3 days as previously described in Zamperone et al. [53]. To evaluate the potential osteo-inductive effects of the particles, m17.ASC cells were cultured with Oy-bCCP and apatite NPs at a concentration of 25 µg/mL in the growth medium for 14 days.

Alkaline Phosphatase (ALP) Staining and Quantitative Analysis. The osteogenic differentiation was evaluated by alkaline phosphatase (ALP) staining and quantified with ImageJ software as described in Dupont et al. [55]. Briefly, after 14 days of culture with the particles, cells were washed three times with PBS, fixed with 4 % paraformaldehyde (4 % PFA; Sigma-Aldrich) for 15 min and stained with an alkaline phosphatase detection kit (Millipore, Merk Millipore, Milano, Italy) according to the manufacturer's protocol. Cells cultured alone (without particles) or with the osteogenic differentiation medium were used as negative and positive control, respectively. Images were acquired under the optical microscopy at 200x magnification. For ALP quantification, the intensity of violet staining was estimated as the integrated density (INT.DEN.) by ImageJ analysis. This value was normalized to the number of cells for each picture and was expressed as the arbitrary unit (a.u.). Experiments were performed at least 3 times.

Alizarin Red Staining (ARS) and Quantitative Analysis. The calcium deposition of m17.ASC cells was assessed by Alizarin Red S staining after the induction of osteogenic differentiation with or without the NPs for 14 days as previously described [53]. Briefly, cells were washed

with PBS pH 7.2, fixed with PFA (2 wt% in PBS) and then were stained with Alizarin Red S solution (40 mM), pH 4.1 for 30 min at room temperature. Afterward, the wells were washed thrice with bi-distilled water to remove the non-specific precipitation, and then samples were analyzed and photographed by optical microscopy at 200x. To quantify the staining, mineralized deposits were dissolved in 10 % acetic acid (Sigma-Aldrich) for 30 min, and then 150 µL of each sample were collected in a 96-well plate to measure their optical density in a multiwell reader (2030 Multilabel Reader Victor TM X4, Perkin Elmer) at 405 nm. Experiments were performed at least 3 times using 3 replicates for each sample.

Statistical Analysis. Data were statistically analyzed and are expressed as mean ± standard deviation of at least 3 triplicates. Statistical analyses were performed using a one-way ANOVA with Bonferroni's post test for grouped analyses using GraphPad Prism version 7.0 for Mac, GraphPad Software (GraphPad Prism, San Diego, CA, USA). Statistical differences between the treatments were considered significant when p values were $p < 0.05$ (*), $p < 0.01$ (**), $p < 0.001$ (***), and $p < 0.0001$ (****).

Results and discussion

Influence of P/bCCP molar ratio, P reagent, and temperature on bCCP to apatite transformation

Figure 1 summarizes the main results of XRD and spectroscopic characterizations (FTIR and Raman) of the precipitates resulting in experiments with initial molar ratios P/bCCP = 0.24 at 1 month (Fig.1a-c), P/bCCP = 0.60 at 1 week (Fig. 1d-f), and P/bCCP = 0.96 at 1 week (Fig. 1 g-i). For the sake of simplicity, the figure shows the results at 25 °C and at the minimum temperature yielding the highest transformation (Fig. 1a-c), or at temperatures yielding full transformation (Fig. 1d-f, and 1g-i). In these plots, the starting material Oy-bCCP presents the characteristic XRD pattern of calcite (PDF 00-005-0586), with reflections at 2θ=29.3 º (104) and 23.03 º (012) marked in the diffractogram [56]. The XRD pattern of a carbonated-apatite blank [57] shows the main reflections at 2θ = 25.87 º (002) and the quadruplet 31.77 º (211), 32.19 º (112), 32.90 º (300), and 33.97 ° (202), respectively (PDF 01-1008) (Fig. 1a). The FTIR spectrum of Oy-bCCP in the range 400-1200 cm^{-1} shows the $\upsilon_2(CO_3)$ and $\upsilon_4(CO_3)$ vibration modes at ~875 cm^{-1} and 713 cm^{-1} [58] while for the HA it shows the characteristic asymmetric stretching $\upsilon_3(PO_4)$ at 1000-1100 cm^{-1}, symmetric stretching $\upsilon_1(PO_4)$ at ~ 960 cm^{-1}, and the

bending mode $\upsilon_4(PO_4)$ at 562 cm^{-1} and 603 cm^{-1}. The presence of a small band in the $\upsilon_2(CO_3)$ region is due to the CO_3^{2-} ions substituting both OH^- (A-type) and PO_4^{3-}(B-type) (Fig. 1b) [57, 20]. Concerning the Raman spectra in the range 800 cm^{-1} to 1200 cm^{-1} (Fig. 1c), we find the bands of HA $\upsilon_1(PO_4)$ at ~ 960 cm^{-1}, [59] and calcite $\upsilon_1(CO_3)$ at ~ 1086 cm^{-1}, [60] as the most representative ones.

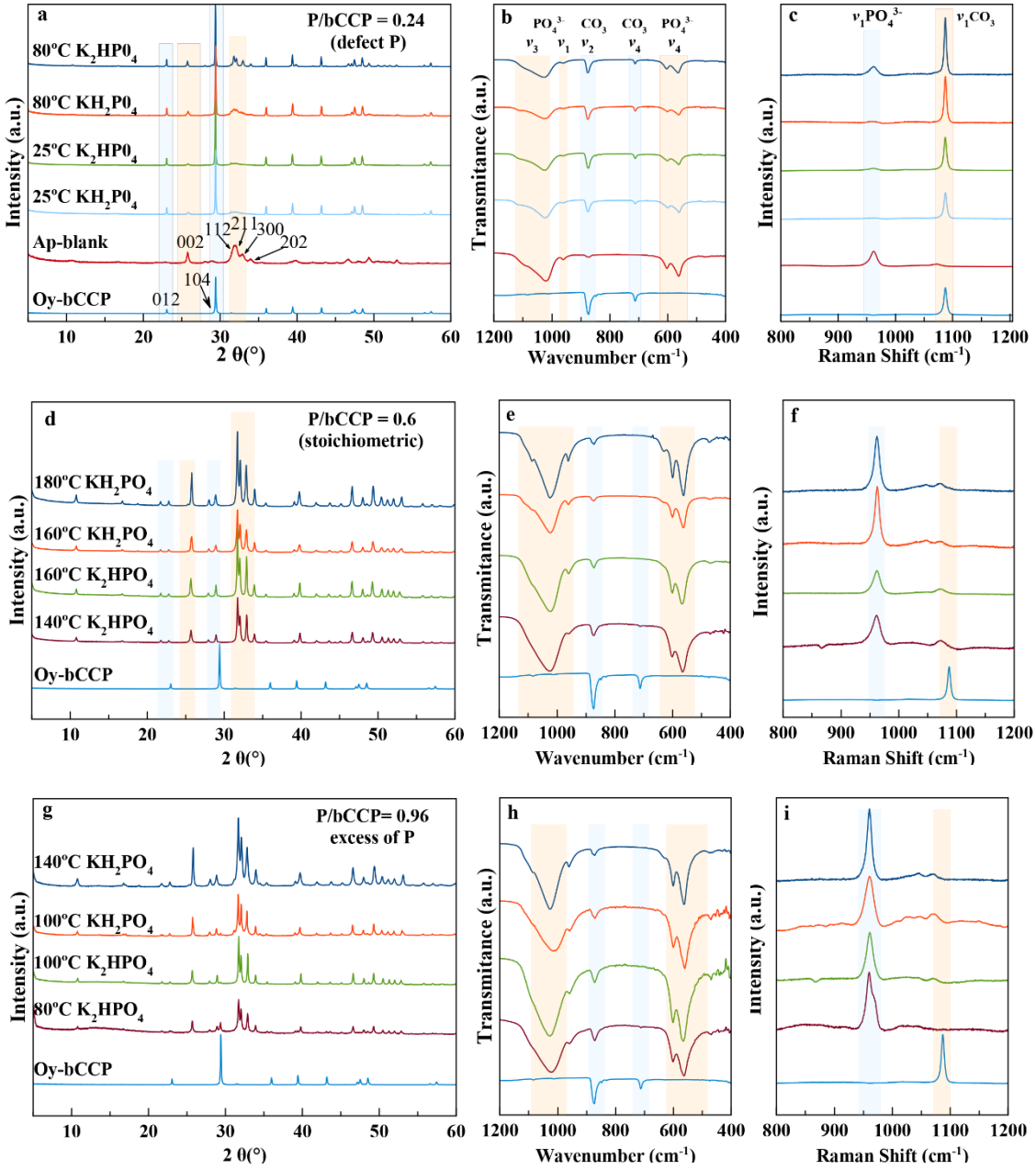

Figure 1. XRD patterns (a, d, g), FTIR (b, e, h) and Raman (c, f, i) spectra of precipitates obtained from aqueous suspensions with initial P/bCCP ratios 0.24 (defect of P) at 1 month, 0.6 (stoichiometric composition with respect to HA) at 1 week, and 0.96 (excess of P) at 1 week, at 25 ºC and at the minimum temperatures allowing the maximum or full transformation percentage.

In the experiments with P/bCCP ratios 0.24 (Fig. 1a-c and Fig. 2) we obtained mixtures of bCCP and HA. This P/bCCP ratio allowed us a preliminary screening of the influences of time (t), temperature (T) and P reagent on the evolution of the precipitation. The effect of these parameters on HA wt% was quantified by Rietveld analysis of the XRD patterns using TOPAS 6.0 software (Fig. 3). The plot shows an increase of transformation with T within the range from 25 ºC to 80 ºC (Fig. 3a), with a maximum percentage at 80 ºC of 39.5 wt%, which was attained with 120 mM KH_2PO_4. The conversion percentages when using K_2HPO_4 were worse (34.4 wt% and 30.4 wt% for 120 and 30 mM, respectively) but improved when the digestion time doubled to 2 months (37.1 wt%) (Fig. 3b). Only when increasing the temperature to 180 ºC and 200 ºC the HA wt% increased to around 43.6 wt%, even reducing the time to 1 week. The experiments using H_3PO_4 (at 25 ºC) did not produce any transformation, so this reagent was ruled out in further experiments using higher P/bCCP molar ratios.

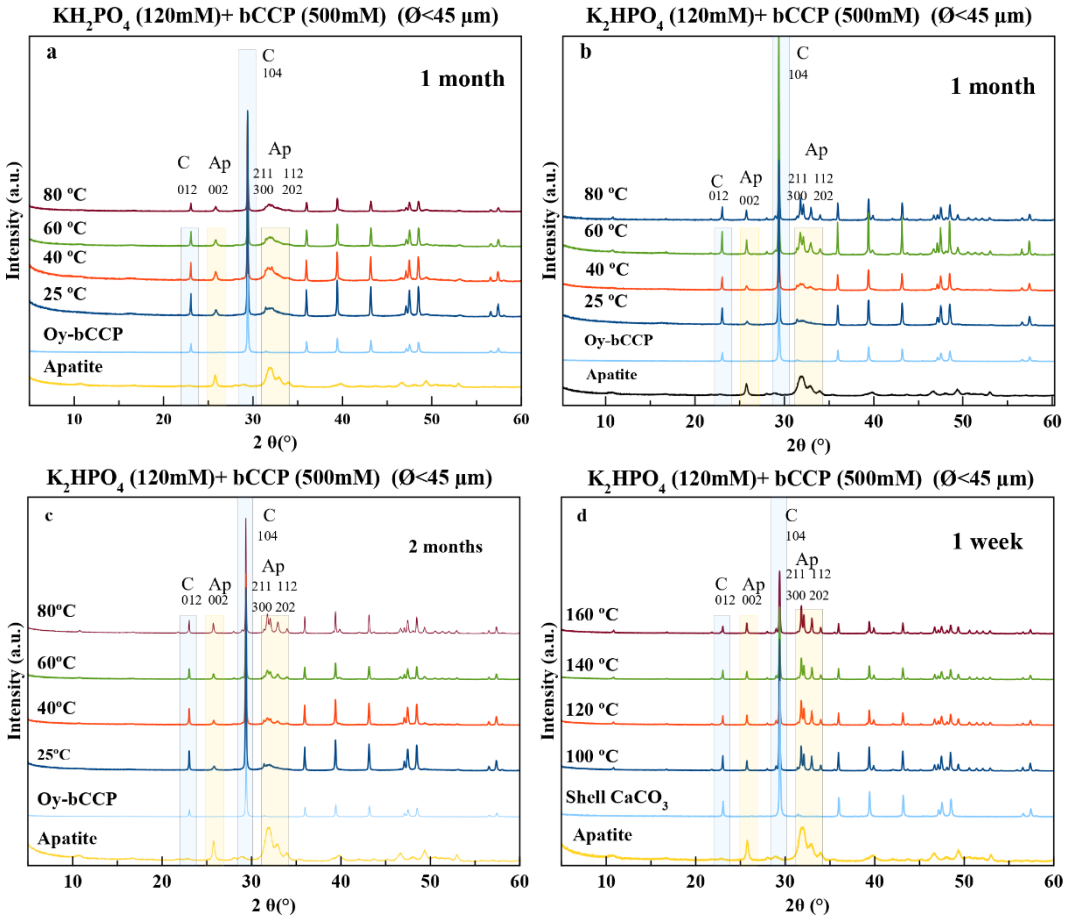

Figure 2. XRD patterns of precipitates obtained from aqueous suspensions with initial P/bCCP ratios 0.24 (defect of P) at 1 month using KH_2PO_4 (a), and at 1 month (b), 2 months (c) and 1 week (d) using K_2HPO_4.

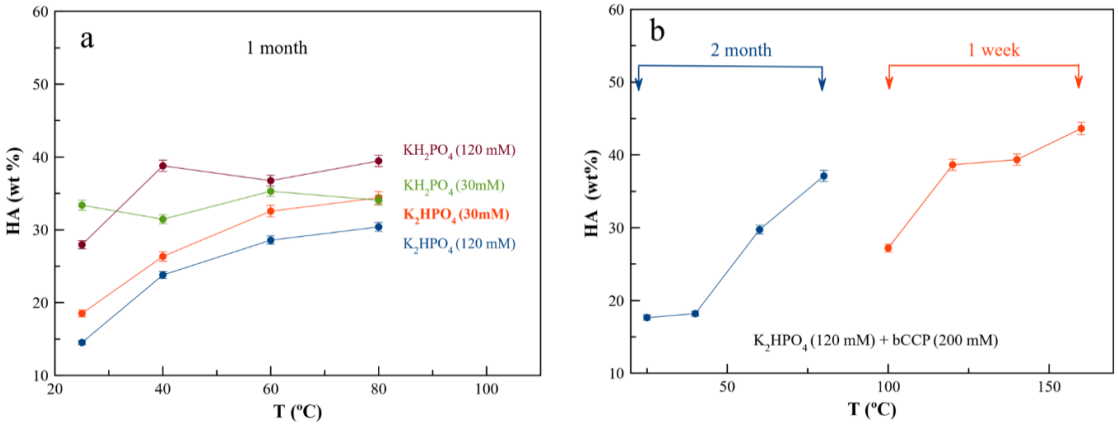

Figure 3. Evolution of apatite wt% with the temperature in experiments with initial P/bCCP ratios 0.24 (defect of P) between 25 ºC to 80 ºC for 1 month (a), between 25 ºC to 80 ºC for 2 month and between 100 ºC to 180 ºC for 1 week (b).

At P/bCCP molar ratios 0.6 (stoichiometric) and 0.96 (excess of P) the study shows the influences of P reagent (KH_2PO_4 or K_2HPO_4) and T (25 ºC to 200 ºC) at t=1 week. A detailed examination of Figures 1d-f and 4 for the P/bCCP ratio 0.6, and Figures 1g-i and 5 for the ratio 0.96 allowed us to determine the minimum temperature (T_{min}) to yield the full conversion. The examination considered the disappearance of the calcite reflection (104) in the XRD pattern and the lack of both the C(υ_4CO_3) vibration mode in the FTIR spectrum and C(υ_1CO_3) in the Raman spectrum at the same T. It was observed that for P/bCCP ratios 0.6 the T_{min} is 160 ºC when using KH_2PO_4 and 120 ºC for K_2HPO_4. However, for P/bCCP ratios 0.96 the T_{min} was 120 ºC when using KH_2PO_4 and 80 ºC when using K_2HPO_4.

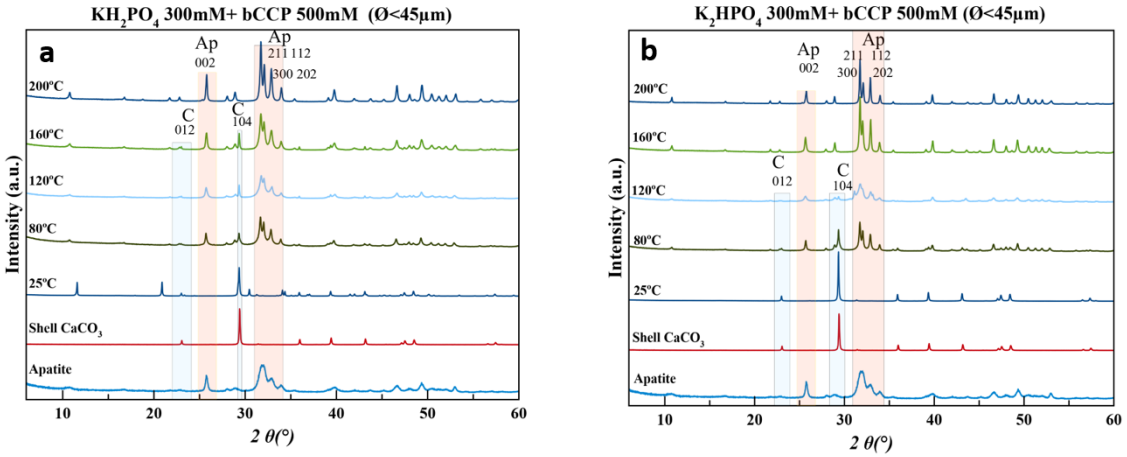

Figure 4. XRD patterns of precipitates obtained from aqueous suspensions with initial P/bCCP ratios 0.6 (stoichiometric composition respect to HA) at 1 week using bCCP size fraction Ø<45 µm and KH_2PO_4 (a) or K_2HPO_4 (b) at different temperatures in the range from 25 ºC to 200 ºC.

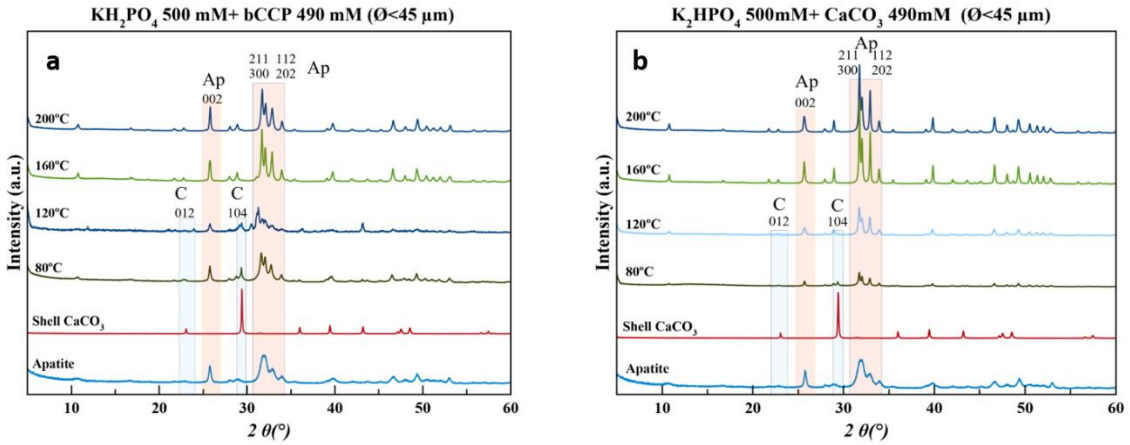

Figure 5. XRD patterns of precipitates obtained from aqueous suspensions with initial P/bCCP ratios 0.96 (excess of P) at 1 week using bCCP size fraction Ø<45 µm and KH_2PO_4 (a) or K_2HPO_4 (b) at different temperatures in the range from 25 ºC to 200 ºC.

Thermogravimetric analyses (TGA) of HA particles obtained at molar ratios 0.6 using both reagents (Fig. 6) revealed the presence of three main regions. The first one between 25 ºC and 230 ºC is associated to adsorbed surface water, the second one up to 500-600 ºC is due to loss of internal or structural water, and the third one between 600 and 950 ºC is due to loss of CO_2 by decomposition of CO_3^{2-} [61]. The latter region is divided into two sub-regions in the CO_3-apatite obtained with KH_2PO_4 (Fig. 6a), with losses of 3.4 wt% and 2.3 wt%, and the associated first derivative (DTG) peaks centered at 708 ºC and 795 ºC. These losses can correspond to A- and B-type CO_3^{2-} substituted groups in AB-type CO_3-apatites [62]. The presence of both types of substitutions is reflected in the $\upsilon_2(CO_3)$ region of the FTIR spectrum, which is decomposed into two small peaks at 879-880 cm^{-1} and 870-872 cm^{-1} attributable to A-type and B-Type CO_3^{2-} substitutions [18, 63]. In the CO_3-apatite prepared with K_2HPO_4 (Fig. 6b) only one temperature region was found with a loss of 6.8 wt% and a DTG peak centered at 796 ºC. The $\upsilon_2(CO_3)$ of the FTIR spectrum shows a main peak at ~872 cm^{-1} attributable to B-type CO_3 [18, 63]. When increasing the conversion temperature to 200 ºC, the CO_2 region shifted to around 750-950 ºC in both apatites, with losses of 1.6 and 1.7 wt%, evidencing the minor content of carbonate of these samples. The three mentioned thermal regions of HA compare with those of Oy-$CaCO_3$. The first from 25-260 ºC is due to the loss of adsorbed water, the second one to the loss of internal structural water and organics, and the third one between 650 and 790 ºC, with DTG peak at 760 ºC, to the loss of CO_2 yielding the residue of CaO.

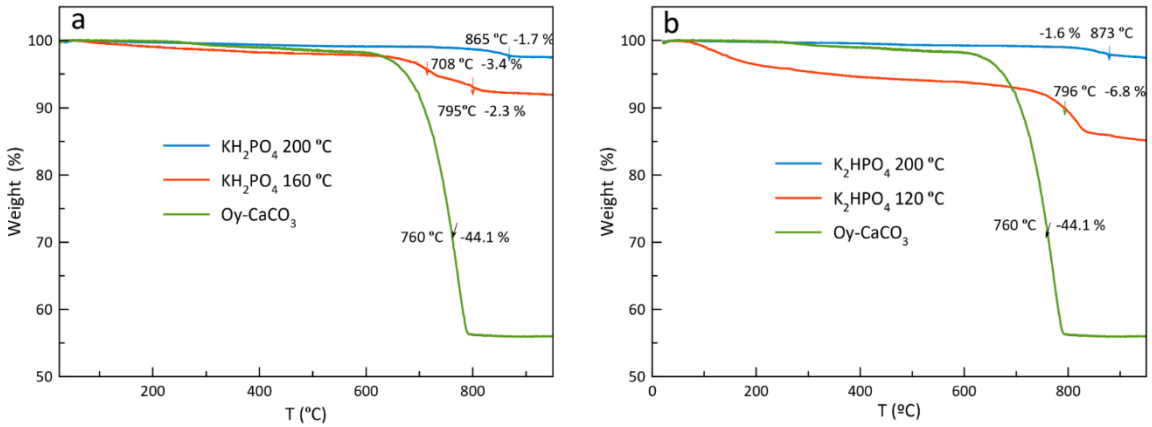

Figure 6. TGA of Oy-$CaCO_3$ and CO_3-apatites obtained by one-step hydrothermal conversion of Oy-$CaCO_3$ at 160 ºC and 200 ºC using KH_2PO_4 (a) and at 120 ºC and 200 ºC using K_2HPO_4 (b) at P/$CaCO_3$ molar ratios 0.6. Arrows indicate the temperature of the endothermic peak associated to loss of CO_2 by carbonate decomposition from the CO_3-apatite samples.

The type of P reagent regulated the initial pH of the suspensions, i. e. 5.6-5.8 when using KH_2PO_4 and 8.5-8.8 in the case of K_2HPO_4 (Table 1), while the conversion process was responsible for the higher pH at the end of the experiment, reaching in some cases values higher than 10.0. This increase of pH is explained by the progressive dissolution of bCCP that favors the increase of activities of Ca^{2+}, CO_3^{2-}, HPO_4^{3-}, PO_4^{3-}, OH^-, as well as of neutral ($CaHPO_4°$) and ion pair ($CaPO_4^+$) species up to reach the critical supersaturation for the nucleation of the HA phase. The favorable balance between HA precipitation and $CaCO_3$ dissolution, due to the lower solubility product of HA than that of calcite, was responsible for the whole dissolution of $CaCO_3$.

Table 1. Initial and final pHs of aqueous suspensions in the experiments using initial KH_2PO_4/bCCP and K_2HPO_4/bCCP ratios 0.6 and 0.96.

	pH₀	**25ºC**	**40ºC**	**60ºC**	**80ºC**	**100ºC**	**120ºC**	**140ºC**	**160ºC**	**180ºC**	**200ºC**
KH_2PO_4/bCCP (0.6)	5.64	8.51	7.17	9.55	8.54	9.41	10.76	9.12	9.27	9.58	9.97
K_2HPO_4/bCCP (0.6)	8.68	9.20	9.45	9.62	9.66	10.26	10.65	9.37	9.69	9.80	9.94
KH_2PO_4/bCCP (0.96)	5.82	8.85	7.68	8.05	7.08	10.96	7.39	8.52	7.14	9.56	9.95
K_2HPO_4/bCCP (0.96)	8.51	9.18	9.28	6.67	10.12	9.62	9.46	9.45	9.27	9.56	9.71

For a better understanding of the process, Figure 7 shows the results of a simulated experiment using K_2HPO_4 and P/$CaCO_3$ 0.96 in which the full conversion was attained at 80 ºC. It is observed the decrease of activities of the aqueous species Ca^{2+} and $CaHPO_4°$ with an increase in pH and a slow decrease of HPO_4^{2-} (Fig. 7a, c), which indicates that these are the species involved in the nucleation process. Recently, some authors showed pieces of evidence that the non-classical calcium phosphate precipitation pathway involves prenucleation clusters (PNC) identified as $Ca_2(HPO_4)_3^{2-}$, which are constituted by a molecule of $CaHPO_4°$ plus HPO_4^{2-} and an extra Ca^{2+} ion [64], or ion associations of the type $Ca(HPO_4)_3$ [4, 65]. Going back to the simulation, the decrease of the activities of Ca^{2+}, $CaHPO_4°$, and HPO_4^{2-}, also agrees with the formation of these types of PNCs. The crucial role of PNCs in the formation of the solid phase could explain the decrease in T_{min} to attain the full $CaCO_3$ to HA transformation when using K_2HPO_4.

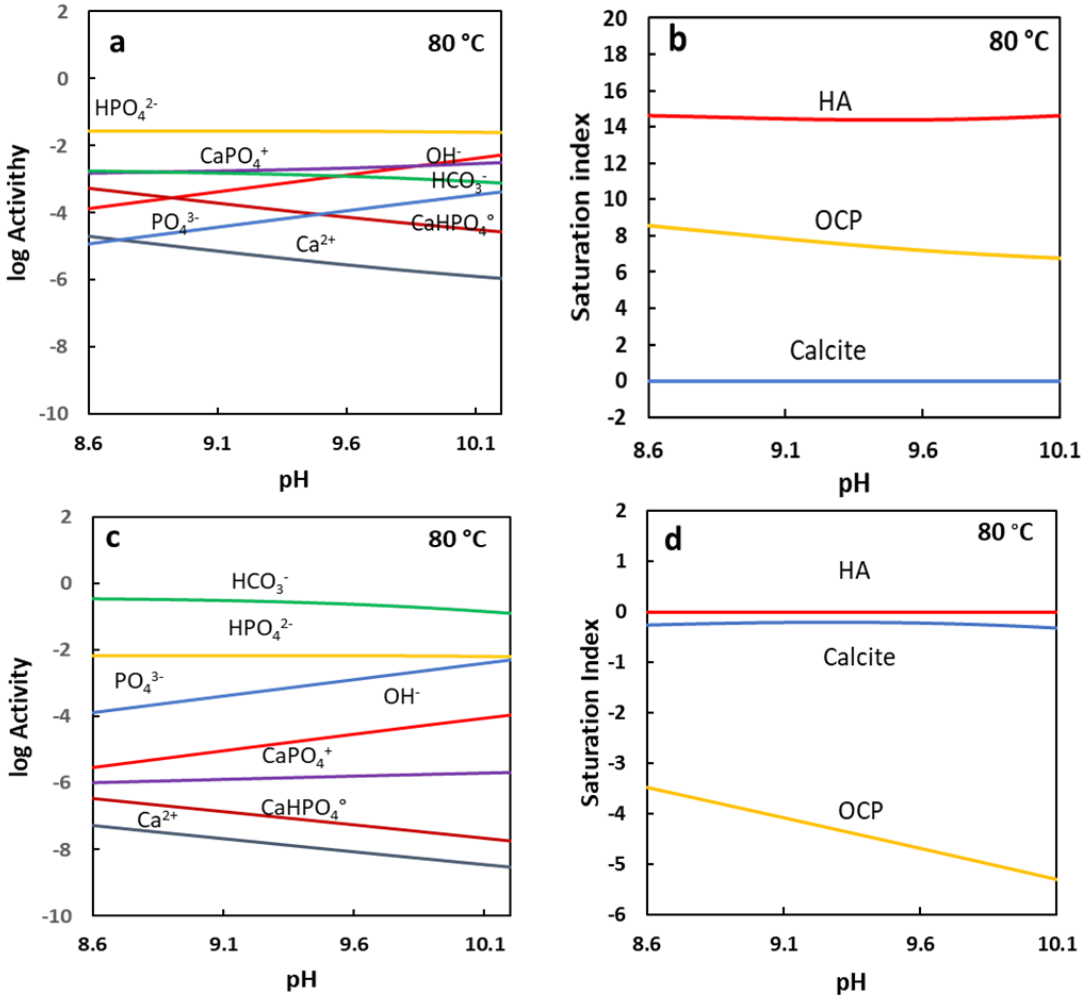

Figure 7. Simulation results with Visual MinteQ 3.1 of the experiment P/$CaCO_3$ 0.96 using K_2HPO_4 as P reagent in which full conversion was obtained at 80 ºC. (a) Speciation vs pH considering calcite as a

finite solid; (b) Saturation indexes (S.I.) vs pH of hydroxyapatite (HA), octacalcium phosphate (OCP) and $CaCO_3$ (calcite) considering calcite at finite solid (S.I.=0); (c) speciation vs pH after full conversion giving rise to calcite=0 mol/l and HA=0.1 mol/l; (d) Saturation indexes vs pH of HA, OCP and calcite, showing the mother solution in equilibrium with HA (S.I.=0), and subsaturated respect to calcite and OCP (S.I. < 0). In the simulation the "activity" units are mol/l and S.I.= log IAP-log K_{sp}, being IAP the ionic activity product, and K_{sp} the solubility product.

In particular, the simulation shows the evolution of the aqueous activities of Ca^{2+}, HCO_3^-, HPO_4^{3-}, PO_4^{3-}, OH^-, $CaPO_4^+$ and $CaHPO_4°$ versus pH (Fig. 7a) as well as of S.I. respect to HA and OCP (Fig. 7b) considering both calcite as the calcium source (S.I.=0) and no precipitation of a new phase. It is shown the slow increase of PO_4^{3-}, OH^- and $CaPO_4^+$ activities with pH while the activity of the other species decreases, and the higher S.I (HA) compared to S.I.(OCP) indicating the preferred precipitation of HA at these pHs. Once the experiment finishes the amount of calcite is 0 and that of HA is 0.1 mol/l (full conversion). The activity of all species in the remaining solution is now generally lower than in Figure 7a expected for HCO_3^- and PO_4^{3-}. Under this condition, the solution remains undersaturated with respect to OCP and calcite, and just saturated (S.I.=0) with respect to HA (Fig. 7d).

Morphological and microstructural characteristics of the precipitated HA particles

Following the precipitation processes at different temperatures, the FESEM micrographs (Fig. 8) show that the initial micrometer-sized Oy-bCCP layered rods (Fig. 8a) were coated with HA nanoparticles in the experiments at 25 ºC, irrespective of P/bCCP molar ratio and P reagent used (Figs. 8b, e, f, i, j). In experiments with P/bCCP 0.24, at the temperatures for maximum transformation (Figs. 8c, d), the HA nanoparticles displayed mostly isometric morphologies. At P/bCCP molar ratios 0.6 and 0.96, the obtained nanoparticles displayed predominant morphologies depending on the P reagent type, i. e. thin needle- and plate-like anisometric morphologies when using KH_2PO_4 (Figs. 8g, k) or more isometric quasi-spherical rods when using K_2HPO_4 (Figs. 8h, l).

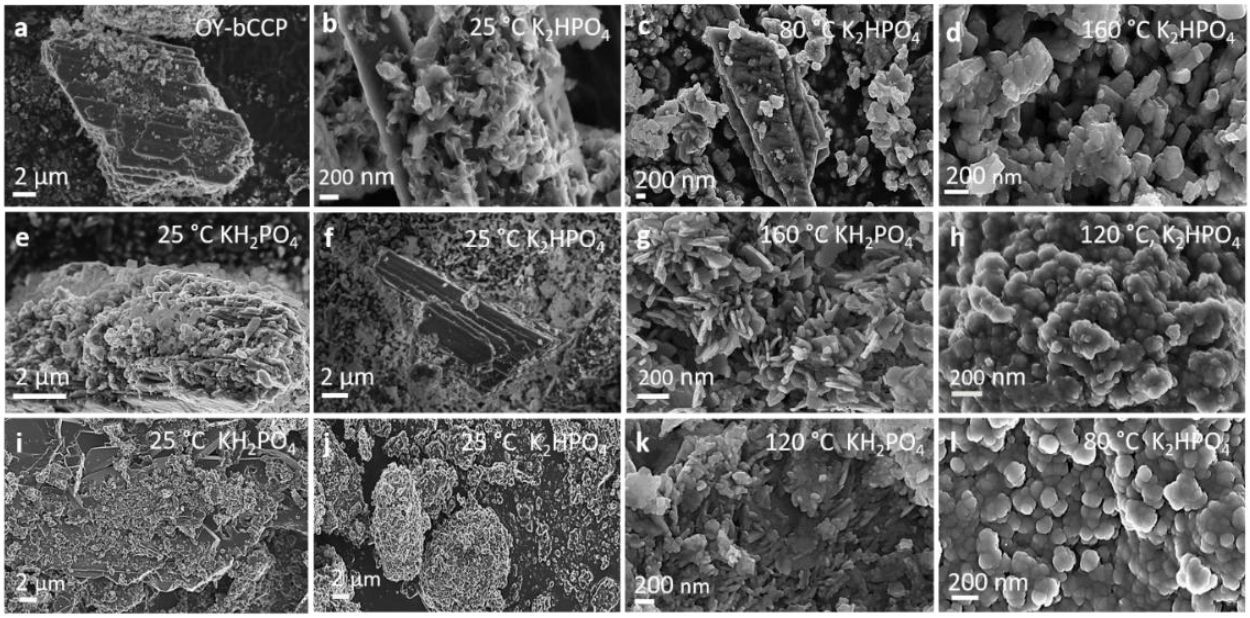

Figure 8. FESEM micrographs of bCCP and apatites obtained at 25 ºC and at the minimum temperature allowing full transformation using KH_2PO_4 and K_2HPO_4 at P /bCCP molar ratios 0.24 (a-d), 0.6 (e-h), and 0.96 (i-l).

The results are confirmed by HRTEM characterizations of samples transformed at 200 ºC. Figures 9a and 9i show the high-angle annular dark field (HAADF) images of samples prepared at P/bCCP molar ratios 0.6, using KH_2PO_4 and K_2HPO_4, respectively. While the former particles are mostly needle-like, the latter are more isometric. In both cases, the EDX elemental mappings reveal the presence of Ca, P, and in minor extent Mg (Figs. 9b, c, d and j, k, l) with a (Ca+Mg)/P of 1.73 ± 0.03 when using KH_2PO_4, and 1.72 ± 0.08 or 1.81 ± 0.08 when using K_2HPO_4 as revealed in 2 different zones of this sample. The indexed selected area electron diffraction (SAED) pattern of the first sample (Fig. 9e) shows the characteristic crystallographic planes of HA, i.e. (002), (211), (310), (152), while the HRTEM image (Fig. 9f) shows lattice fringes of the elongated particles structured as single crystal domains whose d-spacing of 8.15 Å corresponds to planes (100).

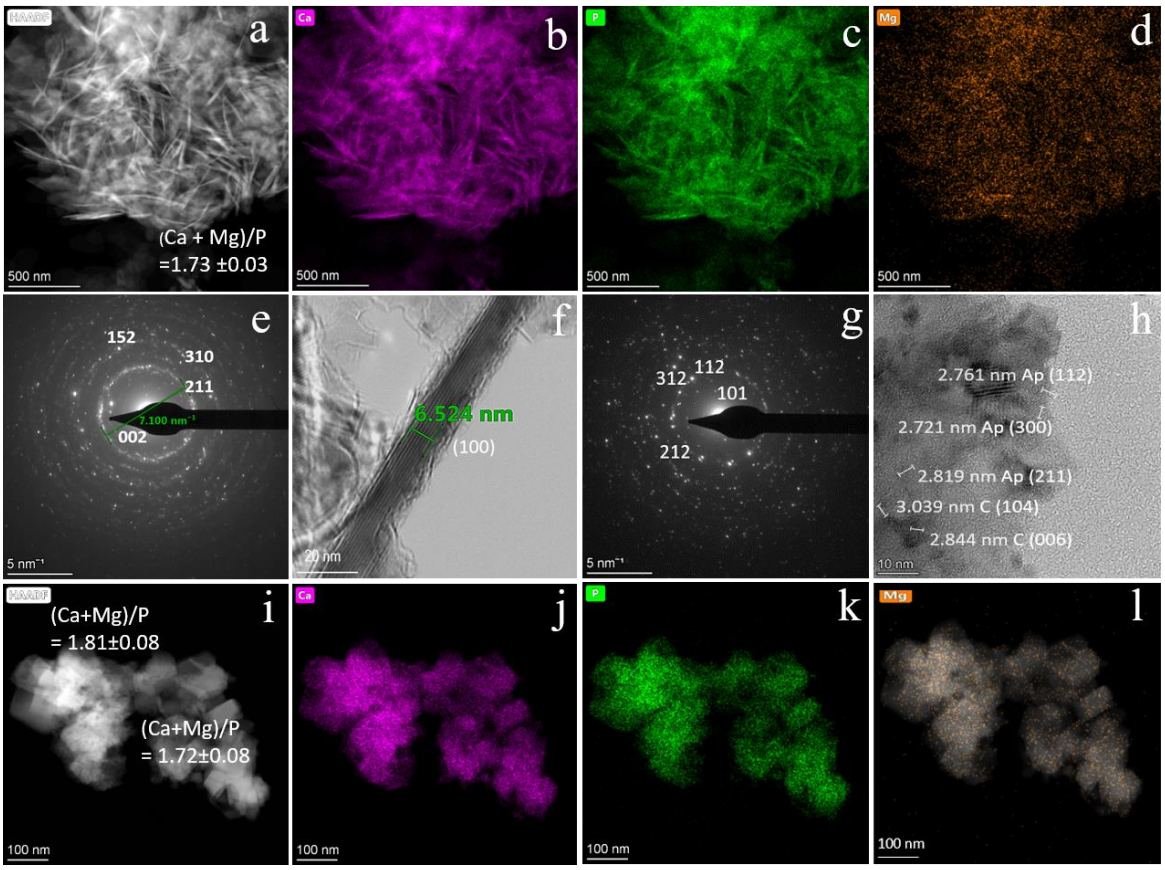

Figure 9. (a, i) HAADF-STEM micrographs of samples prepared with KH_2PO_4 and K_2HPO_4, respectively; (b, c, d) and (j, k, l) EDX element mapping analysis of Ca, P, and Mg of particles of the image (a) and (i), respectively. (e, g) SAED patterns of samples prepared with KH_2PO_4 and K_2HPO_4, respectively showing the planes of the apatite phase. (f, h) HR-TEM images showing the lattice fringes of particles prepared with KH_2PO_4 and KH_2PO_4, respectively. Note than in the latter image, lattice fringes correspond to the apatite planes (112), (211) and (300), and calcite planes (104) and (006).

On the other hand, the indexed SAED pattern of the second sample (Fig. 9g) shows different crystallographic planes of the HA phase, i.e. (101), (112), (212), (312), but the HRTEM image (Fig. 9h) displays in addition, lattice fringes corresponding to the (104) and (006) planes of calcite. This finding indicates that even after increasing the digestion temperature, a small amount of calcite, not detected by XRD, is present in the samples. Whether it is untransformed bCCP or precipitated crystals in the experiment is not possible to be distinguished by microscopy. Most likely, they correspond to freshly precipitated calcite due to oscillations in the solution saturation index at the stationary state (dynamic) once attaining the full transformation. Note in the simulated experiment of Figure 7 that after full transformation the solution remains only slightly undersaturated with respect to calcite.

Crystal size distribution and electrophoretic mobility -ζ-potential- of the HA particles

The crystal size distribution (CSD) and electrophoretic mobility (ζ-potential) against pH of aqueous suspensions of both Oy-bCCP and HA-derived particles are relevant properties to assess their potential biomedical applications as carriers for drug delivery or as osteoinductive implantable bone filling materials. The trend of a colloidal suspension to disperse in simulated physiological conditions of the blood (pH~7.4), in a tumor microenvironment, or in an inflamed tissue (pH 5-6), depends on the size and surface charge of their particles. While the dispersion of the colloidal particles is essential for their use as carriers of chemotherapeutic or anti-inflammatory drugs [18, 66] it seems *a priori* not a crucial feature for its use as an osteoinductive implantable material.

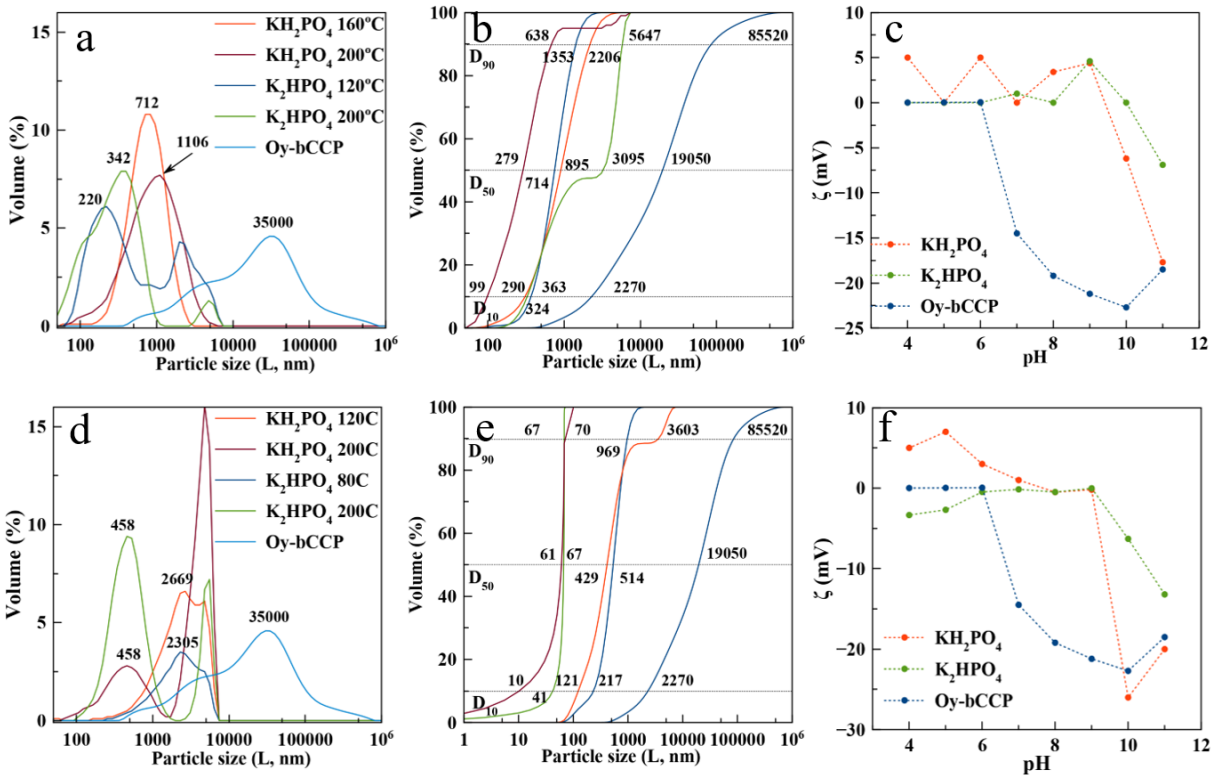

Figure 10. Volume based CSD (a, d), cumulative volume based CSD (b, e), and ζ-potential versus pH (c-f) of Oy-bCCP and HA particles prepared at different temperatures using KH_2PO_4 and K_2HPO_4, and P /bCCP molar ratios 0.6 (a-c), and 0.96 (d-f). Note that CSD of HA and Oy-bCCP particles, though plotted in the same figures, were measured by different techniques i. e. DLS and laser diffraction, respectively.

The CSD is here plotted as both volume-based (Figs. 10a, d) and cumulative volume-based distribution (Figs. 10b, e) because these latter plots allow measuring the percentiles D_{10}, D_{50} and D_{90} of the distribution. The percentiles characterize the percentage of cumulative volume

undersize distribution. D_{10} is close to the individual particle size observed microscopically while D_{50} (the median of the population), and D_{90} are influenced by the aggregation of particles. We can observe the big reduction of the particle size experienced when transforming the Oy-bCCP particles to HA, with D_{10} reducing from 2270 nm to 99 nm (ratio P/bCCP 0.6) or to 10 nm (ratio P/bCCP 0.96), in both experiments using KH_2PO_4 at 200 ºC. The influence of P/bCCP ratio, P reagent, and T on the percentiles is evident. The experiments with P/bCCP ratio 0.96 at 200 ºC yielded a lower particle size with negligible aggregation, with D_{10}, D_{50} and D_{90} percentiles equal to 10, 61 and 67 nm, respectively when using KH_2PO_4, and 41, 67 and 70 nm when using K_2HPO_4. However, by decreasing the temperature to 120 ºC and 80 ºC, the percentiles increased greatly. In experiments with P/bCCP ratio 0.6 there is not a clear trend. Using this molar ratio both the particle size and aggregation tendency are higher. Following the discussion, the particles prepared at P/bCCP ratio 0.96 at 200 ºC could find application as drug carriers, while those prepared at P/bCCP ratio 0.6 could find applications as implantable materials. For these particles, we have studied their osteoinductive properties.

Biological tests

Cytocompatibility of the Oy-bCCP and HA derived nanoparticles

The cytocompatibility of Oy-bCCP and HA derived NPs was tested in a MTT assay on the MG-63 human osteosarcoma cells and on the m17.ASC murine mesenchymal stem cells, after 3-day incubation at different concentrations ranging from 100 to 0.1 μg/mL. No significant toxicity was observed on MG-63 cells at any particle concentration (Fig. 11A), since in all cases the cell viability is higher than 85 %.

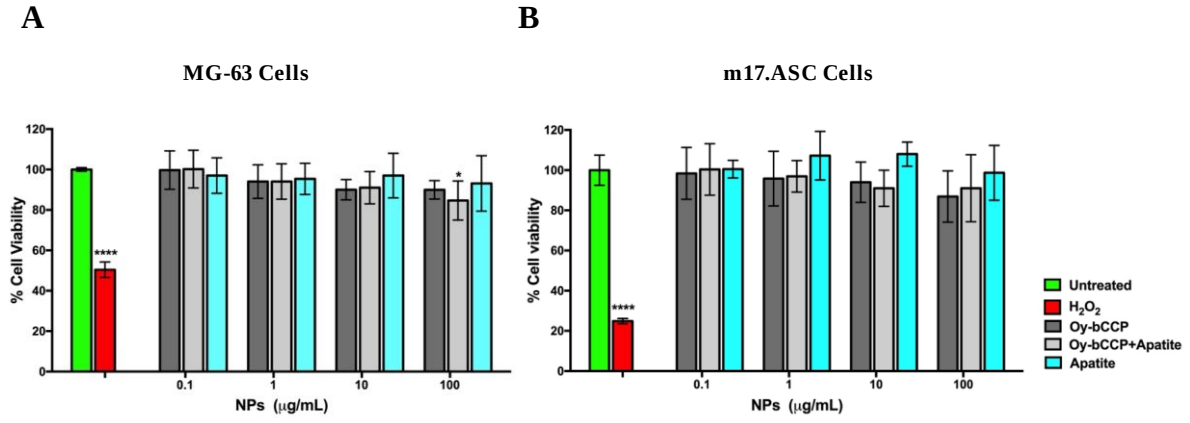

Figure 11. Viability of MG-63 (A) and of m17.ASC cells (B) incubated for three days with different nanoparticles derived from the oyster shell and with different concentrations. Viability was assessed in MTT assays. Data represent means ± SD of three independent experiments performed in triplicate and

statistical analyses were carried on using One-way ANOVA, with Bonferroni comparison test. For statistical analysis all data were compared to untreated samples (* $p < 0.05$, **** $p < 0.0005$).

On the other hand, the mesenchymal stem cells are more sensitive to the inorganic particles than the osteosarcoma cell line, especially when they were incubated with the highest particle concentration of 100 µg/mL (Fig. 11B). Nevertheless, in all cases the cell viability was always higher than 80 %, which is above the cut-off of 70 % indicated by ISO 10993-5:2009 [67]. As expected, all the cells were affected by the addition of 1 µM hydrogen peroxide, which reduced their viability to less than 50 %. Thus, these data show the good cytocompatibility of the different Ca-based materials that will be used in this study focused on the osteogenic differentiation of the stem mesenchymal cells.

HA particles Derived from Oyster Shell Induce Osteogenesis and Mineralization in m17.ASC Cells

Since calcium-based nanomaterials play a critical role in the osteogenesis process [68, 69] we analyzed the ability of Oy-bCCP and apatite-derived nanoparticles to induce the osteogenic differentiation of the mesenchymal cell line m17.ASC. It has been reported that the increase of ALP enzyme activity is a pivotal event during the early stage of the osteogenesis and generally reaches the maximum level at 2 weeks [70]. Hence, after m17.ASC cells were incubated with 25 µg/mL (minimum effective dose reported in the literature) of particles for 14 days in the absence of osteogenic stimulators and then we evaluated the ALP activity by the staining assay.

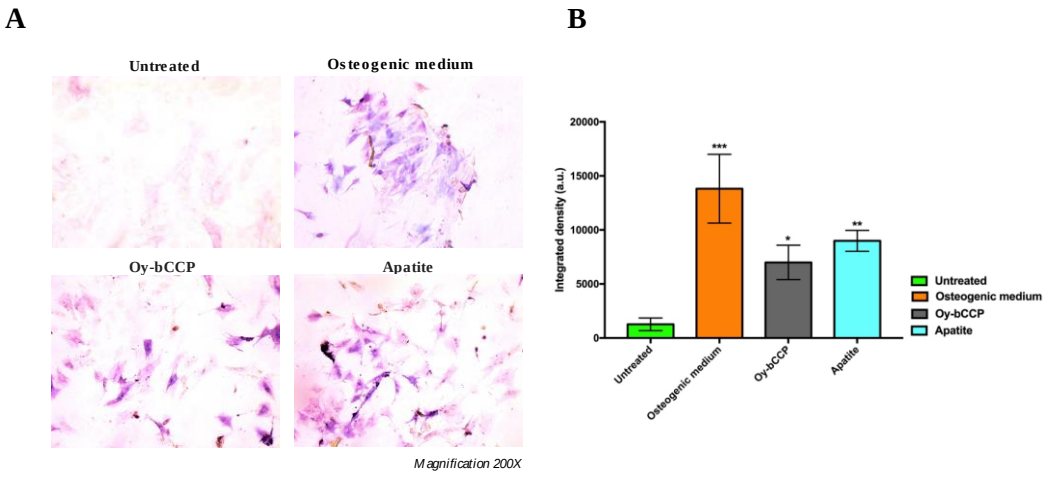

Figure 12. Effects of Oy-bCCP and apatite particles on ALP activity of m17.ASC cells after 14 days incubation with 25 µg/mL particles or with the osteogenic induction medium used as positive control. (A) Representative images of ALP staining assay obtained at optical microscopy. Magnification 200X. (B) Quantitative analysis of ALP activity obtained by counting ALP spots with ImageJ software. Data

representing three independent experiments are reported in the histogram as an average (A.U. ± SD) and statistical analyses were carried on using One-way ANOVA, with Bonferroni comparison test. Significance was considered as follows: * $p < 0.05$, ** $p < 0.01$, *** $p < 0.001$.

As shown in Figure 12A, a strong violet signal, typical of ALP staining, was visualized in both particle-treated groups, in contrast to untreated cells. In fact, the quantitative analysis (Fig. 12B) showed that the intensity of violet staining associated with the particles (7000 and 9000 a.u. for Oy-bCCP and apatite, respectively) is nearly comparable to the signal detected (12000 a.u.) in the case of differentiated cells with osteogenic medium. Thus, these findings suggest that the tested particles could play a role at early stages of the osteogenesis process.

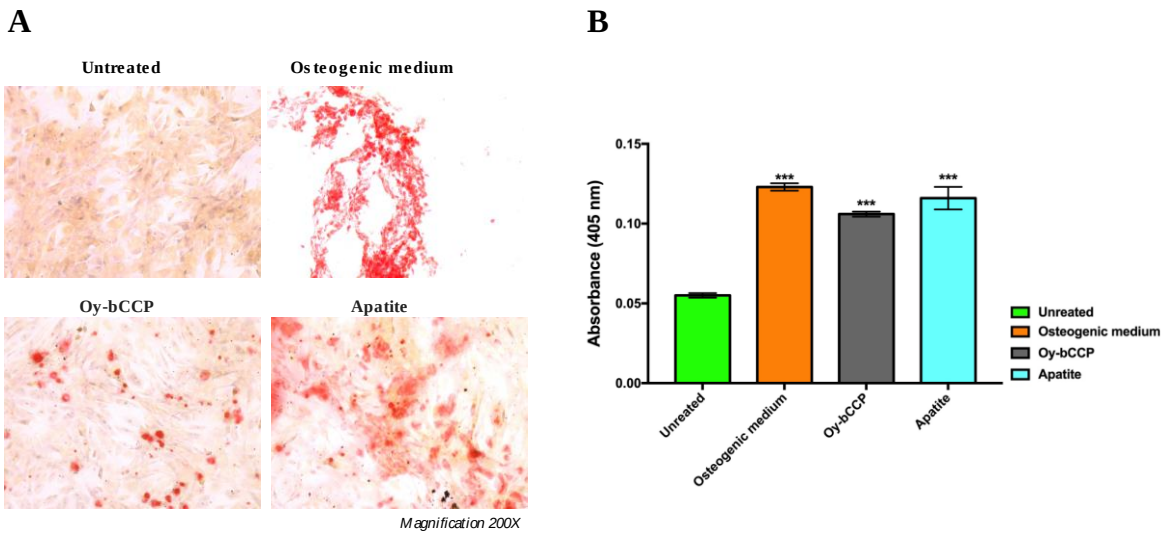

Figure 13. Effects of Oy-bCCP and apatite nanoparticles on the mineralization process of m17.ASC cells. (A) The extracellular calcium deposition was visualized by Alizarin Red S staining after cells were cultured with 25 µg/mL particles or with the osteogenic induction medium used as positive control. Magnification 200x. (B) Mineralization was quantified following the colorimetric analysis of Alizarin Red S solution from calcium deposition. Results were obtained in three independent experiments made in triplicates and they were reported in the histogram as an average ± SD of the optical density measured in a multiwell reader at 405 nm. For statistical analysis all data were compared to untreated samples using One-way ANOVA, with Bonferroni comparison test (*** $p < 0.001$).

As a matter of fact, mineralization is another hallmark of the osteogenesis contributing to the final stage of the differentiation process, which is characterized by the calcium salts deposits forming the bone matrix [71]. Therefore, we evaluated whether Oy-bCCP and apatite particles were also able to induce the mineralization in cell line m17.ASC performing the alizarin red staining after the cells underwent the same treatments without or with the particles as described above. The formation of mineralized matrix, which was visualized as a red nodule-like staining,

was not only detectable in differentiated cells with osteogenic factors, but also when cells were incubated with both types of NPs (Fig.13A). For quantitative analysis, we measured the intensity of ARS extracted from the stained wells and expressed it as the optical density (O.D.). It is clear from Figure 13B that particle-treated groups attained O.D. values similar to the positive control. Thus, the data obtained after 14 days of incubation illustrate that both Oy-bCCP and apatite particles significantly increased the mineralized matrix depositions in cells compared to the untreated group (negative control). Taken together, these results suggest that these calcium-based materials derived from oyster shells benefit the osteogenic capacity even in the absence of osteogenesis stimulators. Two recent studies have tested the osteoinductive properties of calcium-based materials derived from oyster shells, indicating the interest in reusing this waste material in the biomaterials field. In the first one, Coringa et al. [72] tested the internal layer of the shell (i. e. nacre) of the species *Crassostrea rhizophora* from Northeastern Brazil as a bone substitute material and concluded that nacre presents good biocompatibility and promoted the stimulation for bone-forming cells. In the second one, Ho et al. [73] produced biphasic calcium phosphate (HA/β-TCP) granules from oyster shells and found that this material was able to promote the differentiation of induced pluripotent stem cells [73]. Based on the results of the current work the bCCP recovered from *Crassostrea gigas* oyster shells and the HA derived particles can be useful osteo-inductive platforms for translational applications in bone tissue engineering.

Conclusions

We have set up a one-pot low-temperature hydrothermal method to transform oyster shell bCCP particles into HA micro-nanoparticles. The following crystallization parameters were screened to find the minimum temperature allowing the complete transformation: P reagent (H_3PO_4, KH_2PO_4, and K_2HPO4), P/bCCP molar ratio (0.24, 0.6, 0.96), temperature (25-200 ºC) and time (1week-2 months) in absence of any additive and without pH adjustment. The digestion temperature significantly reduced from 160 ºC to 120 ºC by using K_2HPO_4 instead of KH_2PO_4 in experiments with P/bCCP molar ratio to 0.6, and even to 80 ºC when increasing the P/bCCP molar ratio to 0.96. The P reagent also influenced the HA morphology and its carbonation type. The transformation process followed a dissolution-reprecipitation mechanism driven by the favorable balance between HA precipitation and $CaCO_3$ dissolution, due to the lower solubility product of HA than that of calcite at any of the temperatures tested. Both the bCCP and the derived HA particles were cytocompatible when were incubated with MG-63 human

osteosarcoma cells and with the m17.ASC murine mesenchymal stem cells. In addition, both materials promoted the osteogenic differentiation of the m17.ASC cells in the absence of osteogenic differentiation media, especially the HA particles. We conclude that due to their biological features, both particles can be employed as osteoinductive platforms with applications in bone tissue engineering.

Author Contributions

CT carried out the preparation of biogenic calcium carbonate from oyster shells of *Crassostrea gigas* and the particles characterization by X-ray powder diffraction analysis, FTIR and Raman spectroscopic analysis and thermal analysis. CT also contributed to the writing of this manuscript.

References

[1] J. P. Morris, T. Backeljau and G. Chapelle, *Reviews in Aquaculture*, 2019, **11**, 42–57.

[2] Anonymous, *The State of World Fisheries and Aquaculture*, 2020, 1-206,I-XIII.

[3] Y. Hou, A. Shavandi, A. Carne, A. A. Bekhit, T. B. Ng, R. C. F. Cheung and A. E. A. Bekhit, *Critical Reviews in Environmental Science and Technology*, 2016, **46**, 1047–1116.

[4] K. H. Mo, U. J. Alengaram, M. Z. Jumaat, S. C. Lee, W. I. Goh and C. W. Yuen, *Construction and Building Materials*, 2018, **162**, 751–764.

[5] N. Yan and X. Chen, *Nature*, 2015, **524**, 155–157.

[6] D. Suteu, D. Bilba, M. Aflori, F. Doroftei, G. Lisa, M. Badeanu and T. Malutan, *CLEAN – Soil, Air, Water*, 2012, **40**, 198–205.

[7] P. Morseletto, *Resources, Conservation and Recycling*, 2020, **153**, 104553.

[8] D. E. Jacob, A. L. Soldati, R. Wirth, J. Huth, U. Wehrmeister and W. Hofmeister, *Geochimica et Cosmochimica Acta*, 2008, **72**, 5401–5415.

[9] A. Hart, *Waste Manag Res*, 2020, **38**, 514–527.

[10] C. McLaughlan, P. Rose and D. C. Aldridge, *Environmental Management*, 2014, **54**, 1102–1109.

[11] A. O. Oso, A. A. Idowu and O. T. Niameh, *Journal of Animal Physiology and Animal Nutrition*, 2011, **95**, 461–467.

[12] C. H. Lee, D. K. Lee, M. A. Ali and P. J. Kim, *Waste Management*, 2008, **28**, 2702–2708.

[13] E.-I. Yang, S.-T. Yi and Y.-M. Leem, *Cement and Concrete Research*, 2005, **35**, 2175–2182.

[14] W.-T. Kuo, H.-Y. Wang, C.-Y. Shu and D.-S. Su, *Construction and Building Materials*, 2013, **46**, 128–133.

[15] J. Gómez-Morales, M. Iafisco, J. M. Delgado-López, S. Sarda and C. Drouet, *Progress in Crystal Growth and Characterization of Materials*, 2013, **59**, 1–46.

[16] A. Ressler, A. Žužić, I. Ivanišević, N. Kamboj and H. Ivanković, *Open Ceramics*, 2021, **6**, 100122.

[17] M. Okada and T. Furuzono, *Science and Technology of Advanced Materials*, 2012, **13**, 064103.

[18] S. M. Cano Plá, A. D'Urso, J. F. Fernández-Sánchez, D. Colangelo, D. Choquesillo-Lazarte, R. Ferracini, M. Bosetti, M. Prat and J. Gómez-Morales, *Nanomaterials*, 2022, **12**, 562.

[19] J. Gómez-Morales, C. Verdugo-Escamilla, R. Fernández-Penas, C. M. Parra-Milla, C. Drouet, F. Maube-Bosc, F. Oltolina, M. Prat and J. F. Fernández-Sánchez, *RSC Adv.*, 2018, **8**, 2385–2397.

[20] J. Gómez-Morales, R. Fernández-Penas, F. J. Acebedo-Martínez, I. Romero-Castillo, C. Verdugo-Escamilla, D. Choquesillo-Lazarte, L. D. Esposti, Y. Jiménez-Martínez, J. F. Fernández-Sánchez and M. Iafisco, *Nanomaterials*, 2022, **12**, 1257.

[21] J. Knaus, D. Schaffarczyk and H. Cölfen, *Macromolecular bioscience*, 2020, **20**, 1900239.

[22] *Proficient Market Insights*.

[23] A. Szcześ, L. Hołysz and E. Chibowski, *Advances in Colloid and Interface Science*, 2017, **249**, 321–330.

[24] S. V. Dorozhkin, *Acta Biomaterialia*, 2010, **6**, 715–734.

[25] Y. Cai, Y. Liu, W. Yan, Q. Hu, J. Tao, M. Zhang, Z. Shi and R. Tang, *J. Mater. Chem.*, 2007, **17**, 3780–3787.

[26] N. K. Nga, N. T. Thuy Chau and P. H. Viet, *Colloids and Surfaces B: Biointerfaces*, 2018, **172**, 769–778.

[27] S. Scialla, F. Carella, M. Dapporto, S. Sprio, A. Piancastelli, B. Palazzo, A. Adamiano, L. Degli Esposti, M. Iafisco and C. Piccirillo, *Marine Drugs*, , DOI:10.3390/md18060309.

[28] A. Pal, S. Maity, S. Chabri, S. Bera, A. R. Chowdhury, M. Das and A. Sinha, *Biomedical Physics & Engineering Express*, 2017, **3**, 015010.

[29] S. Hajar Saharudin, J. Haslinda Shariffuddin, N. Ida Amalina Ahamad Nordin and A. Ismail, *Materials Today: Proceedings*, 2019, **19**, 1208–1215.

[30] S. Rujitanapanich, P. Kumpapan and P. Wanjanoi, *Energy Procedia*, 2014, **56**, 112–117.

[31] A. Shavandi, A. E.-D. A. Bekhit, A. Ali and Z. Sun, *Materials Chemistry and Physics*, 2015, **149–150**, 607–616.

[32] Y. Xu, D. Wang, L. Yang and H. Tang, *Materials Characterization*, 2001, **47**, 83–87.

[33] H. Ivankovic, E. Tkalcec, S. Orlic, G. Gallego Ferrer and Z. Schauperl, *Journal of Materials Science: Materials in Medicine*, 2010, **21**, 2711–2722.

[34] G. Magnabosco, D. Giuri, A. P. Di Bisceglie, F. Scarpino, S. Fermani, C. Tomasini and G. Falini, *ACS Sustainable Chem. Eng.*, 2021, **9**, 6203–6208.

[35] A. G. Checa, E. M. Harper and A. González-Segura, *Scientific Reports*, 2018, **8**, 7507.

[36] R. Higuera-Ruiz and J. Elorza, *Estuarine, Coastal and Shelf Science*, 2009, **82**, 201–213.

[37] S.-C. Wu, H.-C. Hsu, S.-K. Hsu, C.-P. Tseng and W.-F. Ho, *Advanced Powder Technology*, 2017, **28**, 1154–1158.

[38] Z. Wang, S. Jiang, Y. Zhao and M. Zeng, *Materials Science and Engineering: C*, 2019, **105**, 110102.

[39] S. Santhosh and S. Balasivanandha Prabu, *Materials Letters*, 2013, **97**, 121–124.

[40] B. N. Alhussary, G. A.Taqa and A. A. A. Taqa, *Journal of Applied Veterinary Sciences*, 2020, **5**, 25–32.

[41] K. Salma-Ancane, L. Stipniece and Z. Irbe, *Ceramics International*, 2016, **42**, 9504–9510.

[42] D. L. Goloshchapov, A. S. Lenshin, D. V. Savchenko and P. V. Seredin, *Results in Physics*, 2019, **13**, 102158.

[43] M. A. M. Castro, T. O. Portela, G. S. Correa, M. M. Oliveira, J. H. G. Rangel, S. F. Rodrigues and J. M. R. Mercury, *Boletín de la Sociedad Española de Cerámica y Vidrio*, 2022, **61**, 35–41.

[44] J. R. M. Ferreira, L. H. L. Louro, A. M. Costa, J. B. De Campos and M. H. Silva, *Cerâmica*, 2016, **62**, 386–391.

[45] D. F. Fitriyana, R. Ismail, Y. I. Santosa, S. Nugroho, A. J. Hakim and M. Syahreza Al Mulqi, in *2019 International Biomedical Instrumentation and Technology Conference (IBITeC)*, 2019, vol. 1, pp. 7–11.

[46] G. S. Kumar, L. Sathish, R. Govindan and E. K. Girija, *RSC Adv.*, 2015, **5**, 39544–39548.

[47] G. S. Kumar, A. Thamizhavel and E. K. Girija, *Materials Letters*, 2012, **76**, 198–200.

[48] S.-C. Wu, Y.-L. Kao, Y.-C. Lu, H.-C. Hsu and W.-F. Ho, *Journal of the Australian Ceramic Society*, 2021, **57**, 1541–1551.

[49] P. Agalya, G. Suresh Kumar, K. M. Prabu, S. Cholan, G. Karunakaran, J. Hakami, M. Shkir and S. Ramalingam, *Ceramics International*, 2022, **48**, 28299–28307.

[50] F. Cestari, F. Agostinacchio, A. Galotta, G. Chemello, A. Motta and V. M. Sglavo, *Nanomaterials*, , DOI:10.3390/nano11020264.

[51] S. Balu, M. V. Sundaradoss, S. Andra and J. Jeevanandam, *Beilstein journal of nanotechnology*, 2020, **11**, 285–295.

[52] A. A. Coelho, *Journal of Applied Crystallography*, 2018, **51**, 210–218.

[53] A. Zamperone, S. Pietronave, S. Merlin, D. Colangelo, G. Ranaldo, E. Medico, F. Di Scipio, G. N. Berta, A. Follenzi and M. Prat, *Stem cells and development*, 2013, **22**, 2873–2884.

[54] J. Gómez-Morales, R. Fernández-Penas, I. Romero-Castillo, C. Verdugo-Escamilla, D. Choquesillo-Lazarte, A. D'Urso, M. Prat and J. F. Fernández-Sánchez, *Nanomaterials*, 2021, **11**, 322.

[55] S. Dupont, L. Morsut, M. Aragona, E. Enzo, S. Giulitti, M. Cordenonsi, F. Zanconato, J. Le Digabel, M. Forcato and S. Bicciato, *Nature*, 2011, **474**, 179–183.

[56] C. Triunfo, S. Gärtner, C. Marchini, S. Fermani, G. Maoloni, S. Goffredo, J. Gomez Morales, H. Cölfen and G. Falini, *ACS Omega*, , DOI:10.1021/acsomega.2c05386.

[57] J. M. Delgado-López, M. Iafisco, I. Rodríguez, A. Tampieri, M. Prat and J. Gómez-Morales, *Acta biomaterialia*, 2012, **8**, 3491–3499.

[58] F. Marchegiani, E. Cibej, P. Vergni, G. Tosi, S. Fermani and G. Falini, *Journal of crystal growth*, 2009, **311**, 4219–4225.

[59] G. B. Ramírez-Rodríguez, J. M. Delgado-López and J. Gómez-Morales, *CrystEngComm*, 2013, **15**, 2206–2212.

[60] M. De La Pierre, C. Carteret, L. Maschio, E. André, R. Orlando and R. Dovesi, *The Journal of Chemical Physics*, 2014, **140**, 164509.

[61] Z. Zyman and M. Tkachenko, *Journal of the European Ceramic Society*, 2011, **31**, 241–248.

[62] S. Barinov, J. Rau, S. N. Cesaro, J. Urisin, I. Fadeeva, D. Ferro, L. Medvecky and G. Trionfetti, *Journal of Materials Science: Materials in Medicine*, 2006, **17**, 597.

[63] P. Ducheyne, K. E. Healy, D. W. Hutmacher, D. W. Grainger and C. J. Kirkpatrick, *Comprehensive biomaterials*, Elsevier, 1st edn., 2011, vol. 1.

[64] W. J. Habraken, J. Tao, L. J. Brylka, H. Friedrich, L. Bertinetti, A. S. Schenk, A. Verch, V. Dmitrovic, P. H. Bomans and P. M. Frederik, *Nature communications*, 2013, **4**, 1507.

[65] X. Yang, C. Zhang, X. Yang and Z. Xu, *Journal of Molecular Liquids*, 2023, 121585.

[66] M. Iafisco, J. M. Delgado-Lopez, E. M. Varoni, A. Tampieri, L. Rimondini, J. Gomez-Morales and M. Prat, *Small*, 2013, **9**, 3834–3844.

[67] I. Iso, *International Organization for Standardization, Geneva*.

[68] X. Yang, Y. Li, X. Liu, W. He, Q. Huang and Q. Feng, **生物材料**转化电子杂志 (**英文**), 2020, **1**, 58.

[69] W. Liang, P. Ding, G. Li, E. Lu and Z. Zhao, *Drug Design, Development and Therapy*, 2021, **15**, 905.

[70] X. Yang, Y. Li, X. Liu, R. Zhang and Q. Feng, *Stem cells international*.

[71] C. Yi, D. Liu, C.-C. Fong, J. Zhang and M. Yang, *ACS nano*, 2010, **4**, 6439–6448.

[72] R. Coringa, E. M. de Sousa, J. N. Botelho, R. S. Diniz, J. C. de Sá, M. C. F. N. da Cruz, M. A. B. Paschoal and L. M. Gonçalves, *Plos one*, 2018, **13**, e0198697.

[73] W.-F. Ho, M.-H. Lee, J. L. Thomas, J.-A. Li, S.-C. Wu, H.-C. Hsu and H.-Y. Lin, *International Journal of Molecular Sciences*, 2021, **22**, 9444.

Chapter 5. Nano-crystalline and amorphous calcium carbonate from waste seashells by ball milling mechanochemistry processes

(Published in Crystal Growth & Design)

Nano-crystalline and amorphous calcium carbonate from waste seashells by ball milling mechanochemistry processes

Chiara Marchini,[1] Carla Triunfo,[1, 2] Nicolas Greggio,[3] Simona Fermani,[1] Devis Montroni,[1] Andrea Migliori,[4] Alessandro Gradone,[4] Stefano Goffredo,[2, 3] Gabriele Maoloni,[5] Jaime Gómez Morales,[6] Helmut Cölfen,[7] and Giuseppe Falini[1, *]

[1] Department of Chemistry "Giacomo Ciamician", University of Bologna, via F. Selmi 2, 40126 Bologna, Italy.

[2] Fano Marine Center, The Inter Institute Center for Research on Marine Biodiversity, Resources and Biotechnologies, viale Adriatico 1/N 61032 Fano, Italy.

[3] Department of Biological, Geological and Environmental Sciences, University of Bologna, Bologna, Italy.

[4] Institute for Microelectronics and Microsystems (IMM) - CNR section of Bologna, via P. Gobetti 101, 40129 Bologna, Italy.

[5] Finproject S.p.A., Plant Ascoli Piceno, Via Enrico Mattei, 1-Zona Ind.le Campolungo, 3100 Ascoli Piceno, Italy.

[6] Laboratorio de Estudios Cristalográficos, Instituto Andaluz de Ciencias de la Tierra (CSIC-UGR), Avda Las Palmeras 4, 18100 Armilla (Granada), Spain.

[7] Department of Chemistry, Physical Chemistry, University of Konstanz, Universitätsstrasse 10, Box 714, D-78457 Konstanz, Germany.

Abstract

Nano-crystalline calcium carbonate ($CaCO_3$) and amorphous $CaCO_3$ (ACC) are materials of increasing technological interest. Nowadays, they are mainly synthetically produced by wet reactions using $CaCO_3$ reagents in the presence of stabilizers. However, it has been recently

discovered that ACC can be produced by ball milling of calcite. Calcite and/or aragonite are the mineral phases of mollusk shells, which formed from ACC precursors. Here, we investigated the possibility to convert, on a potentially industrial scale, the biogenic $CaCO_3$ (bCC) from waste mollusk seashells into nano-crystalline $CaCO_3$ and ACC. Waste seashells from the aquaculture species, namely oysters (*Crassostrea gigas*, low Mg-calcite), scallops (*Pecten jacobaeus*, medium Mg-calcite), and clams (*Chamelea gallina*, aragonite) were used. The ball milling process was carried out by using different dispersing solvents and potential ACC stabilizers. Structural, morphological and spectroscopic characterization techniques were used. The results showed that the mechanochemical process produced a reduction of the crystalline domain sizes and formation of ACC domains, which co-existed in micro-sized aggregates. Interestingly, bCC behaved differently from the geogenic $CaCO_3$ (gCC), and upon long milling times (24 hours) the ACC reconverted into crystalline phases. The aging in diverse environments of mechanochemically treated bCC produced a mixture of calcite and aragonite in a species-specific mass ratio, while the ACC from gCC converted only into calcite. In conclusion, this research showed that bCC can produce nano-crystalline $CaCO_3$ and ACC composites or mixtures having specie-specific features. These materials can enlarge the already wide fields of applications of $CaCO_3$, which span from medical to material science.

Keywords: Biogenic calcium carbonate; ball milling; amorphous calcium carbonate; nano-crystalline calcium carbonate; aging; calcium carbonate polymorphs.

Introduction

The polymorphs of calcium carbonate ($CaCO_3$) include amorphous calcium carbonate (ACC), three anhydrous crystalline phases (calcite, aragonite, and vaterite), and two hydrated ones (monohydrate and hexahydrate). Calcite and aragonite are by far the most common and stable forms, whereas ACC is the least stable polymorph from the viewpoint of thermodynamics [1]. ACC has been widely found in organisms, where it plays an important role in the biomineralization of crystalline $CaCO_3$ [2]. It is generally accepted that biogenic ACC can broadly occur in one of two forms: stable or transient [3]. While the stable form remains non-crystalline, the transient phase can act as a precursor to either calcite or aragonite.

Stable ACC was found in various organisms like mollusk shells [4], American lobsters [5], coral skeletons [6], and so forth. In addition, evidence suggests that calcific biominerals, such as the mollusk nacre [7] and the urchin's spine [8], are formed from an amorphous precursor.

The popular involvement of ACC in biological processing organisms [9, 10], usually via complex non-classical crystallization pathways [11], has aroused interest in the scientific community. In recent years, a lot of work has been carried out on the preparation and application of ACC.

Since ACC is not a stable phase from the viewpoint of thermodynamics, temporal stabilization is achieved by the incorporation of organic molecules and specific ions in both biological and synthetic systems. The synthesis and stabilization of ACC have been pursued by freeze-drying [12, 13], with polymers [14] and proteins [15, 16], or by using foreign ions like Mg^{2+}, [17-19] and phosphate [20]. These approaches start from the Ca^{2+} and CO_3^{2-} ion constituents in aqueous solution, and the crystallization process is stopped at the ACC stage by stabilizing the product kinetically [21].

The local structure in ACC is a matter of debate [22]. A "protostructuring" of ACC with respect to different crystalline $CaCO_3$ polymorphs has been proposed [23], and the concept of "polyamorphism" has been considered for biogenic ACC [22].

Although the short-range order in ACC is pH dependent [24] and OH^- groups were found to be incorporated in ACC [25], there are no indications for the presence of hydrogen carbonate (HCO_3^-) ions in ACC or any hydrated form of it.

Recent literature has shown that there is enormous potential for ACC precursor phases to be exploited in materials synthesis [26], with their promise of superior control over nucleation and growth and access to rapid growth rates and "non-crystalline" morphologies [12-20].

ACC actually represents a family of phases whose structure and composition are dependent on the particular synthesis method and solution conditions (*e.g.* temperature, pH) [27].

Treatments following precipitation such as drying or washing with agents such as ethanol can also make significant changes to the ACC and its crystallisation behaviour [28]. Consequently, synthetic ACC can vary considerably in terms of stability [29], co-precipitated ions, and the amount of structural and surface water [30]. Upscaling of ACC synthesis has been studied as well [31].

ACC can be used for several technological and industrial applications. Calcium carbonate cements were prepared from ACC that (re)crystallizes into calcite during the setting reaction. The hardened samples were microporous and showed excellent bioactivity rates, although their mechanical properties were poor [32]. Tree-dimensional objects were printed from long-term, Mg-stabilized ACC pastes with high solid loading. This ACC remained stable for at least a couple of months, even after printing. Crystallization, if desired, occurred only after the 3D

object was formed at low temperatures [18]. Patterns of continuous 2D ACC films supported rat bone marrow stromal cell attachment and differentiation into osteoblast- and osteoclast-like cells [33]. The aqueous instability of ACC, which leads to a fast release of its payload, was applied to realize burst drug release within cancer cells [34].

Mechanochemistry ball-milling allows producing out-of-equilibrium structures, and it can be employed for breaking down bulk materials to nano-size [35, 36]. Defect formation on a large scale leads to an amorphization of crystalline solids [37]. Ball milling treatment of $CaCO_3$ has been studied [38, 39]. The transformation of calcite to aragonite has been reported [40], as well as the reverse transformation from aragonite to calcite [41]. Similarly, vaterite was transformed to calcite mechanochemically [42]. Recent studies have shown that ACC could be prepared by ball milling only using calcite, when Na_2CO_3 was used as a stabilizer of ACC [43, 44].

An important source of biogenic $CaCO_3$ (bCC), which represents an alternative to the synthetic and geogenic ones, is given by waste seashells [45, 46]. These materials are formed from an ACC precursor and naturally contain organic macromolecules and ions that can stabilize ACC [47].

The aim of this work is to compare the capability of different sources of $CaCO_3$, from quarries or biogenic, to be converted into ACC. The main hypothesis is that the bCC can lead to a more stable ACC. The mollusk shells of oyster *C. gigas* (low Mg-calcite), scallop *P. jacobaeus* (medium Mg-calcite), and clam *C. gallina* (aragonite) were used as bCC sources. The working hypothesis is that different polymorphs, the content of Mg, and species-specific organic matrices can produce ACCs diverse in stability and transformation pathways into crystalline phases. The knowledge that can be gained from this research has a double interest, for material science but also for a better understanding of the biomineralization processes. The novelty in this study is represented by the use of biogenic calcium carbonate, which formed by ACC precursors before to stabilize in crystalline phases.

Experimental section

Treatment of samples. Seashells of *Crassostrea gigas*, *Pecten jacobaeus*, and *Chamelea gallina* were provided by F.lli Terzi (Palosco, BG, Italy). Samples were washed with tap water, treated with a 5 vol% sodium hypochlorite solution for 24 hours to remove the organic residues from the seashell surface, washed again with deionized water, and air dried. The, the dry seashells were crushed by a hammer mill. gCC was provided by Italcementi spa. These powdered samples are referred to as starting samples. To uniform particle size of the $CaCO_3$ from the

different sources, both geogenic and biogenic, the powders (30 g) were dry milled in a 500 ml zirconia jar together with 125 g of zirconia balls having a 20 mm diameter with the planetary ball milling PM 100 by Retsch (milling: 400 rpm, 1 hour) and sieved at 45 μm. These samples are referred to as dry milled. For amorphization tests, 1.8 g of dry milled powder was wet milled in the zirconia jar together with 100 g of zirconia balls having a 2 mm diameter, 200 ml of solvent (ethanol, isopropanol, cyclohexane, heptane, or butanol), and 0.2 g of additive (Na_2CO_3, $MgCO_3$, Li_2CO_3, K_2CO_3, and $Ca(OH)_2$) and ground at 400 rpm in the planetary ball milling (milling: 400 rpm, pause: 20 min every 10 min of grinding), according to a reported procedure [43]. Different grinding times, additives, and solvents were tested. These samples are referred to as wet milled.

X-ray powder diffraction analysis. X-ray powder diffraction (XRD) patterns were collected using a PanAnalytical X'Pert Pro diffractometer equipped with a multiarray X'Celerator detector using Cu Kα radiation (λ = 1.54056 Å), generated at 40 kV and 40 mA. The diffraction patterns were collected in the 2θ range between 20 ° and 60 ° with a step size (Δ2θ) of 0.02 ° and a counting time of 60 s.

An estimation of the mass percentage of amorphous material, i.e. ACC, organic matter and water, in the sample was calculated as the percentage of the integrated intensity of the amorphous diffraction band with respect to the integrated total diffraction intensity. We suppose that this diffraction band is due to the ACC, being the content of organic matrix and water very low and these materials are formed by atoms having low diffraction scattering factors (i. e. carbon, nitrogen, oxygen and hydrogen).

Spectroscopic Analysis. A Thermo Scientific Nicolet iS10 FTIR Spectrometer was used to collect the FTIR spectra. The disk specimen for Fourier transform infrared (FTIR) analysis was obtained by mixing a small amount (about 2 mg) of sample with 98 mg of KBr and applying a pressure of 45 psi (620.5 MPa) to the mixture using a press. The spectra were obtained with 4 cm^{-1} resolution and 64 scans.

Thermogravimetric Analysis. Thermogravimetric analysis (TGA) was performed using an SDT Q600 V 8.0 instrument (TA Instruments). The system was pre-equilibrated at 30 °C, then a ramp from 30 to 600 °C with a 10 °C min^{-1} heating rate was performed under nitrogen flow (100 mL min^{-1}). The measurement was performed three times on 20 mg of each sample. The temperature range considered to estimate the content of the intraskeletal organic matter and water was between 150 and 450 °C.

Particle Size Distribution Analysis. Particle size analyses were performed using a Malvern Mastersizer 2000 laser diffraction particle size analyser (Malvern Panalytical). The particles from each sample were dispersed in isopropanol for the measurement.

Scanning Electron Microscopy observations. The scanning electron microscopy (SEM) images were acquired using two different microscopes operating at 5 kV: a ZEISS Leo 1530 Gemini and a Thermo Fisher Quattro S equipped with a Schottky FEG. All samples were dried under vacuum in a desiccator, deposited on a carbon tape, and 10 nm gold-coated before their observation.

Transmission Electron Microscopy investigations. The structure and composition analysis on the nanoscale was carried out with a FEI Tecnai F20ST high-resolution Transmission Electron Microscope (HR-TEM) operated at 200 kV. All samples were ground in an agate mortar and suspended in ethanol. The powders were deposited directly on a Cu grid with a holey-type - carbon film. The solvent was evaporated at 50 °C for about 3 min.

Inductively Coupled Plasma–Optical Emission Spectroscopy (ICP-OES). All the powders (200 mg) were dissolved in HNO_3 50 vol% and were measured three times, 12 s each, with 60 s of pre-running, using ICP-OES, Spectro Arcos-Ametek, Inductive Coupled Plasma Optical Emission Spectroscopy with an axial torch and high salinity kit. The calibration curve was made using certified standards in water.

Results and discussion

Synthesis and characterization of the starting materials

As a source of biogenic $CaCO_3$ (bCC) particles this research used seashells from species that have (*i*) a strong relevance in aquaculture, (*ii*) are made of a single $CaCO_3$ polymorph and (*iii*) have diverse crystalline textures. They were the oyster *C. gigas*, the scallop *P. jacobaeus*, and the clam *C. gallina*, which shells were made of low Mg-calcite (about 1 mol%), medium Mg-calcite (1.4 mol%) and aragonite, respectively.

Control experiments were performed using gCC, made of calcite. The elemental, compositional, and structural characterization of these materials is reported in Table 1.

Table 1. Percentage of $CaCO_3$ polymorph, organic matrix (OM) content, elemental composition, and crystallite size of geogenic calcium carbonate, oyster shell, scallop shell and clam shell powder after hammer mill grinding. The crystallite size was calculated along the (104) and the (111) zone axis for calcite and aragonite respectively.

Sample	**Calcite** (wt%)*	**Aragonite** (wt%)*	**OM content** (wt%)#	**Mg** (at%)	**Sr** (at%)	**$d_{(104)}/d_{(111)}$** (nm)
geo $CaCO_3$	100	/	0.2	1.24	0.00	1525 ± 3/ -
oyster shell	99.41	0.59	1.1	0.99	0.09	92 ± 3/ -
scallop shell	96.23	3.77	0.7	1.36	0.04	88 ± 3/ 70 ± 16
clam shell	5.78	94.22	0.7	0.28	0.18	43 ± 16/161 ± 8

The starting materials were dry-milled and sieved to homogenize the particle size. The obtained materials, referred to as dry milled, were used for the subsequent amorphization experiments. The compositional and structural features of these materials are reported in Table 2 and Figure 1.

Table 2. Percentage of $CaCO_3$ polymorphs, organic matrix content, grain size, and crystallite size of gCC, oyster shell, scallop shell, and clam shell powder after dry ball milling and sieving at 45 μm. The instrumental error is reported.

Sample	**Calcite** (wt%)$	**Aragonite** (wt%)$	**ACC** (wt%)#	**O.M.** (wt%)	**D_{50}** (μm)	**S. A.** (m^2/g)	**$d_{(104)}/d_{(111)}$°** (nm)
geo $CaCO_3$	100 ± 2	-	0 ± 2	0 ± 0.1	8.34	4.3	14.4 ± 0.2
oyster shell	97 ± 2	-	3 ± 2	0.7 ± 0.1	8.13	7.6	13.9 ± 0.2
scallop shell	90 ± 2	4 ± 2	6 ± 2	0.9 ± 0.1	15.54	6.6	13.7 ± 0.2
clam shell	7 ± 2	89 ± 2	4 ± 2	0.6 ± 0.1	13.80	7.3	15.8 ± 0.2/12.3 ± 0.3

$ Percentage of crystalline phases. # Percentage of ACC in the particles. °The crystallite size was calculated along the (104) and the (111) zone axis for calcite and aragonite respectively. O.M. indicates

intraskeletal organic matter and water. D_{50} indicates that up to 50 % percent of the total particles having a grain size smaller than the reported value. S.A. indicates specific surface area. $d_{(hkl)}$ indicates the size of the crystalline domain along the direction indicated by the Miller indices.

The diffraction patterns (Fig. 1, Table 2) showed that a transition from aragonite to calcite associated with the dry grinding process occurred in clam shell powder, an effect already reported in the literature [48]. The calcite phases were not affected by the grinding process.
The analyses of the XRD diffraction patterns showed that gCC particles are free of ACC, while the bCC particles contain ACC in a percentage that is species-dependent. The presence of ACC is expected since this phase is a precursor of the crystalline phases in the formation of mollusk shells and in general of many calcifying organisms. The content of ACC reported in Table 2 has been evaluated by the X-ray diffraction patterns. It includes also a contribution from the intraskeletal organic matter and water. It is considered that these latter components have a minimal effect on the overall scattering, being composted of elements like carbon, nitrogen, oxygen and hydrogen that have a low X-ray scattering factor with respect to calcium.

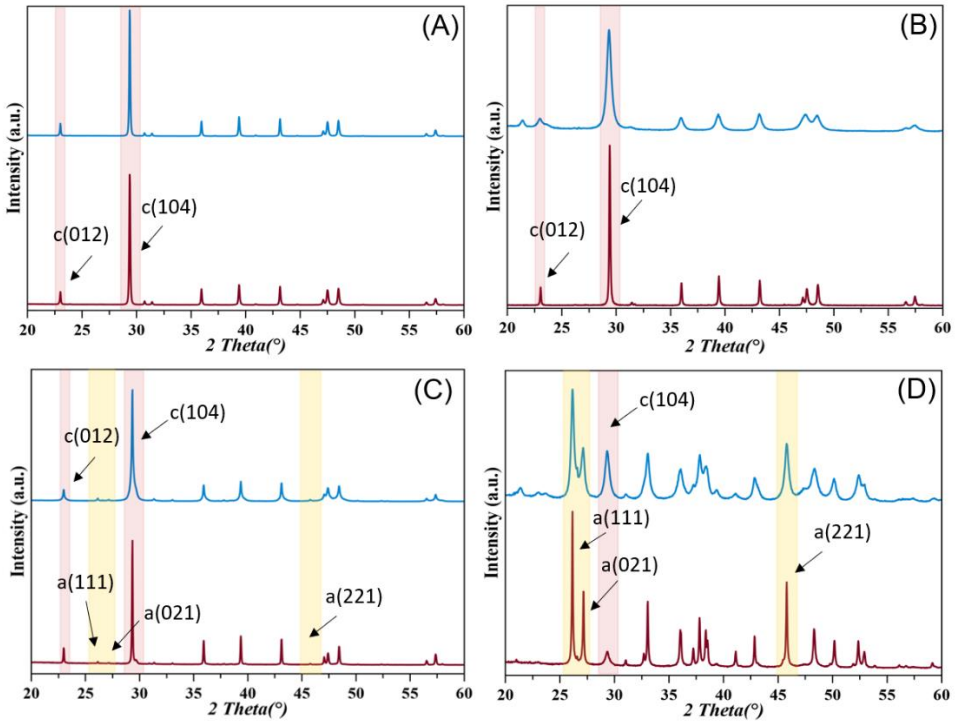

Figure 1. X-ray powder diffraction patterns from starting materials (red line) and dry milled materials (blu line) of geogenic $CaCO_3$ (A), oyster shells (B), scallop shells (C), and clam shells (D). The intensity is in linear scale. The diffraction patterns were indexed according to PDF 00-005-0586 and PDF 00-005-0453 for calcite and aragonite, respectively.

The content of water, which could increase the intensity of the amorphous diffraction band, is below 1 wt%, as indicated by the TGA data that show always a content of water and organic matter lower than 1 wt% (Table 2; Fig. 2). This content is very low in the gCC, as expected. The elemental composition agrees with the literature data [49], being calcite and aragonite able to host in the crystalline lattices Mg ion and Sr ions, respectively.

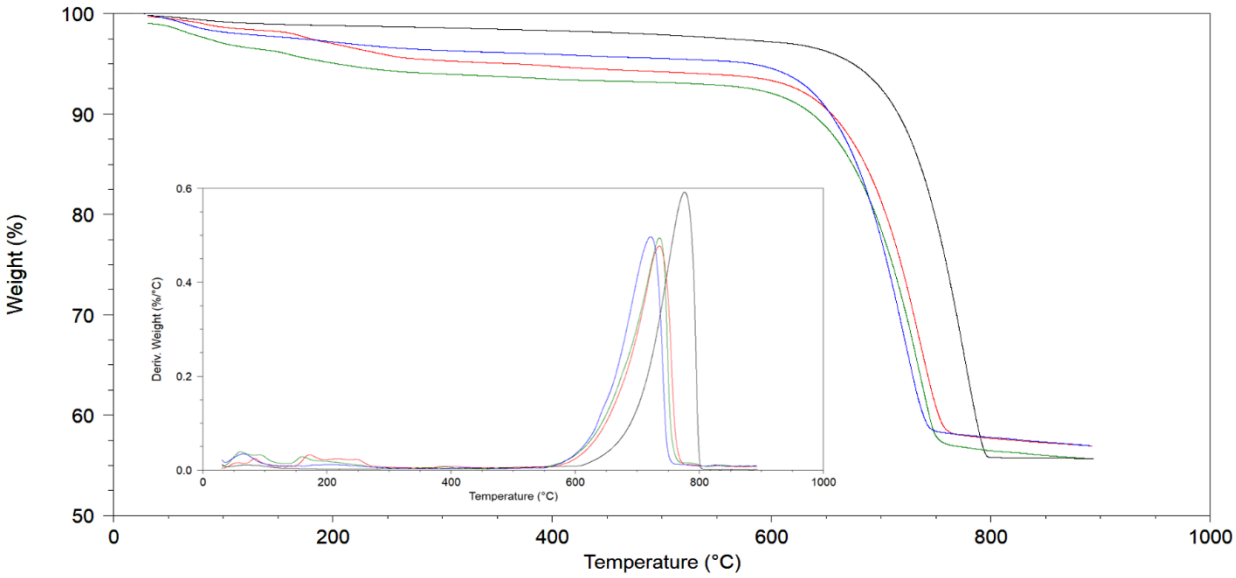

Figure 2. Thermogravimetric analysis (TGA) profiles of geogenic $CaCO_3$ (black), oyster (blu), scallop (red), and clam (green). The temperature range considered to estimate the content of intraskeletal organic matrix was between 300 °C and 500 °C.

In order to study the morphology of the dry-milled powders, SEM images have been collected (Fig. 3). The gCC powder appeared as a mixture of big particles (around 35 µm) and small ones of about 1 µm size. Many of them were showing typical crystalline shapes in which rhombohedral {104} faces are visible in the small grain. The big particles are aggregates in which the crystalline faces are not clearly defined. The powder from oyster shells was also heterogeneous, but in this case, the bigger particles were preserving the typical foliated structure of the Mg-calcite shells, and the small ones appeared as spheroidal grains. Their size along the main axis was about 500 nm. The powder from the scallop shell was similar to that from the oyster shell with the difference that the big particles did not show the foliated crystalline texture. A different scenario was shown by the powder from the clam shells. In this case, the bigger particles appeared as aggregates of the small ones, which were spheroids that had a size lower than 500 nm along their main axis. The morphological analysis of the data agrees with the measures of the specific surface area. The bCC powders, having a family of smaller particles

with lower size than the geogenic ones, have a higher surface area (6-7 m^2 g^{-1}) compared to the gCC (about 4 m^2 g^{-1}). The dimension of the crystalline domains does not show a correlation with the above experimental data.

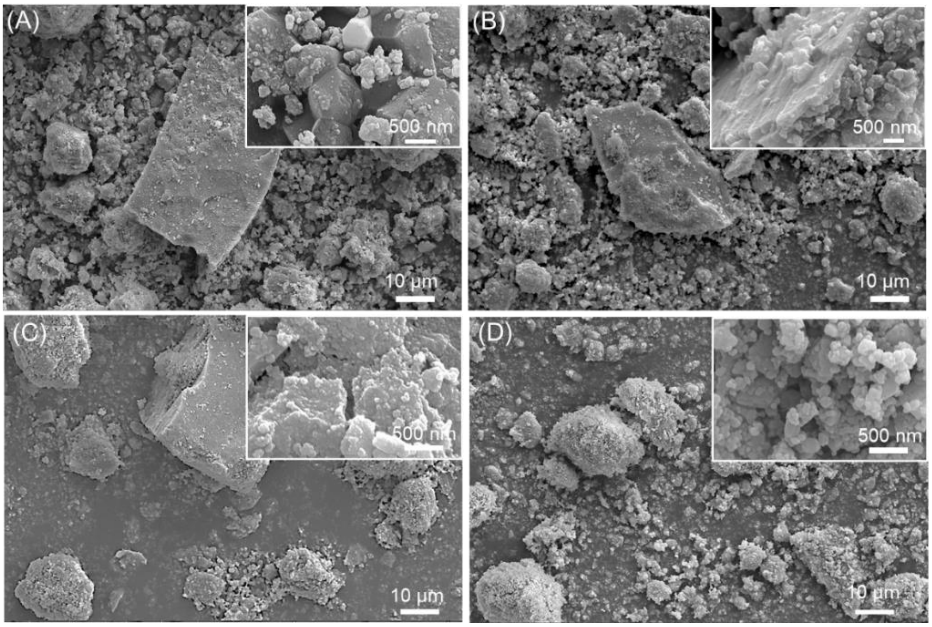

Figure 3. SEM images of (A) gCC, (B) oyster shell, (C) scallop shell, and (D) clam shell powders dry milled. The inset shows a higher-magnification view.

Optimization of the $CaCO_3$ mechanochemical process

This amorphization process of $CaCO_3$ finds inspiration from the work of Tremel et al. [43, 44]. The optimization of the experimental conditions was performed using bCC from oyster shells. The optimal ball milling time was evaluated using 10 wt% Na_2CO_3 as additive and cyclohexane as dispersion liquid. Ball milling times of 1, 3, 6, 12, and 24 hours were used (Fig. 4).

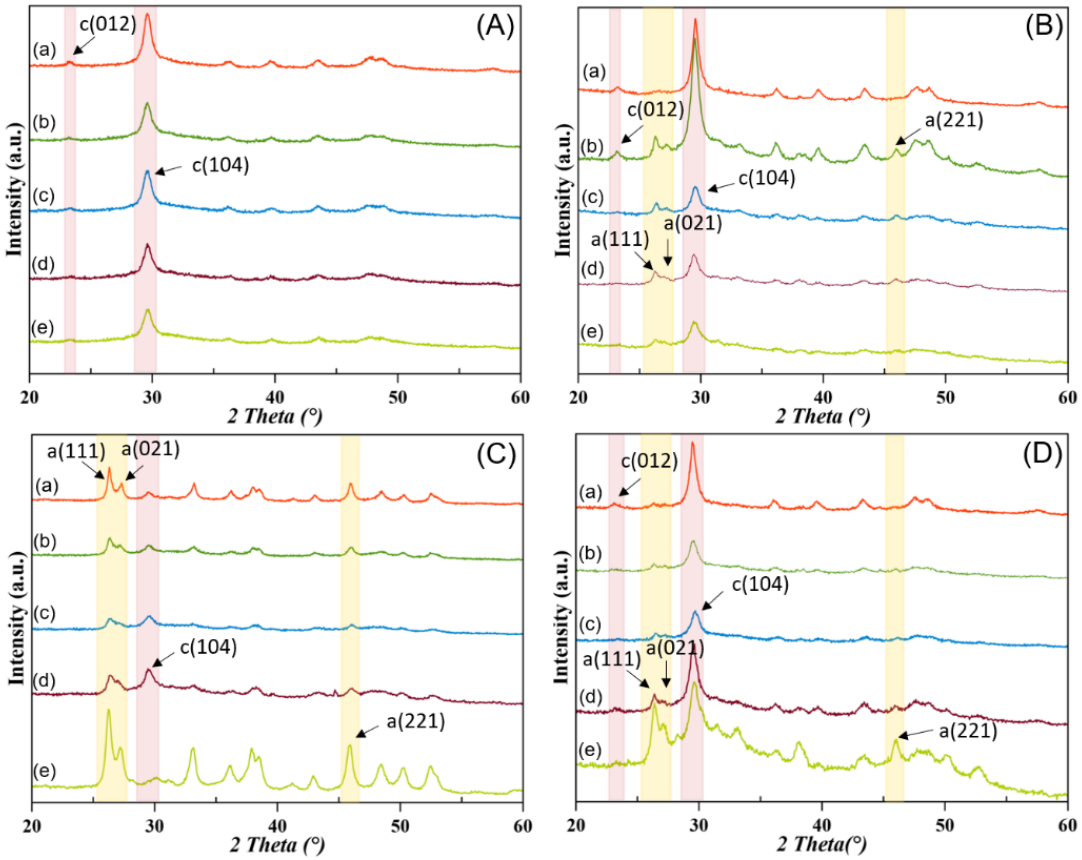

Figure 4. Powder X-ray diffraction patterns of geogenic $CaCO_3$ (A), oyster (B), scallop (C), and clam (D) shells wet milled for 1 hour (a), 3 hours (b), 6 hours (c), 12 hours (d), and 24 hours (e). The intensity is in linear scale. The diffraction patterns were indexed according to PDF 00-005-0586 for calcite and PDF 00-005-0453 for aragonite.

The analyses of the diffraction patterns indicated that after 6 hours of ball milling the highest content of ACC was observed from bCC (Table 3, Fig. 4). Fixing the ball milling time at 6 h, the effect of several solvents such as ethanol, isopropanol, cyclohexane, heptane, and butanol was tested, keeping 10 wt% Na_2CO_3 as additive (Fig. 5).

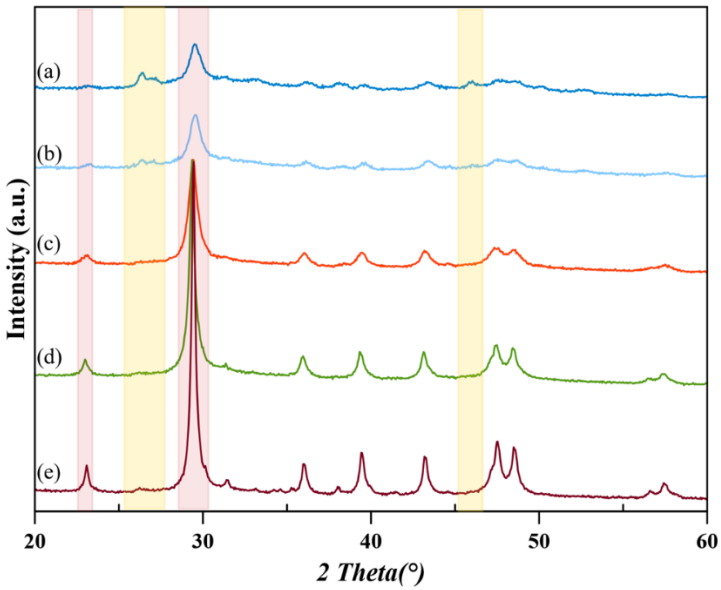

Figure 5. Powder X-ray diffraction patterns of oyster wet milled for 6 hours with different solvents: (a) Cyclohexane; (b) Heptane; (c) Isopropanol; (d) Ethanol; (e) Butane. The intensity is in linear scale. The diffraction patterns were indexed according to PDF 00-005-0586 for calcite and PDF 00-005-0453 for aragonite.

A higher amorphization degree was obtained using cyclohexane, suggesting that the lower the solubility of water in the solvent, the higher the amorphization degree (Fig. 5). Such observation could mean that by displacing water, the recrystallization of ACC is prevented. Indeed, it has been reported that increased water content accelerates the transformation of ACC in crystalline phases [50].

Having optimized ball milling time and solvent, trials were performed using different additives, such as Na_2CO_3, $MgCO_3$, Li_2CO_3, K_2CO_3, and $Ca(OH)_2$ (Fig. 6).

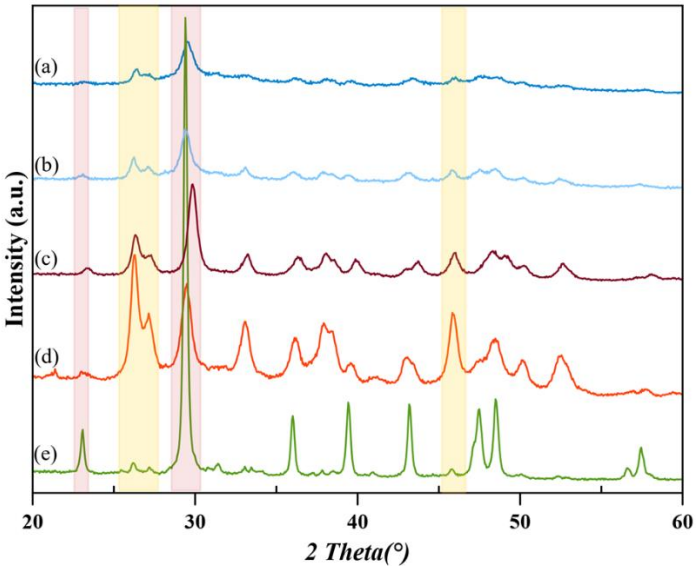

Figure 6. Powder X-ray diffraction patterns of oyster wet milled for 6 hours with different additives: a) Na_2CO_3; b) $Ca(OH)_2$; c) $MgCO_3$; d) Li_2CO_3; e) K_2CO_3. The intensity is in linear scale. The diffraction patterns were indexed according to PDF 00-005-0586 for calcite and PDF 00-005-0453 for aragonite.

The material obtained using Na_2CO_3 as an additive showed a higher amorphization degree. Interestingly, when $MgCO_3$ was used as additive, Mg substitution in the calcite phase occurred (Fig. 6).

Reduction of crystalline domain size and amorphization of $CaCO_3$ from different sources in the presence of Na_2CO_3

Mechanochemical experiments on gCC and bCC from the three mollusk species were performed using cyclohexane as a solvent and 10 wt% of Na_2CO_3 as an amorphizing additive. The powders milled for 1, 6, and 24 hours were characterized by several techniques that provided converging results (Figs. 6 and 7; Table 3). A complete amorphization was never achieved, this observation contrasts with the experiments of Tremel et al. [43].

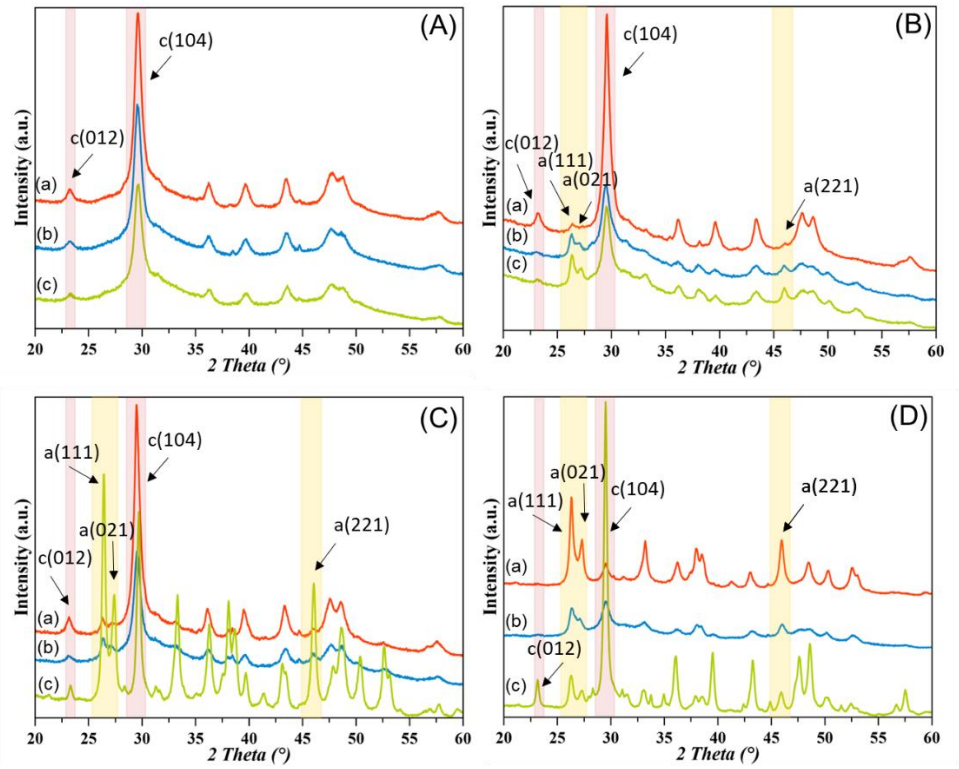

Figure 6. Powder X-ray diffraction patterns of (A) gCC, (B) oyster, (C) scallop, and (D) clam shells powders wet milled for (a) 1 hour, (b) 6 hours, and (c) 24 hours. The diffraction patterns were indexed accordingly to the PDF 00-005-0586 for calcite and PDF 00-005-0453 for aragonite.

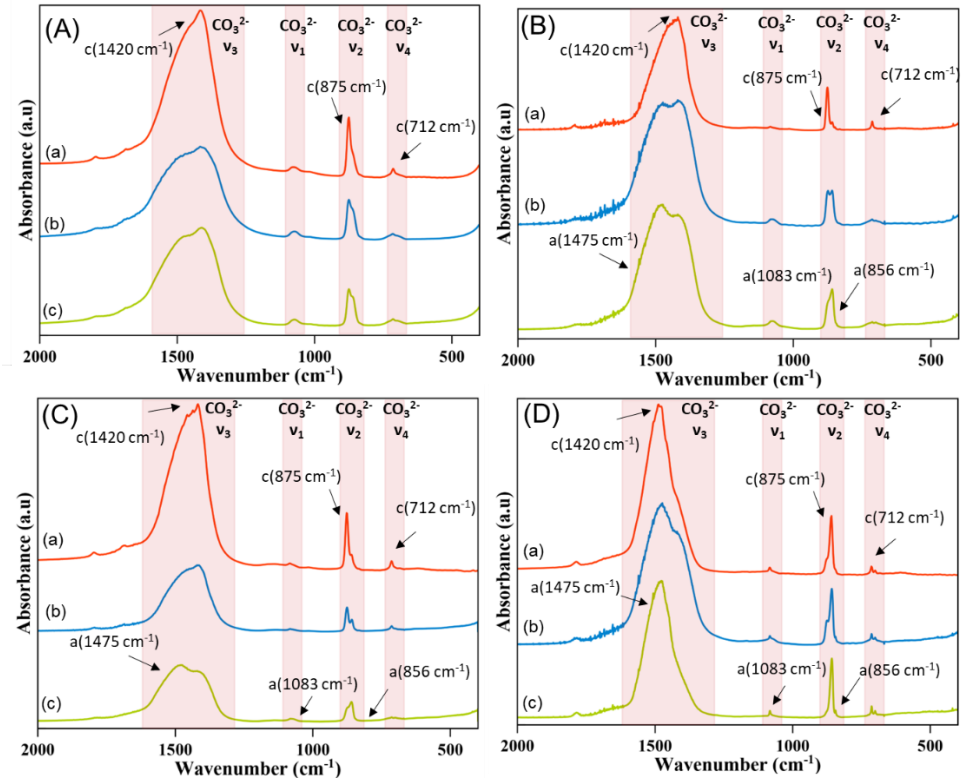

Figure 7. FTIR spectra of geogenic $CaCO_3$ (A), oyster (B), scallop (C), and clam (D) shells wet milled for 1 hour (a), 6 hours (b), and 24 hours (c).

However, it has to be considered that in the presented research different experimental conditions were used (e. g. a bigger jar, 500 ml versus 10 ml) with the aim to test also experimental conditions relevant for a process scale-up. Among the bCC the one formed by Mg-calcite showed a higher degree of amorphization, being 40 wt% and 49 wt% for oyster and scallop powder, respectively. Under the same experimental conditions, the clam powder amorphized for 39 wt%. These degrees of amorphization were achieved after 6 hours of grinding. Interestingly, the gCC had a degree of amorphization of 36 wt% after 6 hours of ball milling and this value increased to 42 wt% after 24 hours of ball milling. Diversely, the degree of amorphization in bCC for times longer than 6 hours decreased and the conversion into a different polymorph occurred. The oyster and the scallop powders converted to aragonite and this occurred more for scallops than oysters.

Table 3. Percentage of $CaCO_3$ polymorphs, organic material content, grain size, and crystallite size of gCC, oyster shell, scallop shell, and clam shell powder after different times of ball milling using cyclohexane as dispersing agent and 10 wt% Na_2CO_3 as additive for amorphization. The instrumental error is reported.

Sample	**Mill time** (hour)	**Calcite** (wt%)	**Aragonite** (wt%)[$]	**ACC** (wt%)[#]	**O.M.**[#] (wt%)	$\mathbf{d_{(104)}/d_{(111)}}$[°] (nm)
geo $CaCO_3$	1	70 ± 2	/	30 ± 2	0.1 ± 0.1	11.1 ± 0.3
	6	64 ± 2	/	36 ± 2	0.1 ± 0.1	8.3 ± 0.1
	24	58 ± 2	/	42 ± 2	0.1 ± 0.1	7.5 ± 0.1
oyster shell	1	79 ± 2	5 ± 2	16 ± 2	0.5 ± 0.1	14.2 ± 0.5
	6	42 ± 2	18 ± 2	40 ± 2	0.5 ± 0.1	6.7 ± 0.2 / 12 ± 1.2
	24	45 ± 2	26 ± 2	28 ± 2	0.5 ± 0.1	7.1 ± 0.2 / 13.7 ± 0.9
scallop shell	1	65 ± 2	10 ± 2	25 ± 2	0.4 ± 0.1	14.3 ± 0.6 / 15 ± 1
	6	38 ± 2	16 ± 2	46 ± 2	0.5 ± 0.1	8.9 ± 0.3 / 12.2 ± 0.8
	24	27 ± 2	68 ± 2	5 ± 2	0.6 ± 0.1	29 ± 3 / 40 ± 3
clam shell	1	11 ± 2	68 ± 2	21 ± 2	0.7 ± 0.1	11.5 ± 0.7 / 18.6 ± 0.3
	6	29 ± 2	31 ± 2	39 ± 2	0.8 ± 0.1	6.7 ± 0.1 / 12.0 ± 0.3
	24	72 ± 2	23 ± 2	4 ± 2	0.7 ± 0.1	24 ± 1 / 52 ± 22

[$] Percentage of crystalline phases. [#] Percentage of ACC in the powder material determined by analysing the X-ray diffraction profile. O.M. indicates intraskeletal organic matter and water. °The crystallite size was calculated along the (104) and the (111) zone axis for calcite and aragonite, respectively.

The higher content of Mg ions in scallops can justify this observation since Mg ions kinetically favour the formation of aragonite [1], but since the solvent used is almost water free this classical explanation supported by the strong hydration sphere of Mg ion cannot be applied. On the contrary clam powder converted to calcite upon longer time of ball milling. The conversion of aragonite to calcite has been reported as a solid phase transition [51], but this mechanism could not occur during the milling process in cyclohexane in the presence of Na_2CO_3. The diffraction peaks broadening process should be due to a reduction of the crystalline domain sizes with the ball milling time, which may proceed with the generation of defects in the crystalline domain during the plastic deformation [52]. Accordingly, the bCC powders show shorter crystalline domain sizes after 6 hours of grinding (Table 3).

The experimental data indicated that in the absence of Na_2CO_3, the formation of the ACC does not occur and only a reduction of the crystalline domain size is observed. The role of the Na_2CO_3 in stabilizing ACC was demonstrated by Leukel et al. (2018) [43] where they suggested that Na ions stabilize ACC. The proposed mechanism reports that the formation of ACC from calcite occurs due to the high energy released during the ball milling process. It can be controversial to demonstrate the reason for which the stable phase of calcite transforms to the unstable solid phase ACC. We may suppose that the transformation of a crystalline $CaCO_3$ to ACC may take place via a surface liquid state, which may form when Na_2CO_3, or similar substances, generates relatively low eutectic temperature composites [53, 54], when in contact with solid $CaCO_3$ at elevated temperatures due to the friction in grinding [55]. This potential melted doped $CaCO_3$ may rapidly be cooled and may transform to ACC or other phases.

The morphology of the powders obtained after 6 hours of ball milling, the condition that produced the higher content of ACC from bCC, was investigated by SEM (Fig. 8). The samples, when observed at low magnifications appeared as aggregates having wide distribution in sizes and assuming diverse shapes. The high magnification images showed that the aggregates were formed of nano-particles having a size below 500 nm. Interestingly the gCC nanoparticles were more compact than the bCC ones. This differentiation could be associated with a higher surface stabilization of the bCC nanoparticles from the various components, molecules, and ions, of the pristine shells. The geogenic ones have a high surface energy missing the biological stabilization and strongly aggregate in compact big particles. This consideration is supported by the estimation of the content of the intra-crystalline organic matrix, a unique signature of the bCC, that remains almost constant during the grinding processes, as reported in Table 3.

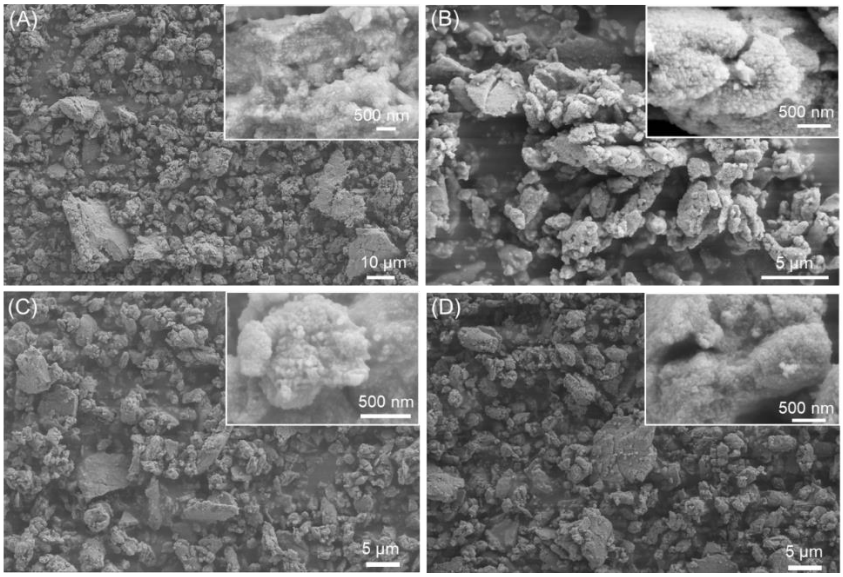

Figure 8. SEM images of (A) gCC, (B) oyster shell, (C) scallop shell, and (D) clam shell powders wet milled for 6 hours. The inset shows a higher-magnification view.

The mechanochemical-treated $CaCO_3$ materials were also investigated by transmission electron microscopy (TEM) and selected area electron diffraction (SAED). The low magnification TEM images (Fig. 9) showed that the general morphology of all samples was represented by aggregates formed by the aggregation of smaller structures with different dimensions and in some regions quite regular shapes. This suggested the co-presence of domains with a certain degree of crystallinity and amorphous domains, which were randomly superimposed on each other.

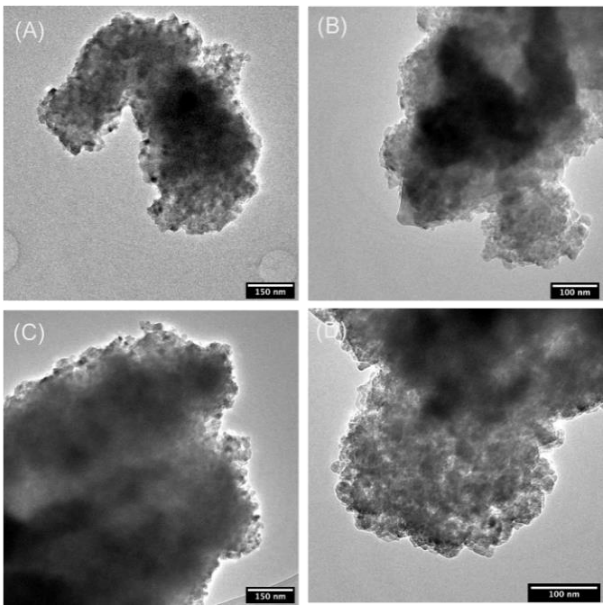

Figure 9. TEM images at low magnification of (A) gCC, (B) oyster shell, (C) scallop, and (D) clam powders wet ball milled for 6 hours.

Additional information on the structure of the mechanochemical-treated material was obtained from the high-resolution TEM (HRTEM) images and the SAED patterns reported in Figure 10. The geogenic calcite sample (Fig. 10A) produced HRTEM images in which the interplanar distances of calcite, and in a few cases of aragonite, were detected. They were easily observable through the Fourier transform in the inset (Fig. 10A). The SAED patterns collected by centering the aperture on two different aggregates, to ensure a better representation of the sample, confirmed the main presence of calcite. The patterns were typical for a polycrystalline structure, due to the aggregation of crystallites of different dimensions and orientations. The evaluated typical d-spacings of calcite were reported in Table 4. In Figure 10C the presence of ACC was not directly observed as single particles from the HRTEM images, suggesting that this phase was embedded in the aggregate particles. Thus, the observation of ACC domains was hindered by the co-existence with crystalline domains.

A quite similar scenario was observed when the mechanochemical-treated bCC samples were analysed (Fig. 10D-L). The HRTEM images from the oyster and scallop powders show a qualitative presence of more intense diffraction peaks for calcite, while in the clam shells, the HRTEM images show the typical and more intense spot of aragonite observable, as illustrated in the Fourier transform insets. These results perfectly match with SAED patterns that display a diffraction spot structure typical of a polycrystalline structure, due to the aggregation of many crystallites of different dimensions and orientations. As discussed for the geogenic calcite the presence of ACC is not very evident.

We suggest that also for the bCC the ACC co-exists with the crystalline phases, and the amorphization process occurs by a possible solid-state transformation involving the progressive reduction of the dimension of the crystalline domains, as also suggested by the analysis of the powder XRD data. Such a phenomenon has been reported for geogenic calcite [52], the researchers showed that mechanical milling was effective in reducing the domain size to the nanoscale and introducing large microstrains. They suggested that the milling process mostly involves impulsive forces between vial, grinding bodies, and powder. Even if the average temperature can be kept constant, the energy released locally during the fast impacts is considerably high. Under these conditions it could be put forward that dislocations glide should be favoured with respect to twinning as the active plasticity mechanism [52].

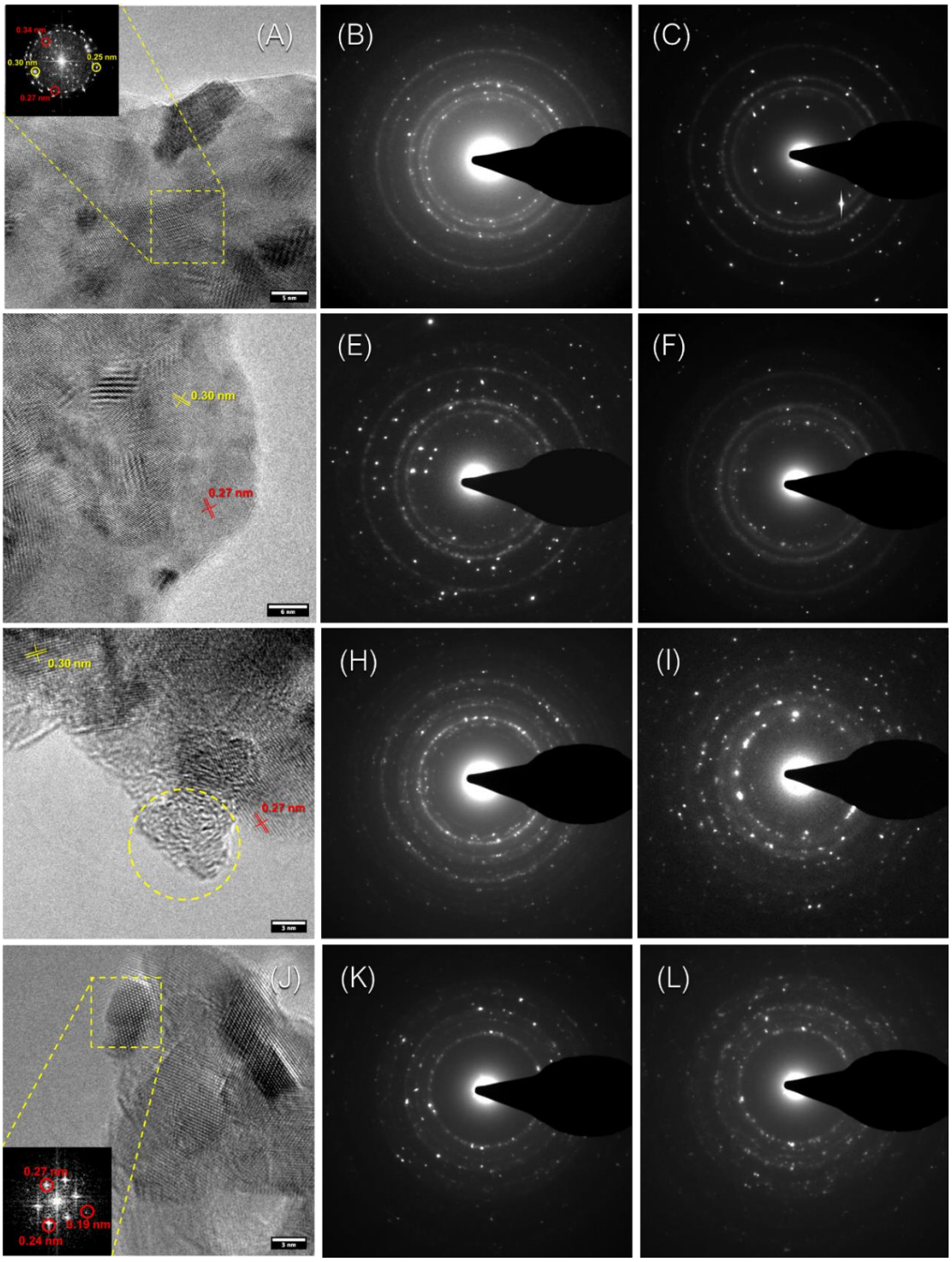

Figure 10. High-Resolution TEM and Selected Area Electron Diffraction micrographs of (A-C) gCC, (D-E) oyster shell, (G-I) scallop, and (K-L) clam powders wet milled for 6 hours. The inset reports the Fourier transform of a crystalline region indicated by the yellow square. The yellow circle shows an amorphous region. The selected area election diffraction micrographs were collected in different regions of the specimen and the two most representative ones are reported.

Table 4. SAED patterns analysis of the sample mechanochemical treated by ball milling for 6 hours. The measured d-spacings are reported for the bCC powders and the geogenic one. The d-spacing of aragonite and calcite are reported for comparison.

Geo-$CaCO_3$ (Å)	Oyster (Å)	Scallop (Å)	Clam (Å)	Aragonite (Å)	Calcite (Å)
3.84	3.80	3.82	3.37	3.39	3.86
3.00	3.01	3.36	2.70	2.70	3.03
2.47	2.75	2.99	2.37	2.37	2.49
2.32	2.40	2.46	1.97	1.98	2.28

Time stability of ACC according to source and aging environment

To study the effects of aging time on the re-crystallization process of ACC and the increase in the size of the crystalline domains, the powders wet milled for 6 hours were stored in different environments: i) in a nitrogen atmosphere for 10, 20, and 30 days; ii) in ethanol under bar-stirring for 15 min, 30 min, and 120 min; iii) in H_2O under bar-stirring for 5 min, 30 min, and 120 min. The results are illustrated in Figures 11 and 12 and reported in Table 5.

In all the investigated environments the gCC converted ACC into calcite. This process was very slow in a nitrogen atmosphere, even after one month, the transition from ACC to calcite was not complete (Table 5; Fig. 11). On the contrary in ethanol and water, the conversion was complete and occurred in two hours and five minutes, respectively (Table 5; Fig. 11). The aging was also associated with an increase of the crystalline size, which was of similar extent in nitrogen or ethanol environment after the longest time of aging, but higher in water (Table 5; Fig. 12). This suggests that in water the recrystallization process is more efficient, as expected considering the higher solubility of $CaCO_3$ in this solvent with respect to ethanol. Thus, it is supposed that a dissolution reprecipitation process occurs in the transformation of ACC in crystalline phase, as supposed above considering the ACC in different water containing solvents. This mechanism of transformation of ACC in aqueous systems has already been reported [50, 56].

The aging of bCC particles gave different results with respect to gCC. The powder from oyster shells, when located in nitrogen or ethanol environment, over time increased the relative content

of calcite while the content of aragonite was almost constant, while it decreased in water (Table 5; Fig. 11). This last effect can be also associated with the highest solubility of $CaCO_3$ in water with respect to ethanol [57]. In all the aging experiments the size of the crystalline domains of calcite increased, having the most marked increase in water (Table 5; Fig. 12). A similar trend was observed for the size of the crystalline domains of aragonite (Table 5; Fig. 12).

When the powder from scallops was aged a behaviour different from that of oysters was observed. In this case, with the aging both the relative amount of calcite and aragonite increased, while the relative content of ACC was progressively decreasing (Table 5; Fig. 11).

The powder from the clam aged in nitrogen and ethanol environments results in a relevant increase of the relative content of aragonite and calcite, while in water over time the relative content of aragonite decreased, suggesting a transition from aragonite to calcite (Table 5; Fig. 11). The size of the crystalline domains increased with the time, for both calcite and aragonite, irrespective of the environment in where the powders were located (Table 5; Fig. 11).

Table 5. Percentage of $CaCO_3$ polymorphs, grain size and crystallite size of geogenic calcium carbonate, oyster shell, scallop shell and clam shell powder after different aging times in diverse solvents. The instrumental error is reported.

Environment	**Aging time**	**Calcite** (wt%)	**Aragonite** (wt%)[$]	**ACC** (wt%)[#]	$\mathbf{d_{(104)}/d_{(111)}}$ (nm)
geo $CaCO_3$					
N_2	10 days	74 ± 2	/	26 ± 2	12.18 ± 0.86
	20 days	84 ± 2	/	16 ± 2	13.61 ± 0.56
	30 days	85 ± 2	/	15 ± 2	15.44 ± 0.43
EtOH	15 min	90 ± 2	/	10 ± 2	12.14 ± 0.38
	30 min	90 ± 2	/	10 ± 2	12.56 ± 0.49
	120 min	97 ± 2	/	3 ± 2	16.00 ± 3.10
H_2O	5 min	100 ± 2	/	0 ± 2	21.60 ± 0.42
	30 min	100 ± 2	/	0 ± 2	23.43 ± 0.65
	120 min	100 ± 2	/	0 ± 2	25.38 ± 0.74
Oyster shell					
N_2	10 days	43 ± 2	18 ± 2	39 ± 2	8.41 ± 0.49/14.20 ± 1.20
	20 days	53 ± 2	27 ± 2	20 ± 2	13.59 ± 0.46/20.17 ± 0.91

	30 days	68 ± 2	27 ± 2	5 ± 2	17.55 ± 0.46/19.82 ± 0.87
EtOH	15 min	51 ± 2	22 ± 2	27 ± 2	7.99 ± 0.17/14.00 ± 1.20
	30 min	47 ± 2	26 ± 2	27 ± 2	9.69 ± 0.18/15.43 ± 0.93
	120 min	51 ± 2	26 ± 2	23 ± 2	12.87 ± 0.21/18.56 ± 0.84
H_2O	5 min	74 ± 2	23 ± 2	4 ± 2	29.38 ± 0.73/19.02 ± 0.60
	30 min	84 ± 2	13 ± 2	3 ± 2	30.05 ± 0.39/19.80 ± 1.20
	120 min	89 ± 2	11 ± 2	0 ± 2	38.24 ± 0.91/23.70 ± 1.40
Scallop shell					
N_2	10 days	48 ± 2	8 ± 2	44 ± 2	7.79 ± 0.17/14.80 ± 1.70
	20 days	46 ± 2	19 ± 2	35 ± 2	8.89 ± 0.19/13.40 ± 1.10
	30 days	49 ± 2	23 ± 2	28 ± 2	12.36 ± 0.46/20.20 ± 1.00
EtOH	15 min	42 ± 2	14 ± 2	44 ± 2	8.68 ± 0.69/13.10 ± 1.50
	30 min	48 ± 2	19 ± 2	33 ± 2	10.17 ± 0.51/17.30 ± 1.30
	120 min	57 ± 2	23 ± 2	20 ± 2	13.58 ± 0.41/18.80 ± 1.00
H_2O	5 min	82 ± 2	14 ± 2	3 ± 2	27.83 ± 0.61/17.84 ± 0.88
	30 min	89 ± 2	9 ± 2	2 ± 2	37.30 ± 1.00/18.70 ± 1.50
	120 min	91 ± 2	8 ± 2	1 ± 2	35.05 ± 0.84/21.30 ± 1.60
Clam shell					
N_2	10 days	36 ± 2	26 ± 2	38 ± 2	6.73 ± 0.38/12.08 ± 0.59
	20 days	38 ± 2	42 ± 2	20 ± 2	12.39 ± 0.81/16.53 ± 0.55
	30 days	43 ± 2	46 ± 2	11 ± 2	16.06 ± 0.64/16.76 ± 0.42
EtOH	15 min	35 ± 2	29 ± 2	36 ± 2	6.65 ± 0.18/11.33 ± 0.54
	30 min	35 ± 2	36 ± 2	29 ± 2	8.81 ± 0.44/14.31 ± 0.54
	120 min	47 ± 2	50 ± 2	3 ± 2	14.93 ± 0.72/16.08 ± 0.47
H_2O	5 min	55 ± 2	43 ± 2	2 ± 2	25.56 ± 0.75/25.90± 1.70
	30 min	65 ± 2	33 ± 2	2 ± 2	32.85 ± 1.00/26.90 ± 1.80
	120 min	66 ± 2	33 ± 2	1 ± 2	32.08 ± 0.87/27.40 ± 1.70

[$] Percentage of crystalline phases. [#] Percentage of ACC in the particles.

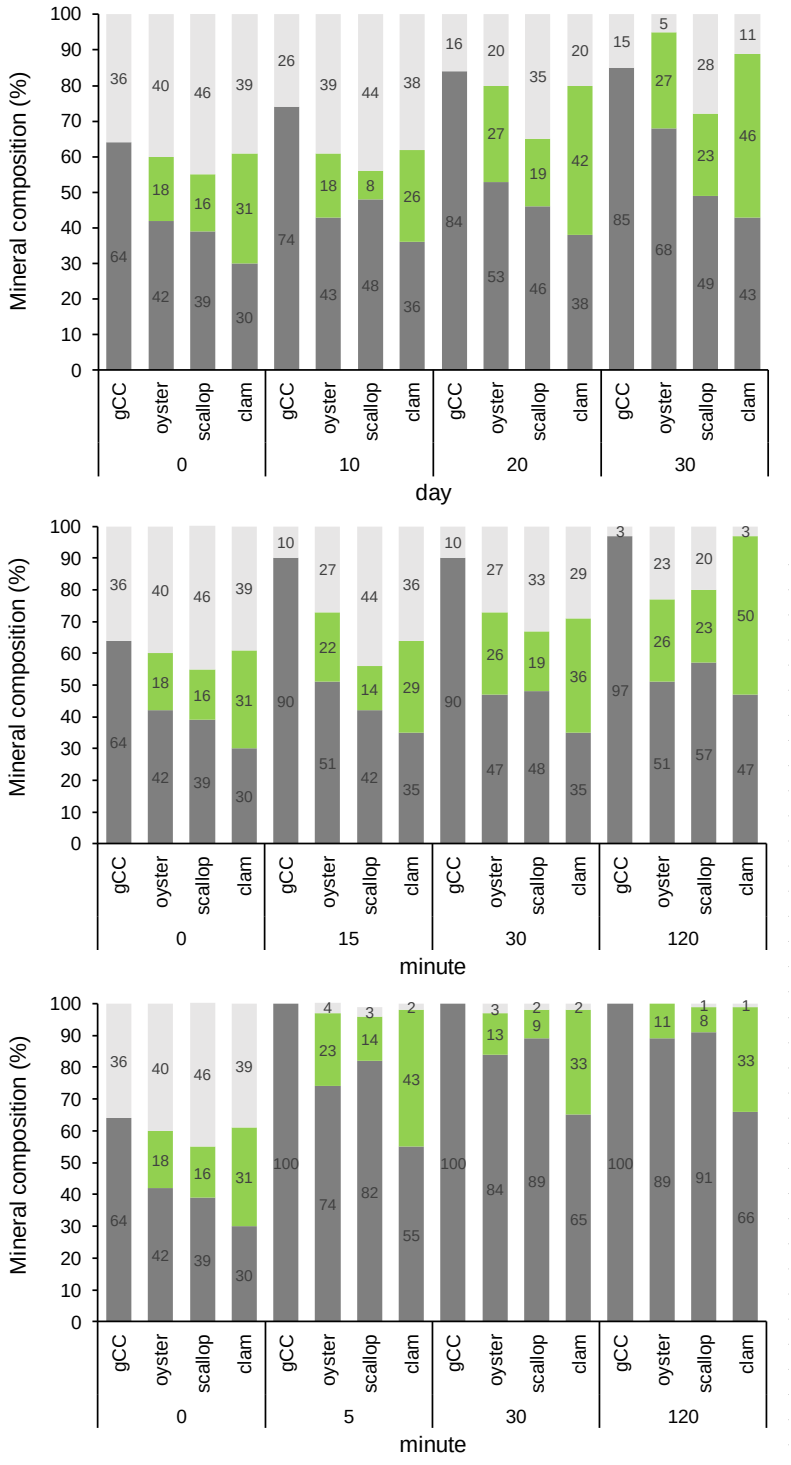

Figure 11. Percentage of $CaCO_3$ polymorphs (Grey: calcite; Green: aragonite; White: ACC) of gCC, oyster shell, scallop shell and clam shell powder after different aging times in diverse environments: (A) Nitrogen, (B) Ethanol, (C) Water.

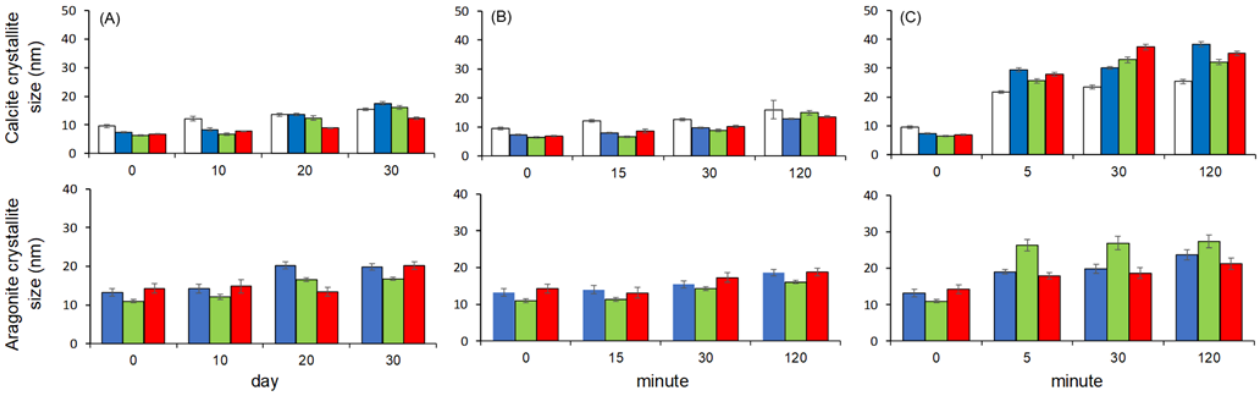

Figure 12. Histograms of calcite and aragonite crystallite size of gCC (white), oyster shell (blue), scallop shell (red), and clam shell (green) powder after different aging times in diverse environments: (A) Nitrogen, (B) Ethanol, (C) Water. The error bars indicate the standard deviation.

The above data indicated, as expected, that the major stability of the ACC occurred in a nitrogen environment. Indeed, the particles in this gas remain quite stable, and only solid-state transition can occur, diversely from the ethanol or water environments where $CaCO_3$ dissolution and reprecipitation processes can take place.

The samples aged for one month in a nitrogen environment were investigated by SEM to detect if some solid-state morphological reorganization occurred. The images reported in Figure 13 indicated that the grains aggregated in bigger particles have different textures, with the most crystalline one observed for the clam powder.

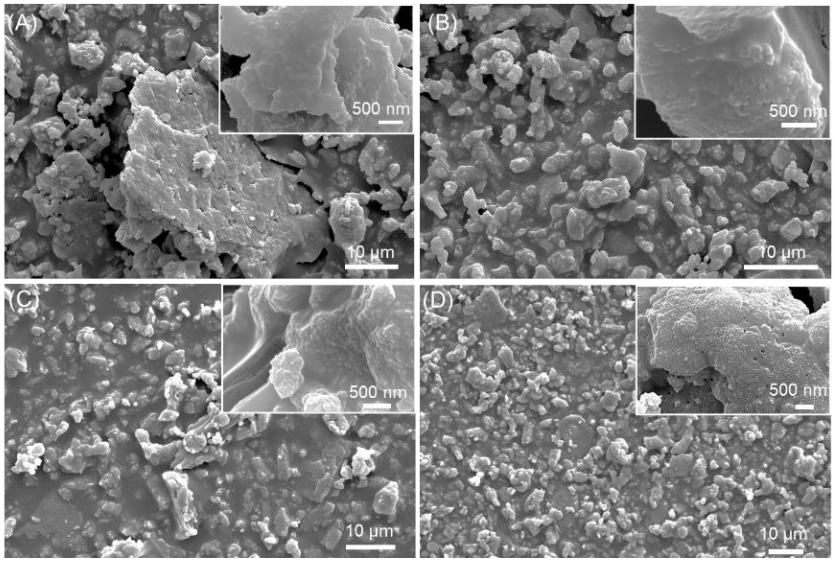

Figure 13. SEM images of the (A) gCC, (B) oyster shell, (C) scallop shell, and (D) clam shell powders wet milled for 6 h and re-crystallized after 3 months in N_2 environment. The inset shows a higher-magnification view.

Conclusions

Ball milling mechanochemistry treatments on bCC and gCC have shown that the amorphization process occurred via a progressive reduction of the sizes of the crystalline domains and may suggest a mechanism which involves the formation of a low temperature eutectic liquid phase in the presence of Na_2CO_3. For all the samples, although to a diverse extent, ACC co-existed with crystalline domains. For the bCC the conversion of the crystalline phase in ACC occurred with the concomitant transition of calcite to aragonite and vice-versa.

On the contrary, gCC converted only into ACC. In addition to this, increasing the ball milling time the ACC from bCC converted into crystalline phases, while gCC increased the content of ACC and decreased the size of the crystalline domains. This diverse behavior could be attributed to the unique presence in the bCC of the intraskeletal organic matrix and of biologically relevant trace elements. The phase transformation of $CaCO_3$ to ACC may occur via a surface eutectic liquid state, which may occur in the presence of Na_2CO_3, that then may transform to ACC or crystalline phases.

The aging in different environments - nitrogen, ethanol, or water - of mechanochemically treated bCC and gCC produced different results, the former being converted into aragonite and calcite and the latter only into calcite.

In view of the potential application of ACC, this research showed that the use of bCC offers a wider scenario of structural features and stabilities with respect to the gCC. This is particularly relevant when different materials are required for diverse applications.

Author Contributions

In collaboration with CM, CT carried out the treatment of the samples, the X-ray powder diffraction analysis, the spectroscopic analysis, the thermogravimetric analysis and the particle size distribution analysis. CT also contributed to the writing of this manuscript.

References

[1] Niu, Y.-Q.; Liu, J.-H.; Aymonier, C.; Fermani, S.; Kralj, D.; Falini, G.; Zhou, C.-H. Calcium Carbonate: Controlled Synthesis, Surface Functionalization, and Nanostructured Materials. *Chem. Soc. Rev.* **2022**, *51*, 7883–7943.

[2] Addadi, L.; Raz, S.; Weiner, S. Taking Advantage of Disorder: Amorphous Calcium

Carbonate and Its Roles in Biomineralization. *Adv. Mater.* **2003**, *15* (12), 959–970.

[3] Jiang, J.; Gao, M.-R.; Xu, Y.-F.; Yu, S.-H. Amorphous Calcium Carbonate: Synthesis and Transformation. *Bioinspiration From Nano to Micro Scales* **2012**, 189–220.

[4] Weiss, I. M.; Tuross, N.; Addadi, L. I. A.; Weiner, S. Mollusc Larval Shell Formation: Amorphous Calcium Carbonate Is a Precursor Phase for Aragonite. *J. Exp. Zool.* **2002**, *293* (5), 478–491.

[5] Reeder, R. J.; Tang, Y.; Schmidt, M. P.; Kubista, L. M.; Cowan, D. F.; Phillips, B. L. Characterization of Structure in Biogenic Amorphous Calcium Carbonate: Pair Distribution Function and Nuclear Magnetic Resonance Studies of Lobster Gastrolith. *Cryst. Growth Des.* **2013**, *13* (5), 1905–1914.

[6] Mass, T.; Giuffre, A. J.; Sun, C.-Y.; Stifler, C. A.; Frazier, M. J.; Neder, M.; Tamura, N.; Stan, C. V; Marcus, M. A.; Gilbert, P. U. P. A. Amorphous Calcium Carbonate Particles Form Coral Skeletons. *Proc. Natl. Acad. Sci.* **2017**, *114* (37), E7670–E7678.

[7] Nudelman, F. Nacre Biomineralisation: A Review on the Mechanisms of Crystal Nucleation. In *Seminars in cell & developmental biology*; Elsevier, 2015; Vol. 46, pp 2–10.

[8] Seto, J.; Ma, Y.; Davis, S. A.; Meldrum, F.; Gourrier, A.; Kim, Y. Y.; Schilde, U.; Sztucki, M.; Burghammer, M.; Maltsev, S.; et al. Structure-Property Relationships of a Biological Mesocrystal in the Adult Sea Urchin Spine. *Proc. Natl. Acad. Sci. U. S. A.* **2012**, *109* (10), 3699–3704. https://doi.org/10.1073/pnas.1109243109.

[9] Beniash, E.; Aizenberg, J.; Addadi, L.; Weiner, S. Amorphous Calcium Carbonate Transforms into Calcite during Sea Urchin Larval Spicule Growth. *Proc. R. Soc. London. Ser. B Biol. Sci.* **1997**, *264* (1380), 461–465.

[10] Politi, Y.; Arad, T.; Klein, E.; Weiner, S.; Addadi, L. Sea Urchin Spine Calcite Forms via a Transient Amorphous Calcium Carbonate Phase. *Science (80-.).* **2004**, *306* (5699), 1161–1164.

[11] Jeon, T.; Na, Y.-E.; Jang, D.; Kim, I. W. Stabilized Amorphous Calcium Carbonate as a Precursor of Microcoating on Calcite. *Materials (Basel).* **2020**, *13* (17), 3762.

[12] Ihli, J.; Kulak, A. N.; Meldrum, F. C. Freeze-Drying Yields Stable and Pure Amorphous

Calcium Carbonate (ACC). *Chem. Commun.* **2013**, *49* (30), 3134–3136.

[13] Khouzani, M. F.; Chevrier, D. M.; Güttlein, P.; Hauser, K.; Zhang, P.; Hedin, N.; Gebauer, D. Disordered Amorphous Calcium Carbonate from Direct Precipitation. *CrystEngComm* **2015**, *17* (26), 4842–4849.

[14] Wang, S.-S.; Xu, A.-W. Amorphous Calcium Carbonate Stabilized by a Flexible Biomimetic Polymer Inspired by Marine Mussels. *Cryst. Growth Des.* **2013**, *13* (5), 1937–1942.

[15] Wolf, S. E.; Leiterer, J.; Pipich, V.; Barrea, R.; Emmerling, F.; Tremel, W. Strong Stabilization of Amorphous Calcium Carbonate Emulsion by Ovalbumin: Gaining Insight into the Mechanism of 'Polymer-Induced Liquid Precursor'Processes. *J. Am. Chem. Soc.* **2011**, *133* (32), 12642–12649.

[16] Bentov, S.; Weil, S.; Glazer, L.; Sagi, A.; Berman, A. Stabilization of Amorphous Calcium Carbonate by Phosphate Rich Organic Matrix Proteins and by Single Phosphoamino Acids. *J. Struct. Biol.* **2010**, *171* (2), 207–215.

[17] Politi, Y.; Batchelor, D. R.; Zaslansky, P.; Chmelka, B. F.; Weaver, J. C.; Sagi, I.; Weiner, S.; Addadi, L. Role of Magnesium Ion in the Stabilization of Biogenic Amorphous Calcium Carbonate: A Structure− Function Investigation. *Chem. Mater.* **2010**, *22* (1), 161–166.

[18] Shaked, H.; Polishchuk, I.; Nagel, A.; Bekenstein, Y.; Pokroy, B. Long-Term Stabilized Amorphous Calcium Carbonate—an Ink for Bio-Inspired 3D Printing. *Mater. Today Bio* **2021**, *11*, 100120.

[19] Zou, Z.; Yang, X.; Albéric, M.; Heil, T.; Wang, Q.; Pokroy, B.; Politi, Y.; Bertinetti, L. Additives Control the Stability of Amorphous Calcium Carbonate via Two Different Mechanisms: Surface Adsorption versus Bulk Incorporation. *Adv. Funct. Mater.* **2020**, *30* (23), 2000003.

[20] Zou, Z.; Polishchuk, I.; Bertinetti, L.; Pokroy, B.; Politi, Y.; Fratzl, P.; Habraken, W. J. E. M. Additives Influence the Phase Behavior of Calcium Carbonate Solution by a Cooperative Ion-Association Process. *J. Mater. Chem. B* **2018**, *6* (3), 449–457.

[21] Lee, K.; Wagermaier, W.; Masic, A.; Kommareddy, K. P.; Bennet, M.; Manjubala, I.; Lee, S.-W.; Park, S. B.; Cölfen, H.; Fratzl, P. Self-Assembly of Amorphous Calcium

Carbonate Microlens Arrays. *Nat. Commun.* **2012**, *3* (1), 725.

[22] Cartwright, J. H. E.; Checa, A. G.; Gale, J. D.; Gebauer, D.; Sainz-Díaz, C. I. Calcium Carbonate Polyamorphism and Its Role in Biomineralization: How Many Amorphous Calcium Carbonates Are There? *Angew. Chemie Int. Ed.* **2012**, *51* (48), 11960–11970.

[23] Gebauer, D.; Gunawidjaja, P. N.; Ko, J. Y. P.; Bacsik, Z.; Aziz, B.; Liu, L.; Hu, Y.; Bergström, L.; Tai, C.; Sham, T. Proto-calcite and Proto-vaterite in Amorphous Calcium Carbonates. *Angew. Chemie Int. Ed.* **2010**, *49* (47), 8889–8891.

[24] Tobler, D. J.; Rodriguez Blanco, J. D.; Sørensen, H. O.; Stipp, S. L. S.; Dideriksen, K. Effect of PH on Amorphous Calcium Carbonate Structure and Transformation. *Cryst. Growth Des.* **2016**, *16* (8), 4500–4508.

[25] Jensen, A. C. S.; Rodriguez, I.; Habraken, W. J. E. M.; Fratzl, P.; Bertinetti, L. Mobility of Hydrous Species in Amorphous Calcium/Magnesium Carbonates. *Phys. Chem. Chem. Phys.* **2018**, *20* (29), 19682–19688.

[26] Cantaert, B.; Kuo, D.; Matsumura, S.; Nishimura, T.; Sakamoto, T.; Kato, T. Use of Amorphous Calcium Carbonate for the Design of New Materials. *Chempluschem* **2017**, *82* (1), 107–120.

[27] Ihli, J.; Kim, Y.; Noel, E. H.; Meldrum, F. C. The Effect of Additives on Amorphous Calcium Carbonate (Acc): Janus Behavior in Solution and the Solid State. *Adv. Funct. Mater.* **2013**, *23* (12), 1575–1585.

[28] Sand, K. K.; Yang, M.; Makovicky, E.; Cooke, D. J.; Hassenkam, T.; Bechgaard, K.; Stipp, S. L. S. Binding of Ethanol on Calcite: The Role of the OH Bond and Its Relevance to Biomineralization. *Langmuir* **2010**, *26* (19), 15239–15247.

[29] Gebauer, D.; Kellermeier, M.; Gale, J. D.; Bergström, L.; Cölfen, H. Pre-Nucleation Clusters as Solute Precursors in Crystallisation. *Chem. Soc. Rev.* **2014**, *43* (7), 2348–2371.

[30] Barhoum, A.; Rahier, H.; Abou-Zaied, R. E.; Rehan, M.; Dufour, T.; Hill, G.; Dufresne, A. Effect of Cationic and Anionic Surfactants on the Application of Calcium Carbonate Nanoparticles in Paper Coating. *ACS Appl. Mater. Interfaces* **2014**, *6* (4), 2734–2744.

[31] Chuzeville, L.; Boury, F.; Duday, D.; Anand, R.; Moretto, E.; Thomann, J.-S. Eco-

Friendly Processes for the Synthesis of Amorphous Calcium Carbonate Nanoparticles in Ethanol and Their Stabilisation in Aqueous Media. *Green Chem.* **2022**, *24* (3), 1270–1284.

[32] Rodríguez-Sánchez, J.; Myszka, B.; Boccaccini, A. R.; Dysthe, D. K. Setting Behavior and Bioactivity Assessment of Calcium Carbonate Cements. *J. Am. Ceram. Soc.* **2019**, *102* (11), 6980–6990.

[33] Popescu, D. C.; van Leeuwen, E. N. M.; Rossi, N. A. A.; Holder, S. J.; Jansen, J. A.; Sommerdijk, N. A. J. M. Shaping Amorphous Calcium Carbonate Films into 2D Model Substrates for Bone Cell Culture. *Angew. Chemie* **2006**, *118* (11), 1794–1799.

[34] Wang, C.; Chen, S.; Yu, Q.; Hu, F.; Yuan, H. Taking Advantage of the Disadvantage: Employing the High Aqueous Instability of Amorphous Calcium Carbonate to Realize Burst Drug Release within Cancer Cells. *J. Mater. Chem. B* **2017**, *5* (11), 2068–2073.

[35] Fecht, H. J.; Hellstern, E.; Fu, Z.; Johnson, W. L. Nanocrystalline Metals Prepared by High-Energy Ball Milling. *Metall. Trans. A* **1990**, *21*, 2333–2337.

[36] Zhang, G.-Y.; Lin, R.-S.; Wang, X.-Y. Effect of Waste Oyster Shell Powder on the Properties of Alkali-Activated Slag–Waste Ceramic Geopolymers. *J. Mater. Res. Technol.* **2023**, *22*, 1768–1780. https://doi.org/https://doi.org/10.1016/j.jmrt.2022.12.052.

[37] Weeber, A. W.; Bakker, H. Amorphization by Ball Milling. A Review. *Phys. B Condens. Matter* **1988**, *153* (1–3), 93–135.

[38] Hu, H.; Li, X.; Huang, P.; Zhang, Q.; Yuan, W. Efficient Removal of Copper from Wastewater by Using Mechanically Activated Calcium Carbonate. *J. Environ. Manage.* **2017**, *203*, 1–7.

[39] Tsai, W.-T.; Yang, J.-M.; Hsu, H.-C.; Lin, C.-M.; Lin, K.-Y.; Chiu, C.-H. Development and Characterization of Mesoporosity in Eggshell Ground by Planetary Ball Milling. *Microporous Mesoporous Mater.* **2008**, *111* (1–3), 379–386.

[40] Burns, J. H.; Bredig, M. A. Transformation of Calcite to Aragonite by Grinding. *J. Chem. Phys.* **1956**, *25* (6), 1281.

[41] Criado, J. M.; Trillo, J. M. Effects of Mechanical Grinding on the Texture and Structure

of Calcium Carbonate. *J. Chem. Soc. Faraday Trans. 1 Phys. Chem. Condens. Phases* **1975**, *71*, 961–966.

[42] Northwood, D. O.; Lewis, D. Transformation of Vaterite to Calcite during Grinding. *Am. Mineral. J. Earth Planet. Mater.* **1968**, *53* (11–12), 2089–2092.

[43] Leukel, S.; Panthöfer, M.; Mondeshki, M.; Kieslich, G.; Wu, Y.; Krautwurst, N.; Tremel, W. Mechanochemical Access to Defect-Stabilized Amorphous Calcium Carbonate. *Chem. Mater.* **2018**, *30*, 6040–6052. https://doi.org/10.1021/acs.chemmater.8b02339.

[44] Opitz, P.; Asta, M. P.; Fernandez-Martinez, A.; Panthöfer, M.; Kabelitz, A.; Emmerling, F.; Mondeshki, M.; Tremel, W. Monitoring a Mechanochemical Reaction Reveals the Formation of a New ACC Defect Variant Containing the HCO3-Anion Encapsulated by an Amorphous Matrix. *Cryst. Growth Des.* **2020**, *20* (10), 6831–6846. https://doi.org/10.1021/acs.cgd.0c00912.

[45] Morris, J. P.; Backeljau, T.; Chapelle, G. Shells from Aquaculture: A Valuable Biomaterial, Not a Nuisance Waste Product. *Rev. Aquac.* **2019**, *11*, 42–57. https://doi.org/10.1111/raq.12225.

[46] Magnabosco, G.; Giuri, D.; Di Bisceglie, A. P.; Scarpino, F.; Fermani, S.; Tomasini, C.; Falini, G. New Material Perspective for Waste Seashells by Covalent Functionalization. *ACS Sustain. Chem. Eng.* **2021**, *9* (18), 6203–6208. https://doi.org/10.1021/acssuschemeng.1c01306.

[47] Addadi, L.; Weiner, S. Biomineralization: Mineral Formation by Organisms. *Phys. Scr.* **2014**, *89*, 098003. https://doi.org/10.1088/0031-8949/89/9/098003.

[48] Gammage, R. B.; Glasson, D. R. The Effect of Grinding on the Polymorphs of Calcium Carbonate. *J. Colloid Interface Sci.* **1976**, *55* (2), 396–401. https://doi.org/10.1016/0021-9797(76)90048-5.

[49] MacDonald, J. Microstructure, Crystallography and Stable Isotope Composition of Crassostrea Gigas. **2011**.

[50] Albéric, M.; Bertinetti, L.; Zou, Z.; Fratzl, P.; Habraken, W.; Politi, Y. The Crystallization of Amorphous Calcium Carbonate Is Kinetically Governed by Ion Impurities and Water. *Adv. Sci.* **2018**, *5* (5), 1701000.

[51] Peterson, L. C. Calcium Carbonates. In *Encyclopedia of Ocean Sciences*; Steele, J., Thorpe, S., Turekian, K., Eds.; Academic Press: London, 2019; pp 336–345. https://doi.org/10.1016/B978-0-12-409548-9.11520-9.

[52] Pesenti, H.; Leoni, M.; Scardi, P. XRD Line Profile Analysis of Calcite Powders Produced by High Energy Milling. *Zeitschrift fur Krist. Suppl.* **2008**, *27* (27), 143–150. https://doi.org/10.1524/zksu.2008.0019.

[53] Podborodnikov, I. V; Shatskiy, A.; Arefiev, A. V; Rashchenko, S. V; Chanyshev, A. D.; Litasov, K. D. The System Na 2 CO 3–CaCO 3 at 3 GPa. *Phys. Chem. Miner.* **2018**, *45*, 773–787.

[54] Arefiev, A. V; Shatskiy, A.; Podborodnikov, I. V; Rashchenko, S. V; Chanyshev, A. D.; Litasov, K. D. The System K 2 CO 3–CaCO 3 at 3 GPa: Link between Phase Relations and Variety of K–Ca Double Carbonates At≤ 0.1 and 6 GPa. *Phys. Chem. Miner.* **2019**, *46*, 229–244.

[55] Kwon, Y.-S.; Gerasimov, K. B.; Yoon, S.-K. Ball Temperatures during Mechanical Alloying in Planetary Mills. *J. Alloys Compd.* **2002**, *346* (1–2), 276–281.

[56] Bots, P.; Benning, L. G.; Rodriguez-Blanco, J.-D.; Roncal-Herrero, T.; Shaw, S. Mechanistic Insights into the Crystallization of Amorphous Calcium Carbonate (ACC). *Cryst. Growth Des.* **2012**, *12* (7), 3806–3814.

[57] Falini, G.; Gazzano, M.; Ripamonti, A. Magnesium Calcite Crystallizatin from Water–Alcohol Mixtures. *Chem. Commun.* **1996**, No. 9, 1037–1038.

Chapter 6. Tunable materials from Chinese mitten crab and Brown shrimp waste shells

(Manuscript under review)

Tunable materials from Chinese mitten crab and Brown shrimp waste shells

C. Triunfo,[1, 2] K. Tsirtsidou,[3] K. Vanhoutte,[3] S. Gärtner,[4] A. Mucaria,[1] D. Montroni,[1] S. Fermani,[1] G. Falini,[1, *] and J. Robbens[3]

[1] Department of Chemistry "Giacomo Ciamician", University of Bologna, via F. Selmi 2, 40126 Bologna, Italy.

[2] Fano Marine Center, The Inter-Institute Center for Research on Marine Biodiversity, Resources and Biotechnologies, viale Adriatico 1/N 61032 Fano, Italy.

[3] Aquatic Environment and Quality, Cell Blue Biotech and Food Integrity, Flanders Research Institute for Agriculture, Fisheries and Food (ILVO), Jacobsenstraat 1, 8400 Ostend, Belgium.

[4] Department of Chemistry, Physical Chemistry, University of Konstanz, Universitätsstrasse 10, Box 714, D-78457 Konstanz, Germany.

Abstract

Crab and shrimp shells are by-product materials from shellfish farming and processing. In this study, we showed that it is possible to obtain individual shell components either individually or in combinations. These diverse materials were composed of calcium carbonate and organic molecules inter- and intra-mineral; of calcium carbonate and organic molecules intra-mineral; of organic molecules, such as chitin and proteins; of only calcium carbonate; and only chitin. These substrates were tested for the adsorption of Methylene Blue and Eosin dyes. The best adsorption for the positively charged Methylene Blue was achieved on the chitin-calcium carbonate substrates, while the negatively charged Eosin adsorbed best on the chitin substrate. In conclusion, this research demonstrates that different materials can be obtained by de-structuring the shells from crabs and shrimps at different levels and that these materials have properties related to the unique properties of the original material, but also lead to new properties.

Keywords: Waste shells; crab; shrimp; chitin; protein; calcium carbonate; adsorption; dyes.

Introduction

Shellfish cultivation is an expanding economic activity worldwide. In recent years, people's awareness of marine resources has improved. Shells are often considered as waste, despite their potential valorization as a residual side-stream, and therefore waste shells have aroused great concern. Every year, close to 8 million tons of waste crab, shrimp, and lobster shells are produced globally [1]. Since only about 40 wt% of the total weight of these crustaceans is edible, the crustacean farming and processing industry will produce a large number of waste shells [2]. However, due to the constraints associated to an integrated utilization technology and to unregulate disposal procedures, a large number of shells are directly discarded or deposited as waste with a wide and complex distribution [3]. Shell piles and burials are common near beaches and seafood processing plants. Thereafter, they modify soils, waters, and marine ecosystems, particularly if their disposal is uncontrolled [4, 5]. Moreover, they cause environmental damage by decomposition, emanating foul odours, as well as adding to visual pollution [6].

From the perspective of resource utilization, crustacean shells, such as those from crabs and shrimps, are rich in α-chitin, protein and calcium carbonate ($CaCO_3$) [7]. It is well known that chitin and its derivatives are widely used in the pharmaceutical [8], cosmetic [9], environment and energy industry [10]. $CaCO_3$ is extensively used in the pharmaceutical, agricultural, construction, chemical, and polymer industry [11].

Current processes for crab and shrimp waste shells utilization focus on the extraction of chitin, chitosan [12] or bioactive compounds [13, 3, 5] often via sustainable and environmentally friendly synthetic extraction approaches. Moreover, mostly discard the other residual shell materials, even if they possess potential value [14].

A processing strategy in which all the components of the waste shell are recovered is desirable. A top-down approach has been used to produce calcium carbonate-enriched chitosan from shrimp shell wastes to valorize $CaCO_3$ [15]. Recycling shell waste could potentially eliminate the disposal problem and could also turn an otherwise useless waste into high value–added products. A cascading approach in which compounds of highest value are initially extracted, after which the residual biomass can be used for low end application, can even lead to zero-waste.

Here, we applied chemical and thermal processes that allowed to extract singularly or combined the main different components of crustacean waste shells. We characterize them for their

chemical and physical features and as proof of concept for their valorisation/utilisation we used them as adsorbent of dyes from model polluted waters.

Materials derived from crustacean waste shells have already largely been used for the removal of contaminants from industrial effluents such as heavy metals [16-18], anionic pollutants [19, 20], nitrogen [21] and dyes [22] but in our study, we are able to design new structures composed from shell material but with different properties.

Crab shell and chitosan powder were used to trap water-soluble dyes present in textile dyeing wastewater [23] . Low molecular weight (20 kDa) crab shell chitosan can also significantly reduce chemical oxygen demand, total suspended solids, total dissolved solids, and turbidity in textile mill wastewater [24]. Dai et al. used calcium-rich biochar obtained from crab shell to adsorb the cationic malachite green (12.5 mg g^{-1}) and the anionic Congo red (20.3 mg g^{-1}) dye but in this case a pyrolysis process was necessary to obtain the adsorbent [25]. Chitosan derived from shrimp shells (or peels) was applied as potential bio-adsorbent for Methyl Orange (MO) dye removal from waste water with the maximum adsorption capability of 0.1297 mg g^{-1} [26]. For $CaCO_3$, what is -next to chitin- the other main fraction of the residual shell, single crystals of calcite and aragonite were used to adsorb organic dyes. It was shown that aragonite and calcite have selective adsorption capability [27].

Since each singular component of crustacean shells has a specific adsorption capability, in this research we explore the hypothesis that newly developed material, consisting of multi-component extract can have an adsorption capability that is increased by the synergic action of the single components. To prove this hypothesis the waste shells from the market relevant species Brown shrimp (BS) *Crangon crangon* and the invasive Chinese mitten crab (CMC) *Eriocheir sinensis* were used. They were differently chemically thermally treated and the obtained materials were tested for the adsorption of acidic and basic dyes relevant in the fabric industries.

Materials and methods

Reagents and solvents were purchased from Merck. For each experiment, daily fresh solutions were prepared. The waste shells from Brown shrimp (*Crangon crangon*) and Chinese Mitten Crab (*Eriocheir sinensis*) were obtained from Nieuwpoort and Grobbendonk (Belgium),

respectively. The shells fragments were washed with tap water and dried in an oven overnight at 50 °C.

Deproteinization reaction. A typical reflux setup was used for the deproteinization reaction where 1 g of each sample was put in a round bottom flask together with 40 ml of a 1 M NaOH solution. The NaOH solution was changed every hour and the total reaction time was of 4 hours for the shrimp and 5 hours for the crab shells. The resultant suspensions were filtered under vacuum and the fragments were washed with water until the pH was neutral, then the samples were dried in an oven overnight at 60 °C.

Bleaching reaction. 1 g of each sample was put in a beaker together with 50 ml of a 5 % v/v NaClO solution and stirred on a rocking table for 8 days. The resultant suspensions were filtered under vacuum and the fragments were first washed with water and then dried under vacuum in a desiccator overnight.

Thermal treatment. A certain amount of the bleached material from each species was thermally treated in an oven at 220 °C for 48 hours.

Chitin extraction. In order to extract chitin from the starting material of each species, two steps were needed i. e. a demineralization and a deproteinization process. The first one was performed suspending the waste shells (1 g) in a 1.5 M HCl solution (10 ml) for the shrimp and 2 M (25 ml) for the crab under magnetic stirring at 500 rpm. The reaction time was 2.5 h for the shrimp and 3 h for the crab. The resultant suspensions were filtered under vacuum and the fragments were washed with deionized water until the pH was neutral, and dried in an oven overnight at 65 °C. The obtained fragments were, then, subjected to a deproteinization reaction. 1 g of fragments was suspended in a 1 M NaOH solution (10 ml for the shrimp and 25 ml for the crab) under magnetic stirring at 500 rpm. The reaction time and the experimental temperature were 2 h and 80 °C for the shrimp and 3 h and 90 °C for the crab, respectively. The resultant suspensions were filtered under vacuum and the fragments were washed with deionized water until the pH was neutral, then the samples were dried in an oven overnight at 60 °C.

X-ray powder diffraction analysis. X-ray diffraction patterns were collected using a PanAnalytical X'Pert Pro diffractometer equipped with a multi-array X'Celerator detector using Cu Kα radiation generated at 40 kV and 40 mA ($\lambda = 1.54056$ Å). The diffraction patterns were collected in the 2θ range between 5 ° and 60 ° with a step size ($\Delta 2\theta$) of 0.05 ° and a counting time of 60 s. Each sample was ground with mortar and pestle before the measurement.

Fourier Transform Spectroscopic analysis. A Thermo Scientific™ Nicolet™ iS™10 FTIR Spectrometer was used to collect the FTIR spectra. Disk sample for FTIR analysis was obtained by mixing a small amount (2 mg) of product with 98 mg of KBr and applying a pressure of 45 tsi (620.5 MPa) to the mixture using a press. The spectra were obtained with 4 cm^{-1} resolution and 64 scans.

Thermogravimetrical analysis. Thermogravimetrical analysis (TGA) were performed using a SDT Q600 V 8.0 instrument (TA Instruments). The system was pre-equilibrated at 30 °C, then a ramp from 30 to 900 °C with a 10 °C min^{-1} heating rate was performed under nitrogen flow. The materials were ground with mortar and pestle and the measurement was performed on 20 mg of each sample. The temperature range considered to estimate the organic material content was between 150 °C and 500 °C.

Scanning electron microscopy observation. All SEM images were acquired using a ZEISS Leo 1530 Gemini field emission scanning electron microscope (SEM) operating at 5 kV. All samples were dried under vacuum in a desiccator and gold-coated before their observation.

BET. The specific surface area of the samples was measured by the multiple BET method using a Gemini VII 2390 Series Surface Area Analyzer (Micromeritics Instrument Corporation) with a nitrogen flow. Each sample was dispersed in isopropanol in order to perform the measurement.

Dye adsorption kinetics experiments. Adsorption kinetics experiments were carried out suspending 25 mg of each material in 5 mL of dye in a 50 mM pH 7.2 bis-tris buffer solution. The suspensions were kept in a 15 mL polypropylene conical centrifuge tubes at room temperature under mechanical stirring. Two dyes were tested that are Blue Methylene and Eosin Y both having an absorption maximum in the visible region (668 nm and 517 nm, respectively). The dye concentration in solution was measured by a UV-Vis spectrophotometer (Cary 300 Bio, Agilent Technologies) and the amount of dye adsorbed q_t (mg g^{-1}) at the time t (min) was calculated using the following the Equation (1):

$$q_t = \frac{(C_0 - C_t)V}{m} \quad (1)$$

where C_0 (mg L^{-1}) is the initial dye concentration, C_t (mg L^{-1}) is the dye concentration at time t, V (L) is the volume of the dye solution and m (g) is the mass of the substrate.

For each measurement, the dye solution was centrifuged at 10000 rpm for 90 s and the

supernatant transferred into a plastic cuvette with 1 cm optical path. The spectra were recorded after 30 minutes, 1 h, 2 h, 4 h and 24 h using a spectral range of 450-800 nm.

Dye adsorption isotherm experiments. Adsorption isotherm experiments were carried out using the same procedure of the adsorption kinetics experiments. Different dye concentrations were tested that are 0.005, 0.0075, 0.01, 0.025 and 0.05 mM. Three isotherm models were tested i. e. the Langmuir isotherm (Eq. (2)), the Freundlich isotherm (Eq. (3)) and the Dubinin-Radushkevich isotherm (Eq. (4)):

$$\frac{1}{q_e} = \frac{1}{Q_{MAX} K_L C_e} + \frac{1}{Q_{MAX}} \tag{2}$$

$$log q_e = log K_F + \frac{1}{n} log C_e \tag{3}$$

$$ln q_e = ln Q_{MAX} - K_D \varepsilon^2 \tag{4}$$

Where q_e (mg g^{-1}) is the amount of dye adsorbed at equilibrium, Q_{MAX} (mg g^{-1}) is the maximum adsorption capacity from the adsorption models, C_e (mg L^{-1}) is the concentration of the adsorbate at equilibrium, K_L (mg^{-1}) is the Langmuir constant, n is a constant representing the favorable degree of adsorption, K_F (mg g^{-1}) is the Freundlich constant, K_D (mol^2 kJ^{-2}) is the Dubinin-Radushkevich constant and ε (J mol^{-1}) is the Polanyi potential calculated as follow:

$$\varepsilon = RT ln(1 + \frac{1}{C_e}) \tag{5}$$

Where R (J mol^{-1} K^{-1}) is the gas constant and T (K) is the experimental temperature.

Results and discussion

Material's properties

An initial characterization of shell fragments from the two species, BS and CMC, was performed after washing with deionized water and drying in an oven overnight at 50 °C (Fig. 1A and B).

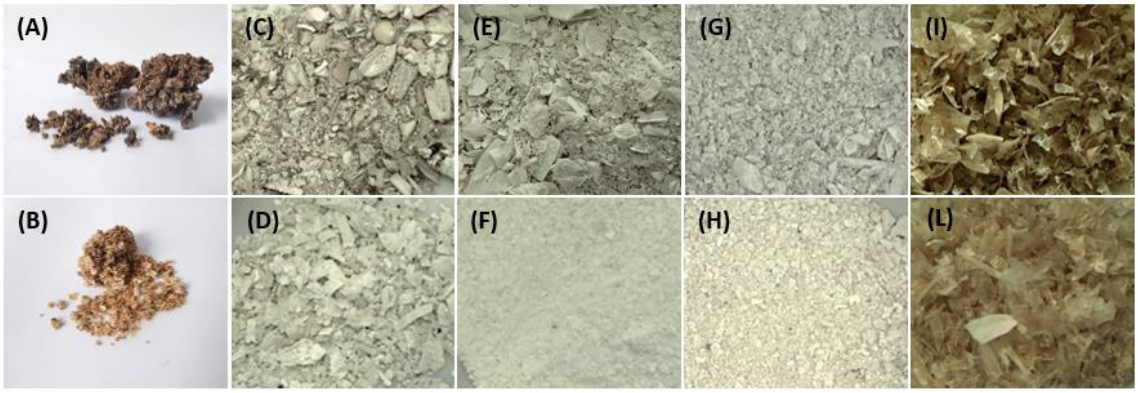

Figure 1. Camera images of CMC and BS raw material (A, B) and deproteinized (C, D), bleached (E, F), bleached/heated (G, H) ones, and chitin (I, L).

The analyses of the X-ray diffraction patterns and the FTIR spectra (Fig. 2) revealed the presence of proteins and crystalline material made of α-chitin and calcite in the carapaces of both species. This was indicated by the occurrence of the characteristic diffraction peaks (020) and (110) of α-chitin at 2theta angles of 9 and 19 °, respectively, while calcite appeared from the diffraction peaks (012), (104), and (013) at 23, 29, and 39 ° respectively. The vibrational adsorption bands due to chitin and proteins at 3400 cm^{-1}, 3100 cm^{-1} and 1700 cm^{-1} corresponding to the O-H stretching, aliphatic compound and the CH_3 stretching, and amide I stretching of C=O group, respectively, and to calcite at 1800 cm^{-1}, 1410 cm^{-1}, 875 cm^{-1} and 712 cm^{-1}, were detected. In addition to these signals, in BS shells but not in CMC shells, the diffraction pattern showed diffraction peaks at 2theta value of 27, 33 and 44 ° and the FTIR spectrum adsorption band at 744 cm^{-1}, both of which indicating the presence of vaterite. This phase represented the 45 wt% of crystalline minerals in BS shells.

Vaterite has been found to form in shrimp shells during frozen storage, specifically in the pink shrimp, *Pandalus borealis*. The white spots, made of calcite and vaterite, increase in size and eventually cover the entire shell, which was originally transparent. It has been suggested that α-chitin is crucial in the crystallization process of these white spots, as it is a key component of

their composition [28]. Vaterite has been reported to form at relatively low temperatures in wet conditions from amorphous calcium carbonate (ACC) [29] , suggesting that vaterite formed from ACC in BS.

No vaterite formation was found in CMC shells, indicating that there may not be significant amounts of ACC present in the original material.

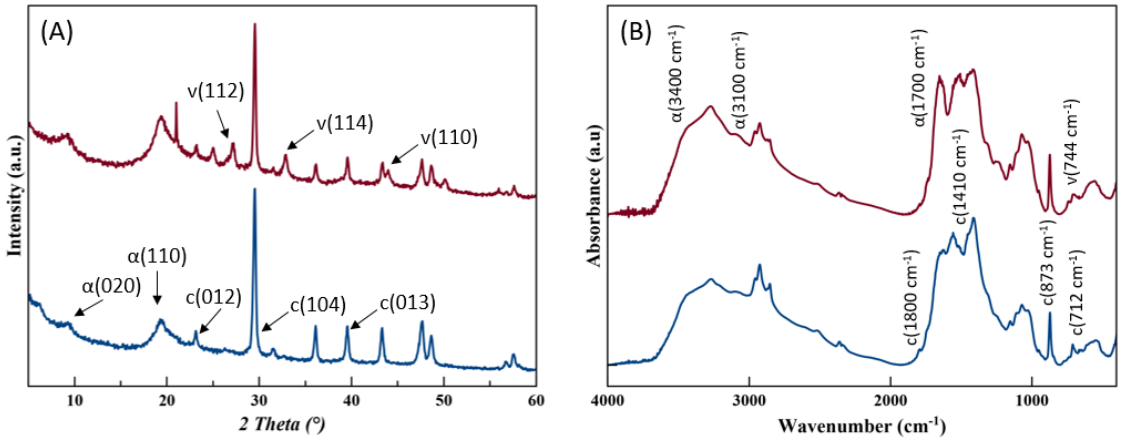

Figure 2. X-ray powder diffraction patterns (A) and FTIR spectra (B) of CMC (blue) and BS (red) waste shells. The diffraction patterns were indexed accordingly to the PDF 00-005-0586 for calcite, PDF 00-024-0030 for vaterite and PDF 00-035-1974 for α-chitin.

The shells' organic material content was evaluated using thermo-gravimetrical analysis (TGA). The analyses of the thermal profiles (Fig. 3) revealed that BS shells have a higher content of water and organic material (61.46 wt%) than the CMC ones (47.50 wt%). The relative content of protein and chitin was not estimated at this stage.

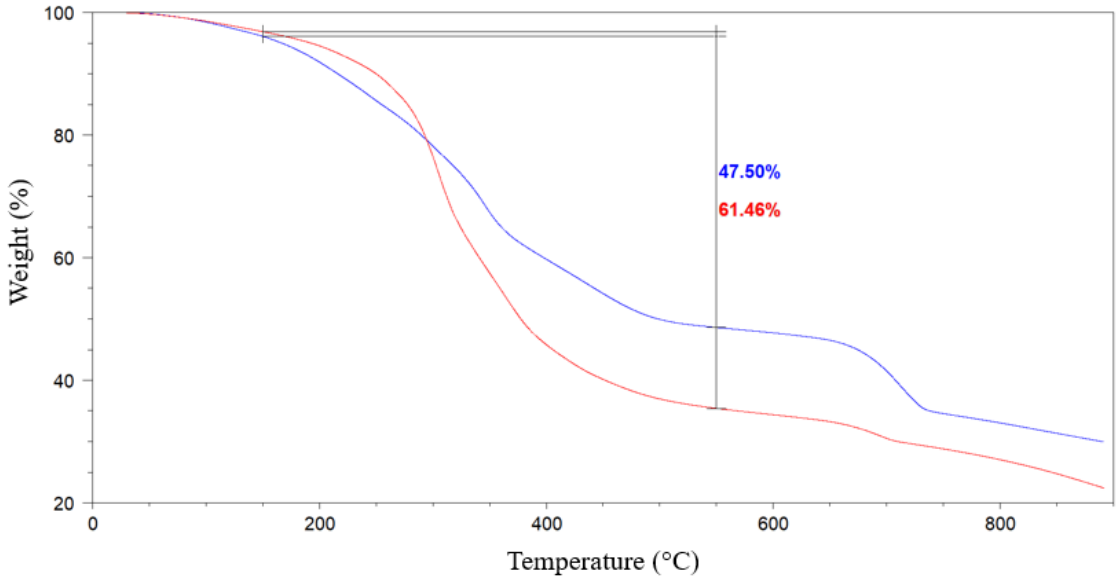

Figure 3. Thermogravimetrical analysis (TGA) profiles of CMC (blue) and BS (red) raw material. The temperature range considered to estimate the organic material content was between 150 °C and 550 °C.

After characterizing the raw material, different chemical treatments were performed: (i) deproteinization using a reflux reaction with 1 M sodium hydroxide solution at 100 °C; (ii) bleaching using a 5 % v/v sodium hypochlorite solution for 8 days to remove organic material, such as proteins, chitin and lipids; (iii) bleaching followed by thermal treatment in the oven at 220 °C for 48 hours to also remove intra-crystalline organic material; (iv) demineralization using hydrochloric acid to dissolve $CaCO_3$, followed by deproteinization to extract chitin from the shells [30].

An interesting finding from the analysis of the materials extracted from the BS shells was the detection of vaterite following the deproteinization process and the application of heat. This was evidenced by the appearance of distinct peaks in the X-ray diffraction patterns (Fig. 4C), which supports our earlier observation from the FTIR analysis of the unprocessed material. This supports the previous finding that vaterite is stabilized by α-chitin [28, 31].

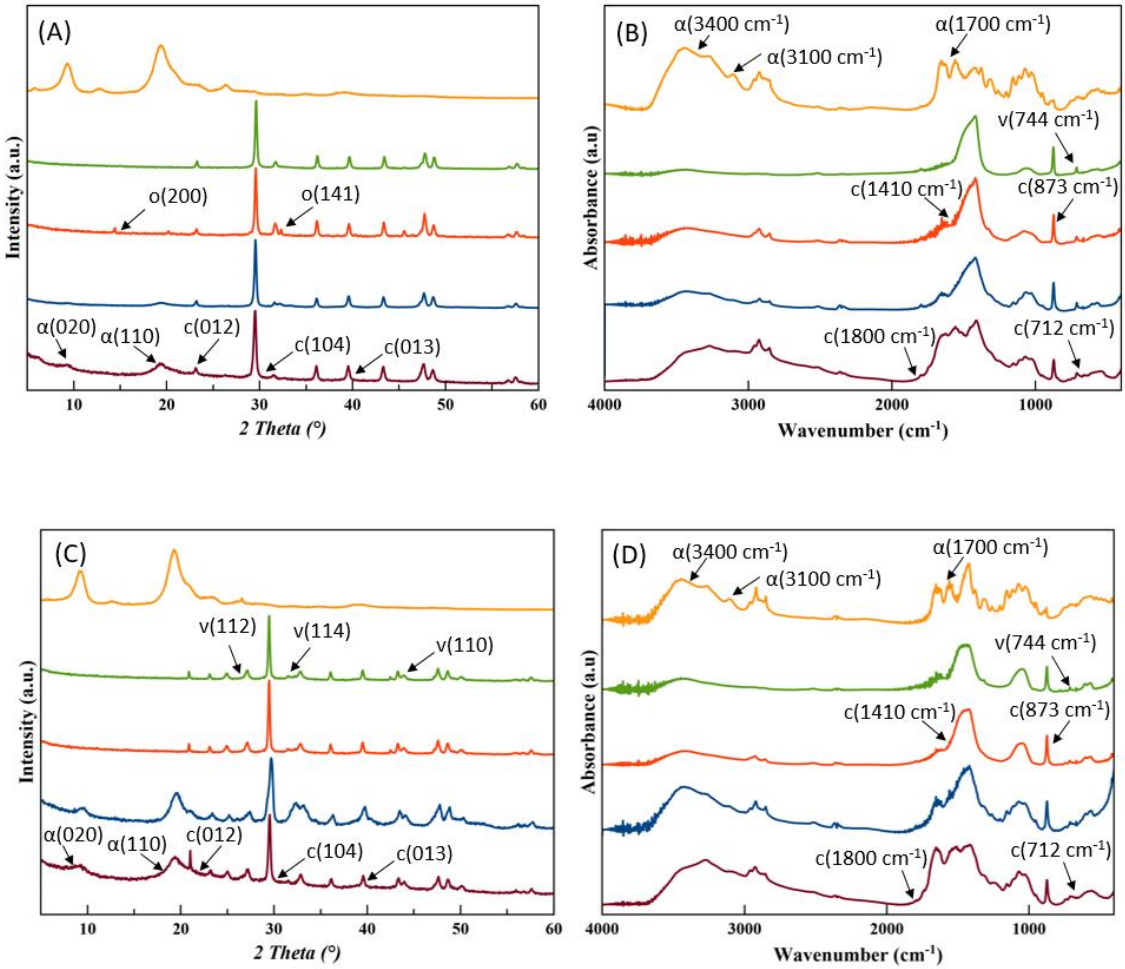

Figure 4. X-ray powder diffraction patterns and FTIR spectra of CMC (A, B) and BS (C, D), respectively, raw material (red), deproteinized (blue), bleached (orange) and bleached/heated (green) one, and chitin (yellow). The diffraction patterns were indexed accordingly to the PDF 00-005-0586 for calcite, PDF 00-024-0030 for vaterite, PDF 00-035-1974 for α-chitin and PDF 01-087-0655 for calcium oxalate.

The FTIR spectra analysis revealed a decrease in protein content in both shell types following alkaline and bleaching treatments, as evidenced by the disappearance of the band at approximately 1600 cm^{-1} corresponding to the N-H bending of the peptide group and an increase in the relative intensities of the vibrational bands associated with $CaCO_3$ (Fig. 4B and 4D). Additionally, thermogravimetrical analysis indicated a decrease in the weight loss associated with the pyrolysis of the organic material after these treatments (Fig. 5 and 6).

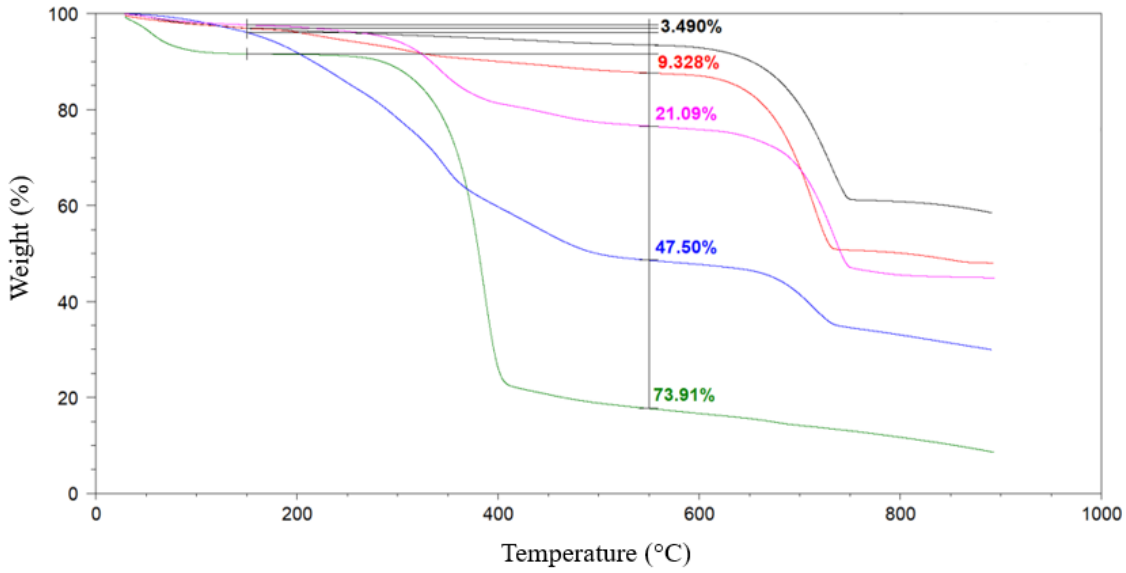

Figure 5. Thermogravimetrical analysis (TGA) profiles of CMC raw material (blue) and deproteinized (pink), bleached (red), bleached/heated (black) ones, and chitin (green). The temperature range considered to estimate the organic material content was between 150 °C and 550 °C.

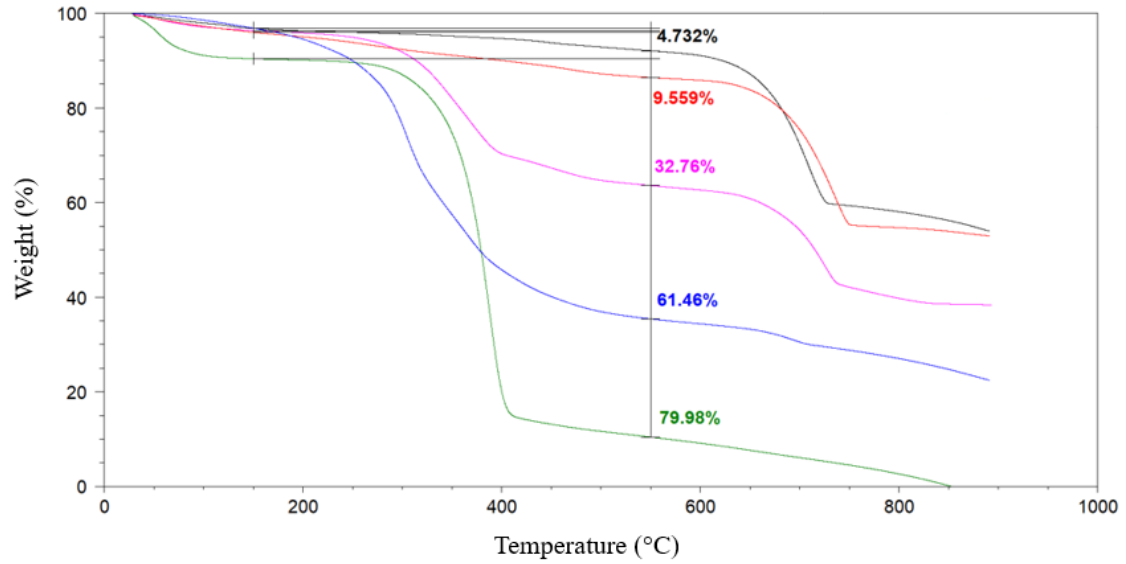

Figure 6. Thermogravimetrical analysis (TGA) profiles of BS raw material (blue) and deproteinized (pink), bleached (red), bleached/heated (black) ones, and chitin (green). The temperature range considered to estimate the organic material content was between 150 °C and 550 °C.

After alkaline treatment the remaining material was 32.76 wt% for shrimp and 21.09 wt% for crab (Table 1), indicating that in the BS shells there is about 29 wt% of proteic material, while in the CMC ones it is about 26 wt%. After the bleaching treatment, the weight loss was 9.56 wt% for the shrimp and 9.32 wt% for the crab. After the bleaching and thermal processes, the

organic material content was lower than in the only bleached sample and it was 4.73 wt% for the shrimp and 3.49 wt% for the crab. These results indicated that chitin was not totally removed in the bleached and the bleached/heated materials, as was also indicated by the vibrational bands from chitin observed in the FTIR spectra (Fig. 4B and 4D). The X-ray diffraction pattern data, however, did not reveal any peak linked to α-chitin, indicating that it may be present in the sample in a quantity too low to be detected by X-ray diffraction or in an amorphous state. Additionally, in the bleached crab diffraction pattern (Fig. 4A), additional diffraction peaks at approximately 14 and 32 °, which are linked to calcium oxalate, were observed. This is a by-product resulting from the chitin oxidation reaction [32].

Table 1. Main shellfish components (prot. = proteins; chit. = chitin; $CaCO_3$ = calcium carbonate), mineral phase and specific surface area (SSA) of CMC and BS raw material (A) and deproteinized (B), bleached (C), bleached/heated (D) ones, and chitin (E).

Sample	Main components	Crab			Shrimp		
		Mass (wt%)	**Mineral Phase*** (wt%)	**SSA** (m^2 g^{-1})	**Mass** (wt%)	**Mineral Phase** (wt%)	**SSA** (m^2 g^{-1})
A	prot. chit. $CaCO_3$	26.41 21.09 52.50	cal.[§]	ND[#]	28.70 32.76 38.54	cal. (55.60) vat.[$] (44.40)	ND[#]
B	chit. $CaCO_3$	21.09 78.91	cal.	27.64	32.76 67.24	cal. (65.70) vat. (34.30)	11.24
C	chit. $CaCO_3$	9.32 90.68	cal. (97.61) CaOx. (2.39)[&]	12.71	9.56 90.44	cal. (55.91) vat. (44.09)	20.22
D	chit. $CaCO_3$	3.49 96.51	cal.	27.93	4.73 95.27	cal. (56.32) vat. (43.68)	48.97
E	chit.	100.00	-	ND[#]	100.00	-	ND[#]

[#] an accurate determination of the specific surface area was not possible. [*] When not indicated the wt% only one mineral phase is present. [§] cal. indicates calcite. [&]CaOx indicates calcium oxalate. [$] vat. indicates vaterite.

In the last step, after the demineralization and deproteinization processes, only the peaks relatives to α-chitin were present in the diffraction patterns, confirming that $CaCO_3$ had been completely removed (Fig. 4A e 4C). The weight loss associated to the organic material in both

species increased and it was 79.98 wt% for shrimp and 73.91 wt% for crab, in agreement with the removal of $CaCO_3$ (Table 1).

The BET technique was used to investigate the specific surface area of the material. This method involves creating a N_2 monolayer on the surface of the sample being studied. This can be challenging to accomplish when the material has a complex morphology and mixed surface chemistry due to its inorganic/organic hybrid composition and high chitin content [33]. For these reasons, it is challenging to explain the specific surface area obtained from the BET measurements (Table 1). Nevertheless, they can be valuable for comparing samples that underwent the same treatment. The samples after bleaching and after bleaching/heating processes have a similar amount of organic material, with the remaining being calcium carbonate. In this instance, the surface area of the shrimp sample is greater than that of the crab. This difference may be linked to the presence of vaterite in the shrimp-derived material, which has a higher surface area than calcite for particles having similar size [34].

The surface area of the chitin material extracted from shrimps and crabs has been reported to be about 3 and 3.6 $m^2\ g^{-1}$, respectively [35]. However, these substrates showed much higher surface area than the ones here presented, when this was calculated considering the capability to absorb dyes [33, 36].

The surface morphology of CMC and BM shells pristine and derived materials was investigated by SEM (Fig. 7 and 8). In a general overview, all the samples were heterogenous and with very complex morphology. The two species show a different texture and organization of the shell fibers and grains, which change after the different chemical-thermal processes. Prior each treatment, the shrimp shell surface (Fig. 8A) shows an ordered fibrous microstructure with chitin fibre embedded in a framework of organic material forming a compact matrix, which is the scaffold where calcium carbonate is located. This structural organization is also observed in the crab pristine cuticle but in this case the organization of chitin fibers result in a porous texture (Fig. 7A). After the deproteinization reaction, the shell structure becomes more disordered and less compact in both species, probably due to the removal of proteins which may act as a fixative for chitin fibers and $CaCO_3$ particles (Fig. 7B and 8B). For the same reason, chitin extracted from both species looks rough and highly exfoliated (Fig. 7E and 8E). After the bleaching processes, the main observable component of the matrix shell is the mineral phase, confirming the reduction of chitin content upon treatments. This is very evident in the crab shell bleached/heated materials where calcite crystals can be observed (Fig. 7D).

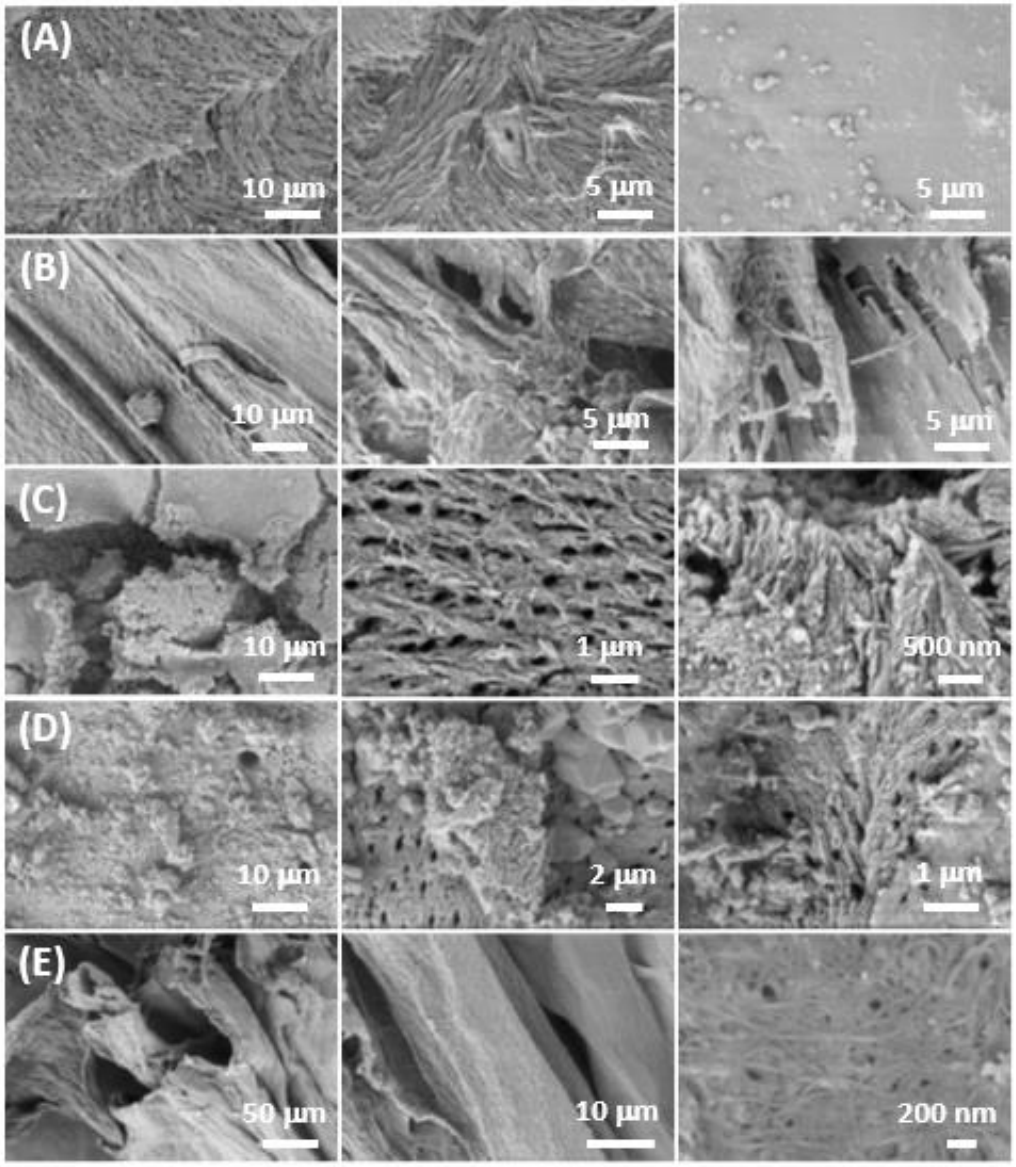

Figure 7. SEM images of CMC raw material (A) and deproteinized (B), bleached (C), bleached/heated (D)ones, and chitin (E).

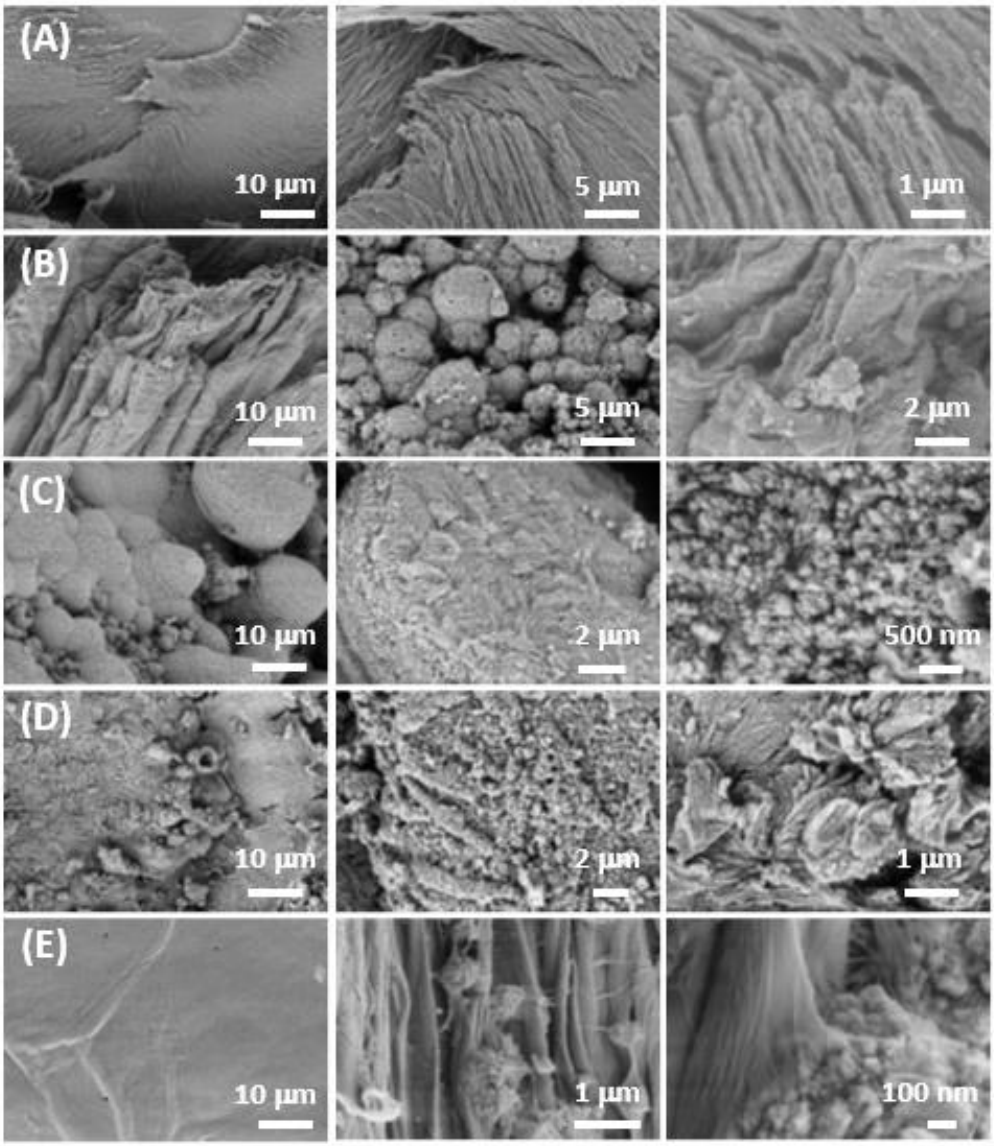

Figure 8. SEM images of BS raw material (A) and deproteinized (B), bleached (C), bleached/heated (D) ones, and chitin (E).

The potential use of all the materials obtained from CMC and BS waste shells was tested in water remediation, in accordance with literature and showing that these low-cost adsorbents have a high capacity for removing specific dyes [37, 38].

Dye adsorption properties

All substrates derived from CMC and BS were examined for their ability to adsorb two common model dyes used in the textile industry: Eosin Y (EY), an anionic dye, and Blue Methylene (BM), a cationic dye. The tests were conducted in a 50 mM pH 7.2 bis-tris buffer solution at a concentration of 0.01 mM, which is both environmentally and industrially significant. The adsorption of both dyes on all the substrates reached equilibrium within 24 h (Fig. 9). Table 2

summarizes the maximum adsorption capacity of the different materials of both dyes, after adsorption kinetics experiments.

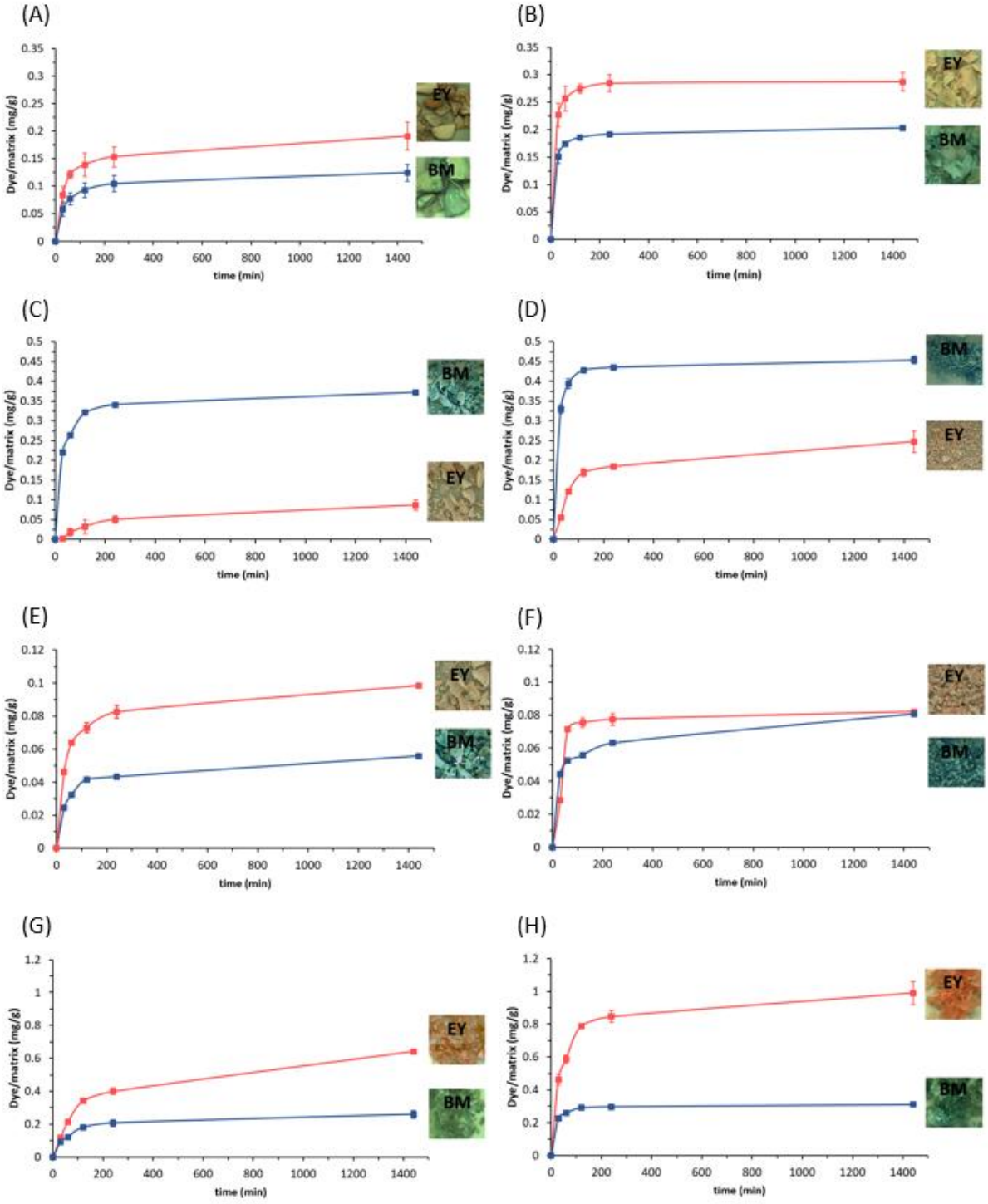

Figure 9. Adsorption kinetics and camera images of BM (blue dots) and EY (red dots) solutions at pH 7.2 on CMC and BS deproteinized (A, B), bleached (C, D), bleached/heated (E, F) shells, and chitin (G, H). The dye adsorbed is reported as the mass of dye (mg), normalized over the mass of substrate (g).

Table 2. Maximum adsorption capacity (q_{MAX}) from the adsorption kinetics experiments of CMC and BS deproteinized (A), bleached (B), bleached/heated (C) shells, and chitin (D) in Blue Methylene (BM) and Eosin Y (EY) 0.01 mM solutions at pH 7.2. The dye adsorbed is reported as the mass of dye (mg) over the mass of substrate (g).

Sample	Crab		Shrimp	
	q_{MAX} BM (mg g^{-1})	q_{MAX} EY (mg g^{-1})	q_{MAX} BM (mg g^{-1})	q_{MAX} EY (mg g^{-1})
A	0.12 ± 0.01	0.19 ± 0.02	0.203 ± 0.003	0.29 ± 0.02
B	0.372 ± 0.001	0.09 ± 0.01	0.454 ± 0.009	0.25 ± 0.03
C	0.0985 ± 0.0007	0.0557 ± 0.0003	0.0809 ± 0.0002	0.0821 ± 0.0006
D	0.26 ± 0.02	0.641 ± 0.005	0.310 ± 0.005	0.99 ± 0.07

Overall, materials obtained from shrimp generally exhibited a greater ability to adsorb both dyes compared to those from CMC. The only exception was the bleached/heated material, which had a higher adsorption capacity for BM on CMC, although the amount absorbed was low and near the limit of detection. Notably, all substrates showed a higher adsorption capacity for EY, except for the bleached ones. These findings indicate that the bleached materials undergo a change in surface chemistry after thermal treatment, leading to the replacement of some carbonate groups with hydroxyl groups in the coordination of calcium ions [39]. When adsorbing BM and EY, the maximum adsorption capacity was exhibited by the shrimp bleached material (0.45 mg g^{-1}) and chitin (0.99 mg g^{-1}), respectively, while the minimum one by the shrimp bleached/heated material (0.081 mg g^{-1}) and the crab bleached/heated ones (0.056 mg g^{-1}), respectively. These results align with the aforementioned considerations on the specific surface of chitin materials and the data reported in Table 1.

To assess the adsorption kinetics mechanism, an analysis of isotherm models was conducted. The experimental data were fitted with: (i) the Langmuir isotherm, which assumes a uniform surface of the substrate and an adsorption mechanism controlled by chemical processes leading to monolayer formation; (ii) the Freundlich isotherm, which assumes a non-uniform surface of the substrates, an adsorption mechanism controlled by physical processes, and the formation of multiple layers; (iii) the Dubinin-Radushkevich isotherm, which is similar to the Freundlich model but takes into account microporous surfaces [40]. In Tables 3 and 4 the calculated parameters from the best fitting of the adsorption isotherms for the substrates in BM and EY, respectively, are reported.

Table 3. Calculated parameters from the best fitting of the adsorption isotherms with different models of CMC and BS deproteinized (A, B), bleached (C, D), bleached/heated (E, F) shells, and chitin (G, H) in Blue Methylene.

Sample	Model	R^2	n	K*	Q_{MAX} (mg g^{-1})
A	Freundlich	0.9934	1.0305	0.0545	/
B	Freundlich	0.9729	1.1050	0.0770	/
C	Dub. - Radush.	0.9193	/	1.4329	0.5430
D	Freundlich	0.9799	1.2054	0.1337	/
E	Freundlich	0.863	3.1387	0.04151	/
F	Freundlich	0.9318	2.6954	0.0458	/
G	Freundlich	0.9484	1.0113	0.0494	/
H	Freundlich	0.9988	0.9505	0.0851	/

*The unit of measure for the parameter K is mg^{-1} for the Langmuir model, mg g^{-1} for the Freundlich and mol^2 kJ^{-2} for the Dubinin-Radushkevich one.

The adsorption data best fit with a Freundlich isotherm, indicating no site-specific interaction and the formation of multilayers. This result is consistent with the complex morphology of the substrates, which have a heterogeneous surface, as shown by SEM observations. (Fig. 7 and 8).

Table 4. Calculated parameters from the best fitting of the adsorption isotherms with different models of CMC and BS deproteinized (A, B), bleached (C, D), bleached/heated (E, F) shells, and chitin (G, H) in Eosin Y.

Sample	Model	R^2	n	K*	Q_{MAX} (mg g^{-1})
A	Freundlich	0.9631	0.9281	0.0245	/
B	Freundlich	0.913	1.0825	0.0591	/
C	Langmuir	0.9129	/	0.0618	0.2750
D	Langmuir	0.6308	/	0.1330	0.2975
E	Freundlich	0.9535	0.9265	0.0085	/
F	Freundlich	0.9524	0.9366	0.0114	/
G	Freundlich	0.9679	0.9800	0.0293	/
H	Freundlich	0.9342	1.2992	0.1531	/

*The unit of measure for the parameter K is mg^{-1} for the Langmuir model, mg g^{-1} for the Freundlich and mol^2 kJ^{-2} for the Dubinin-Radushkevich one.

Conclusions

This work has shown that it is possible to obtain multifunctional materials with different characteristics, such as composition, shape, and morphology, from shrimp and crab shells. Our approach is innovative because we demonstrate the sequential study of the various processes that allows for the isolation of the components of the shells, whose characteristics depend on the species. As a case study, among the many applications of chitin and calcium carbonate, we decided to evaluate the ability of the different substrates to act as absorbent agents for dyes from polluted waters, which is relevant in an industrial area. The results show that materials obtained from shrimp shells have a higher absorbent capacity than those obtained from crab shells. It is important to highlight that the processes adopted to obtain the various materials can be scaled on an industrial level, offering a long-term vision for the application of this experimental strategy for the development of technology for the treatment of these residual bioresources.

Author Contributions

CT performed the deproteinization and the bleaching reaction, the thermal treatment, the chitin extraction, the X-ray powder diffraction analysis, the spectroscopic analysis, the thermogravimetrical analysis, the dye adsorption kinetics and the dye adsorption isotherm experiments. CT also contributed to the writing of this manuscript.

References

[1] Yan, N., & Chen, X. (2015). Sustainability: Don't waste seafood waste. *Nature*, *524*(7564), 155–157.

[2] Morris, J. P., Backeljau, T., & Chapelle, G. (2019). Shells from aquaculture: a valuable biomaterial, not a nuisance waste product. *Reviews in Aquaculture*, *11*, 42–57.

[3] Zou, Y., Heyndrickx, M., Debode, J., Raes, K., de Pascale, D., Behan, P., Giltrap, M., O'Connor, C., Solstad, R. G., Lian, K., Altintzoglou, T., Dragoy, R., Scheers, N., Underland, I., & Robbens, J. (2023). Valorisation of crustacean and bivalve processing side streams for industrial fast time-to-market products: A review from the European Union regulation perspective. *Frontiers in Marine Science*, *10*, 1068151.

[4] Topić Popović, N., Lorencin, V., Strunjak-Perović, I., & Čož-Rakovac, R. (2023). Shell Waste Management and Utilization: Mitigating Organic Pollution and Enhancing

Sustainability. *Applied Sciences (Switzerland)*, *13*(1).

[5] Zou, Y., Robbens, J., Heyndrickx, M., Debode, J., & Raes, K. (2021). Bioprocessing of marine crustacean side-streams into bioactives: a review. *Journal of Chemical Technology & Biotechnology*, *96*(6), 1465–1474.

[6] Cardoso, A. da S., Rabbani, E. R. K., Delmiro, T. D., Mocock, J. F. B., Silva, S. P. R. da, Filippelli, G., Macedo, J. V. da S., & Monteiro, E. C. B. (2023). Mollusk shell waste: alternatives for reuse in construction. *International Journal of Environment and Waste Management*, *31*(1), 61–80.

[7] Nagasawa, H. (2012). The crustacean cuticle: Structure, composition and mineralization. *Frontiers in Bioscience (Elite Edition)*, *4*, 711–720. https://doi.org/10.2741/E412

[8] Kato, Y., Onishi, H., & Machida, Y. (2003). Application of chitin and chitosan derivatives in the pharmaceutical field. *Current Pharmaceutical Biotechnology*, *4*(5), 303–309.

[9] Aranaz, I., Acosta, N., Civera, C., Elorza, B., Mingo, J., Castro, C., Gandía, M. D. L. L., & Heras Caballero, A. (2018). Cosmetics and cosmeceutical applications of chitin, chitosan and their derivatives. *Polymers*, *10*(2), 213.

[10] Peter, S., Lyczko, N., Gopakumar, D., Maria, H. J., Nzihou, A., & Thomas, S. (2021). Chitin and chitosan based composites for energy and environmental applications: a review. *Waste and Biomass Valorization*, *12*, 4777–4804.

[11] Niu, Y.-Q., Liu, J.-H., Aymonier, C., Fermani, S., Kralj, D., Falini, G., & Zhou, C.-H. (2022). Calcium carbonate: controlled synthesis, surface functionalization, and nanostructured materials. *Chemical Society Reviews*, *51*, 7883–7943.

[12] Sreeja, S. J., Tamilarutselvi, K., Tamilselvi, A., Sarojini, K. P., Jasmin, K. J., & Malini, M. M. (2023). Production of chitin and conversion into chitosan from crab (Scylla tranquebarica) shells and evaluation of its antioxidant activities. *Biomass Conversion and Biorefinery*. https://doi.org/10.1007/s13399-023-03776-y

[13] Ambigaipalan, P., & Shahidi, F. (2017). Bioactive peptides from shrimp shell processing discards: Antioxidant and biological activities. *Journal of Functional Foods*, *34*, 7–17.

[14] Mathew, G. M., Mathew, D. C., Sukumaran, R. K., Sindhu, R., Huang, C.-C., Binod, P., Sirohi, R., Kim, S.-H., & Pandey, A. (2020). Sustainable and eco-friendly strategies for

shrimp shell valorization. *Environmental Pollution*, *267*, 115656.

[15] Miron, A., Sarbu, A., Zaharia, A., Sandu, T., Iovu, H., Fierascu, R. C., Neagu, A.-L., Chiriac, A.-L., & Iordache, T.-V. (2022). A Top-Down Procedure for Synthesizing Calcium Carbonate-Enriched Chitosan from Shrimp Shell Wastes. *Gels*, *8*(11), 742.

[16] Anastopoulos, I., Bhatnagar, A., Bikiaris, D. N., & Kyzas, G. Z. (2017). Chitin adsorbents for toxic metals: a review. *International Journal of Molecular Sciences*, *18*(1), 114.

[17] Kim, D. S. (2004). Pb2+ removal from aqueous solution using crab shell treated by acid and alkali. *Bioresource Technology*, *94*(3), 345–348.

[18] Wang, J., & Chen, C. (2014). Chitosan-based biosorbents: modification and application for biosorption of heavy metals and radionuclides. *Bioresource Technology*, *160*, 129–141.

[19] Ahmed, M. J., Hameed, B. H., & Hummadi, E. H. (2020). Review on recent progress in chitosan/chitin-carbonaceous material composites for the adsorption of water pollutants. *Carbohydrate Polymers*, *247*, 116690.

[20] Jeon, D. J., & Yeom, S. H. (2009). Recycling wasted biomaterial, crab shells, as an adsorbent for the removal of high concentration of phosphate. *Bioresource Technology*, *100*(9), 2646–2649.

[21] Robinson-Lora, M. A., & Brennan, R. A. (2009). The use of crab-shell chitin for biological denitrification: batch and column tests. *Bioresource Technology*, *100*(2), 534–541.

[22] Sirajudheen, P., Poovathumkuzhi, N. C., Vigneshwaran, S., Chelaveettil, B. M., & Meenakshi, S. (2021). Applications of chitin and chitosan based biomaterials for the adsorptive removal of textile dyes from water — A comprehensive review. *Carbohydrate Polymers*, *273*, 118604.

[23] Sye, W. F., Lu, L. C., Tai, J. W., & Wang, C. I. (2008). Applications of chitosan beads and porous crab shell powder combined with solid-phase microextraction for detection and the removal of colour from textile wastewater. *Carbohydrate Polymers*, *72*(3), 550–556.

[24] Geetha Devi, M., Dumaran, J. J., & Feroz, S. (2012). Dairy wastewater treatment using low molecular weight crab shell chitosan. *Journal of The Institution of Engineers (India): Series E*, *93*, 9–14.

[25] Dai, L., Zhu, W., He, L., Tan, F., Zhu, N., Zhou, Q., He, M., & Hu, G. (2018). Calcium-

rich biochar from crab shell: An unexpected super adsorbent for dye removal. *Bioresource Technology*, *267*, 510–516.

[26] Meriatna, M., Utari, S. M., Mulyawan, R., Muhammad, M., & Zulmiardi, Z. (2023). Methyl Orange Absorption Using Chitosan from Shrimp Skin as an Adsorbent. *International Journal of Engineering, Science and Information Technology*, *3*(2), 25–30.

[27] Triunfo, C., Gartner, S., Marchini, C., Fermani, S., Maoloni, G., Goffredo, S., Gomez Morales, J., Cölfen, H., & Falini, G. (2022). Recovering and Exploiting Aragonite and Calcite Single Crystals with Biologically Controlled Shapes from Mussel Shells. *ACS Omega*, *7*(48), 43992–43999.

[28] Mikkelsen, A., Engelsen, S. B., Hansen, H. C. B., Larsen, O., & Skibsted, L. H. (1997). Calcium carbonate crystallization in the α-chitin matrix of the shell of pink shrimp, Pandalus borealis, during frozen storage. *Journal of Crystal Growth*, *177*(1–2), 125–134.

[29] Ogino, T., Suzuki, T., & Sawada, K. (1987). The formation and transformation mechanism of calcium carbonate in water. *Geochimica et Cosmochimica Acta*, *51*(10), 2757–2767. https://doi.org/https://doi.org/10.1016/0016-7037(87)90155-4

[30] Vandecasteele, B., Amery, F., Ommeslag, S., Vanhoutte, K., Visser, R., Robbens, J., De Tender, C., & Debode, J. (2021). Chemically versus thermally processed brown shrimp shells or Chinese mitten crab as a source of chitin, nutrients or salts and as microbial stimulant in soilless strawberry cultivation. *Science of The Total Environment*, *771*, 145263.

[31] Falini, G., Fermani, S., & Ripamonti, A. (2002). Crystallization of calcium carbonate salts into beta-chitin scaffold. *Journal of Inorganic Biochemistry*, *91*(3), 475–480.

[32] Queiroz, M. F., Melo, K. R. T., Sabry, D. A., Sassaki, G. L., Rocha, H. A. O., & Costa, L. S. (2019). Gallic acid-chitosan conjugate inhibits the formation of calcium oxalate crystals. *Molecules*, *24*(11), 2074.

[33] Akkaya, G., Uzun, I., & Güzel, F. (2007). Kinetics of the adsorption of reactive dyes by chitin. *Dyes and Pigments*, *73*(2), 168–177.

[34] Sasamoto, R., Kanda, Y., & Yamanaka, S. (2022). $CaCO_3$ vaterite microparticles for biomedical and personal care applications. *Chemosphere*, *297*, 134057.

[35] Jaafarzadeh, N., Mengelizadeh, N., Takdastan, A., Heidari-Farsani, M., & Niknam, N. (2014). Adsorption of Zn (II) from aqueous solution by using chitin extraction from crustaceous shell. *Journal of Advances in Environmental Health Research*, *2*(2), 110–119.

[36] Fabbricino, M., & Pontoni, L. (2016). Use of non-treated shrimp-shells for textile dye removal from wastewater. *Journal of Environmental Chemical Engineering*, *4*(4), 4100–4106.

[37] Crini, G. (2006). Non-conventional low-cost adsorbents for dye removal: a review. *Bioresource Technology*, *97*(9), 1061–1085.

[38] Fomina, M., & Gadd, G. M. (2014). Biosorption: current perspectives on concept, definition and application. *Bioresource Technology*, *160*, 3–14.

[39] Ban, M., Luxbacher, T., Lützenkirchen, J., Viani, A., Bianchi, S., Hradil, K., Rohatsch, A., & Castelvetro, V. (2021). Evolution of calcite surfaces upon thermal decomposition, characterized by electrokinetics, in-situ XRD, and SEM. *Colloids and Surfaces A: Physicochemical and Engineering Aspects*, *624*, 126761.

[40] Majd, M. M., Kordzadeh-Kermani, V., Ghalandari, V., Askari, A., & Sillanpää, M. (2022). Adsorption isotherm models: A comprehensive and systematic review (2010− 2020). *Science of The Total Environment*, *812*, 151334.

Chapter 7. General conclusions and future perspectives

The fishery industry and marine aquaculture produce millions of tonnes of waste by-products every year. The global fish production in 2023, in fact, reached 186 million tonnes and the 70 wt% of the processed seafood is discharged as wastes. These wastes represent an environmental and an economical issue since their disposal involves the use of incineration or burial while in developing countries they are often just dumped in the landfill or the sea causing damages to the ecosystem and people living in proximity. On the other hand, they also harbour useful chemicals such as calcium carbonate, proteins and chitin.

In this context, the aim of my thesis was applying the circular economy concepts to marine organism wastes from different species by recovering and valorising biomaterials, investigating their physical-chemical characteristics, and testing their potential applications in different fields.

The first project showed an alternative to many synthetic strategies aiming to control the shape and morphology of single crystals produced in laboratory replicating the ability of organisms to act as crystal shapers and morphology modifiers. In this work single crystals of calcite and aragonite with a biologically controlled shape and morphology were obtained from waste mussel shells by simple and sustainable chemical and mechanical treatments. The obtained single crystals showed peculiar properties with respect to the calcium carbonate from quarry or synthesis and, due to their unique and no lab reproducible aspect ratio, could be used as substrates for reversible dye removal. Future researches could explore other potential applications of these crystals as filler to improve mechanical properties of matrices or as part of optical devices.

The second project demonstrated that biogenic calcium carbonate from oysters, clams and scallops waste seashells can be successfully coated with an aqueous dispersion of sodium stearate and that the adsorption process is similar to that already reported for synthetic and geogenic calcite but it could adsorb a higher amount of stearate compared to them. Due to the huge amount of waste shells produced worldwide from aquaculture and the consequent massive source of calcium carbonate derived from them, this work finds potential industrial applications. So, the coated oyster powder was tested at large scale as filler in an ethylene vinyl acetate compound used for the preparation of shoe soles and improved the mechanical properties with respect to a control using commercial stearate coated calcium carbonate. Consequently, biogenic calcium carbonate can replace ground and precipitated calcium carbonate, has a higher stearate adsorbing capability, and represents an environmentally friendly and sustainable source of calcium carbonate. To continue this work, other mollusk

species could be tested to verify if the stearate adsorption process is species-specific.

The third project investigated the transformation of biogenic calcium carbonate particles (bCCP) from oyster shell waste into hydroxyapatite (HA) micro/nanoparticles using a one-step hydrothermal process. The most of the methods reported in the literature so far, are two-step processes involving the calcination of $CaCO_3$ to CaO at high temperatures followed by the reaction with a phosphate reagent. The new suggested method, instead, involves the full transformation of bCCP into HA nanoparticles in one step offering, in this way, a more sustainable approach. Moreover, it is low-cost since it can avoid the use of expensive hydrothermal autoclaves, additives, and high-purity calcium reagents, and importantly, can be performed at relatively low hydrothermal temperatures without any pH adjustment. Both the bCCP and the derived HA particles resulted suitable for biomedical applications, for example in bone tissue engineering, since they are cytocompatible and showed osteoinductive properties. Future researches could test this transformation method on other mollusk species, such as clams that are composed of a different calcium carbonate polymorph, i. e aragonite. Moreover, since the proposed transformation mechanism is based on a dissolution-reprecipitation process, smaller particles sizes of the starting bCCP could be tested to verify if the process can be faster and occur at lower temperatures.

The fourth project compared the capability of different sources of calcium carbonate, one geogenic from quarries and three biogenic from mollusk shells (in particular oysters, scallops and clams shells), to be converted, on a potentially industrial scale, into nano-crystalline and amorphous calcium carbonate using the ball milling technique rather than being synthetically produced by wet reactions. The results showed that the mechanochemical process produced a reduction of the crystalline domain sizes and formation of amorphous domains (ACC), which co-existed in micro-sized aggregates. Interestingly, the biogenic $CaCO_3$ (bCC) behaved differently from the geogenic one (gCC). In particular, gCC converted only into ACC while the conversion of the crystalline phase of bCC in ACC occurred with the concomitant transition of calcite to aragonite and vice-versa. This diverse behavior could be attributed to the unique presence in the bCC of the intraskeletal organic matrix. In addition to this, increasing the ball milling time, the ACC from bCC converted into crystalline phases, while gCC increased the content of ACC and decreased the size of the crystalline domains. In view of the potential application of ACC, this research showed that the use of bCC offers a wider scenario of structural features and stabilities with respect to the gCC.

The last project showed that it is possible to obtain individual shell components either

individually or in combinations from shrimp and crab waste shells using different chemical and thermal treatments. These diverse materials were composed of calcium carbonate and organic molecules inter- and intra-mineral; of calcium carbonate and organic molecules intra-mineral; of organic molecules, such as chitin and proteins; of only calcium carbonate; and only chitin. Among the many applications that chitin and calcium carbonate have, it was decided to evaluate the ability of these different substrates to act as absorbent agents for dyes from polluted waters. Since each singular component of crustacean shells has a specific adsorption capability, in this research we demonstrated that newly developed material, consisting of multi-component extract, can have an adsorption capability that is increased by the synergic action of the single components. These multifunctional materials, in the future, could also be tested to adsorb heavy metals from polluted waters in a full wastewater treatment view.